Large-Eddy Simulations with Conjugated Heat Transfer of an Internal Combustion Engine

by

Angela Tjia Sin Wu

A dissertation submitted in partial fulfillment
of the requirements for the degree of
Doctor of Philosophy
(Mechanical Engineering)
in the University of Michigan
2020

Doctoral Committee:

Professor Volker Sick, Co-Chair
Professor Eric Johnsen, Co-Chair
Dr. Seunghwan Keum, General Motors
Professor Venkat Raman

Angela Tjia Sin Wu

atswu@umich.edu

ORCID iD: 0000-0002-6456-5786

Dedication

This dissertation is dedicated to my family and friends.

Acknowledgements

First and foremost, I would like to thank my advisor, Professor Volker Sick, for his unwavering support and guidance throughout my graduate studies and the development of this work. I would also like to thank my co-advisor, Professor Eric Johnsen, for inspiring in me a passion for computational fluid dynamics. I want to thank Dr. Seunghwan Keum for his advice, mentorship, and for answering my endless questions on combustion modeling. I would also like to Professor Venkat Raman for being my committee member and teaching me about turbulence and combustion modeling.

I would like to thank my source of funding for the work presented in this dissertation. This work was partially supported by General Motors through the GM-UM Collaborative Research Lab (GM-UM CRL), the University of Michigan Mechanical Engineering Department NR-Regents Fellowship, and the National Science Foundation (NSF) INTERN Program, supplement to CBET 1402707 grant. The INTERN Program allowed me to intern at General Motors and collaborate with the Diagnostics and Simulations Group. I would especially like to thank Dr. Scott Parrish for accepting me into his group and sharing their facilities with us, Dr. Jian Gao and Dr. Ronald Grover for their support on conjugate heat transfer modeling, and Dr. Xiaofeng Yang for his help with GT-Power. Also, I would like to thank Dr. Tristan Burton, Dr. Nitesh Attal, and Dr. John Etcheverry of Convergent Science for their help with CONVERGE and with licensing.

I would like to thank my friends and colleagues of the Sick Lab at the University of Michigan for making graduate school the best time of my life and for their unfailing support. Thanks to Dr. Ahmet Mazacioglu for our shared love of food, animals, and sense of humor, Dr. Ivan Tibavinsky for our philosophical talks, Dr. Mohammad Alzuabi for our collaboration and shared frustrations with GT-Power, Lucca Henrion for his friendship and advice, and Allison Gibson for being weird with me. Thanks to Dr. Hao Chen for teaching me about PIV and image processing, Dr. Michael Gross for his vast knowledge of all things, Dr. David Reuss for inspiring me with research questions, and James Elkins for his technical support and friendship. I would

also like to thank my friends, Miriam Figueroa and Fanny Pinto, for always being open to trying out new things with me.

I could not have done my Ph.D. without the support of my husband Kenny. He has been there for me for more than 15 years, throughout which we have faced many challenges and shared many triumphs. I would also like to thank my friends and family back in Suriname for their continuous support. I miss them dearly. Finally, I want to thank our dog Oskar, for teaching me about spending time on the important things in life.

Table of Contents

List of Tables

List of Figures

Abstract

Engine heat transfer affects the internal combustion engine's (ICE) efficiency, performance, and emissions. Approximately 20 to 30% of the energy from the combustion process is lost through convective heat transfer across the engine walls. To improve the predictive capability of engine simulations, engine heat transfer needs to be simulated accurately. This requires that we capture the temporal, spatial, and cycle-to-cycle variations (CCV) in engine heat transfer. In conventional engine CFD, uniform and constant surface temperature boundary conditions are often applied. To improve these boundary conditions, conjugate heat transfer (CHT) can be used which couples the heat transfer solution between fluid and solid domains. In this work, CHT was integrated with large-eddy simulations (LES), with moving valves and pistons, to improve heat transfer predictions for motored and fired operating conditions using a commercial CFD software. The quality of these simulations was evaluated against bulk flow, near-wall flow, and near-wall temperature measurements performed by the Quantitative Laser Diagnostics Laboratory (QLDL) group at the University of Michigan. Such comparisons to the near-wall flow and temperature fields have not been available to date and are described here for the first time. By using CHT, improved heat transfer predictions were obtained compared to baseline LES with uniform temperature boundary conditions.

In the first part of the study, the motored operating condition was simulated with uniform temperature boundary conditions, and modeling methods were analyzed, including turbulence models, wall models, near-wall mesh resolution, and thermal boundary conditions, which improved heat transfer predictions. A statistical convergence criteria was developed using the well-known LES quality index, and statistical convergence was demonstrated for the motored LES after 10 cycles. However, more LES cycles are likely needed to capture the measured level of CCV. Bulk flow analysis shows that the simulation of the intake jet largely impacted the predicted vortex center locations and heat transfer. Near-wall flow analysis shows that improvements in the wall models are needed.

In the second part of the study, CHT was integrated with LES for motored and stoichiometric fired operating conditions, and validated with measured surface temperature within 1.4% and 3% error for the motored and fired conditions, respectively. Spatial, temporal, and CCV in the surface temperatures were predicted. The results show the impact of surface temperature on the predicted flow and temperature fields. For example, the spark plug surface temperature experienced a large spatial temperature range from 350 to 1000 K, which significantly impacts the heat transfer at the spark plug and the early combustion process. The LES CHT method improved the predicted level of CCV in the surface heat flux which compared better with the measurement. This work was performed in a parallel effort in near-wall PLIF temperature field measurements to assess the LES CHT predictive capability in the near-wall temperature field. Length scale analysis was performed in the wall-normal direction to provide insights into the spatial scales that are important in engine heat transfer. These length scales decrease towards the wall, indicating that temperature gradients increased towards the wall leading to increased heat transfer. Their distribution also became more homogeneous towards TDC, and therefore, heat transfer becomes more spatially uniform with increased compression.

Chapter 1 Introduction

1.1 Background and Motivation

The invention of the internal combustion engine (ICE) in the late 19th century revolutionized transportation, but not without consequences in energy usage, public health, and human safety. The world consumed approximately 572 quadrillion BTU of energy in 2016 [1], with the United States alone using approximately 97 quadrillion BTU that year [2]. The transportation sector makes up 29% of the energy consumption in the U.S., with 92% of the energy derived from fossil fuels [3], an ever-dwindling resource. Energy consumption is projected to increase by almost 40% in 2040, and the use of fossil fuels is only going to increase [4] (see Figure 1.1). Emission of greenhouse gases is also a large concern due to their contribution to climate change. About 6500 million metric tons of CO_2 were emitted in 2016 in the US, of which 28% is from the transportation sector [5]. Nitrogen oxides (NOx) and unburned hydrocarbons (HC) are additional harmful emissions. With ever-tightening regulations on engine emissions and fuel economy, ICEs will need to be designed with low emissions and high fuel efficiency.

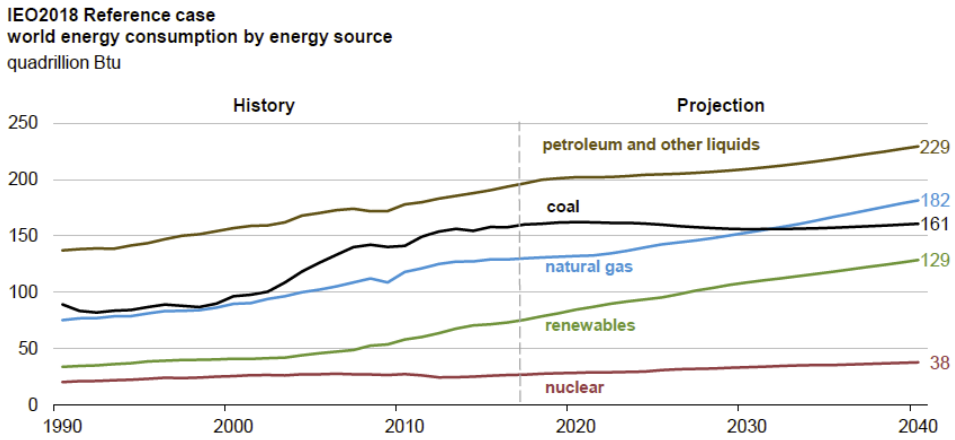

Figure 1.1. Projected energy consumption broken down into energy sources [4].

1.1.1 Importance of Accurate Heat Transfer Modeling

Engine heat transfer occurs through conduction, convection, and radiation. Conduction is the main heat transfer mode in the engine solid components and has a significant impact on surface temperature. Convection is the transfer of thermal energy between a moving fluid and a solid

surface and is the main mode of heat transfer within the engine. This convective heat transfer is controlled by the boundary layer. Therefore, it is important to accurately model the boundary layer development in ICEs. However, periodic changes in the thermodynamic states throughout the engine cycle and large cycle-to-cycle variation (CCV) prevents a well-established boundary layer and makes modeling of the boundary layer difficult. Finally, radiation occurs in engines as the gases emit energy through electromagnetic waves. Radiation is considered negligible in spark-ignition (SI) engines but is significant in compression ignition (CI) engines [6]. Recent spectroscopic measurements, however, have shown that radiation accounts for about 10% of the engine heat loss, and 50% of the radiation is reabsorbed by the burnt gases before reaching the walls. [7]. Thus, radiation helps to redistribute the thermal energy within the combustion chamber, and CFD modeling in the future should use accurate molecular radiation and reabsorption models. But, compared to convective heat transfer, radiation reaching the wall is small. As shown by [8], convective heat loss at full load was approximately 293 J, while radiation reaching the wall was only 15 J or about 5% of the convective heat loss. Therefore, the dominant heat transfer processes in engines are convection and conduction.

Heat transfer is important as it affects the engine's efficiency, performance, and emissions. [9-15]. A typical energy split in ICEs is shown in Figure 1.2. Depending on the engine load, about 20 to 30% of the energy from the combustion process is lost to the coolant as heat is transferred to the engine walls. Too much wall heat transfer leads to lower gas temperatures, lower in-cylinder pressure, and reduces engine efficiency. But if wall heat transfer is too low, this can cause high gas temperatures which lead to conditions that induce auto-ignition and engine knock. This results in high thermal stresses and eventual damage to the engine. This wall heat transfer is influenced by the surface temperature and the gas temperature profile in the near-wall region (NWR). NOx formation is also influenced by the gas temperature, as shown in Figure 1.3. The engine cooling load, wear and tear on the piston rings, and friction are also all affected by engine heat transfer.

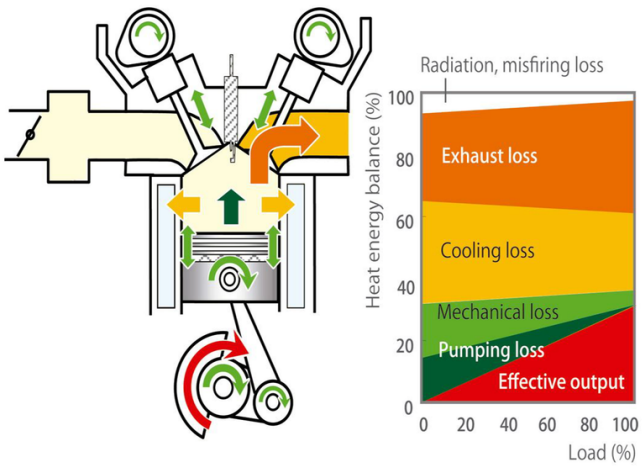

Figure 1.2. Typical energy split in internal combustion engines [16].

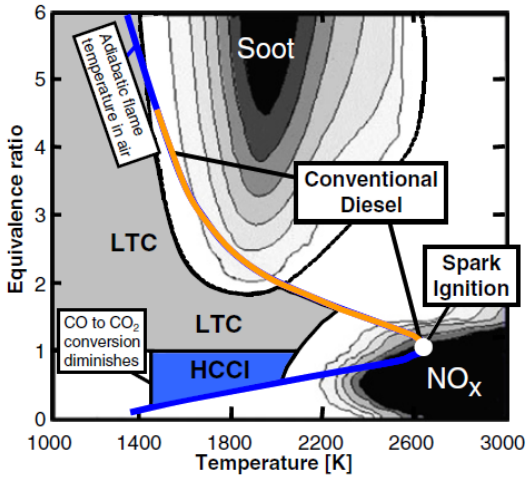

Figure 1.3. Temperature and equivalence ratio dependence of NOx and soot formation [14].

Myers and Alkidas [9] found decreased NOx emissions with decreasing surface temperature. This surface temperature affects the unburnt gases at the beginning of compression and leads to lower maximum burnt gas temperatures and, therefore, NOx emission reduction. The sensitivity of the NOx emissions to surface temperature increased with leaner mixtures. Therefore, as engine operations move towards leaner mixtures, controlling the surface temperature and thus engine heat transfer becomes important in reducing NOx emissions.

Alkidas and Myers [10] measured the surface temperature and surface heat flux at several locations on the cylinder head. They found significant spatial, temporal, and cyclic variations in the engine heat transfer. The local heat flux and its cycle-to-cycle variation (CCV) are strongly correlated with the CCV in the flame arrival at the heat flux probe. The peak heat flux also

increased with volumetric efficiency due to increased convective heat transfer coefficient as gas density increased with volumetric efficiency, and the peak heat flux reached a maximum at near-stoichiometric conditions.

Harigaya et al. [11] studied the relationship between engine heat transfer and knock. They found that under knocking condition, the surface temperature and heat flux increased rapidly, with much higher peak heat flux compared to non-knocking conditions. The peak heat flux also increased with increasing knock intensity. The local surface temperatures and heat flux closer to the knock zones are much higher than those far away from the knock zones. It was found that the heat transfer coefficient is affected by knock intensity for intensities higher than 0.3 MPa. Therefore, to estimate the heat transfer coefficient correctly using empirical correlations, the effects of knock should be included in the equation if knock is present. It is also evident that the local heat transfer condition should be used to locate the knock zones accurately.

Ezekoye et al. [12] studied the relationship between heat flux and surface temperature of a laminar quenching flame in a constant volume chamber. They found that the maximum heat flux decreased with increasing wall temperatures. In contrast, numerically obtained maximum heat flux values increased with increasing wall temperatures due to the single-step mechanism and simplified chemical transport models.

Wang et al. [13] studied the relationship between ignition timing and equivalence ratio on the engine heat flux in a direct-injection engine. Advancing the ignition timing leads to a higher peak heat flux due to higher peak cylinder pressure and temperatures as combustion occurred closer to top-dead-center (TDC), as well as an earlier rise in the heat flux due to the earlier start of combustion. Leaner equivalence ratio leads to lower peak heat flux, and the phasing of the peak heat flux is advanced with richer mixtures due to faster burn rates. They also found significant spatial variations in the heat flux and warned against comparing local heat flux to global heat transfer correlations.

Advanced engine combustion techniques exist that lead to increased efficiency and reduced emissions. Low-temperature combustion (LTC) is such a technique, and as shown in Figure 1.3, they span the low NOx and low soot region of engine operations. Homogeneous charge compression ignition (HCCI) engines are a type of LTC engine, where compression of the homogeneous fuel-air mixture leads to auto-ignition. However, implementing such advanced engines is limited due to difficulty in controlling the combustion phasing and their high-load limit

due to high pressure rise and engine knock [14]. The combustion phasing of HCCI engines is strongly correlated with the onset of increase in heat flux and its peak value [15]. Surface temperature measurements show significant spatial variation, but surface heat flux seems to be more uniformly distributed in this type of engine. The surface temperatures on the engine head were also affected by the coolant flow within the head.

One way to increase the high-load limit and to control the combustion phasing is to control the thermal stratification of the in-cylinder flow [14]. This thermal stratification is affected by turbulent mixing and wall heat transfer and occurs throughout the boundary layer and the bulk gas mixture. By increasing the thermal stratification, the pressure rise rate is reduced and the high load limit can be extended. Engine knock can also be prevented by limiting the surface temperatures. Therefore, understanding and controlling the engine heat transfer in such advanced combustion systems can lead to their increased implementation on the road.

As evident from [9-13], engine performance depends strongly on the amount of heat transfer. It is therefore important to model the engine heat transfer accurately to improve engine CFD. This will aid in the design of more efficient engines that use advanced LTC techniques as these rely on accurate predictions of the gas temperatures to increase the load limit.

1.1.2 Characterization of the Engine Boundary Layer

Engine heat transfer occurs largely through convection in the boundary layer where temperature gradients are large. The near-wall flow controls this convective heat transfer in the boundary layer. Understanding and characterizing this heat transfer in the boundary layer is therefore critical in improving the performance of engines, reducing their emissions, and preventing knock and thermal stress damage [17, 18]. This will also lead to an enhancement of predictive capabilities of computational fluid dynamic (CFD) simulations applied to ICEs, allowing for further optimization of engine designs.

Given the importance of engine heat transfer in ICEs, experiments have been performed to elucidate the behavior of engine boundary layers since the 1980s. Efforts have been made to characterize the momentum boundary layer using different methods. Hall and Bracco [19] performed the first boundary layer measurements in a fired ICE using Laser-Doppler Velocimetry (LDV). They measured the tangential and radial velocity components down to 0.5 mm and 1.5 mm, respectively, from the cylinder wall, and reported the existence of a very thin boundary layer

in motored and fired engines. They also found that the turbulence intensity increased sharply near the wall, indicating that wall-generated turbulence was significant.

A year later, Foster and Witze [20] used LDV to measure velocity and turbulence intensity profiles in the boundary layer as close as 60 μm to the engine wall at two swirl conditions. For motored engine operation and high swirl, the boundary layer was less than 200 μm, and the same turbulence intensity increase towards the wall was found. At low swirl, a thicker boundary layer was found with no increase in turbulence intensity near the wall. Firing the engine leads to increased boundary layer thickness for both swirl levels due to increased viscosity as gas temperature increased.

While LDV can provide highly-resolved velocity measurements at a single point, the flow within the engine is spatially distributed. Particle Image Velocimetry (PIV) allows for spatially resolved measurement of flow velocities in a planar field of view, and it was first used to measure the in-cylinder flow in 1989 [21]. The focus of PIV in ICEs has been mainly the bulk flow regions [21-25]. Very few studies have measured the flow in the NWR. Pierce et al. [26] used both LDV and PIV to study the boundary layer development of five different engines. They showed that the behavior of the boundary layer depends on the engine geometry and operating condition. They characterized the NWR flow behavior in two categories. In the first category, the flow in the near-wall region behaves as a low momentum fluid with an imbalance in the radial pressure gradient forces and centripetal forces due to combined effects of fluid rotation and shear. This type of flow can be found in gas exchange systems that do not promote scrubbing of the wall, and in in-cylinder geometry that does not cause flow normal to the wall. The second, more common category is a very thin layer of low momentum fluid with direct interaction of the wall and turbulent structures. This form is found in engines with overhead valves or two-stroke engines with boost ports. They did not find conventional boundary layers because of fluid rotation, wall scrubbing, and the unsteadiness of the engine flow.

Alharbi and Sick [27] used a hybrid micro-PIV and particle-tracking velocimetry (PTV) approach to measure the near-wall flow down to 45 μm of the cylinder head of a gasoline direct-injection (GDI) engine. They found that recirculation in the core flow near the spark plug caused a reversal of the near-wall flow in the opposite direction. They also identified small-scale vortices that moved around within the boundary layer. The ensemble-averaged near-wall velocity profile

and fluctuation intensity profile changed throughout the engine cycle. In addition, the fluctuation intensities were on the order of the ensemble average velocities throughout the entire engine cycle.

Jainski et al. [28] used micro-PIV to resolve the boundary layer down to 50 μm of the cylinder head, and PIV to measure the bulk flow. Due to the unsteady and not fully developed nature of the engine boundary layer and influence from the three-dimensional core flow, the law of the wall model failed to predict the flow velocity in the outer layer, while in the viscous sublayer the velocity was predicted adequately. The thickness of the viscous sublayer decreased with increasing engine speed. They also found the small-scale vortices described earlier [27].

Greene [29] performed PIV measurements of the near-wall flow at the cylinder head and piston surface of a motored and fired engine and simultaneously measured the surface temperature and heat flux at the head. Several flow phenomena in the NWR were found to exist, including vortices interacting with the wall, impinging flow on the wall with relatively large wall-normal velocities, and narrow shear layers generated due to a flow reversal. Large CCV in the near-wall flow field is found, with the standard deviation of the velocity being greater than the ensemble average value. This is due to the interaction of the turbulent structures from the core flow with the near-wall flow. The log law in the outer region of the momentum boundary layer did not represent the engine near-wall flow well. The influence of the wall on the wall-normal velocity also extended further into the flow than the wall-parallel component. The surface temperature and heat flux varied temporally. The gas temperatures increased during the compression stroke due to compression heating, and the surface heat flux increased to a peak value. During the expansion stroke, the pressure and temperature of the gases decreased, and the surface heat flux decreased with expansion. Reversal of heat flux in the intake and expansion strokes occurred due to the surface being cooled by the incoming charge from the valves.

MacDonald et al. [30] hypothesized that the turbulence in engine boundary layers comes from a balance of turbulence created by wall shear and dissipation of turbulence of the large-scale core flow on the NWR. The core-turbulence dominance over wall-generated turbulence was apparent due to higher Reynolds stress compared to the log-law model. They performed a spatial correlation analysis to identify the extent of the influence of the wall on the core flow and vice versa.

The thermal boundary layer has also been characterized by several studies [31-37]. Lyford-Pike and Heywood [31] measured the thermal boundary layer thickness using Schlieren

photographs and reported an increase in the boundary layer thickness to a maximum at the end of the expansion stroke on the cylinder wall. The boundary layers were also much thicker on the cylinder head and piston surfaces. This difference in thickness was attributed to the different velocity fields at each surface. The thickness also reduced with increasing engine speed. Unsteady boundary layer scaling correlated well with the measured thermal boundary data.

Lucht and Maris [32] used Coherent Anti-Stokes Raman Scattering (CARS) to measure the burnt gas temperature profiles near the cylinder head in a fired engine and were able to fit the data to a ¼ power law. Thickening of the thermal boundary layer was also found during the expansion stroke.

Dec et al. [34] analyzed the development of thermal stratification using planar imaging thermometry in a horizontal plane close to the cylinder head. They observed increased thermal stratification towards TDC, and distinct hot and cold turbulent structures late into the compression stroke. By moving the laser sheet closer to the wall, they observed increased thermal stratification towards the wall, and as TDC was approached, this thermal stratification appeared in laser sheet locations further away from the wall.

Snyder et al. [33] investigated the thermal stratification under fired operation using Planar Laser-Induced Fluorescence (PLIF) in a horizontal plane close to the cylinder head. The thermal stratification developed very similarly for motored and fired condition, with increased thermal stratification towards TDC. The amount of thermal stratification was higher for the motored operating condition, likely due to lower surface temperatures that led to increased wall heat transfer.

Kaiser et al. [35] used PLIF to measure the spatial temperature fluctuations in the compression stroke. The thermal stratification increased from bottom-dead-center (BDC) to TDC due to wall heat transfer, and the spatial distribution also changed, with increasing inhomogeneities near the engine head or piston top. These near-wall fluctuations differed in structure at the piston top and engine head.

Cundy and Sick [36] measured the temperature distribution in the NWR with PLIF thermometry in a motored engine. They found temperature fluctuations that increased towards the cylinder head surface during late compression stroke.

Peterson et al. [37] measured the temperature and velocity fields simultaneously in a motored engine using high-speed PLIF thermometry and PIV. They found colder gas temperatures

near the cylinder head below the exhaust valve during compression. The temperature distribution was also fairly homogeneous near TDC, with increased thermal stratification during early expansion and colder regions near the cylinder head. They also were unable to identify any temperature gradient that one would expect of a canonical thermal boundary layer. This was attributed to the very thin boundary layer due to the short time scales in an ICE and the small temperature difference between the surface and the gas, and therefore the measurement was unable to resolve this boundary layer. The simultaneous measurement of velocity and temperature revealed that the colder gases are mostly transported by the in-plane velocity components. However, there is likely an out-of-plane motion that also contributes to the transport of the colder gases.

Alzuabi [38, 39] has performed PLIF work in the NWR, complementary to the near-wall PIV measurements of Greene [29]. His measurements showed cold and hot structures that move in and out of the plane, and these structures interact with the thermal boundary layer. Temperature fluctuations were found in the near-wall regions, and large values of CCV in the temperature fluctuations were confined in the region close to the head surface. The integral length scales of relative temperatures, obtained from subtracting the instantaneous temperatures from their spatial means, decreased towards TDC and their distribution became more homogeneous.

1.2 Current Engine Modeling Practices

Computational fluid dynamics (CFD) modeling of ICEs has been advancing since the 1970s and has allowed researchers to study the full three-dimensional engine domain. This has led to a better understanding of, for example, how tumble is formed and is affected by the spark plug placement [40], sources of combustion CCV [41, 42], how CCV can be reduced [43], and how the in-cylinder flow affects the mixing process [44].

The accuracy of engine CFD depends on several key parameters, including the turbulence model, mesh quality, discretization scheme, initial and boundary conditions, and wall models. These modeling practices are important considerations especially in the near-wall region where accurate near-wall flow and temperature field predictions are needed due to the importance of engine heat transfer. A review of current engine modeling practices is given next.

1.2.1 RANS vs LES

Internal combustion engines have been traditionally modeled using Reynolds-Averaged Navier-Stokes (RANS) turbulence models. RANS models are based on statistical averaging in which all turbulence is modeled. These models solve for the ensemble-averaged engine flow. In RANS models, "turbulence" is defined as any deviation of the flow from the average. While engine flows are turbulent, there are significant CCV in the engine flow that contributes to the deviation from the ensemble average flow, and therefore contribute to engine "turbulence" [18]. RANS models typically have higher numerical viscosity than LES, which dampens out variations that lead to CCV [45]. Reducing the numerical viscosity has allowed some researchers to use multi-cycle RANS simulations to study CCV [46]. However, since RANS provides ensemble-averaged results, variations in multi-cycle RANS simulations should be considered ensemble-to-ensemble average variations.

Turbulent flows are characterized as having a large range of turbulent length scales L. These range from the smallest scales known as the Kolmogorov scales, all the way up to the integral length scales which are usually defined by the geometry of the flow. Energy is transferred from the large scales to the smallest length scales, after which it is dissipated into heat. The energy spectrum as a function of wavenumber $\kappa = 2\pi/L$ is shown in Figure 1.4.

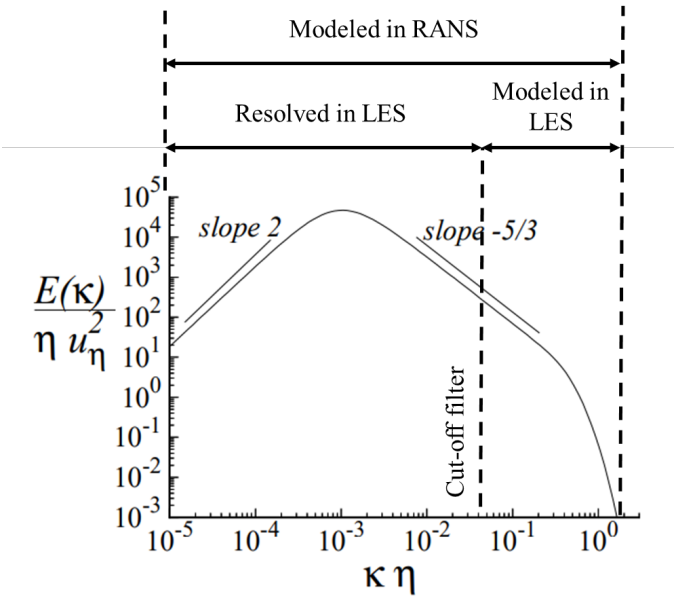

Figure 1.4. Energy spectrum as a function of wavenumber $\kappa = \frac{2\pi}{L}$, where L is the length scale. The length scales that are modeled by RANS and LES are also shown.

In RANS models, the contributions of turbulent energy from all scales are modeled. This modeling may be easiest at the smallest scales which are assumed to be statistically isotropic at large enough Reynolds numbers, but the large length scales are typically not statistically isotropic or universal. Modeling of the large length scales are therefore associated with large uncertainties. In addition, RANS provides the ensemble average flow. If multiple engine cycles are performed with RANS, the resulting variations are actually about the ensemble average. Therefore, CCV cannot be studied with RANS.

In large-eddy simulations (LES), the flow is spatially filtered. Spatial scales larger than the spatial filter used are directly solved for, while spatial scales below the spatial filter size are modeled. Hence, LES turbulence models are typically also known as subgrid-scale models. The statistics of the small scales are assumed to be more universal than the larger scales. Compared to RANS, there is less turbulence modeling required in LES. Also, the LES provides the instantaneous flow instead of the ensemble average as is the case with RANS. The results are individual engine cycles, and when multiple cycles are simulated with LES, researchers can study engine CCV

There are several reasons that make LES well suited to address the flow physics in ICEs, including the unsteadiness of the flow, the moderate size of the computational domain, the importance of the large-scale flow structures, and modest Reynolds numbers [45]. It is expected that with LES we can capture more flow structures due to lower dissipation in the LES subgrid-scale model than RANS. LES can also provide better predictive capabilities by modeling only the subgrid-scale turbulence. With the use of dynamic subgrid-scale models, less input is required in the model parameters with LES. In contrast with RANS, which solves for the ensemble average flow field, LES solves for the instantaneous cycle. This allows the study of CCV with multi-cycle LES [41, 42, 45, 47-52]. However, it should be noted that while LES has been largely used by engine researchers for turbulence modeling, the modeling of other physical processes in the engine are still largely RANS-based [45].

1.2.2 LES Convergence

In terms of capturing CCV, multiple consecutive LES engine cycles should be simulated. Usually the first few cycles are discarded to prevent contamination of the solution field from assumed initial conditions. However, there is no consensus on the number of cycles needed for

statistical convergence of such simulations, nor is there a common quantity of interest that would indicate that statistical convergence has been achieved. To study CCV effectively, enough cycles need to be simulated such that the ensemble average and standard deviation of the flow field and other quantities reach statistical convergence.

There is a general disagreement about the number of cycles needed to reach statistical convergence for the ensemble average and root-mean-square (RMS) quantities. According to Granet et al. [50] and Goryntsev et al. [53], to reach statistically meaningful results, 25 cycles are needed for the mean flow and 50 cycles for CCV. However, many LES studies simulated different numbers of cycles. Truffin et al. [42] used 10 cycles for their stable case with low CCV. They reproduced the ensemble-averaged cylinder pressure but underestimated the level of CCV. For their unstable, high CCV case, they simulated 28 cycles, and captured the slower combustion cycles but were unable to predict the faster cycles found in the experiments. Nicollet et al. [40] simulated 12 consecutive cycles for validation of the mean flow field, and 35 consecutive cycles for the CCV analysis of the velocity fields.

Several studies did not show statistical convergence of their results, but the number of cycles will affect the comparisons between experiments and simulations. Toledo et al. [54] simulated 10 cycles for a square engine. They found good agreement in the mean velocity profiles during the intake stroke, but the predictions did not perform well in the compression stroke due to slower convergence of the statistics as turbulence intensity increased. Hasse et al. [55] simulated the same square engine for 10 consecutive cycles. Compared to the ensemble-averaged measurement of 100 cycles, their simulation captured a more pronounced recirculation zone that was not averaged out due to the low number of simulated cycles. They also compared the ensemble-averaged mean velocity profiles and turbulent kinetic energy during the intake and compression strokes. Like the previous study [54], the agreement declined during the compression stroke due to increased turbulence intensity. Abraham et al. [56] compared 60 LES cycles to 60 measured PIV cycles. Their comparisons show that the kinetic energy of the ensemble average and the standard deviation of the velocity fields differ between measured and simulated results during the intake stroke, mainly due to differences in the intake jet. Also, cyclic variability in the LES data was much higher than the PIV.

To show statistical convergence, several different metrics can be used. One frequently used metric is trapped mass. Enaux et al. [41, 57] showed that the trapped mass stabilized after the first

two cycles. Pera et al. [58] showed that the first cycle was heavily influenced by initial conditions as that cycle's trapped mass was different from the rest of the simulations. Analysis of the trapped mass alone showed that the cycles have converged after 16 cycles. Baumann et al. [59] and Kuo et al. [60] used trapped mass to show that the simulation converged after the third cycle. Nichani et al. [61] found that the trapped mass converged after 10 cycles.

But trapped mass alone cannot be used to show that all variables have reached statistical convergence. The statistical convergence of the in-cylinder dynamics need to be considered as well. Enaux et al. [41] used the internal burnt gas recirculation rate as a second convergence criteria. While the trapped mass stabilized after cycle 2, the internal burnt gas recirculation rate did not reach statistical convergence within 25 cycles. Enaux et al. [57] showed that 25 cycles are needed to evaluate the mean in-cylinder dynamics, as the phase average over 25 cycles was about 6% different from the phase average over 100 cycles. Increasing the sample size led to smoother flow fields. Dugué et al. [62] indicated that their LES results reached statistical convergence through analyzing the convergence of the resolved turbulent kinetic energy. Vermorel et al. [63, 64] simulated 9 cycles and evaluated the statistical convergence using the in-cylinder pressure curves for each cycle. They found no convergence towards the ensemble average pressure, but their simulations spanned the width of the experimental pressure envelope. Baumann et al. [59] showed that the trapped mass converged after cycle 3, but found discrepancies when comparing the flow field to the measurement, and attributed this difference to the limited number of samples. For example, they compared the RMS velocities of the LES and PIV measurement which consists of 600 cycles. They found the simulated RMS velocities are not as smooth as those of the measurements, and this might indicate that the second-order moments of the velocity fields at this location have not yet converged.

However, the location of the velocity statistics analyzed will also affect the statistical convergence analysis. For example, velocities near the tumble core and intake jets need more than 2700 cycles to reach convergence. Kuo et al. [60] also analyzed the convergence of the average in-cylinder pressure in addition to the trapped mass. While trapped mass reached statistical convergence within 3 cycles, the in-cylinder pressure reached it within 10 cycles. Hasse et al. [65] compared the ensemble average flow field from 13 simulated cycles to 100 measured cycles. Asymmetry in the simulation results was found and was attributed to the small number of simulated cycles. Also, differences were found in the structure of the RMS velocity field due to

the small number of simulated cycles. They concluded that 50 measured cycles are needed to obtain stable statistics for the experimental RMS velocities.

Some studies developed other convergence criteria besides trapped mass, in-cylinder pressure, and velocity field comparisons. Kuo et al. [60] also used the relevance index as a statistical converge indicator. The relevance index is obtained by projecting one flow field onto another and shows the difference in flow structure (i.e. velocity vector direction). If a value of 1 is obtained, the flow structures are very similar between the two flow fields. They projected the 56-cycle planar averaged flow field to various selected number of cycles averaged flow field and compared the mean and RMS velocities at two crank angle degree locations. It is shown that the flow field structures become similar as the number of cycles is increased to 56. 10 cycles are needed to reach statistical convergence of the mean and RMS velocities. From their 56 consecutive cycles, they discarded the first 10 cycles.

Janas et al. [66] proposed a criteria for the number of cycles needed in a simulation. A large enough number of samples is reached when the combined modeling and numerical error is approximately equal to the difference of the mean from the simulation from the mean of the experiment. For example, error bars were drawn on the velocity profiles at two locations. They compared these profiles to the measurement. If the error of the simulation becomes smaller such that the experimental profile is outside of the error bars, then the simulations can be stopped since statistical convergence was reached. However, sampling of the velocity profiles is highly dependent on spatial location, and therefore this criteria would need to be performed over many points in the cylinder.

Nichani et al. [61] developed a convergence index to study the statistical convergence of the velocity field. This index quantifies the similarity between the average planar flow fields of the first n cycles with the average of $n + 1$ cycles. This is done by projecting the ensemble average velocity field of n cycles onto the ensemble average velocity field of $n + 1$ cycles. A value of 1 is reached when the velocity fields have reached statistical convergence. They analyzed both the ensemble average and RMS velocity fields and found statistical convergence was reached after 10 cycles.

Schiffmann et al. [22] showed that the convergence of the ensemble-averaged and the standard deviation of the velocity field, obtained using PIV, is dependent on the number of cycles in the ensemble averaging process and that there are some correlations between the flow fields of

the previous cycle to the next. It was also shown that regions of low coefficients of variance (COV), which is the standard deviation divided by the ensemble average, converged faster than regions of high COV. The measured in-plane velocity components did not show convergence until 1500 cycles were ensemble-averaged. Such a large number of cycles is, of course, too computationally expensive to compute. Therefore, comparisons of simulations to measured data need to be done carefully, and perhaps subsamples of the PIV data need to be taken for a more objective comparison.

Because of these different metrics, there is a general disagreement on how many initial cycles should be removed to reduce initial condition bias on the statistics of the simulations. For example, for a 2-D engine LES, Moureau et al. [67] discarded the first 5 of 20 cycles. Truffin et al. [42] and Yue et al. [68] discarded the first 2 cycles. On the other hand, Wang et al. [43] and Kuo et al. [60] discarded the first 10 cycles.

It is clear that there is a large discrepancy in the engine LES community about the number of LES cycles that need to be simulated, how many cycles need to be discarded to remove initial condition bias, and a common convergence criteria that reduces sampling effects such as the spatial location. One of the objectives of this dissertation is to develop consistent and effective criteria for LES convergence so that enough cycles are simulated such that statistical convergence is met.

1.2.3 Modeling of the Near-Wall Region

Due to the importance of heat transfer in engines, it is essential that the near-wall flow and temperature fields are modeled accurately. Engine CFD simulations do not fully resolve the boundary layer, which generally shows stiff gradients and requires a very fine grid and small time steps. Instead, the near-wall flow and heat transfer are modeled by empirical wall models, such as the law of the wall [69]. Due to the ease and low computational costs of wall models, they have been used extensively in ICE modeling and provide reasonable predictions, see for example [40, 50, 60, 70, 71].

These wall models were developed based on several assumptions, such as steady-state and no adverse pressure gradients, which may not be valid in IC engines [72]. The law of the wall model was also developed for wall-parallel flows, but engine flows are highly three-dimensional. Heat transfer in engines is also highly correlated with the wall-normal velocity [73], but this velocity component is not included in the wall model. As shown by previous experiments, the wall

model works well within the viscous sublayer but fails in the outer region due to interactions with the core flow [27-30]. This wall model can be implemented perhaps more accurately if the near-wall grid is within the viscous sublayer. However, this is infeasible since it requires a very fine near-wall grid.

Engine simulations often model the momentum boundary layer with the law of the wall [69], or, if LES subgrid-scale models are used, the Werner and Wengle model as described later in Chapter 2 [74], but improvements have been suggested that have yet to be implemented in CFD [72, 75]. Ma et al. [72] analyzed several wall models frequently used in engine CFD against measurements of a motored near-wall flow [28]. This was not a three-dimensional CFD study, but a simple evaluation of different models over a small sub-volume near the wall, with boundary conditions obtained from the measured data. They showed that the law of the wall had several shortcomings when applied to a motored ICE flow, one of which is that the first gridpoint has to be within the viscous sublayer to obtain reasonable shear velocity predictions. From these shortcomings, a non-equilibrium wall model was developed to include effects from the transient, convective, wall-normal velocity, pressure gradient, and pressure work terms, which improved the predicted velocity profile. They also predicted a non-monotonic behavior of the temperature profile in the NWR but did not have experimental data for validation. In a follow-up study, Ma et al. [75] extended their non-equilibrium wall model to a fired engine flow. Their model included the heat release rate from combustion in the energy equation. In comparison to the law of the wall and several heat transfer correlations, their non-equilibrium model improved velocity and heat flux predictions. Peak heat flux was also well predicted for the fired condition.

The non-equilibrium wall model is a set of partial differential equations and requires several gridpoints within the boundary layer to be solved numerically. This may be impractical in engine simulations due to increased mesh and computational requirements. Engine CFD requires a quick turnaround time and thus dense grids cannot be used [45]. Therefore, for practical engine simulations, conventional wall models such as the law of the wall and the Werner and Wengle model still have value within the engine community with supposedly reduced accuracy.

The thermal boundary layer model has been investigated and improved over decades, mainly to incorporate the effects of variable density and temperature effects on heat transfer [76-82]. The most used heat transfer models in engine CFD are the Angelberger model [76] and the Han and Reitz model [77]. Due to the strong temperature gradient in the NWR, the Angelberger

model is based on the thermal law of the wall but includes non-isothermal effects on the variable fluid properties. The Han and Reitz model includes effects of variable density and turbulent Prandtl number, and the model parameters were optimized with a RANS turbulent model. Recently, there have been efforts to develop more advanced heat transfer models for ICEs that are not yet implemented in commercial CFD codes. In addition to the effects of variable density and variable turbulent Prandtl number, Keum et al. [78] also included variable viscosity in their wall model. Berni et al. [79] used mean thermodynamic properties from the near-wall cells in their thermal wall model with time-variable Prandtl number, which performed better for engines with smaller temperature gradients at the wall. In contrast, they demonstrated that the Angelberger or Han and Reitz models worked well for engines with higher wall temperature gradients. Šarić et al. [80, 81] developed a hybrid model using the Han and Reitz model and used a more advanced RANS k-ζ-f turbulence model to improve heat flux predictions. Nuutinen et al. [82] developed a wall model that include temperature gradient-induced density and property variations with a low-Reynolds number turbulence model, and imbalance contributions from transients, convection, pressure gradients, and sources.

Validation of these heat transfer models in ICE simulations requires further experimental investigation, especially in the NWR, through detailed velocity and temperature field measurements. A thorough evaluation of the near-wall flow and temperature fields of ICEs is sparse due to a lack of near-wall measurements, which have only recently become available [27-29]. This is especially important when wall models are used in multi-dimensional engine CFD since these wall models will affect the predicted near-wall region and engine heat transfer. Therefore, if wall modeling in multi-dimensional engine CFD is to be improved, we first need to validate the near-wall distributions and analyze the shortcomings of current wall models. Such an evaluation is currently lacking in the literature.

1.2.4 Conjugate Heat Transfer Modeling

In addition to the wall models, the boundary conditions will also affect the accuracy of heat transfer predictions. Typically, the no-slip boundary condition is applied for the flow side of the simulation. For the thermal side, uniform and constant wall temperatures are applied due to lack and/or difficulty in obtaining surface temperature data, especially on the inner surfaces of the combustion chamber. But, as shown in Figures 1.5 and 1.6, there are significant spatial, temporal,

and cycle-to-cycle variations in the surface heat flux and surface temperature in SI engines [15, 83]. Such variations are caused by the local velocity and temperature conditions within the engine. Therefore, using a constant and uniform wall temperature as the thermal boundary condition can be detrimental to engine heat transfer predictions.

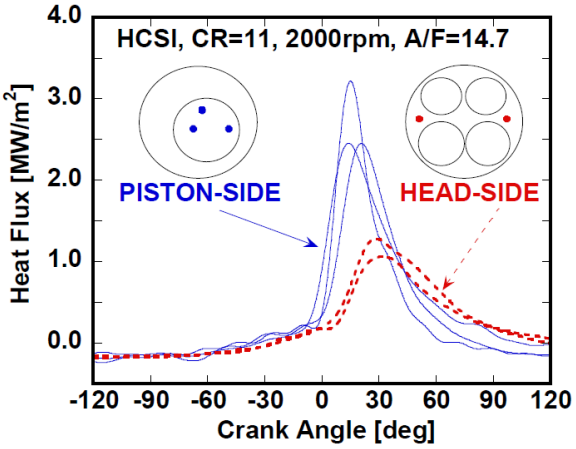

Figure 1.5. Heat flux at multiple locations on the cylinder head and piston surfaces showing spatial and temporal variations [15].

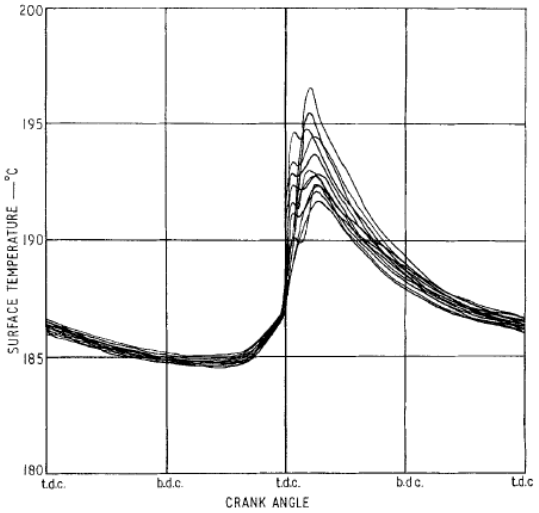

Figure 1.6. Cycle-to-cycle variation in surface temperature [83].

Conjugate heat transfer (CHT) solves the coupled heat transfer between fluid and solid domains and solves for the surface temperature at the fluid-solid interface. CHT modeling can provide improved thermal boundary conditions as it results in spatially and temporally varying temperatures, leading to more accurate engine heat transfer predictions. Recently, CHT has been applied to engine modeling with RANS turbulence models [84-101]. The CFD and CHT simulations are coupled by the resulting wall temperatures from the CHT simulation, and the heat

transfer coefficients and fluid temperatures from the CFD calculation. These CHT simulations can then be used in the optimization of coolant jackets, predicting engine knock, improved emissions studies, and thermal stress analysis of the engine components.

There are three typical multi-dimensional CHT modeling methodologies. One is to use CHT to solve the coupled heat transfer between the engine solid components and liquid cooling jacket, while the in-cylinder flow is solved using CFD [86, 90, 93, 94, 96, 98, 100]. A second method is to use CHT to couple the in-cylinder gas and solid components without any cooling jacket simulations [84, 85, 88, 89, 92, 97, 101, 102]. The third method is to use CHT to solve the heat transfer between the engine solid components and the in-cylinder flow, while the liquid cooling jacket is simulated using CFD [88, 91, 95, 99].

Blank [84] created one of the first engine CHT model with RANS to model the conduction in the valve and its effect on the velocity and temperature fields, and reported results in the exhaust stroke. It was found that the moving valve and the heat transfer within had a large influence on the temperature field. Eight years later, Liu and Reitz [85] developed a more comprehensive engine model with KIVA code to obtain the surface temperatures of the combustion chamber using CHT. They first computed the heat flux along the combustion chamber surface using CFD with constant surface temperatures, which was then applied to a solid heat transfer simulation. This provided updated surface temperatures which were subsequently applied to the CFD simulation. This iterative method continued until the wall temperatures converged. They were able to predict the temporal evolution of the surface temperature on the cylinder head very accurately for motored and fired engine operations.

Xin et al. [86] used CHT to solve for a fired engine operation, but excluded the CHT calculation in the valves. They iterated between a RANS CFD combustion model and a CHT model and showed that three iterations were required for converged boundary conditions. They predicted heat flux with CHT that differed more than 20% from the heat flux obtained from simulations using uniform wall temperatures. The computed surface temperatures also showed that the cooling path needs to be improved between the valve bridges. With their CHT calculations, they also predicted higher gas temperatures and peak in-cylinder pressures. However, with the valves excluded, most likely the heat transfer at the valve bridges is overestimated.

Urip et al. [88] implemented the CHT model in KIVA-3V for a direct injection engine but also excluded the CHT calculation in the valves. The vaporization of the fuel was much faster with

the CHT model than with a uniform temperature model. In a second study, Urip et al. [87] implemented CHT between the in-cylinder flow and solid components, and a separate liquid coolant simulation was performed. They predicted hot spots around the exhaust valve due to the blowdown process when the exhaust valve opened. Again, since their study did not involve CHT calculation of the valves, this heat transfer may be overestimated.

Nuutinen et al. [89] performed CHT calculations with different wall models using two RANS turbulence models. Heat transfer in the piston was predicted, and it was found that the surface temperature and total piston heat transfer differed considerably depending on the turbulence and wall model configurations.

Fontanesi et al. [90] examined the influence of uniform heat flux obtained from a 1D engine model, versus spatially varying heat flux obtained from CHT calculations, on the heat transfer predictions of a multi-cylinder engine. Only the spatially varying surface heat flux predicted the correct surface temperatures at the engine head at multiple locations.

Li and Kong [91] studied the influence of CHT on emissions and heat release rates and compared the results to a uniform temperature simulation. Their CHT model predicted lower surface temperatures than the applied temperature for the uniform temperature simulation. This led to the formation of more liquid film from the fuel spray, causing a lower heat release rate, higher soot formation, and lower NOx emissions.

Dong et al. [92] excluded the valves in their CHT simulation They found that the thermal boundary condition significantly influenced the steady and transient temperature field as well as the heat flux on the engine wall. For example, the steady-state temperature distribution within the piston depends on the thermal boundary condition. This then affected the piston surface temperature which showed spatial and temporal variation during the engine cycle.

Iqbal et al. [93] compared the use of a full 3D RANS model which gives spatially varying convective boundary conditions and a 1D GT-Power simulation that provides a cycle-averaged uniform heat source for the CHT model. Using a uniform heat source as the convective boundary condition leads to an overprediction of the temperature at the intake valve bridge. Overall, the 3D CFD approach leads to the most realistic convective boundary conditions for the CHT calculation, as it compares better with temperature measurements.

Fontanesi et al. [94] also performed CHT to analyze the impact of wall temperature on knock predictions. Their study showed that knock sensitivity depends strongly on the wall

temperature distribution, as more knock-prone areas were identified with the CHT model than the uniform temperature simulations. In addition, the spatially varying wall temperature also affected the flame front development. The laminar flame speed increased, resulting in faster combustion compared to the uniform wall temperature simulation.

Iqbal et al. [95] were able to predict temperatures within 10% of the experimental measurement at several locations using a CHT model for three engine load conditions. The largest temperatures were found in the exhaust valves and exhaust valve bridge. However, the valves in the CHT model were in the closed position, which neglects the heat transfer influence from flow past the valves when they are open, and most likely leads to an overestimation of heat transfer between the valves and the valve seats.

Cicalese et al. [96] fixed the valves in their CHT simulation but used a variable thermal resistance to simulate the effects of valve motion on heat transfer. The surface temperatures on the engine head and block were overpredicted due to overestimated wall heat fluxes from CFD simulation, which they attributed to the thermal wall function. The Angelberger and the Han and Reitz heat transfer models were both tested, and they showed that the time-averaged heat fluxes from both models were 30% larger than the heat flux from a heat rejection analysis. This was mainly due to their engine which operated more isothermally compared to pancake chamber engines. They then modified the Angelberger model by introducing new scaling for the velocity, temperature, and wall distance, and accounting for Prandtl number temporal variations. Cicalese et al. [98] applied the same methodology to a Diesel engine, with fixed valves and variable thermal resistance, and were able to predict heat rejection to the coolant within a 3% error.

Kundu et al. [97] solved the heat transfer through the piston using CHT for a fired engine. This study shows the importance of the thermal boundary conditions on the outer surfaces of the solid components. Applying a single surface temperature on the outer surface of the piston led to large errors between the measured and simulated temperatures on the piston bowl surface. By dividing the outer piston walls into four different areas and applying different temperatures to each region, they were able to reduce the error to approximately 5%.

Leguille et al. [99] preserved the valve motion in their CHT simulations to better account for the cooling effects of the valves when they are in contact with the valve seats. Their CHT model underpredicted the surface temperatures at four points on the cylinder head by 9 to 12 K.

Significant spatial variation in the surface temperature at the cylinder head and valves were predicted.

Wu et al. [100] found that the resulting spatially varying temperatures from a CHT simulation of a gasoline DI engine significantly influenced the predicted velocity and temperature fields, mixture formation, and fuel evaporation process.

Broatch et al. [101] tested two approaches to obtain the boundary condition for their solid simulation: a combustion CFD model and a rate of heat release (ROHR). With the ROHR method, a spatially averaged convection boundary condition is applied, while the combustion CFD model provides a spatially varying convective boundary condition. The CHT-CFD approach resulted in hotter regions on the piston surface that cannot be obtained with the CHT-ROHR method. It turns out that while the CHT-CFD approach is more expensive time-wise, it was the most precise method compared to the CHT-ROHR and CFD only models.

Misdariis et al. [102] were the first to use CHT with LES by coupling the CFD with a solid simulation of the cylinder head with fixed valves. They were able to predict CCV in the instantaneous heat flux and the cycle-averaged heat flux, and spatially varying surface temperature as shown in Figure 1.7. But, the impact of the cyclic variation of the heat flux on the surface temperature was low. The non-uniformity of the surface temperature affected the flow field and therefore the combustion process. The problem with the study is the use of fixed valves in their CHT model. Using fixed valves is detrimental to the heat transfer predictions as the flow and temperature fields are influenced by the moving valves.

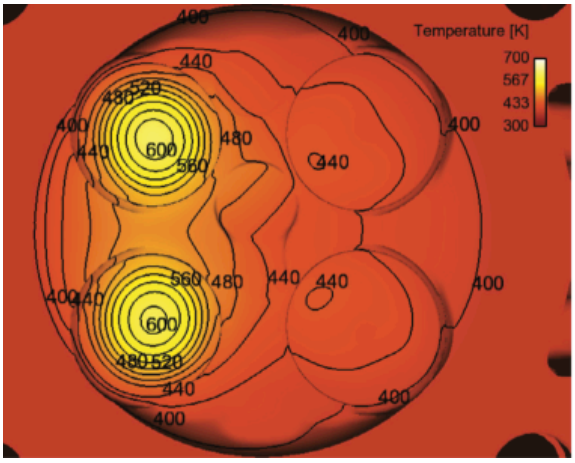

Figure 1.7. Spatially varying surface temperatures on the cylinder head were obtained from conjugate heat transfer [102].

While not a direct LES CHT study, Robert et al. [103] used wall temperatures from a separate RANS CHT study and applied those to an engine LES as the thermal boundary conditions. The valves were not included in the CHT simulation but temperatures were estimated from thermal imaging. Their study focused on the ability of LES to predict knock, and no conclusions were made about whether the RANS CHT provided better predictions due to improved thermal boundary conditions. However, knock is highly dependent on temperature, and it would be prudent to have better thermal boundary conditions to improve knock predictions using LES.

These efforts show that more accurate heat transfer predictions can be obtained with CHT, since it provides improved thermal boundary conditions at the fluid-solid interfaces, compared to applying constant wall temperature boundary conditions in conventional engine modeling. By using LES with CHT, cyclic variation in the surface temperature can be obtained enabling improved CCV studies. However, most CHT studies were done using RANS, and therefore CCV cannot be studied. Currently, there is only one study that combined LES with CHT [102], but the study used fixed valves which leads to an overestimation of heat transfer at the valves. Also, the previous CHT studies were not validated with spatial velocity or temperature field measurements. The major contribution of this dissertation is to improve the LES CHT methodology by including moving solid components and validating the results with flow, temperature, and heat flux measurements.

1.3 Problem Statement

Engine heat transfer needs to be predicted accurately in engine CFD so that these simulations can be used effectively to improve engine efficiency, reduce harmful emissions, and advance engine technology. This requires that we capture the heat transfer physics accurately, i.e. their transient, spatial, and cyclic variations need to be correctly simulated. Significant efforts have been made by the Quantitative Laser Diagnostics Laboratory (QLDL) group at the University of Michigan to obtain in-cylinder flow and temperature measurements, including the NWR, of the transparent combustion chamber (TCC-III) engine. The near-wall data was not available until recently. To improve the accuracy of engine heat transfer modeling, CHT should be used with engine CFD so that temporally and spatially varying surface temperatures can be obtained at the fluid-solid interface. This should be combined with multi-cycle LES which could potentially predict CCV in the surface temperature. Currently, only one engine study using LES CHT exists with inaccurate assumptions such as fixed valves.

1.4 Purpose of the Study

The purpose of the study is to investigate the modeling approaches of ICEs to improve engine heat transfer predictions. First, conventional modeling methods using uniform temperature boundary conditions were analyzed, and the results are compared between different RANS and LES models, wall models, near-wall mesh resolution, and uniform temperature boundary conditions. There is also no clear consensus on the number of LES cycles that need to be simulated for statistical convergence. In this dissertation, a convergence criteria for the number of LES cycles needed to achieve statistical convergence was developed using the LES quality index.

Then, the conjugate heat transfer method was integrated with LES for motored and fired operating conditions. It is hypothesized that the use of CHT will improve the thermal boundary conditions leading to more accurate heat transfer predictions. A collaborative effort with Alzuabi [38, 39], who performed PLIF temperature measurements in the near-wall region of the TCC-III engine, was done to assess the predictive capability of the LES CHT method. Comparisons are made to LES with uniform temperature boundary conditions as the baseline cases.

The simulations are compared and validated with measured bulk flow, near-wall flow and temperature fields, and heat flux of the TCC-III engine. Such an evaluation of the near-wall region from PIV and PLIF resolved measurements has not been available to date. The relevance and kinetic energy indices are used as quantitative metrics between the simulations and measurements. In addition, spatial correlation and length scale analysis was performed to study the structures that are important in engine heat transfer.

1.5 Organization of the Dissertation

The dissertation is organized as follows. In chapter 1, the importance of engine heat transfer is discussed, and the difference between RANS and LES turbulence models is shown. The motivations for using LES for CCV studies and CHT for improved engine heat transfer predictions are provided. In chapter 2, the background is provided on boundary layers, wall models, and different heat transfer models. The methodology of the computational study is discussed in Chapter 3. Chapter 4 discusses motored engine simulations that use uniform temperature boundary conditions, and the effects of turbulence models, near-wall mesh refinement in LES, wall models, and temperature boundary conditions on predictions are shown. Chapter 5 discusses the motored operating condition of LES with CHT and is compared against LES with uniform temperature boundary conditions. Chapter 6 compares the fired operating condition of LES with CHT against

a uniform temperature LES. Finally, the dissertation is concluded and recommendations for future work are provided in Chapter 7.

Chapter 2 Background

The importance of engine heat transfer was discussed in the previous chapter. Convection is the main mode of thermal energy transport in the engine as shown in the previous chapter. A large portion of this convective heat transfer occurs in a very thin region near the surfaces of the combustion chamber, known as the boundary layer. Here, large temperature gradients exist due to differences in the surface and surrounding gas temperatures. Engine flows are highly unsteady, period, and turbulent, and as such, canonical boundary layers do not exist in internal combustion engines. However, a review of canonical flat plate boundary layers is warranted since these are well understood, and wall models in engine simulations are derived from such boundary layers. Therefore, canonical boundary layers are first reviewed, followed by momentum wall models. Differences between canonical boundary layers and in-cylinder engine flows will be discussed. Finally, some of the most used engine heat transfer models are described.

2.1 Laminar Boundary Layer

Parallel flow over a flat surface can be divided into two regions, an outer core flow where the flow is irrotational, and a thin region near the surface known as the boundary layer where viscosity plays a large role [69]. In the boundary layer region, shear stress works to retard the fluid particles, so that the flow velocity from the wall to the core region gradually changes from zero velocity at the wall to the free-stream velocity U_∞. This results in a velocity gradient $\frac{\partial u}{\partial y}$ in the wall-normal direction y, as shown in Figure 2.1. The laminar boundary layer is characterized by non-intersecting streaklines, and exchange of mass or momentum occurs between the adjacent layers on a microscopic level.

If the surface temperature T_s is different from the free-stream temperature T_∞, the temperature field itself can be divided into a core region where thermal conductivity is negligible, and a region close to the wall where thermal conductivity is significant. A thermal boundary layer also develops, as shown in Figure 2.2.

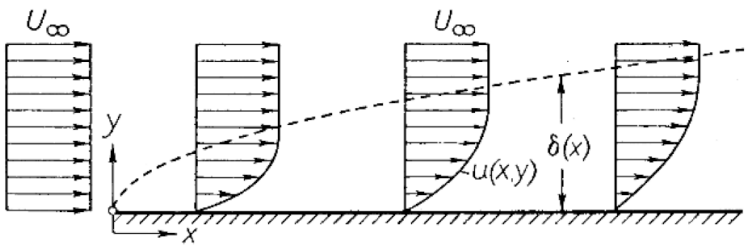

Figure 2.1 Laminar boundary layer development [69].

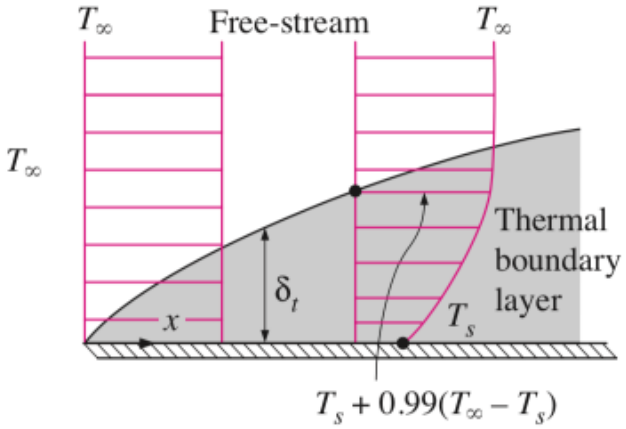

Figure 2.2 Thermal boundary layer [104].

2.2 Turbulent Boundary Layer

In a laminar flow, viscous forces dominate the inertial forces and any instabilities that occur are dampened out by viscosity. In contrast, in a turbulent flow, inertial forces dominate the viscous forces and instabilities are not dampened out. These instabilities cause fluctuations of the flow which are superimposed on the main flow [69].

For boundary layer flows, the Reynolds number depends on the wall-parallel distance x. At large enough distances, a critical number $Re_{x,c}$ is reached, typically on the order of $O(10^5)$, and transition to turbulence occurs as shown in Figure 2.3. Turbulent boundary layers are characterized by mixing across several layers on a macroscopic scale. The velocity gradient of the turbulent boundary layer is much steeper near the wall than that of the laminar boundary layer. The transition of the laminar to turbulent boundary layer leads to an increase in the boundary layer thickness and the wall shear stress. Turbulence also enhances the convective heat transfer due to increased mixing. Figure 2.4 shows qualitatively how turbulent eddies of size l with fluctuating velocity u help to enhance mixing near the wall. This length scale l is orders of magnitude larger

than the mean free path, which is the length scale where molecular transport occurs at. Hence, turbulence promotes wall heat transfer several orders of magnitude above molecular transport [17].

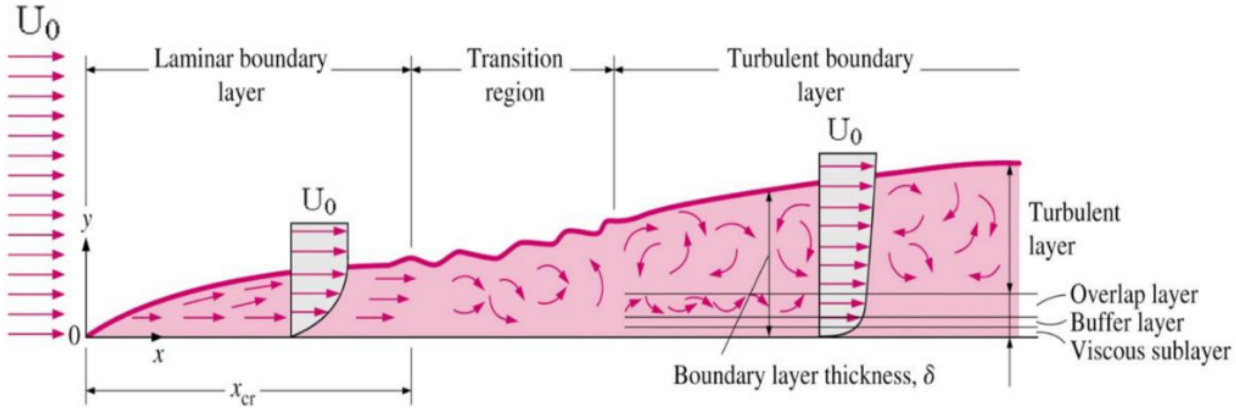

Figure 2.3 Transition from laminar to turbulent boundary layer [104].

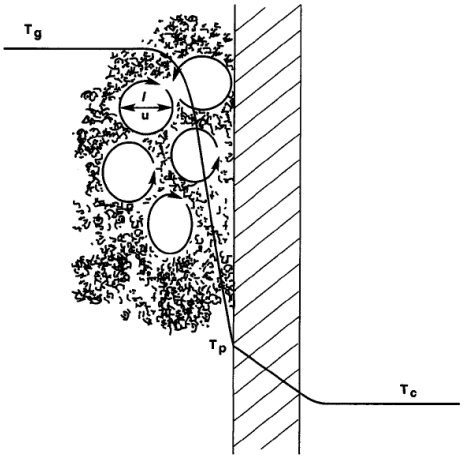

Figure 2.4 Turbulent flow structures promote heat transfer at the engine wall [17].

2.3 Momentum Boundary Layer Model

2.3.1 The Law of the Wall

The law of the wall is a model used to represent the turbulent boundary layer, where the wall-parallel velocity is a function of the wall distance. This wall model assumes the following for the hydrodynamic and thermal boundary layers [77, 105]:

1. The core flow is wall-parallel and quasi-steady,
2. The wall-normal gradients are much larger than wall-parallel gradients,
3. The density and transport properties are constant within the boundary layer,
4. Pressure gradients in the stream-wise direction are negligible,

5. There are no chemical reactions in the gas or on the wall surface,
6. The Reynolds number of the flow is large.

The hydrodynamic boundary layer is then non-dimensionalized by the shear velocity $u_\tau = \sqrt{\frac{\tau_w}{\rho_w}}$, where τ_w is the wall shear stress, which is not known a priori [106]. The wall shear stress is obtained from the velocity gradient at the wall

$$\tau_w = \mu_w \left.\frac{\partial \bar{u}}{\partial y}\right|_w \tag{2.1}$$

Here, ρ_w and μ_w are the fluid density and dynamic viscosity evaluated at the wall. The velocity and the wall-distance are then normalized according to

$$u^+ = \frac{u}{u_\tau} \tag{2.2}$$

$$y^+ = \frac{u_\tau \rho_w y}{\mu_w} \tag{2.3}$$

Turbulent boundary layers are divided into three regions: the viscous sublayer, the buffer layer, and the outer layer. In the viscous sublayer, molecular viscosity plays a significant role, while turbulent stresses are negligible. Outside of the viscous sublayer, turbulent stresses begin to dominate, and an additional apparent viscosity due to turbulence needs to be added.

Based on the assumptions above, the hydrodynamic law of the wall is

$$u^+ = \begin{cases} y^+, & for\ y^+ < 11.8 \\ \frac{1}{\kappa} ln\, y^+ + B, & for\ y^+ > 11.8 \end{cases} \tag{2.4}$$

Here, κ is the von Kármán constant, and B is a constant, with usual values being $\kappa = 0.41$ and $B = 5.2$. The wall shear stress is then solved for iteratively and fed to the rest of the CFD domain as a boundary condition.

2.3.2 Werner and Wengle Wall Model

Werner and Wengle [74] developed a wall model to be used with LES turbulence models. The velocity profile u^+ follows the linear law of the wall $u^+ = y^+$ when $y^+ \leq 11.8$, but instead of the log law for $y^+ > 11.8$, a power law of the form $u^+ = A(y^+)^B$ is used, with $A = 8.3$ and $B = \frac{1}{7}$. This was a consequence of experimental results from Ruderich and Fernholz [107]. In their study, the flow encounters a bluff plate, separates, and reattaches to a splitter plate behind it. This

type of flow is found in many engineering problems where the flow encounters sharp objects and corners. They found that the log law does not hold in reverse flow regions or downstream from where the flow reattaches.

The wall shear stress is then calculated analytically using:

$$|\tau_w| = \begin{cases} \dfrac{2\mu|u_{tang}|}{y} & if \quad |u_{tang}| \le \dfrac{\mu}{2\rho y} A^{\frac{2}{1-B}} \\ \rho\left[\dfrac{1-B}{2} A^{\frac{1+B}{1-B}} \left(\dfrac{\mu}{\rho y}\right)^{1+B} + \dfrac{1+B}{A}\left(\dfrac{\mu}{\rho y}\right)^{B} |u_{tang}|\right]^{\frac{2}{1+B}} & if \quad |u_{tang}| > \dfrac{\mu}{2\rho y} A^{\frac{2}{1-B}} \end{cases} \tag{2.5}$$

Here, $|u_{tang}|$ is the velocity magnitude tangential to the wall. This wall model removes the need for iteration to solve for the wall shear stress.

2.4 Heat Transfer Modes

Heat transfer is the transfer of energy due to a temperature gradient. The three modes of heat transfer are conduction, convection, and radiation. Conduction is the transfer of thermal energy in a solid or stationary fluid via diffusion of energy, which occurs due to random molecular motion. The heat flux is quantified using Fourier's law:

$$q''_{cond,i} = -k\frac{\partial T}{\partial x_i} \tag{2.6}$$

$q''_{cond,i}$ is the heat flux vector, k is the thermal conductivity, and $\frac{\partial T}{\partial x_i}$ is the temperature gradient. Conduction is the main heat transfer mode in the solid components of the ICE and has a significant impact on surface temperatures, for example the surface temperature of the spark plug, which affects heat transfer and therefore influences the flame kernel development. The energy equation for conduction through solids, assuming constant properties, is given by

$$C_p\rho\frac{\partial T}{\partial t} = k\frac{\partial^2 T}{\partial x_j^2} \tag{2.7}$$

Convection is the transfer of thermal energy between a moving fluid and a solid surface. It is a combined process of diffusion and advection. Diffusion occurs near the surface where the fluid particles are slowed down by the solid surfaces, while advection is the transfer of energy due to bulk movement of the fluid. If the temperature of the surface is T_s while the fluid is at T_∞, the heat flux is determined by Newton's law of cooling:

$$q''_{conv} = h(T_s - T_\infty) \tag{2.8}$$

where h is the convective heat coefficient. Convection is the main mode of heat transfer within the engine.

Radiation occurs in objects at finite temperatures where energy is emitted via electromagnetic waves. The net radiative heat flux between an object exchanging energy with the surroundings is

$$q''_{rad} = \epsilon\sigma(T_s^4 - T_{surr}^4) \tag{2.9}$$

where ϵ is the emissivity, σ is the Stefan Boltzmann constant, T_s is the surface temperature of the object, and T_{surr} is the surrounding temperature. Radiation is considered negligible in SI engines but is significant in compression ignition (CI) engines [6]. However, recent spectroscopic measurements have revealed that radiation accounts for about 10% of the engine heat loss, and 50% of the radiation is reabsorbed by the burnt gases before reaching the walls [7]. Thus, radiation helps to redistribute the thermal energy within the combustion chamber, and CFD modeling in the future should use accurate molecular radiation and reabsorption models.

2.5 Heat Transfer Modeling in Engines

Engine heat transfer has been modeled using global models, local models, and thermal boundary layer models. A review of the most used heat transfer models follows.

2.5.1 Global Heat Transfer Models

Global models provide the heat transfer coefficient through correlations based on Nusselt and Reynolds numbers. Annand [108] represented the engine heat transfer through a power law:

$$Nu = a(Re)^b \tag{2.10}$$

From this correlation, assuming quasi-steady heat transfer, the global heat flux with contributions from convection and radiation can be estimated using

$$q'' = a\frac{k}{B}(Re)^b(T - T_s) + c\sigma(T^4 - T_s^4) \tag{2.11}$$

Here, k is the fluid thermal conductivity, B is the bore of the engine, T is the bulk gas temperature, T_s is the surface temperature, and σ is the Stefan-Boltzmann constant. For a four-stroke engine, the recommended values for the constants are $a = 0.26, b = 0.75 \pm 0.15$, and $c = (1.67 \pm 0.6)\times 10^{-12}$. The radiation constant c is zero during the compression stroke, while different values are recommended for SI and CI engines since it is hypothesized that the radiation heat transfer in SI engines is smaller than that of the CI engines.

Annand and Ma [83] sought to improve their model by including the first derivative of the gas temperature to add the effects of unsteady heat transfer in their correlation:

$$q'' = \frac{k}{B}(Re)^b \left[a(T - T_s) + \frac{a'}{\omega}\frac{dT}{dt}\right] + c\sigma(T^4 - T_s^4) \tag{2.12}$$

Here, ω is the angular velocity of the engine crankshaft. This model better captured the rise of the heat flux in the CI engine compared to the original Annand model.

The heat transfer correlation by Woschni [109] is a widely used engine heat transfer model. This correlation was originally developed for diesel engines and is defined as

$$h = CB^{-0.2}p^{0.8}T^{-0.53}\left(C_1\bar{v}_p + C_2\frac{V_sT_1}{p_1V_1}(p - p_o)\right)^{0.8} \tag{2.13}$$

Here, C_1 is a constant that allows for scaling the mean piston speed $\bar{v}_p$ to the engine stroke; during the gas exchange period, $C_1 = 6.18$, while during compression and expansion, $C_1 = 2.28$. The other constants are $C_2 = 3.24\times10^{-3}$ m/s-°C and $C = 110$. The second term in the parentheses accounts for the additional gas motion effects due to combustion. T_1 and p_1 are the known temperature and pressure of the working fluid at a reference cylinder volume V_1, while V_s is the cylinder volume at that instant, and $p - p_o$ is the pressure difference between a fired and motored engine. Woschni [18, 110] later modified the correlation to include the effects of swirl in the constants C_1:

$$C_1 = \begin{cases} 6.18 + 0.417\dfrac{v_s}{\bar{v}_p} & for\ gas\ exchange\ period \\ 2.28 + 0.308\dfrac{v_s}{\bar{v}_p} & for\ the\ rest\ of\ the\ cycle \end{cases} \tag{2.14}$$

Here, v_s is the swirl velocity.

Hohenberg [111] remarked that the engine heat transfer should depend on local velocity conditions and the combustion chamber geometry. Modifications were made to the Woschni correlation by changing the characteristic length from the bore of the engine to the instantaneous cylinder volume, the exponent of the temperature, and a different mean velocity defined as:

$$v = p^{-0.6}T^{-0.7}\left(\bar{v}_p + C_2\right) \tag{2.15}$$

This velocity is related to the in-cylinder pressure and temperature, and this equation captures their change throughout the engine cycle. The mean piston speed $\bar{v}_p$ accounts for the effects of engine

speed on velocity. The constant C_2 adds additional turbulence due to combustion and radiation, although the latter portion is small. The Hohenberg correlation for diesel engines is then

$$h = C_1 V^{-0.06} p^{0.8} T^{-0.4} \left(\bar{v}_p + C_2\right)^{0.8} \tag{2.16}$$

where V is the combustion chamber volume, p is the cylinder pressure, T is the mean gas temperature, and C_1 and C_2 are constants. For a direct injection (DI) diesel engine, the recommended values are $C_1 = 130$ and $C_2 = 1.4$. The correlation needs to be modified for gasoline engines since flow and pressure conditions are very different.

The previously described models work well in estimating the heat flux for the specific engine type, condition, and geometry that they were calibrated with, but they are not universally applicable. Extrapolating the correlations to operating conditions and/or geometries outside of those of the original studies can lead to inaccurate heat flux predictions. Modifications of the constants were needed, for example, in the Woschni swirl-correlation, for intake-generated tumble and swirl motions during the closed part of the engine cycle [112]. For a DI engine, the Hohenberg correlation provides more accurate heat flux predictions, while the Woschni correlation underpredicts the heat flux during the compression stroke and overpredicts it during the expansion stroke [13]. Applying the Woschni correlation to an HCCI engine showed deficiencies mainly due to the combustion velocity term. On the other hand, the Hohenberg correlation worked well for HCCI engines, but the effects of engine load on heat flux were hard to capture [15].

In addition, these correlations provide a spatially averaged heat flux value and do not provide good estimates of the local and temporal heat transfer conditions. Using such correlations for SI engines is therefore detrimental since these engines have large spatial variations in the heat flux [15, 113]. If the engine is operated in a stratified mode, even larger spatial variations in the heat flux is found. For example, for a stratified mode, the Woschni correlation overpredicted the global heat flux, while the Hohenberg correlation worked well [114]. Both the Annand and Woschni correlations failed to estimate the temporal variation in the heat flux correctly in a pancake combustion chamber engine [75]. The effects of knock on the heat flux is also not captured by the Woschni correlation [11]. Since engine knock is a local phenomenon that can happen sporadically, capturing the local and temporal heat transfer conditions is important.

2.5.2 Local Heat Transfer Models

Clearly, a local heat transfer model is needed to calculate the local heat fluxes correctly. LeFeuvre et al. [115] used a local Reynolds number in a heat transfer correlation for a diesel engine, since Annand, Woschni, and other previously developed correlations did not predict the instantaneous and local heat flux accurately. They argue against the use of a uniform gas temperature in the combustion chamber in the heat transfer correlation of the cylinder walls. Only by using the local gas velocities and temperatures can accurate local heat fluxes be obtained.

Through local surface temperature measurements, Dent and Sulaiman [116] found two distinct zones in the diesel engine combustion chamber: a high-temperature zone near the piston bowl and head surface, and a lower temperature zones in the squish region. They used the flat-plate forced convection heat transfer correlation with local velocity and the zone temperature.

Another method to calculate the local heat transfer is to use a two-zone model, which divides the in-cylinder gas temperature into a high-temperature region, containing the burnt gases, and a lower temperature, unburnt region ahead of the flame, and using local velocities and gas properties [18]. This leads to two different heat transfer rates depending on if the engine surface is in contact with unburnt or burnt gases. A useful extension of this model is to divide the in-cylinder temperature into a core region where heat transfer is negligible (as in an adiabatic core), and a thermal boundary layer, where heat transfer is important. From the thermal boundary layer region, the local heat flux can be obtained using

$$q'' = \frac{k}{\delta}(T_{core} - T_s) = h(T_{core} - T_s) \tag{2.17}$$

Here, k is the effective thermal conductivity of the thermal boundary layer, T_{core} is the adiabatic core temperature, T_s is the local surface temperature, and δ is the boundary layer thickness.

2.5.3 Thermal Boundary Layer Models

The local heat transfer correlations above depend on the knowledge of the local condition of the gases, which is difficult to obtain experimentally. Instead, one can perform CFD to obtain local gas conditions. To reduce computational resources that are required to resolve the thermal boundary layers, heat transfer models analogous to the momentum wall model have been developed.

Similar to the non-dimensionalization of the wall-parallel velocity component, the thermal boundary layer is non-dimensionalized by a shear temperature $T_\tau = \frac{q_w}{\rho_w C_p u_\tau}$ [117], where q_w is the wall heat transfer rate

$$q_w = k_w \left.\frac{\partial \bar{T}}{\partial y}\right|_w \tag{2.18}$$

Here, k_w is the thermal conductivity of the fluid at the wall. The temperature is then normalized by

$$T^+ = \frac{(T - T_s)}{T_\tau} \tag{2.19}$$

where T_s is the surface temperature. Assuming quasi-isothermal flow near the wall and constant fluid properties, the thermal law of the wall derived by Launder and Spalding is then [118]

$$T^+ = \begin{cases} Pr\, y^+, & for\ y^+ \leq 11.8 \\ \dfrac{1}{\kappa_T} ln\, y^+ + B_T, & for\ y^+ > 11.8 \end{cases} \tag{2.20}$$

Here, $\kappa_T = \frac{\kappa}{Pr_t}$, κ is the von Karman constant, Pr_t is the turbulent Prandtl number, and Pr is the laminar Prandtl number. The constant B_T is defined as

$$B_T = Pr_t \left(B + \frac{\frac{\pi}{4}}{sin\left(\frac{\pi}{4}\right)} \left(\frac{A}{\kappa}\right)^{\frac{1}{2}} \left(\frac{Pr}{Pr_t} - 1\right) \left(\frac{Pr_t}{Pr}\right)^{\frac{1}{4}} \right) \tag{2.21}$$

Here, A is the Van Driest constant, equal to 26.

The Angelberger and the Han and Reitz models are two of the most frequently used heat transfer models in ICEs. Angelberger et al. [76] reformulated the thermal law of the wall for non-isothermal flows, which is more applicable in engine flows due to temperature changes throughout the engine cycle and during combustion. New non-dimensional numbers are introduced for the wall distance $\eta^+$and temperature θ^+ to incorporate variable flow properties:

$$d\eta^+ = \frac{\nu_w}{\nu} dy^+ \tag{2.22}$$

$$d\theta^+ = \frac{\rho}{\rho_w} dT^+ \tag{2.23}$$

Here, ν is the molecular kinematic viscosity. A constant Pr_t number was used in the wall model. The Angelberger model is then

$$\theta^+ = \begin{cases} Pr\,\eta^+, & for\ \eta^+ \leq 13.2 \\ 2.075\ln\eta^+ + 3.9 & for\ \eta^+ > 13.2 \end{cases} \quad (2.24)$$

Han and Reitz also included non-isothermal effects in their wall model, including the turbulent Prandtl number which varies with y^+. The thermal wall model becomes:

$$T^+ = 2.1\,ln(y^+) + 2.5 \ \ for\ all\ y^+ \quad (2.25)$$

As can be seen from the formulation, this model was used for both the viscous and turbulent regions of the boundary layer.

Cicalese et al. [96] recently analyzed the performance of the Angelberger and the Han and Reitz models in a RANS CHT study. The Han and Reitz model predicted a higher heat flux than the Angelberger model that is closer to the measured heat flux. However, both models underpredicted the heat flux in a more recent study, and only by fully resolving the viscous boundary layer were they able to match the measured heat flux [119]. But this study utilized constant wall temperature as the thermal boundary condition, which is an oversimplification as the authors stated, and increasing the accuracy of the thermal boundary condition could lead to better predictions of the heat flux using these heat transfer models.

2.6 Engine Bulk Flow and Heat Transfer Behavior

The engine boundary layer development is highly affected by the bulk flow and heat transfer, as the velocity and temperature fields undergo significant changes through the intake, compression, expansion, and exhaust strokes. When the intake valve opens during the intake stroke, a strong turbulent intake jet enters the combustion chamber with the help of the downward motion of the piston that causes a vacuum in the cylinder. This intake jet brings a cooler charge into the combustion chamber so that heat transfer is from the hotter engine surfaces to the incoming charge. Flow around the intake jet is entrained due to the exchange of momentum with the surrounding fluid. Under the valves, recirculation zones form. The intake jet impinges on the engine wall, generating large-scale flow structures known as tumble and swirl as depicted in Figure 2.5. These flow structures cause stratification in the in-cylinder flow and temperature fields.

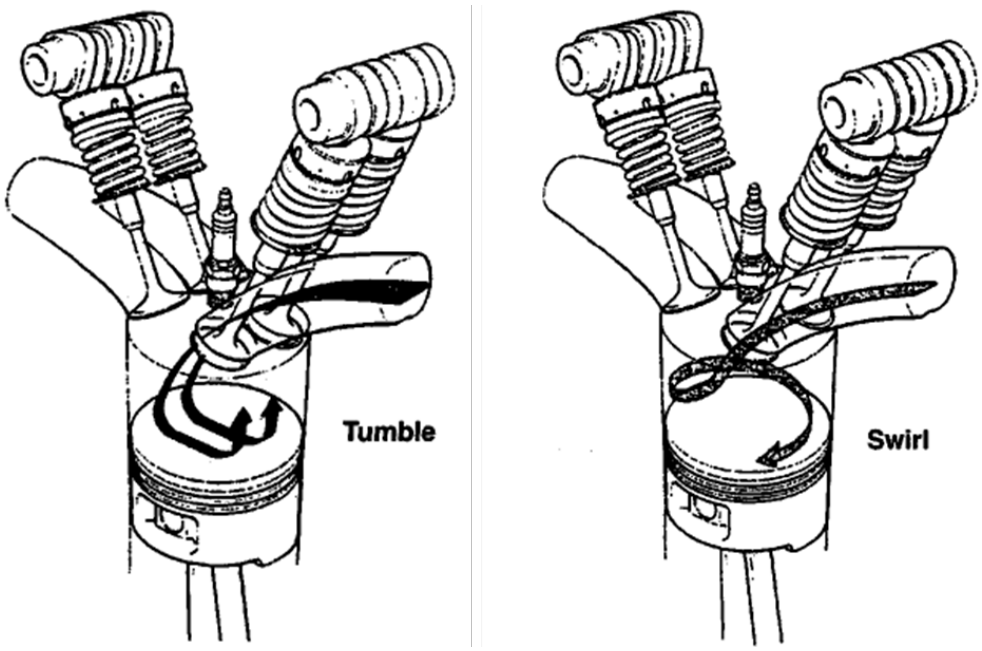

Figure 2.5. Tumble and swirl flows in internal combustion engines [17].

As the engine goes through the compression stroke, the large-scale flow structures are compressed into an ever-decreasing volume. The tumble structure is especially affected by compression, causing it to break down into smaller and smaller structures. Turbulent energy is then transferred from the large tumble structure to smaller and smaller turbulent eddies, leading to an increase in turbulent kinetic energy towards the end of the compression stroke. This is favorable for flame propagation as turbulence promotes flame wrinkling. At the same time, the pressure and gas temperature start to increase. The gas temperature increases above the surface temperature, and heat is now transferred from the gases to the walls. When combustion occurs, gas temperatures increase even more, with the expanding gas causing an increase in the flow velocity. Heat transfer rates are now at their peak. It is also possible that some of the gas is forced into the crevice regions, increasing the surface area over which heat transfer occurs.

During the expansion stroke, the increase in volume and subsequent drop in pressure leads to decreasing gas temperatures, velocities, and heat transfer rates. Then, during the exhaust stroke, the exhaust valves open, and hot gases escape through the exhaust valve opening, known as the blowdown process. Additional heat losses occur during this process from the exhaust gases to the exhaust valves, ports, and manifold.

In addition to temporal changes in heat transfer within the engines, spatial variation in the heat transfer can be significant. The coolant jacket design leads to spatially varying temperatures

in the solid engine components. Local flow velocities can redistribute cooler or hotter gases within the combustion chamber. CCV in the flame kernel development leads to different flame shapes during each cycle, which affects the temperature field.

2.7 Engine Near-Wall Region Behavior

The effects of the turbulent core velocity and temperature fields on the momentum and thermal boundary layer development are significant [69]. This leads to differences in the boundary layers found in ICEs and canonical flat plate flows. This puts into question the validity of using the law of the wall model. The core flow is turbulent and periodic and imposes a turbulent intensity on the boundary layer, which affects its laminar-to-turbulent transition, boundary layer development, and wall heat transfer. Vortical structures and jets are known to interact with the boundary layer [26-29]. Temporal and spatial variations in the heat transfer affect the thermal boundary layer.

Through an order of magnitude calculation, it has been shown that the laminar-to-turbulent transition occurs at a stream-wise distance on the order of 1 m, larger than the typical length scales in engines [29]. Therefore, boundary layers within the engines should be laminar, and wall-shear generated turbulence should be negligible. However, turbulent structures have been found to interact with these boundary layers [26-29]. This means that engine boundary layers are neither laminar nor turbulent. This poses a problem in CFD modeling of engines, which uses wall models such as the aforementioned law of the wall. This wall model was derived for turbulent boundary layers, while turbulence in engine boundary layers is imposed by the core flow.

The assumptions used to derive the law of the wall also do not apply to engine flows, which are three-dimensional, non-uniform, turbulent, and unsteady as it changes considerably throughout the engine cycle. In addition, pressure gradients are non-negligible [72]. Of course, chemical reactions occur within engines, and the Reynolds number is typically much lower than that of canonical boundary layer flows. In addition, compressibility effects from the piston and from combustion, in which the hot gases compress the cooler unburnt gases ahead of the flame, are important in engines, and therefore flow properties such as density are not constant. The boundary layer development at the cylinder head, piston, and cylinder wall is also very different from each other. As the piston moves along the cylinder wall, it scrapes the flow, which causes boundary layers to restart constantly in this region. At the cylinder head, the boundary layer undergoes compression from the piston motion and flame propagation. However, the practicality of such wall

models in industrial engineering applications cannot be overlooked. As such, it is important to evaluate the use of wall models in multi-dimensional engine simulations, since their use will affect the predicted near-wall flow and temperature fields, and engine heat transfer predictions are sensitive to these distributions.

Chapter 3 Methodology

In this chapter, the existing experimental database of bulk flow, near-wall flow, and near-wall temperature measurements conducted at the University of Michigan by previous members of the Quantitative Laser Diagnostics Lab are described first. Then, the numerical methodology used in this dissertation is described in detail. Conjugate heat transfer is integrated with LES, and the methodology is improved upon by including the moving solid components, such as the valves and pistons, to increase the accuracy of the heat transfer modeling.

3.1 Experimental Data

Experiments were conducted in the transparent combustion chamber (TCC-III) engine. This is a two-valve, four-stroke, single-cylinder engine with a pancake-shaped combustion chamber and a centrally installed spark plug in the cylinder head. The engine provides optical access through a quartz liner and a flat quartz piston window. A detailed description of this engine can be found in [22]. Engine specifications are described in Table 3.1, and a schematic is shown in Figure 3.1. For the motored operating condition, only air was introduced. For the fired operating condition, a homogeneous mixture of propane and air was introduced into the combustion chamber. 12 mg of propane fuel was used for each cycle for a stoichiometric air-fuel ratio. The spark timing was at -18 crank angle degree (CAD) after TDC compression (aTDCc). A large collection of the TCC-III datasets is available on Deepblue archive via a permanent URL [120].

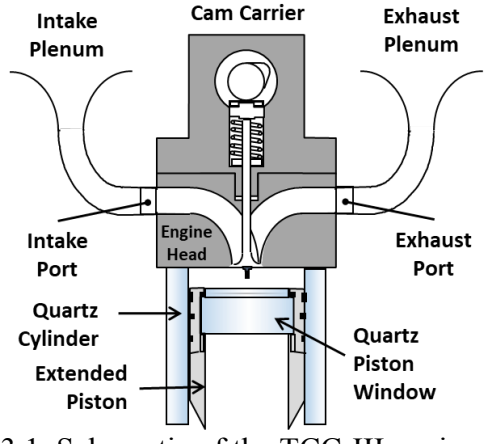

Figure 3.1. Schematic of the TCC-III engine [38].

Table 3.1. TCC-III engine specifications.

Parameter	Value
Bore (mm)	92
Stroke (mm)	86
Clearance at TDC (mm)	9.5
Displacement volume (cm^3)	570
Clearance volume (cm^3)	64
Compression ratio	10:1
Steady-flow swirl ratio	0.4
Connecting-rod length (mm)	231
Intake valve opening (CAD aTDCc)	352.8
Intake valve closing (CAD aTDCc)	-119.2
Exhaust valve opening (CAD aTDCc)	124.8
Exhaust valve closing (CAD aTDCc)	-347.2
Valve seat angles (degrees)	30/45/60/75
Spark plug	AC Delco R44LTS
Spark timing (CAD aTDCc)	-18
Fuel	Propane
Equivalence ratio	Stoichiometric
Combustion mode	Premixed

3.1.1 Bulk Flow Data

Bulk flow measurement data obtained using PIV at the central plane $y = 0$ mm, as shown in Figure 3.2 [22, 120] were used to validate the bulk flow. The engine was operated at 1300 RPM, 40 intake MAP, with intake air heated to 45 °C. For the motored operating condition, dataset S_2013_10_24_01 was used. This dataset contains every 5 CAD from -360 to 330 CAD aTDCc, and 240 cycles were recorded. For the fired operating condition, dataset S_2013_11_07_03 was used. This dataset contains every 5 CAD from -330 to -20 CAD aTDCc, and every 2.5 CAD from -19 to 5 CAD aTDCc, and 457 cycles were recorded. PIV processing was done in LaVision DaVis. The images were interrogated with a decreasing window size from 128 × 128 pixels, 50% overlap, to a final window size of 32 × 32 pixels at 50% overlap, resulting in a spatial resolution of 2.4 mm, oversampled to a final vector spacing of 1.2 mm.

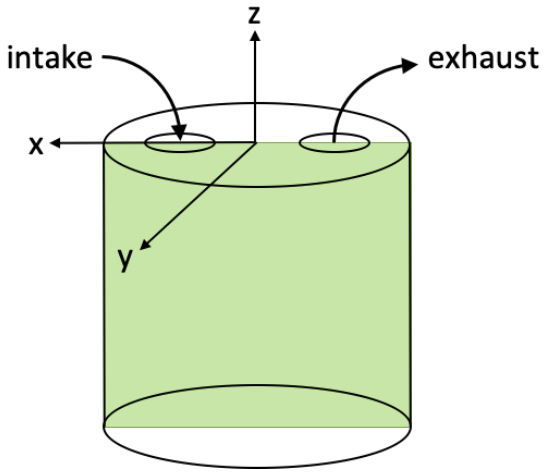

Figure 3.2. Bulk flow PIV measurement plane at $y = 0$ mm.

3.1.2 Near-Wall Flow Data

Near-wall experimental flow data was also used to validate the simulated results [29]. The in-plane velocity components were measured using PIV in a vertical plane, 28 mm offset from the central tumble plane. The locations of the near-wall PIV plane and heat flux probe are shown in Figure 3.3. The nominal field of view (FoV) of this PIV plane was 5 × 6 mm^2, which allowed sampling of the core flow. The engine was operated at 1300 RPM, 40 and 98 kPa intake and exhaust MAP, with intake air heated to 80 °C. The datasets used are shown in Table 3.2. The number of cycles and CAD resolution are both dependent on the available memory of the camera, and the chosen datasets are the best balance of both parameters. PIV processing was done in LaVision DaVis. The images were interrogated with a 128 × 128 windows at 75% overlap, down to two passes at a final window size of 32 × 32 pixels at 50% overlap, resulting in a spatial resolution of 250 μm, oversampled to a final vector spacing of 125 μm. The first vector from the wall was located at 250 μm.

Table 3.2. Near-wall PIV datasets used.

Dataset	Operating Condition	CAD resolution	Range	Cycles
S_2016_03_13_08	Motored	2.5	-360:350	35
S_2016_03_13_04	Motored	10	-360:350	141
S_2016_03_25_09	Fired	5	-270:0	184

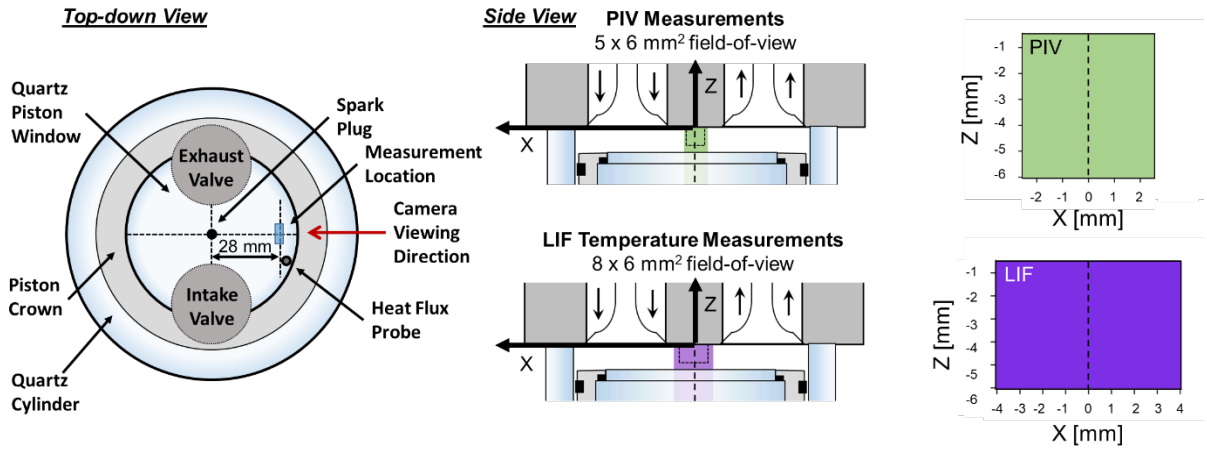

Figure 3.3. Top-down view of the TCC-III engine with measurement volume and heat flux probe locations, and side-view with PIV and PLIF planes at the cylinder head surface. The dashed line is the overlapping midline of both fields of view.

Due to the difference in spatial resolution of the near-wall PIV and LES, the near-wall PIV data is smoothed using a Gaussian spatial filter at each point (x_o, y_o) to match the spatial resolution of the simulations. The Gaussian filter is defined as

$$G(x_i, y_j, f) = \frac{1}{2\pi f^2}\sqrt{\frac{2}{\pi^3}}exp\left(-\frac{8}{f^2}\left((x_i - x_o)^2 + (y_j - y_o)^2\right)\right) \tag{3.1}$$

The filtered velocity at point (x_o, y_o) can then be obtained using

$$\widetilde{U_i}(x_o, y_o, f) = \sum_{i,j} G(x_i, y_j, f)U_i(x_i, y_j) \tag{3.2}$$

A filter width f of 1 mm is used to match the in-cylinder mesh size of 1 mm in the LES. This filter is applied to individual cycles before further data analysis. Figure 3.4 shows the effects of applying the Gaussian spatial filter on an individual cycle at -180 CAD aTDCc. The Gaussian filter averages out the small-scale features while the large-scale flow features are conserved. The magnitude of the velocity vectors are reduced after filtering since they are averaged with neighboring vectors. Also, slight changes in the direction of the velocity vectors can be seen.

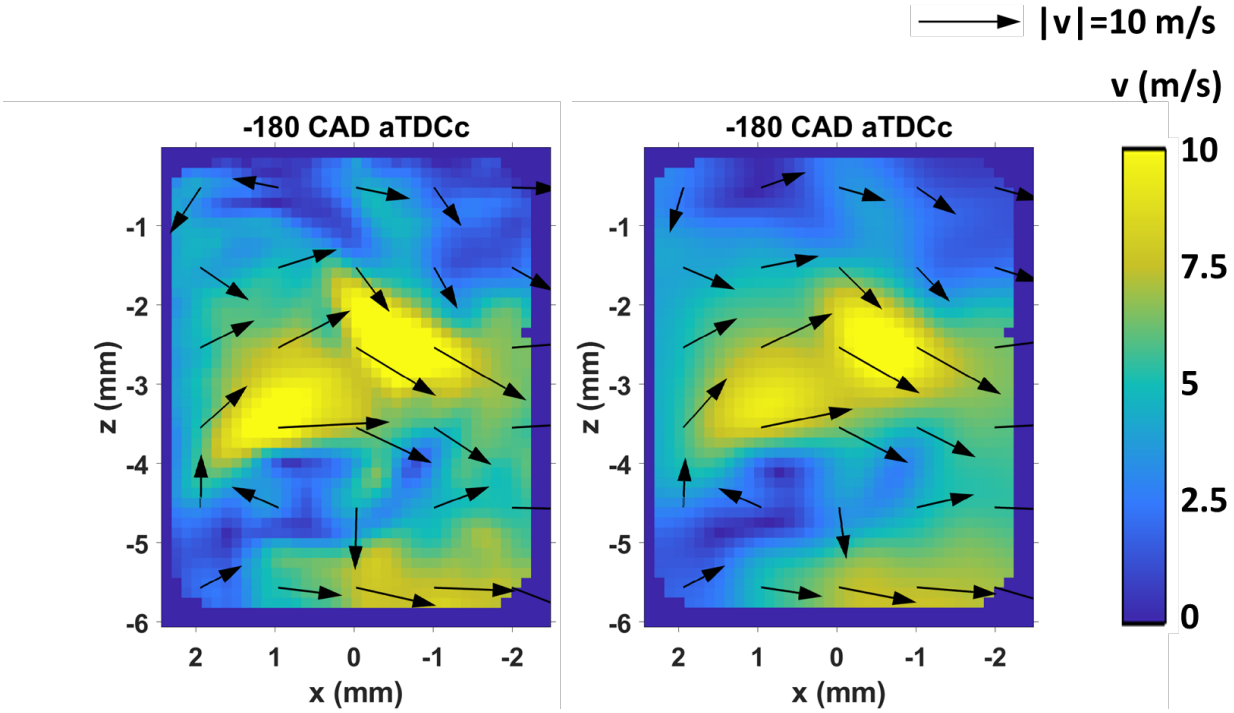

Figure 3.4. Near-wall PIV a) before and b) after applying Gaussian spatial filtering at -180 CAD aTDCc of an individual cycle. Figure updated from [121].

In the near-wall PIV measurements [29], there were occasions when no seeding particles were present near the wall so that no velocity vectors could be obtained in this region. Such events were excluded from statistical analysis by conditionally sampling the non-zero velocities. Figure 3.5(a) quantifies the number of velocity vectors available in the field of view at -270 CAD aTDCc for dataset S_2016_03_13_04. The maximum number of samples is 141, equal to the number of cycles. The minimum number of samples occurred mostly at the top edge of the FoV at this crank angle degree location near the head surface. This can be problematic for the analysis since less data is available in this region for the ensemble averaging process. Figure 3.5(b) shows the spatially averaged number of samples in this region over the entire engine cycle. It can be seen that the number of samples decreases mainly due to valve opening events, as the intake jet and exhaust blowdown remove seeds from the NWR. During most of the compression stroke, the number of samples available is equal to the number of cycles. Before the near-wall PIV is ensemble-averaged, it is advised to first test the convergence requirement of the PIV data and whether there are enough samples in this region, especially for the datasets that have a small number of cycles recorded.

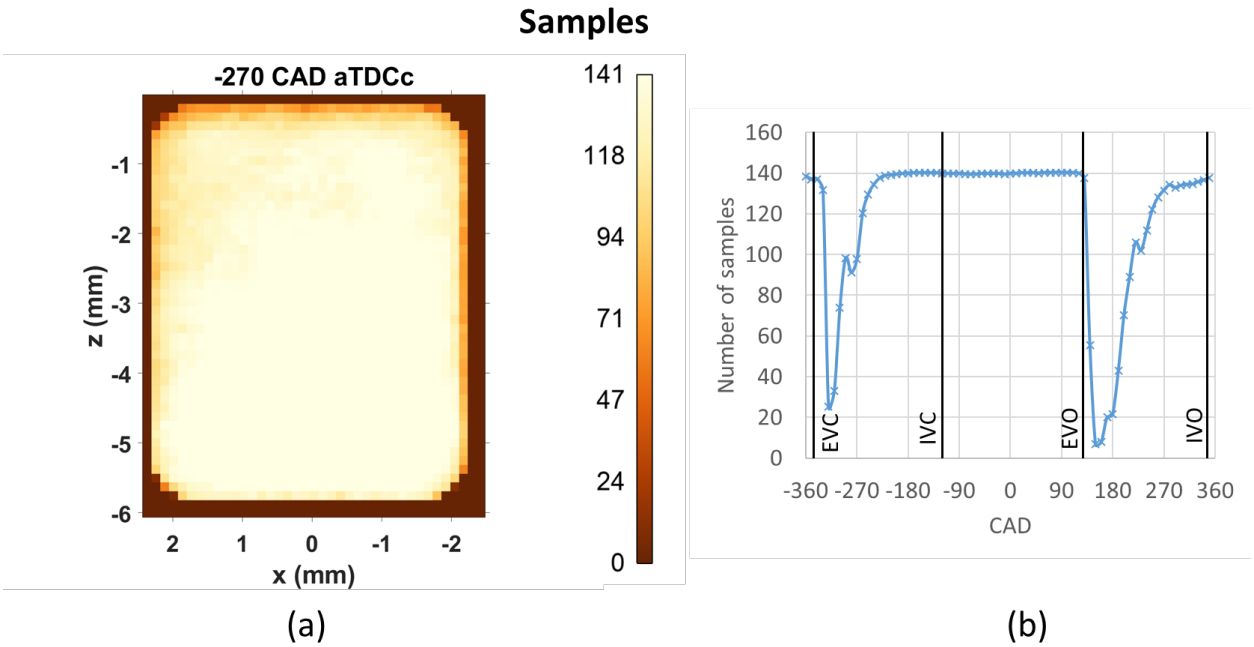

Figure 3.5. (a) The number of velocity vector samples in near-wall PIV measurement at -270 CAD aTDCc, and (b) the spatially-averaged number of samples throughout the engine cycle.

3.1.3 Near-Wall Temperature Data

High-speed toluene PLIF thermometry was conducted separately to capture near-wall temperature distributions in an 8 × 6 mm^2 FoV [39], at the same measurement location as the near-wall PIV data shown in Figure 3.3. Toluene was premixed with air (4% by volume) upstream of the intake plenum. PLIF images at every 1.3 CAD were recorded during the compression and expansion strokes for 73 and 145 consecutive cycles under motored and fired operating conditions, respectively, using LaVision DaVis software. The spatial resolution of the PLIF detection system is determined to be approximately 0.1 mm. Information about the post-processing steps can be found in [38, 39]. The spatial average PLIF signal was extracted from a 1 × 1 mm^2 calibration region in the ensemble average images at a distance of 4 mm from the in-cylinder head surface. This distance was chosen to avoid the effects of the near-wall flow on the bulk gas temperature, as will be described later in Section 5.3. PLIF signals at each CAD during the compression stroke were then calibrated to the predicted in-cylinder temperature from a 1D GT-Power simulation tuned to match the experimental pressures within ± 5% error.

3.1.4 Surface Temperature and Heat Flux Data

The surface and temperatures at 3.96 mm depth were measured at every 0.5 CAD using a Medtherm heat flux probe, located at 35.5 mm from the cylinder axis, mounted flush with the cylinder head. The instantaneous heat flux was calculated from the measured temperatures using the method by Nijeweme et al. [122]:

$$q_s = k\left[\frac{(\bar{T}_s - \bar{T}_{id})}{\delta} + \sum_{n=1}^{j}\frac{\sqrt{n\omega}}{2\alpha}(A_n + B_n)\,cos(n\omega t) + \sum_{n=1}^{j}\frac{\sqrt{n\omega}}{2\alpha}(B_n - A_n)\,sin(n\omega t)\right] \quad (3.3)$$

q_s is the instantaneous surface heat flux at the cylinder head surface, k and α are the thermal conductivity and thermal diffusivity of the probe material, and δ is the distance between the thermocouples of the in-depth and surface temperature measurement. $\bar{T}_s$ is the cycle-averaged surface temperature, and $\bar{T}_{id}$ is the cycle-averaged in-depth temperature. A_n and B_n are the coefficients from the Fourier series expansion of the surface temperature trace, n is the harmonic number, and ω is the angular velocity. Further information about the surface and heat flux measurements can be found in [29].

3.2 Numerical Methodology

The TCC-III engine was simulated using CONVERGE 2.4 and 3.0 software [123]. Simulations were performed with different turbulence models: the RANS renormalization group (RNG) k-ε model [124], and the LES dynamic structure model [125]. The momentum boundary layer was modeled with the standard law of the wall model [69] in RANS, and the Werner and Wengle wall model [74] in LES. The Han and Reitz model is used for heat transfer modeling at the wall [77]. All wall models used the same constants as suggested in the original studies. These wall models are implemented at the first cell at the surfaces, and they provide boundary conditions for the rest of the computational domain. Finite volume method is used, with first-order upwind scheme for spatial discretization, and fully implicit first-order time discretization. The PISO algorithm is used to achieve pressure-velocity coupling [126]. Each simulation that was performed is described in more detail in Table 3.3. This table includes details about the combustion modeling parameter b_1, which is described in more detail in Section 3.2.4.

To remove solution contamination from guessed initial conditions, multi-cycle simulations were conducted for both RANS and LES cases. For the RANS uniform temperature boundary

condition cases, four consecutive cycles were simulated and only the last cycle was used for further analysis. For the LES cases, the first cycle was removed from statistical analysis.

The computational domain for all simulations include the intake and exhaust plenums and ports and the engine cylinder. The CHT simulations include additional solid engine components, i.e. the cylinder head, cylinder liner, intake and exhaust valves, valve seats, the full spark plug geometry, and the piston, which contains both the piston crown and piston quartz window. Isotropic material properties are assumed. No fasteners were modeled. The material properties are listed in Table 3.4. The computational domain for the uniform temperature and CHT models are shown in Figures 3.6 and 3.7.

The operating conditions match those of the experimental database. The engine is operated at 1300 RPM, 40 kPa intake and 98 kPa exhaust MAP. For the fired condition, a stoichiometric fuel/air mixture was introduced, with propane as the fuel. 12 mg of propane was premixed with air and introduced in the inlet of the simulation. This matches the experimental fueling amount and combustion mode. Spark was initiated at -18 CAD aTDCc.

Table 3.3. Specifications of the TCC-III simulation cases.

Simulation	Turbulence Model	Momentum Wall Model	Thermal Boundary Condition	Operation	CONVERGE	b_1
Case 1	RANS RNG k-ε	Law of the wall	Uniform temperature, 318.16 K	Motored	2.4	-
Case 2	LES dynamic structure	Law of the wall	Uniform temperature, 318.16 K	Motored	2.4	-
Case 3	LES dynamic structure	Werner and Wengle	Uniform temperature, 318.16 K	Motored	2.4	-
Case 4	LES dynamic structure	Werner and Wengle	Uniform temperature, 353.16 K	Motored	2.4	-
Case 5	RANS RNG k-ε	Law of the wall	CHT	Motored	2.4	-
Case 6	LES dynamic structure	Werner and Wengle	CHT	Motored	2.4	-
Case 7	LES dynamic structure	Werner and Wengle	Uniform temperature, varies	Fired	2.4	5.5
Case 8	RANS RNG k-ε	Law of the wall	CHT	Fired	2.4	1.4
Case 9	LES dynamic structure	Werner and Wengle	CHT	Fired	3.0	8

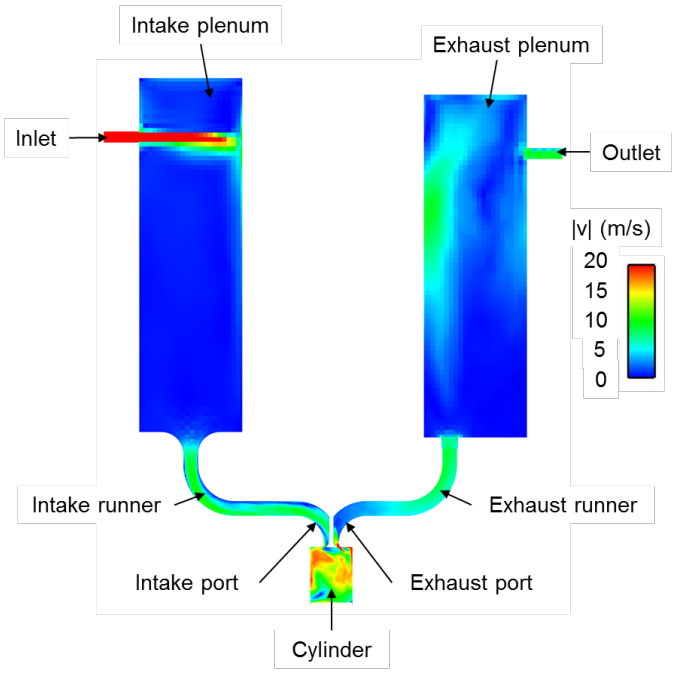

Figure 3.6. Computational domain of the uniform temperature models.

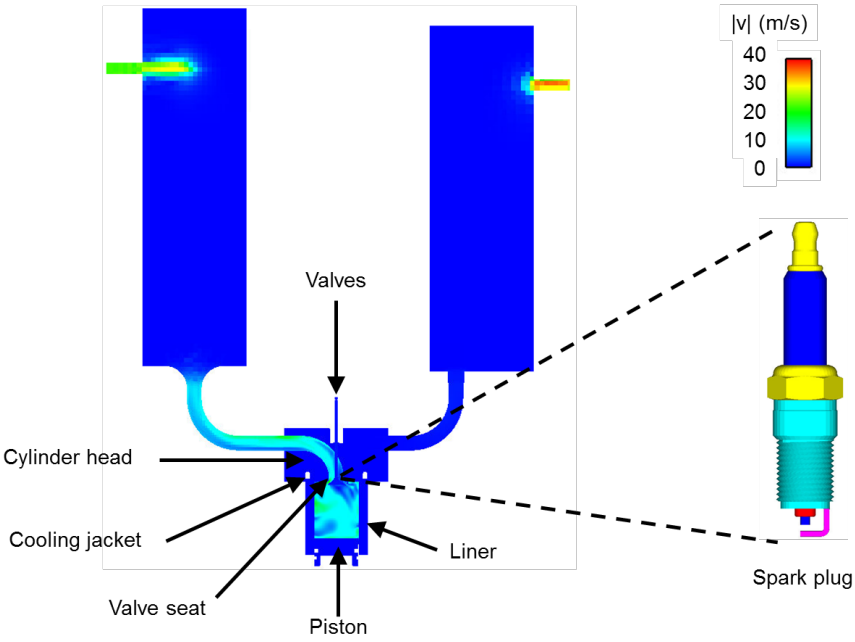

Figure 3.7. Computational domain of the CHT models. The spark plug geometry is also shown.

Table 3.4. Material properties of the solid engine components.

Component	Material	T_{melt} (K)	ρ (kg/m^3)	C_p (J/kg-K)	k (W/m-K)
Cylinder liner, piston window	quartz	1873	2203	703	1.38
Piston crown	steel 4340	1700	7850	475	44.5
Cylinder head	steel 1020	1789	7870	486	51.9
Valves	steel 21-4N	1789	7700	500	14.5
Spark plug insulation	Al_2O_3	2345	3965	730	35
Spark plug ground strap	NiCr8020	1698	8300	450	13
Spark plug casing	carbon steel	1700	7830	434	63.9
Spark plug core electrode	copper	1700	8930	385	401
Valve seat	valve seat material	1800	7600	471	42

3.2.1 Governing Equations

The governing equations solved by CONVERGE are the Navier-Stokes equations. Within the solid, conduction is solved by Equation 2.7. For compressible flows, an equation of state is needed to couple density, pressure, and temperature. For this work, the Redlich-Kwong equation of state is used:

$$p = \frac{RT}{v-b} - \frac{0.42748\frac{R^2T_c^{\frac{5}{2}}}{P_c}}{\left(v^2 + 0.08664\frac{RT_c}{P_c}\right)T^{\frac{1}{2}}} \tag{3.4}$$

These equations can be solved without any turbulence modeling if all turbulent scales are resolved in the computation using direct numerical simulation (DNS). Currently, there have been a few attempts to use DNS to simulate engine and engine-like geometries [73, 127, 128], but these are limited to low engine speeds and/or single cycles. To reduce computational costs, RANS and LES turbulence models are used.

3.2.2 RANS RNG k-ε Model

In RANS simulations, the Navier-Stokes equations are averaged. The velocity can be decomposed into a mean and a fluctuating component:

$$u_i = \tilde{u}_i + u_i' \tag{3.5}$$

This is known as Reynolds decomposition. This leads to the averaged Navier-Stokes equations and the Reynolds stress tensor $\bar{\rho}\widetilde{u_i' u_j'}$, which requires modeling since the correlation between the fluctuating components is unknown.

The RANS Renormalization (RNG) k-ε turbulence model was used in this study [124]. It is a two-equation model, with a transport equation for the turbulent kinetic energy k and a modified transport equation for turbulent diffusion ε. The constants used in the RANS simulations are defined in Table 3.5.

Table 3.5. RANS RNG k-ε model constants.

Constants	Value
C_μ	0.0845
Pr_k	0.7194
Pr_ε	0.7194
$C_{\varepsilon 1}$	1.42
$C_{\varepsilon 2}$	1.68
$C_{\varepsilon 3}$	-1.0
β	0.012
η_0	4.38

3.2.3 LES Dynamic Structure Model

In LES, a spatial filter is applied to the Navier-Stokes equations. Scales larger than the spatial filter are directly computed, while the subgrid scales need to be modeled. The velocity can then be decomposed into a resolved and subgrid component:

$$u_i = \bar{u}_i + u_{i,sgs} \tag{3.6}$$

Applying the filtering operation to the Navier-Stokes equations lead to a subgrid stress tensor $\tau_{ij}^R = \widetilde{u_i u_j} - \tilde{u}_i \tilde{u}_j$, which is different from the Reynolds stress tensor from RANS, but also requires modeling.

The dynamic structure model is a one-equation, non-viscosity based turbulence model that relates the subgrid stress tensor to the subgrid kinetic energy [125]. No turbulent viscosity is used to model the subgrid stress tensor, and therefore the model is not purely dissipative [45]. A

transport equation for the subgrid kinetic energy is added to provide scaling and enforce the budget on the energy flow between resolved and subgrid scales. The SGS stress tensor is modeled by

$$\tau_{ij}^{R} = c_{ij}k \tag{3.7}$$

An additional filtering operation G_T, known as the test filter and equal to twice the spatial filter, is applied to the resolved velocity. The test filtering operation is denoted by overhat (^) symbol:

$$\widehat{\overline{u}_i}(x_i, t) = \int G_T(x_i, r_i)\overline{u}_i(x_i - r_i, t)dr_i \tag{3.8}$$

A test-level stress tensor is defined as

$$T_{ij} = \frac{1}{2}\left(\widehat{\overline{u_i}\overline{u_j}} - \widehat{\overline{u}_i}\widehat{\overline{u}_j}\right) \tag{3.9}$$

The test-level stress tensor is related to the subgrid stress tensor through the Germano identity,

$$L_{ij} = T_{ij} - \widehat{\tau_{ij}} \tag{3.10}$$

where L_{ij} is known as the modified Leonard stress, and is equal to $L_{ij} = \widehat{\overline{u}_i\overline{u}_j} - \widehat{\overline{u}}_i\widehat{\overline{u}}_j$, which is entirely obtained from the resolved velocity field $\overline{u}_i$. The coefficient tensor c_{ij} then can be dynamically obtained:

$$c_{ij} = 2\left(\frac{L_{ij}}{L_{ii}}\right) \tag{3.11}$$

3.2.4 Combustion and Emission Modeling

The G-equation model is a level-set approach used for premixed combustion. As such, it is appropriate for simulating the fired operating condition of the TCC-III engine, where the fuel and air are homogeneously mixed before entering the combustion chamber. It is assumed that the premixed combustion is in the thin reaction zone regime, where turbulent eddies at the Kolmogorov length scales enter into the preheat zone of the flame causing unsteady perturbations, or the corrugated flamelet regime, where the laminar flame thickness is smaller than the Kolmogorov length scale. The G-equation model solves for a non-reactive scalar, G, which tracks the flame evolution as shown in Figure 3.8. The flame front is represented by $G = G_0 = 0$, while the burnt gas region is where $G > 0$ and the unburnt gas region is where $G < 0$.

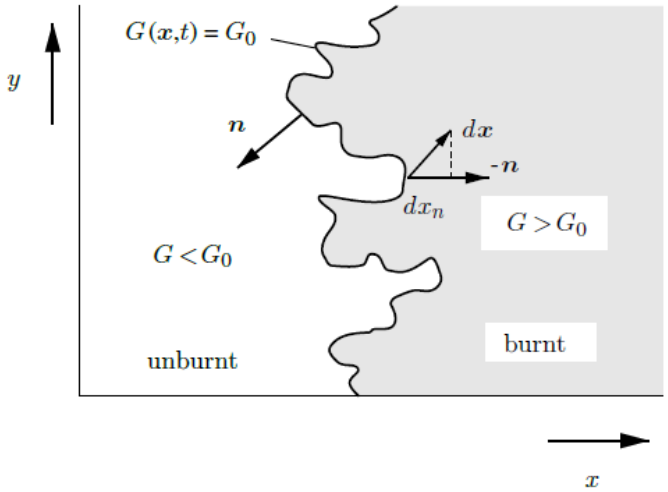

Figure 3.8. Schematic of the G-equation model, with G_o being the isoscalar surface that represents the flame front [129].

The G equation is [129]:

$$\frac{\partial \bar{\rho}\tilde{G}}{\partial t} + \frac{\partial \bar{\rho}\tilde{u}_i\tilde{G}}{\partial x_j} = \bar{\rho}s_T^0\left|\frac{\partial \tilde{G}}{\partial x_j}\right| - \bar{\rho}D_t\tilde{\kappa}\left|\frac{\partial \tilde{G}}{\partial x_j}\right| \tag{3.12}$$

Here, D_t is the turbulent diffusivity, and $\tilde{\kappa}$ is the mean flame front curvature.

s_L^0 is the laminar flame speed, the velocity at which the flame front propagates normal to itself relative to the unburnt mixture. The laminar flame speed depends on the equivalence ratio, the unburnt mixture temperature, and pressure. To calculate the laminar flame speed, the Gülder correlation is used with model parameters appropriate for propane fuel [123, 130].

s_T^0 is the turbulent flame speed and its model depends on the turbulence model used. For RANS, the turbulent flame speed model is given by the Peters model [129]:

$$s_T^0 = s_L^0 + v'\left(-\frac{a_4 b_3^2}{2b_1}Da + \left[\left(\frac{a_4 b_3^2}{2b_1}Da\right)^2 + a_4 b_3^2 Da\right]^{\frac{1}{2}}\right) \tag{3.13}$$

The original model used constants $b_1 = 2$ based on experimental data, $b_3 = 1$ based on Damköhler's suggestion and a DNS study, and $a_4 = 0.78$. Da is the turbulent Damköhler number.

The turbulent flame speed model for LES subgrid-scale models is the Pitsch model [131]:

$$s_T^0 = s_L^0 + s_L^0\left(-\frac{b_3^2}{2b_1}\frac{\mu_t}{\mu}\frac{1}{u_{sgs}} + \left[\left(\frac{b_3^2}{2b_1}\frac{\mu_t}{\mu}\,s_L^0\right)^2 + b_3^2\frac{\mu_t}{\mu}\right]^{\frac{1}{2}}\right) \tag{3.14}$$

Here u_{sgs} is the subgrid-scale velocity, μ_t is the turbulent viscosity, μ is the molecular viscosity, and b_1 and b_3 are modeling constants with the suggested values from [129].

The b_1 value was originally based on experimental data, but after analyzing some of the combustion simulations, this parameter needed to be changed to increase the in-cylinder pressure to match the measured pressure envelope. Also, when the CONVERGE version was changed from 2.4 to 3.0, the combustion simulations were affected, and b_1 require modification. The turbulence model used also affected the combustion simulations so that different values of b_1 was used for the RANS and LES models. The procedure is to do several multi-cycle simulations and to increase the b_1 value when the pressures are under-predicted, or decrease b_1 when pressures are over-predicted. The b_1 values used in the different cases are listed in Table 3.3.

To simulate the spark event, a spherical energy source of diameter 0.5 mm is used. This sphere was initiated at the spark timing of -18 CAD aTDCc. If the temperature in a cell exceeds a cutoff temperature of 3000 K, the G value in that cell is initialized with a positive value, and the G-equation model is then used to propagate the flame from the initialized cells. The energy source rate is shown in Figure 3.9 and represents a total of 32 mJ spark energy used in the experiment.

For emissions modeling, NOx is modeled using the Extended Zel'dovich Model [18, 123]. Soot is not modeled since soot levels are low in homogeneous-charge SI engines [6].

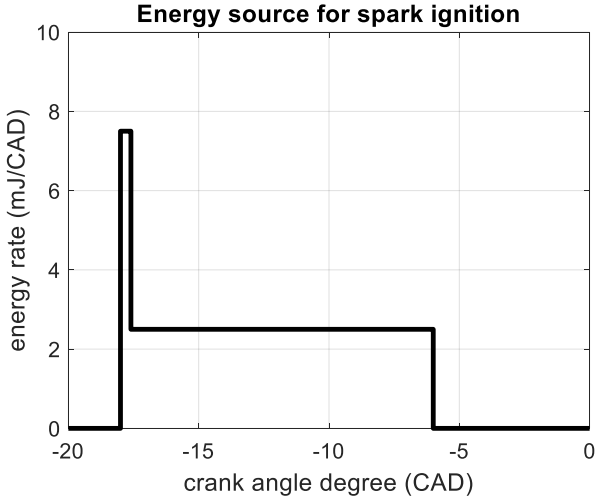

Figure 3.9. Energy source rate for simulating the spark ignition.

3.2.5 Meshing

In CONVERGE, the finite volume method is used. Meshing is done automatically by application of orthogonal cubic meshes during the simulation run-time. In this study, a base mesh

of $8 \times 8 \times 8$ mm^3 was used, with additional embedding of finer grids within the cylinder, as shown in Figure 3.10. The mesh was gradually reduced from 8 to 1 mm in the cylinder, with 0.5 mm mesh in the spark plug vicinity and at the valve seats and valve angles to capture the smaller-scale flows in these regions. In the CHT model, a 0.5 mm mesh is used between the solid-solid and fluid-solid interfaces. Within the solid domains, 1 mm mesh is used for the piston crown and quartz, the intake and exhaust valves, the cylinder liner, and the cylinder head. A 0.5 mm mesh is used for the spark plug geometry and the valve seats.

While dense grids are impractical for engine simulations, the mesh size is known to affect the resolved velocity field in LES [60, 71, 132], especially near the walls [133], and surface heat flux [134]. A workaround is to refine only the near-wall mesh instead of the entire in-cylinder volume [60, 133]. Therefore, a mesh study was conducted with the LES uniform temperature models. For the LES base mesh, the near-wall mesh at the cylinder head, liner, and piston surfaces was kept at 1 mm. For the LES mesh refinement study, this near-wall mesh was reduced from 1 mm to 0.5 mm. The mesh topologies of the base and refined meshes are shown in Figure 3.11. Information on the mesh size and cell count at TDC and bottom dead center (BDC) are listed in Table 3.6. Note that the LES base and refined mesh cases are too coarse for the models to be considered scientific LES, and instead should be categorized as engineering LES [45]. The CHT cases have approximately 4800000 cells at top-dead-center (TDC) and 6100000 cells at bottom-dead-center (BDC).

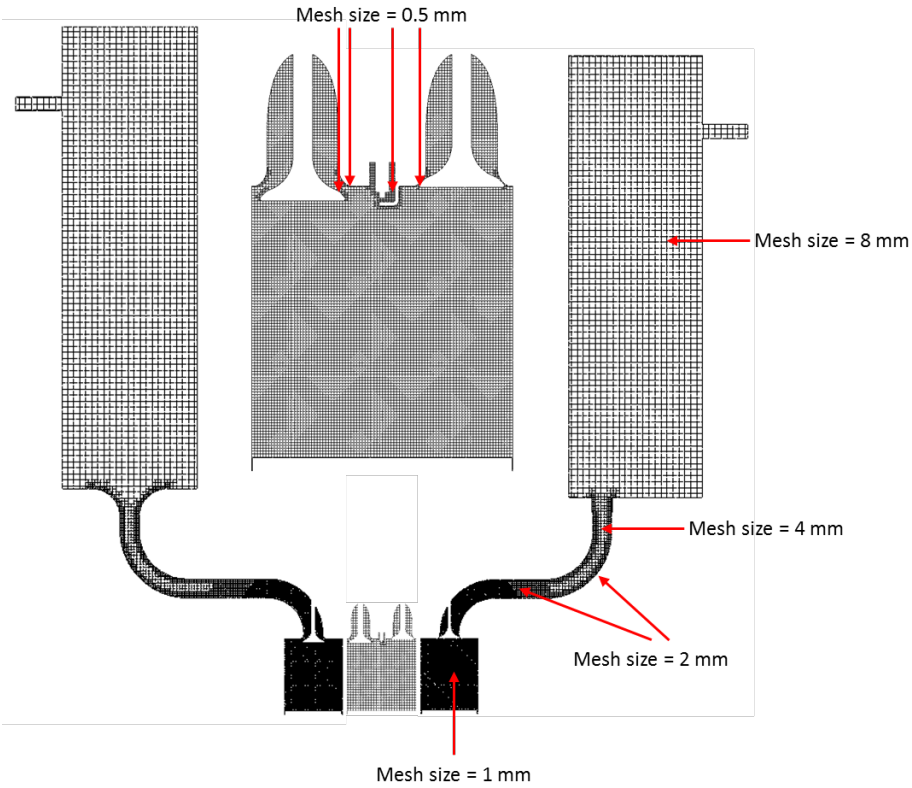

Figure 3.10. Base mesh with additional embedding towards the cylinder.

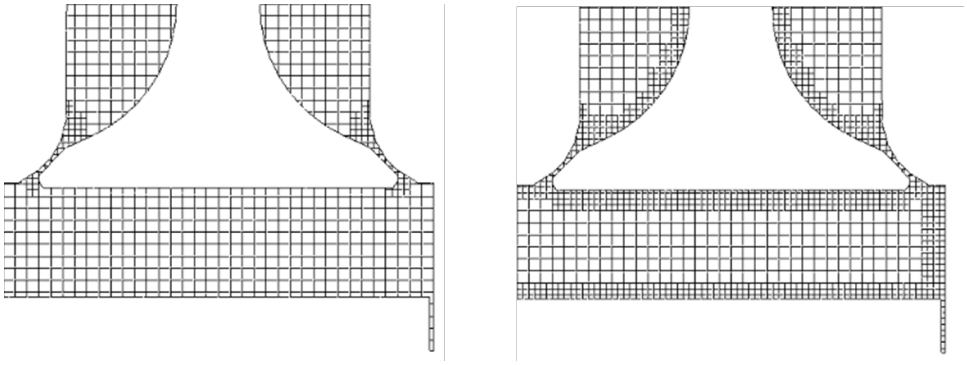

(a) (b)

Figure 3.11. Mesh topology of (a) base and (b) refined meshes.

Table 3.6. Mesh size of the uniform temperature model and cell count of LES refinement study.

	In-cylinder mesh size (mm)	**Near-wall mesh size (mm)**	**Cell count TDC**	**Cell count BDC**
base mesh	1	1	341000	938000
refined mesh	1	0.5	527000	1440000

3.2.6 Boundary Conditions

The boundary conditions for the simulations were obtained from a detailed 1D flow simulation using GT-Power, following procedure from [60], with intake temperature controlled at 80 ºC. The GT-Power models for motored and fired operating conditions were validated with experimental data and the detailed pressure curves are shown below in Figure 3.12 for the motored condition, and in Figure 3.13 for the fired condition. The GT-Power model parameters are shown in Table 3.7. Note that a blowby of 9.35 mg/s was added to the cylinder in the motored condition to match the experimental pressure, while the fired condition required no blowby. When the engine is fired, the better sealing of the compression rings will lead to less blowby [135]. Both GT-Power models perform well as the error in the intake and exhaust plenum pressures are within ±1%, the intake and exhaust port pressures are within ±5% except at intake valve opening (IVO) and exhaust valve opening (EVO), and the in-cylinder pressure is within ±5% during the compression stroke. The intake and exhaust pressures and the intake temperature are then taken as temporal boundary conditions for the inlet and outlet of the plenums.

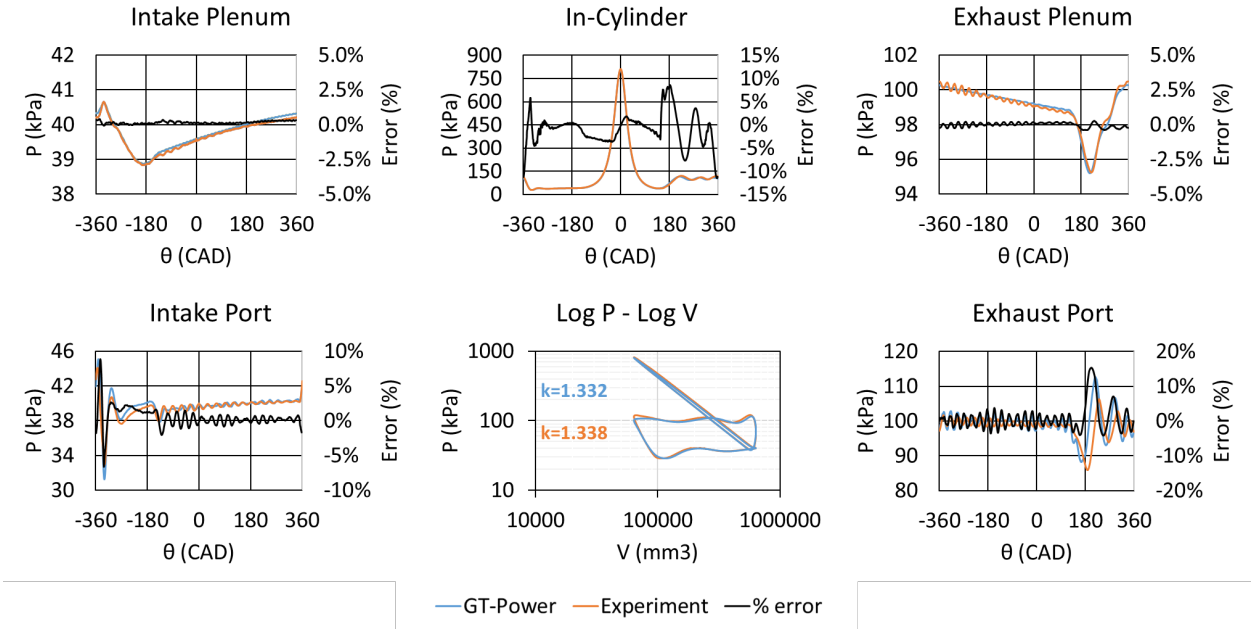

Figure 3.12. GT-Power simulation vs experiment – motored operating condition.

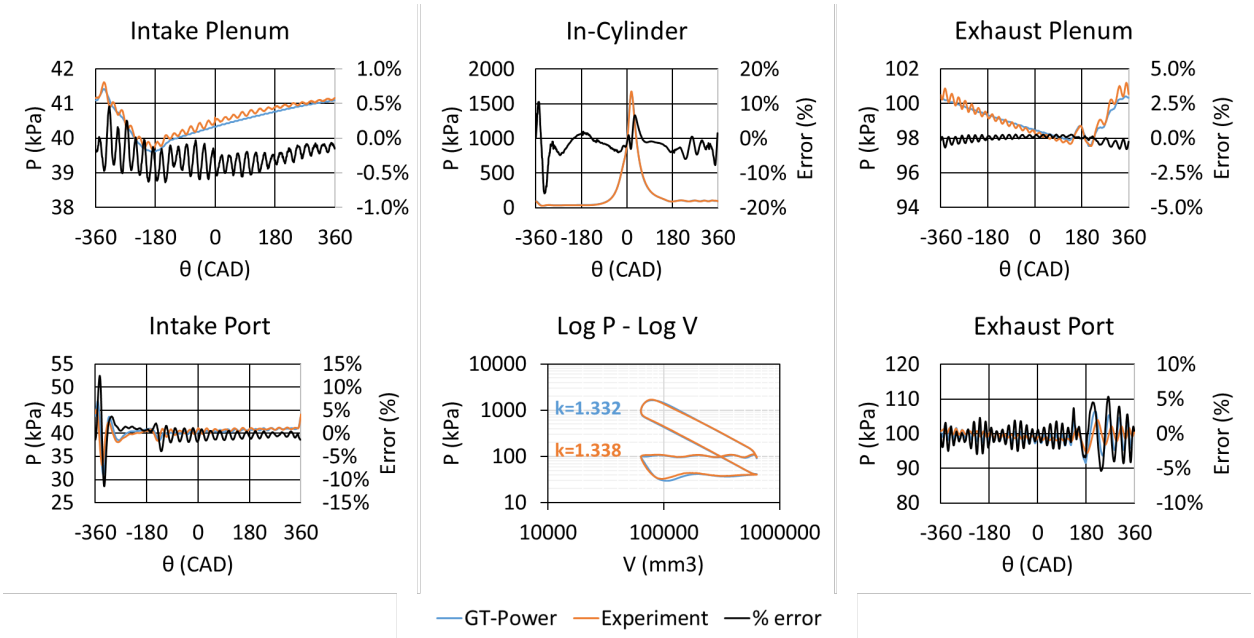

Figure 3.13. GT-Power simulation vs experiment – fired operating condition.

Table 3.7. GT-Power simulation parameters.

	Intake Pressure (kPa)	**Exhaust Pressure (kPa)**	**Blowby (mm)**	**Species Composition**
Motored	39.75	99	0.6 (equivalent to 9.35 mg/s)	Air: 76.7% N_2, 23.3% O_2
Fired	40.5	99	0	Air with propane, stoichiometric: 75.23% N_2, 20.18% O_2, 0.90% Ar, 0.039% CO_2, 3.65% Propane

For the uniform temperature simulations, the motored operating condition used a constant, isothermal temperature of 353.16 K for all surfaces. For the fired operating condition, based on best practices, different constant temperatures are assumed on the surfaces as shown in Figure 3.14.

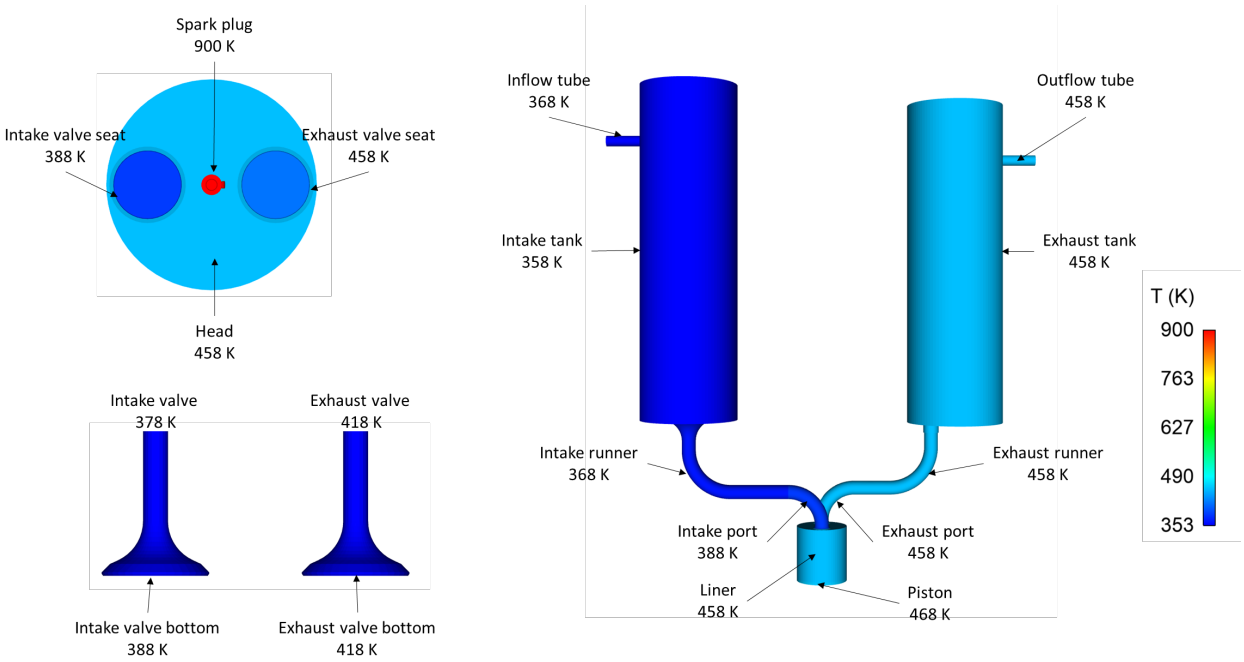

Figure 3.14. Surface temperature boundary conditions for fired simulations.

For the CHT model, the temperature of the top of the cylinder head, valve stems, and head groove is set to 353.16 K. Convective boundary condition is applied to the exposed sides and bottom of the cylinder head, with heat transfer coefficient h set at 10 W/m^{2}K, a typical value for natural convection with the environment [104], and ambient temperature at 298.16 K. The piston bottom and the liner outer surface are exposed to a cooling air jet. Assuming that this cooling air jet is impinging on the flat surface at a relatively low Reynolds number of 10000, surface average Nusselt numbers range from 20 to 80 [136]. If the jet's nozzle diameter is assumed to be 3 mm, this leads to convective heat transfer coefficient values ranging from 175 to 700. Therefore, a convective heat transfer coefficient of 200 W/m^{2}K was chosen with an ambient temperature of 298.16 K. Adiabatic boundary conditions were applied to the piston skirt, liner bottom, and inner liner surfaces.

3.2.7 Liquid Coolant Simulation

In the CHT model, the motion of the piston and valves are preserved by coupling the heat transfer of the in-cylinder flow and the solid domains. A separate liquid coolant simulation was performed for the coolant jacket in the cylinder head. The turbulence model for the coolant jacket is the RANS RNG k-ε model [124]. A base grid of 1 × 1 × 1 mm^3 was used, with additional embedding on the wall boundary of 0.5 mm. Adaptive mesh refinement (AMR) was used to

increase the grid resolution. The mesh topology is shown in Figure 3.15. The scalable wall function is used for the wall model, which ensures that proper log-law behavior is reproduced if grid refinement due to AMR puts the first cell in the buffer region [123].

A mixture of 50:50 by volume of ethylene glycol and water was fed through the inlet at 3.15×10^{-4} m/s, with an inlet temperature of 353.16 K. The coolant wall temperature is initially assumed to be uniform and was set at 353.16 K. This coolant model provides a spatially varying convective boundary condition for a RANS CHT model. The RANS CHT model provides an updated spatially varying wall temperature for the second iteration of the coolant model. This iterative process was performed three times until a converged boundary condition at the coolant wall was obtained. The iterative process is outlined in Figure 3.16. The last RANS CHT iteration provided the initial and boundary conditions for the first LES CHT cycle.

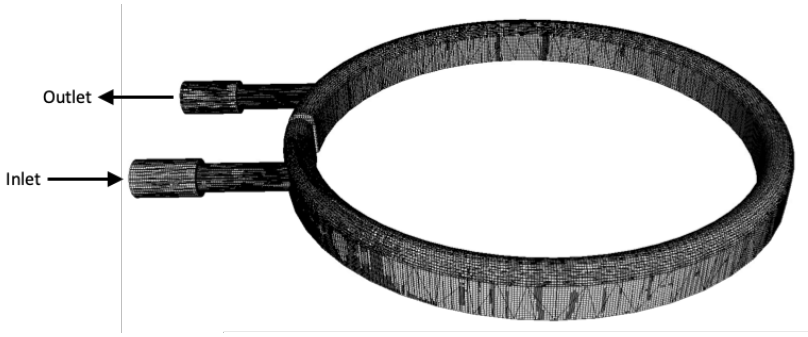

Figure 3.15. Mesh topology of the cooling jacket within the cylinder head.

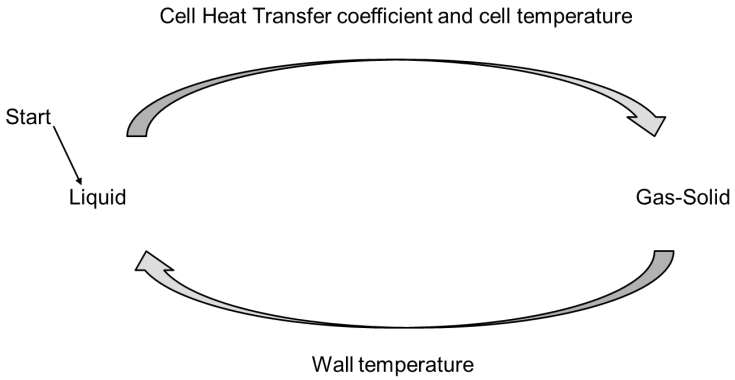

Figure 3.16. Iteration between liquid and CHT simulations using the RANS RNG k-ε model.

3.2.8 Super-Cycling Method

In CHT, the time-scale for the heat transfer in the solid is several orders of magnitudes larger than the fluid time-scale [99]. This discrepancy would lead to an increase in the number of engine cycles needed before the solid components reached thermal equilibrium. CONVERGE uses

a super-cycling method [123], which takes advantage of the time scale difference between solid and fluid heat transfer, allowing the solid to reach thermal equilibrium in fewer engine cycles. This method iterates between a fully-coupled transient fluid-solid solver, and a steady-state solid solver which calculates and updates the surface temperature at the fluid-solid interface.

First, the fluid and solid domains are solved together using a transient solver, and the heat transfer coefficient and near-wall temperature at the solid-fluid interface are stored. The super-cycling is done every 60 CAD interval, where the near-wall temperature and heat transfer coefficient at the interface is averaged over the last 720 CAD interval. This time-averaged data is used as a convective boundary condition for the steady-state solid solver. After the steady-state solution is converged, the solid temperature reaches a steady-state, after which this solid temperature is used as the surface temperature boundary condition for the transient fluid-solid solver.

Shortening the time interval for the super-cycling stages will inherently increase the computational cost. A parametric study of the super-cycling time interval from 0.5 to 10 CAD was performed by [97], where CHT is performed with the RANS RNG model for a four-valve engine. Their study showed that the heat loss at the piston surface has converged when a super-cycling time interval of 1 CAD is used. However, this leads to a wall clock time of 110 hours on 20 CPUs. The current LES-CHT setup with 60 CAD interval requires a wall clock time of approximately 216 hours on 64 CPUs per engine cycle using CONVERGE 2.4. Reducing the super-cycling interval would lead to impractical wall clock times. Therefore, the super-cycling interval was set at 60 CAD as a tradeoff between accuracy and available computing resources.

Chapter 4 Uniform Temperature Simulation Results

This chapter contains a systematic analysis of the simulations of the motored operating condition using a uniform temperature boundary condition. Mainly, simulation cases 1 through 4 were analyzed. Case 1 and 2 are the motored RANS and LES, respectively, with the law of the wall model and a uniform surface temperature of 318.16 K. Case 3 is the LES with Werner and Wengle wall model and the surface temperature of 318.16 K. Case 4 is the LES with Werner and Wengle wall model, with an updated surface temperature boundary condition of 353.16 K to better match the coolant and intake temperature of the near-wall measurements. First, ensemble averaging and Reynolds decomposition, relative values, and the comparison indices are defined. Then, the convergence criteria for the number of LES cycles are discussed in detail. Finally, the effects of turbulence models, near-wall mesh refinement, wall models, and surface temperature on the results are discussed, and comparisons are made to bulk flow, near-wall flow, and near-wall temperature measurements.

4.1 Analysis

4.1.1 Ensemble Averaging and Fluctuating Values

The instantaneous velocity vector from PIV and LES is the resolved velocity U_i. Each component of the velocity vector at each crank angle degree location θ and position vector x_i was ensemble averaged over all cycles as

$$\langle U_i(x_i, \theta) \rangle = \frac{1}{N} \sum_{j=1}^{N} U_i(x_i, \theta, j) \tag{4.1}$$

where N is the number of cycles and j is the cycle number. The resolved velocity can be decomposed into a fluctuating velocity component u_i' about the ensemble-averaged velocity using Reynolds decomposition:

$$u_i' = U_i - \langle U_i \rangle \tag{4.2}$$

The standard deviation of the velocity $U_{i,std}$ represents the CCV of the flow field, and was obtained using

$$U_{i,std} = \sqrt{\frac{\sum_{j=1}^{N}(U_i - \langle U_i \rangle)^2}{N-1}} \tag{4.3}$$

The ensemble and standard deviation values of the temperature and heat flux were obtained in the same manner as above.

4.1.2 Relative Values

The analysis that is typically done in this type of study is using fluctuating values about the ensemble average. However, it is relative values about the spatial mean that drive heat transfer, and therefore, the analysis should be repeated with the relative values about the spatial mean.

The relative values are obtained by first obtaining the spatial mean of each image, and subtracting the instantaneous value from the spatial mean:

$$\overline{U_i(\theta, N)} = \frac{1}{M}\sum_{k=1}^{M} U_i(x_i, \theta, k) \tag{4.4}$$

$$u_{i,rel} = U_i - \overline{U}_i \tag{4.5}$$

Here, M is the number of points in each image, and k is the Mth point.

4.1.3 Relevance and Kinetic Energy Index

For quantitative analysis of the velocity field, the local relevance index (RI) and the local kinetic energy index (KEI) have been calculated. The local RI compares the vector alignment of two velocity vectors [137] and is defined by

$$RI = \frac{\vec{U}_1 \cdot \vec{U}_2}{|\vec{U}_1||\vec{U}_2|} \tag{4.6}$$

Here, $|\vec{U}|$ denotes the magnitude of the velocity vector. If the velocity vectors are perfectly aligned, *RI* will be equal to 1. If the velocity vectors are orthogonal to each other, *RI* will be equal to 0. Finally, if the velocity vectors are opposite of each other, RI will be -1.

RI only compares the angle between two velocity vectors, and the velocity magnitude is not compared using this index. To compare velocity magnitude, the KEI can be used [138] and is calculated using

$$KEI = \frac{\left|\vec{U}_1\right|^2}{\left|\vec{U}_2\right|^2} \tag{4.7}$$

The local KEI can take on values equal to or larger than 0. A KEI of 1 means that the kinetic energy between the two velocity vectors are equal and the velocity magnitude matches between the two velocity vectors. A KEI of less than or larger than 1 means that the kinetic energy of the velocity vector is either lower or higher in comparison to the other. The local RI and KEI values can be spatially averaged over the plane to obtain spatially-averaged RI and KEI values.

4.2 Convergence Study

Statistical convergence of the simulations is an important consideration in CFD. Multiple consecutive cycles have been simulated extensively in the LES framework by others, mainly for CCV studies [41, 50, 51]. In any case, the in-cylinder velocity and temperature can be used to analyze statistical convergence, such as described in the convergence study that was published in Wu et al. [121]. For the convergence study, the motored uniform temperature LES with Werner and Wengle wall model (Case 4) is used. The ensemble average and standard deviation of the velocity field were obtained for an increasing number of cycles (i.e. cycles 2-3, cycles 2-4, etc.), and then spatially averaged over the entire domain. The magnitude of the spatially averaged velocity vector was obtained. The results in Figure 4.1 shows that satisfactory statistical convergence of the ensemble-averaged velocity is acquired after including 5 cycles (cycles 2-6) in the ensemble averaging process, as increasing the number of cycles beyond 5 causes less than 2% change in the velocity. At least 7 cycles (cycles 2-8) are needed for the standard deviation of the velocity to reach statistical convergence, as increasing the number of cycles beyond 7 causes less than 2% change in the standard deviation of the velocity.

Figure 4.2 shows the ensemble averaged in-cylinder gas temperature, spatially averaged over the entire cylinder domain, for an increasing number of cycles in the ensemble averaging process. The ensemble-averaged temperature of both cases reached statistical convergence after averaging cycles 2-3, while the standard deviation of the temperature becomes steady after cycles 2-8.

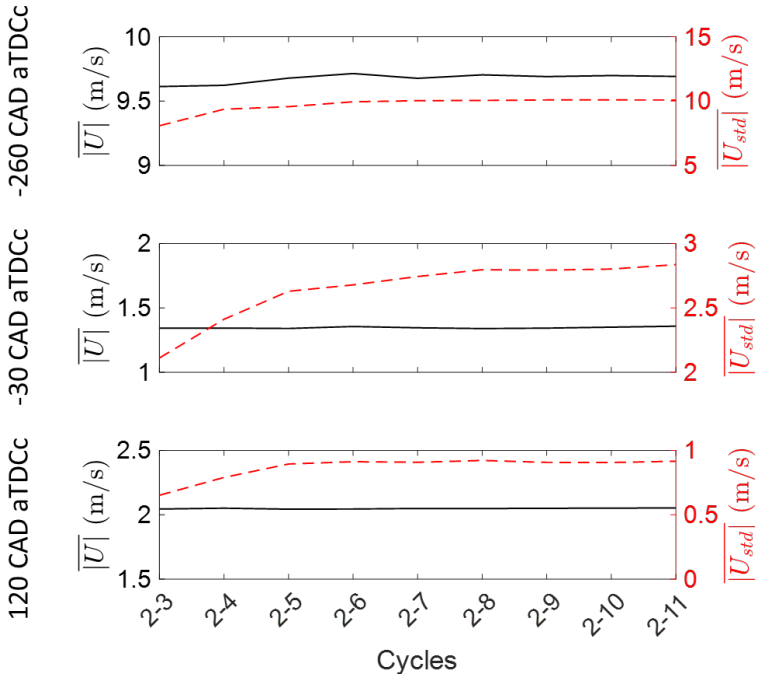

Figure 4.1. Convergence of the ensemble average and standard deviation of the velocity magnitude for Case 4, at three crank angle degree locations. The x-axis shows the cycles that are included in the statistical analysis. Figure extracted from [121].

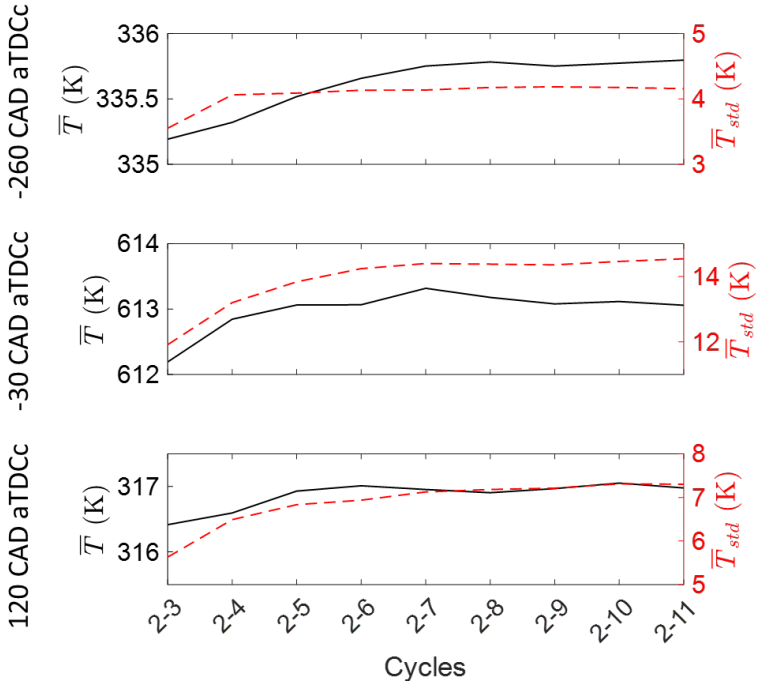

Figure 4.2. Convergence of the ensemble average and standard deviation of the in-cylinder gas temperature for Case 4, at three crank angle degree location. The x-axis shows the cycles that are included in the statistical analysis. Figure extracted from [121].

In LES, large scales are resolved while the subgrid scales are modeled. A quality index M can be used to measure the turbulence resolution of the LES model [139], and it is an indicator of the grid resolution [132]. It is defined as

$$M(x_i, \theta) = \frac{k_{sgs}(x_i, \theta)}{k_{resolved}(x_i, \theta) + k_{sgs}(x_i, \theta)} \tag{4.8}$$

where $k_{resolved}$ is the turbulent kinetic energy of the resolved velocity field, obtained using

$$k_{resolved} = \frac{1}{2}\left(u'^2 + v'^2 + w'^2\right) \tag{4.9}$$

k_{sgs} is the subgrid-scale kinetic energy, which is obtained from the dynamic structure model. M can take values between 0 and 1, where a value of 0 corresponds with DNS (all turbulence scales are resolved), and a value of 1 corresponds with RANS (all turbulence is modeled). Typically, a value of 0.2 or less is recommended, which indicates that 80% or more of the turbulent kinetic energy is resolved by the LES [139].

The quality index is calculated for the uniform temperature LES over the engine cycle with increasing number of cycles in the ensemble averaging process and spatially averaged over the entire cylinder domain. The spatially averaged quality index $\overline{M}$ is shown in Figure 4.3. Evident from the figure is that as the number of cycles in the ensemble averaging process increases, $\overline{M}$ decreases, i.e. the LES quality gets better.

This LES quality index can be used as another indicator of statistical convergence of the LES. By increasing the number of cycles in the ensemble averaging process, the fluctuating velocity u_i' changes. After including 6 cycles (cycles 2-7) in the ensemble averaging process, the LES quality index does not change significantly and therefore statistical convergence is obtained.

By using 10 cycles (cycles 2-11), a quality index of 0.2 and lower is ensured for most of the cycle. Figure 4.4 shows that increasing the number of cycles beyond 10 in the ensemble averaging process does not change the statistical convergence of the LES quality index. However, during the compression stroke and valve opening events, the quality index increases, i.e. the LES quality deteriorates during these events. This occurs because during the compression stroke, the integral length scale decreased due to the piston compressing the flow into a decreasing engine volume, and valve opening events also introduce additional small-scale structures in the flow [140]. These results indicate that during valve opening and the latter compression stroke, the computational mesh is unable to resolve the small turbulent scales. At times of large M values,

grid refinement is needed to resolve more of the turbulent kinetic energy. However, such grid refinement comes at the expense of increased computational costs, and currently, this is not possible due to limited computational resources available. To ensure that the LES quality does not influence the analysis, at least 10 cycles will be analyzed. Also, the analysis will be focused mainly on the compression stroke. It should be noted that the convergence criteria here was tested for only one operating condition at a single engine RPM. The convergence criteria should be analyzed for simulations with different operating conditions.

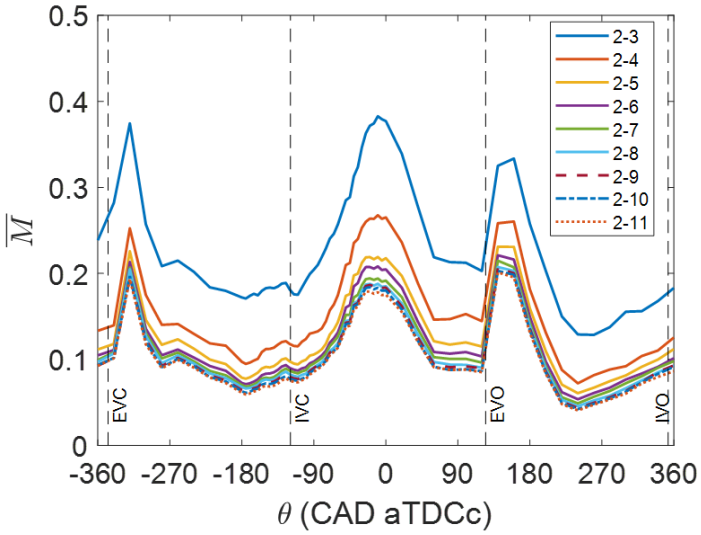

Figure 4.3. LES quality index $\overline{M}$ of Case 4 for increasing number of cycles in the ensemble averaging approach, over the entire engine cycle. Figure extracted from [121].

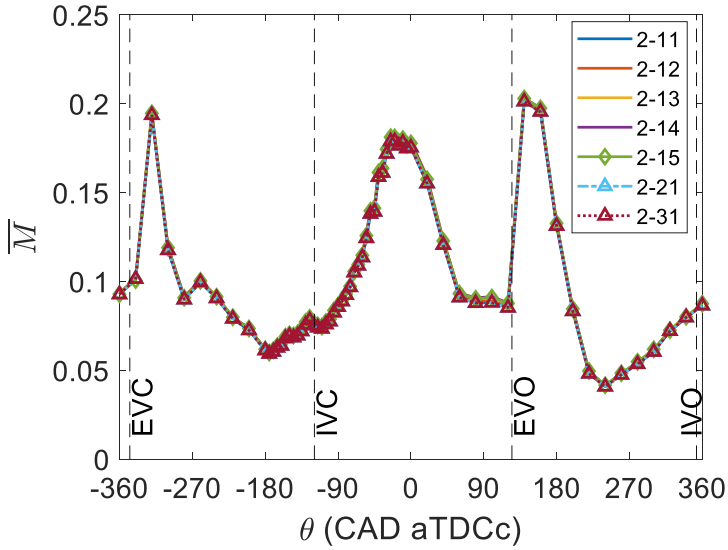

Figure 4.4. LES quality index $\overline{M}$ of Case 4, for increasing number of cycles in the ensemble averaging processes over the entire engine cycle.

4.3 Effects of the Turbulence Model

A study analyzing the combined effects of turbulence and wall models with uniform thermal boundary conditions is warranted due to the widespread use of such modeling methodologies in engine CFD. For this study, the uniform temperature models are analyzed. For this, Cases 1 and 2 are analyzed. Case 1 is the RANS model and only the fourth cycle is analyzed. Case 2 is the LES model which has 31 cycles, but the last 30 cycles were analyzed to remove initial condition bias. Case 2 will also include a near-wall mesh refinement study. Both turbulence models use the law of the wall and the Han and Reitz wall models. They are then compared against PIV measurement datasets (S_2013_10_24_01 for the bulk flow and S_2016_03_13_04 for the near-wall flow regions), and to measured temperature fields using PLIF [39]. The objective of this analysis is to show the differences between the two turbulence models. Parts of this study have been published in [141, 142].

To validate the simulations, the ensemble averaged cylinder pressures are compared and are shown in Figure 4.5. The simulated peak pressures are within 5% of the experimental pressures. The CCV, as indicated by the shaded area, of the LES is small compared to the pressure envelope of the experiment.

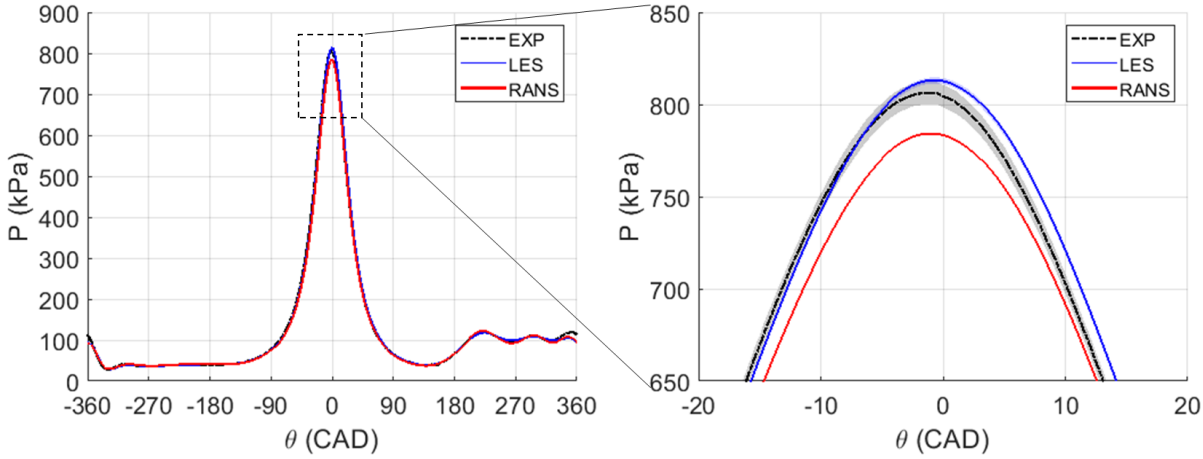

Figure 4.5. The dynamics of the in-cylinder pressure of Cases 1 and 2 compare well to the experimental data. Figure updated from [141, 142].

4.3.1 Bulk Velocity and Temperature Fields

The ensemble-average bulk velocity fields are compared at -260 CAD during the intake stroke, and in the compression stroke at -100 and -30 CAD aTDCc. These crank angle degree locations were chosen as they were common between the simulations and experiments. -260 CAD

was chosen as the intake jet can be seen in the measurement. The intake jet is important in the formation of vortices when the intake jet interacts with the engine surfaces, but also in heat transfer in the valves. -100 CAD represents the early compression stroke after IVC, and -30 CAD the late compression stroke, before the spark timing of the fired condition.

The ensemble-averaged bulk velocity field in the $y = 0$ mm tumble plane is validated at -260 CAD aTDCc for Cases 1 and 2 in Figure 4.6. The measured dataset is S_2013_10_24_01 which has 240 imaged cycles. The velocity magnitude $|v|$ and velocity vectors were calculated from the in-plane velocity components. Qualitative comparison of the velocity field shows that the depth and direction of the intake jet in the top-left corner is well captured by both simulations. The two large vortical structures (regions A and B) next to the intake jet are found in the LES, but only one vortical structure is captured by the RANS case.

For a quantitative analysis, the RI and KEI fields are also shown. The RI field shows that in region A, the velocity vector directions of both simulations do not align well with the experiment. In region B, the velocity vector direction of the LES is better aligned with RI values close to 1, and only in the center of the vortex is the direction misaligned with RI values close to 0. In contrast, because the RANS did not capture the right vortex, the RI values near Region B are low. This could be due to an out-of-plane rotation of the flow in the RANS model. There are also two smaller low RI value regions on the right side of the intake jet of the RANS simulation. Upon further examination of the velocity field at this crank angle degree location, two smaller vortical structures were found that interacted with the right side of the intake jet in the RANS simulation. Region C is influenced by the depth and strength of the intake jet. It can be seen that the intake jet penetrates deeper into the combustion chamber in the RANS simulation, leading to vector misalignment and low RI values in region C. In the LES, the jet penetration depth is closer to the measurement. A smaller area of low RI values is found in region C compared to the RANS simulation.

The KEI fields show that these three regions are areas where the simulations overestimate the velocity magnitude. The kinetic energy is overestimated in regions A and B due to predicted vortex center locations not matching those of the measurement and vortex centers having low kinetic energy. Region C shows that the strength and depth of the intake jet leads to discrepancies in the velocity magnitude. This leads to the conclusion that the intake jet simulation needs to be improved, as the intake jet causes the vortices when it interacts with the in-cylinder flow and

engine surfaces, and the strength of the intake jet will also affect heat transfer predictions. This is particularly important at the valves since a higher kinetic energy means the intake jet has a higher velocity than measured, which leads to higher convective heat transfer at the valves.

Figure 4.7 shows the velocity field at -100 CAD aTDCc. Overall, the RI field shows that the velocity vectors are well aligned with RI values close to 1 for most of the plane, except for Region A, which coincides with a vortical structure in the measurement not captured by both simulations. The KEI field shows that in this region the velocity magnitude is overestimated by the simulations.

Figure 4.8 shows the velocity field at -30 CAD aTDCc. Again, the velocity vector direction in most of the plane is well captured as shown by the RI field with RI values close to 1. The KEI field also shows that the velocity magnitude, in general, is not well predicted by both simulations. Low RI values are confined in a slim region near the wall. This region also coincides with large KEI values.

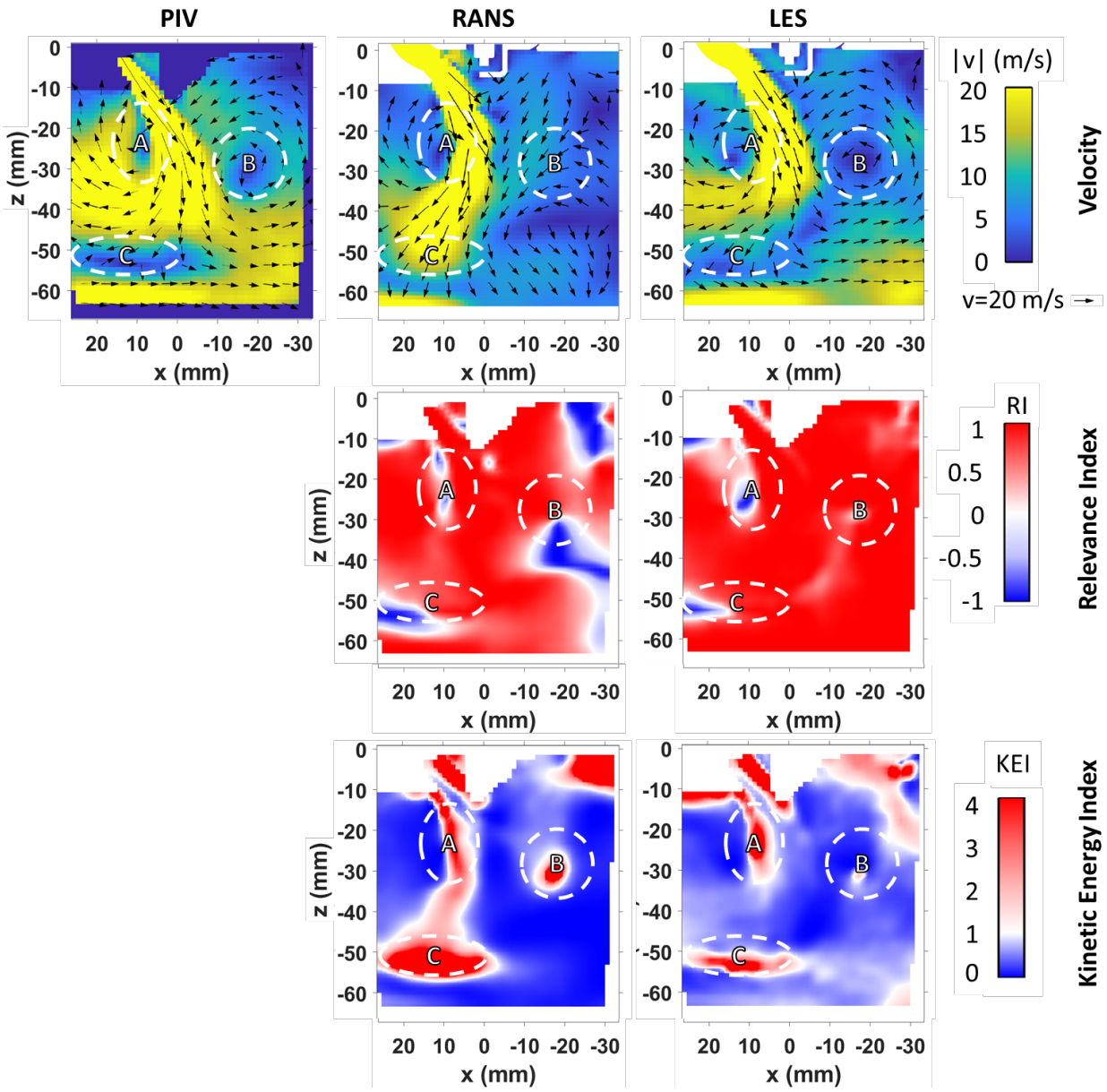

Figure 4.6. Bulk velocity field validation of Cases 1 and 2 in the tumble plane (y=0 mm) with PIV dataset S_2013_10_24_01 at -260 CAD aTDCc.

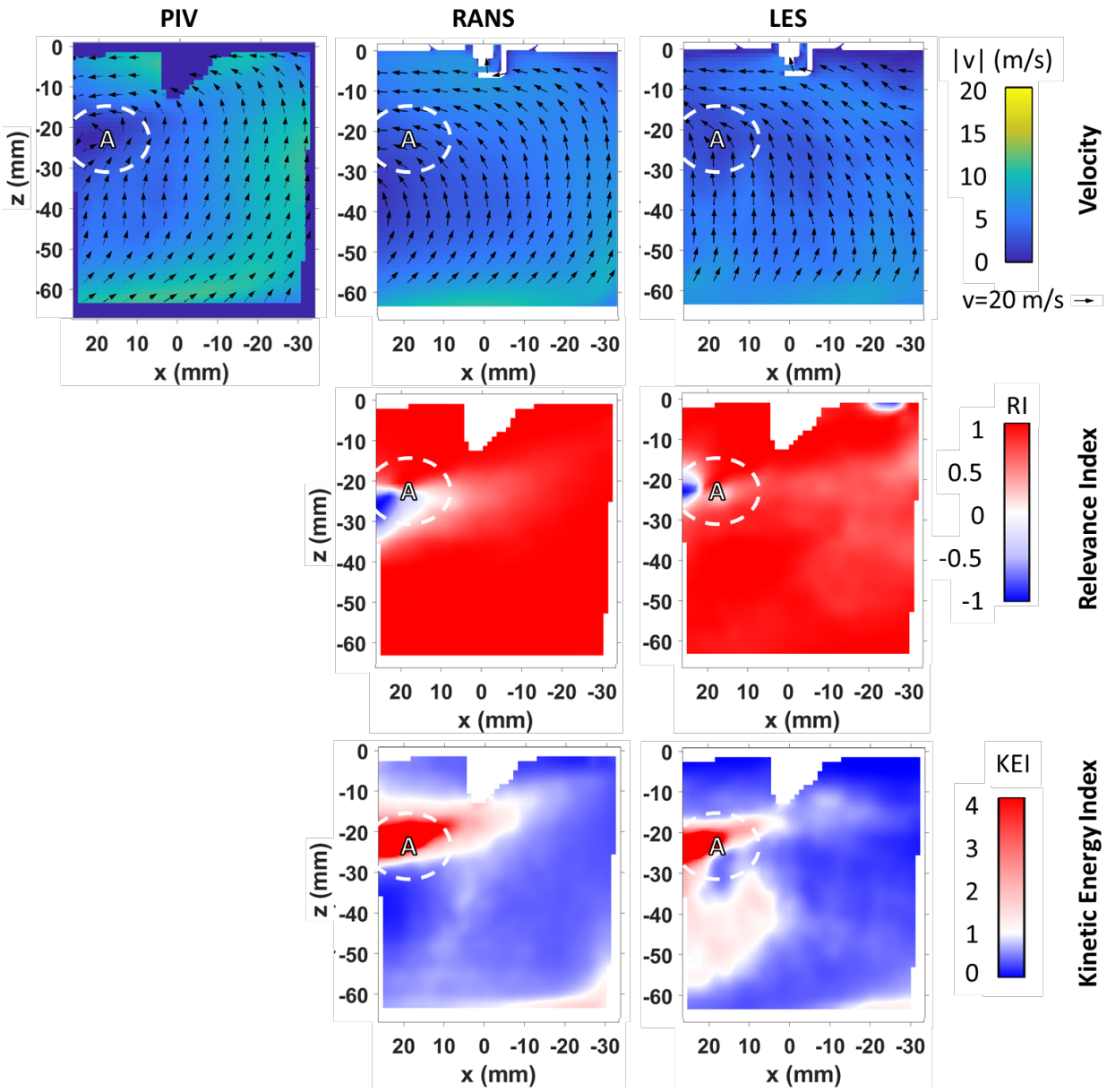

Figure 4.7. Bulk velocity field validation of Cases 1 and 2 in the tumble plane (y=0 mm) with PIV dataset S_2013_10_24_01 at -100 CAD aTDCc.

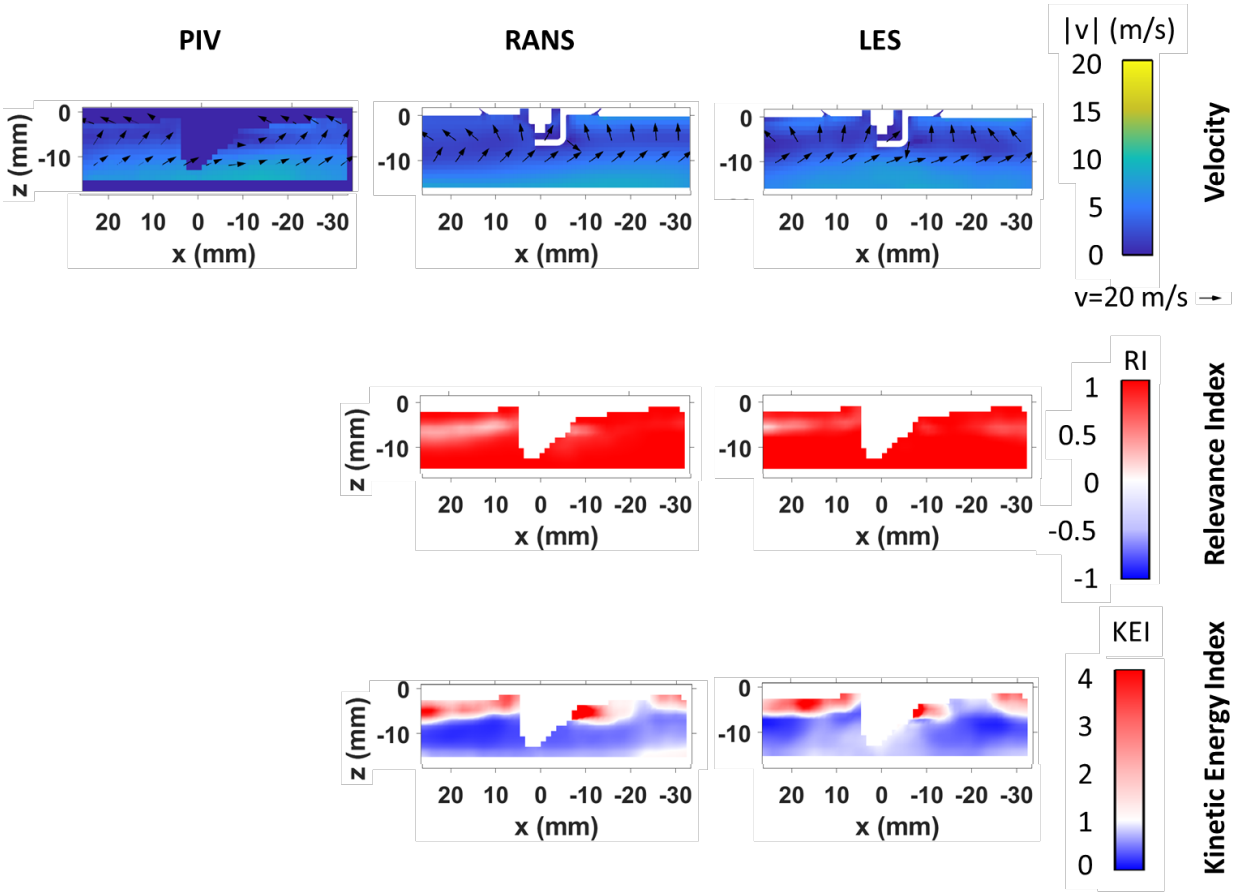

Figure 4.8. Bulk velocity field validation of Cases 1 and 2 in the tumble plane (y=0 mm) with PIV dataset S_2013_10_24_01 at -30 CAD aTDCc.

The spatial average and standard deviation of the RI and KEI fields are shown in Figure 4.9 and Figure 4.11 for both simulation cases. The spatial average RI of both simulations remain high (above 0.8) during most of the cycle, except during intake and exhaust valve opening. These valve opening events lead to a drop in RI values mainly due to the effects of the incoming jets on the directions of the velocity vectors. During the compression stroke, the RI values remain above 0.8 for the RANS simulation. The RI values for the LES during the compression stroke are mostly above 0.8 except from -135 CAD to -105 CAD where the RI value drops down to approximately 0.7.

The standard deviation of the RI field shows the level of spatial stratification of the RI values. A low standard deviation value of the RI field means the spatial stratification is low, and vice versa. When low standard deviation coincides with large spatial average RI values, it indicates that the velocity vector field is well captured. Figure 4.9(a) shows that during the compression stroke, the velocity field has large RI values with low spatial standard deviation. For the LES,

Figure 4.9(b) shows that during the compression stroke, the spatial standard deviation is approximately equal to those of the RANS simulation except during the beginning of the compression stroke. For example, at -140 CAD, the LES has a spatial standard deviation of RI value of 0.6, with a spatial average value of 0.8, while the RANS had a standard deviation of 0.3 and a spatial average of 0.9. When the velocity fields were analyzed at -140 CAD aTDCc in Figure 4.10, it was found that the low RI value was mainly due to a mismatch of the tumble center location. In the RANS simulation, a tumble vortex center can be found in the lower-right corner, but the location is lower than the tumble vortex center in the PIV measurement. In the LES, a more complex structure is found in the lower-right corner with no identifiable tumble center. This leads to a lower RI and increased stratification of the RI field. In addition, the kinetic energy is also affected by the mismatch of the tumble center.

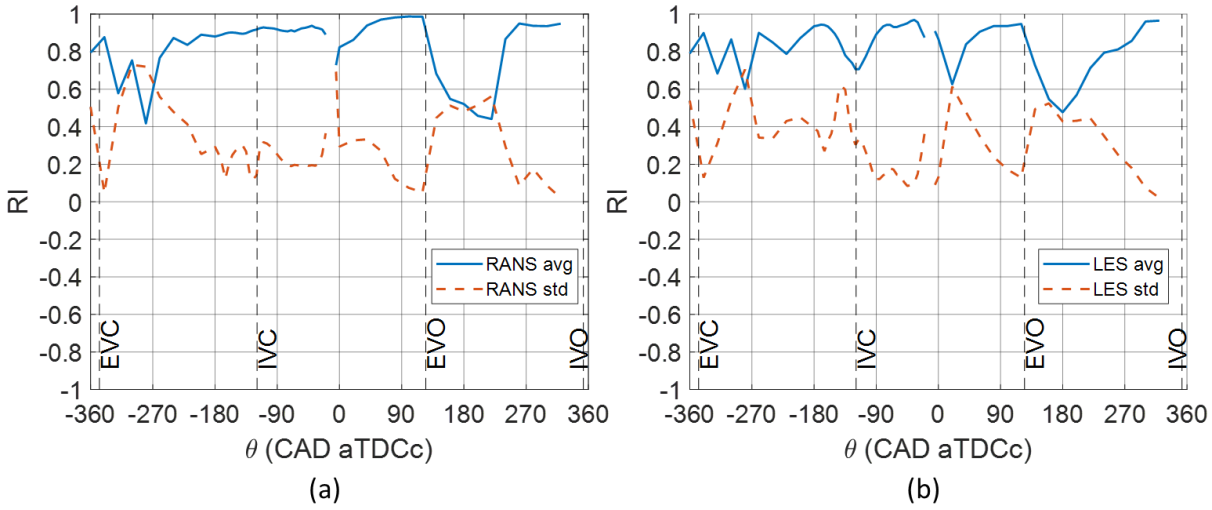

Figure 4.9. Spatial average and spatial standard deviation of the Relevance Index for (a) Case 1 and (b) Case 2.

Figure 4.11 shows the spatial average and standard deviation of the KEI values for the two cases. The KEI of the RANS simulation is fairly close to 1 for most of the compression stroke. The KEI of the LES, on the other hand, is lower than that of the RANS during this time. This means that the spatial average kinetic energy content of the LES is more severely underestimated than that of the RANS. During valve opening events, the KEI of both simulations increased above 1, which means that the kinetic energy is too large compared to the PIV. Since most of the kinetic energy is introduced by the intake jet and exhaust valve blowdown, this means that the simulation is overestimating the jet's velocity magnitude and therefore its kinetic energy content.

The spatial standard deviation of the kinetic energy remains fairly low throughout the engine cycle, except for several instances during the engine cycle where this spatial standard deviation increased to a maximum. These large values of KEI are mainly due to small regions of the velocity field having large KEI values when the valves are closed. When the exhaust valve opens, the exhaust flow that enters back into the combustion chamber introduces too much kinetic energy leading to large areas of large KEI in the velocity field.

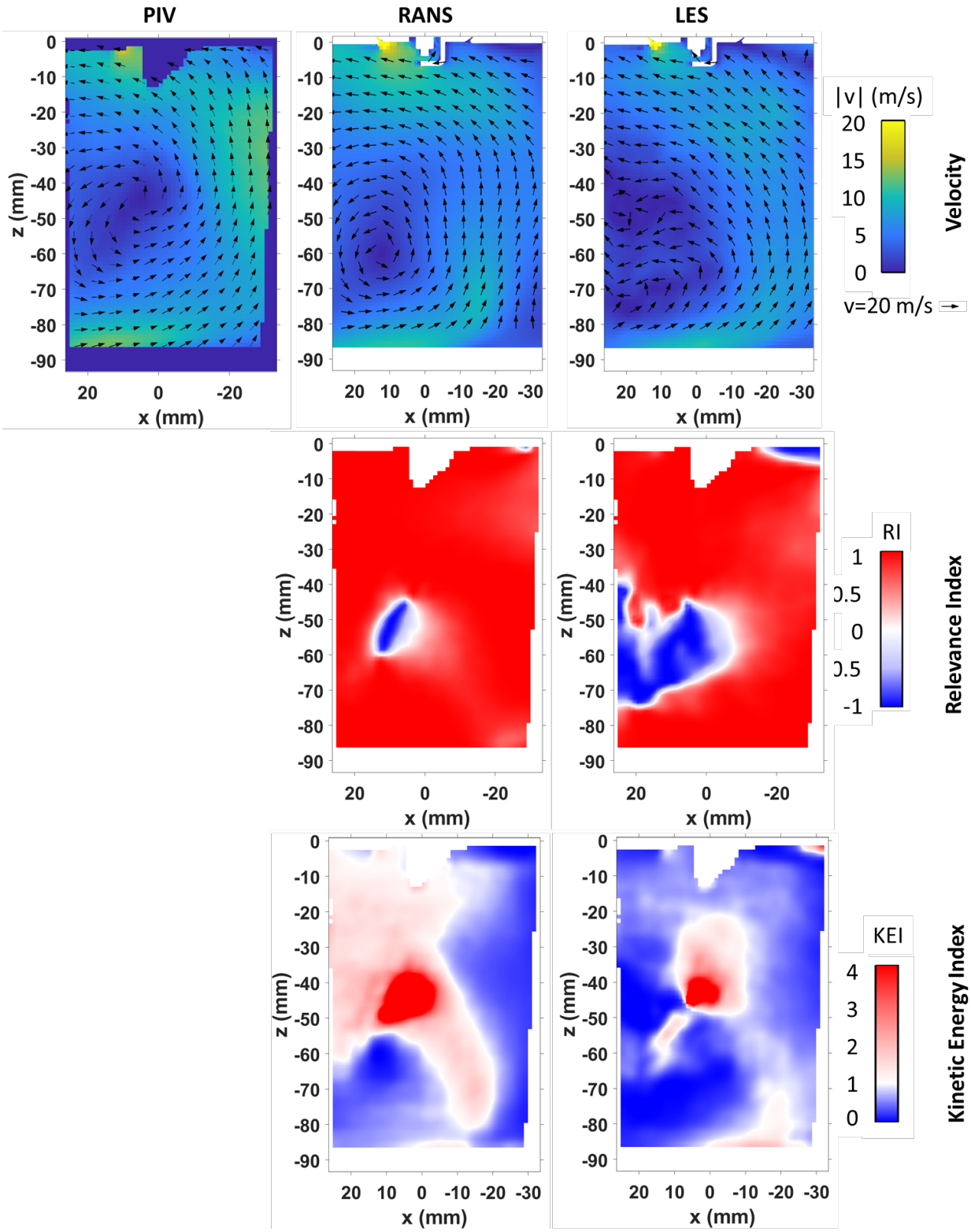

Figure 4.10. Bulk velocity field validation of Cases 1 and 2 in the tumble plane (y=0 mm) with PIV dataset S_2013_10_24_01 at -140 CAD aTDCc.

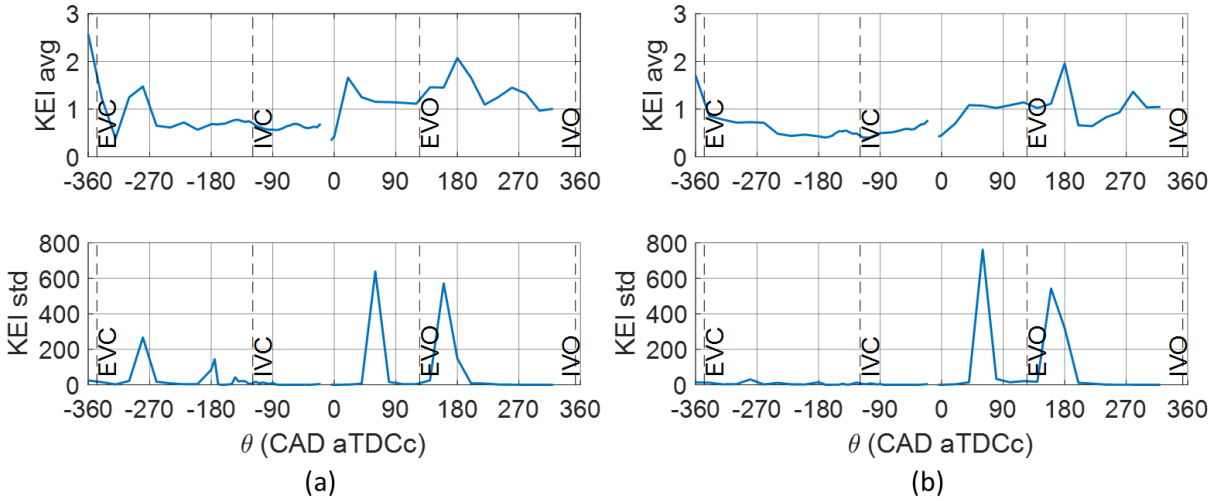

Figure 4.11. Spatial average and standard deviation of the Kinetic Energy Index for (a) Case 1 and (b) Case 2.

The bulk temperature fields from -260 CAD to 120 CAD are shown in Figure 4.12 for Cases 1 and 2. During the intake at -260 CAD, the intake jet structures are different for the two simulations. In the RANS model, vortical structures can be seen on the right side of the intake jet. This coincides with the two small vortical structures on the right side of the intake jet that led to low RI values in Figure 4.6. Such small vortical structures are not found in the LES near the intake jet, which leads to smoother temperature distribution in the jet vicinity. However, the two simulations show very similar temperature distributions from -100 to 120 CAD aTDCc, with slightly higher temperatures found in the LES. This is due to the LES predicting a lower heat transfer to the wall compared to the RANS model.

While there is some discrepancy during the intake stroke between both simulations and the measured bulk flow field, the bulk flow field during the compression stroke is well validated. Also, the bulk flow field has been validated by others who used a similar modeling case set-up as the current study [60]. This indicates that outside of the valve opening events that lead to a large discrepancy in velocity vector direction and kinetic energy, both turbulence models perform well in the bulk region. Therefore, for the rest of this chapter, the focus of the analysis will be the near-wall region.

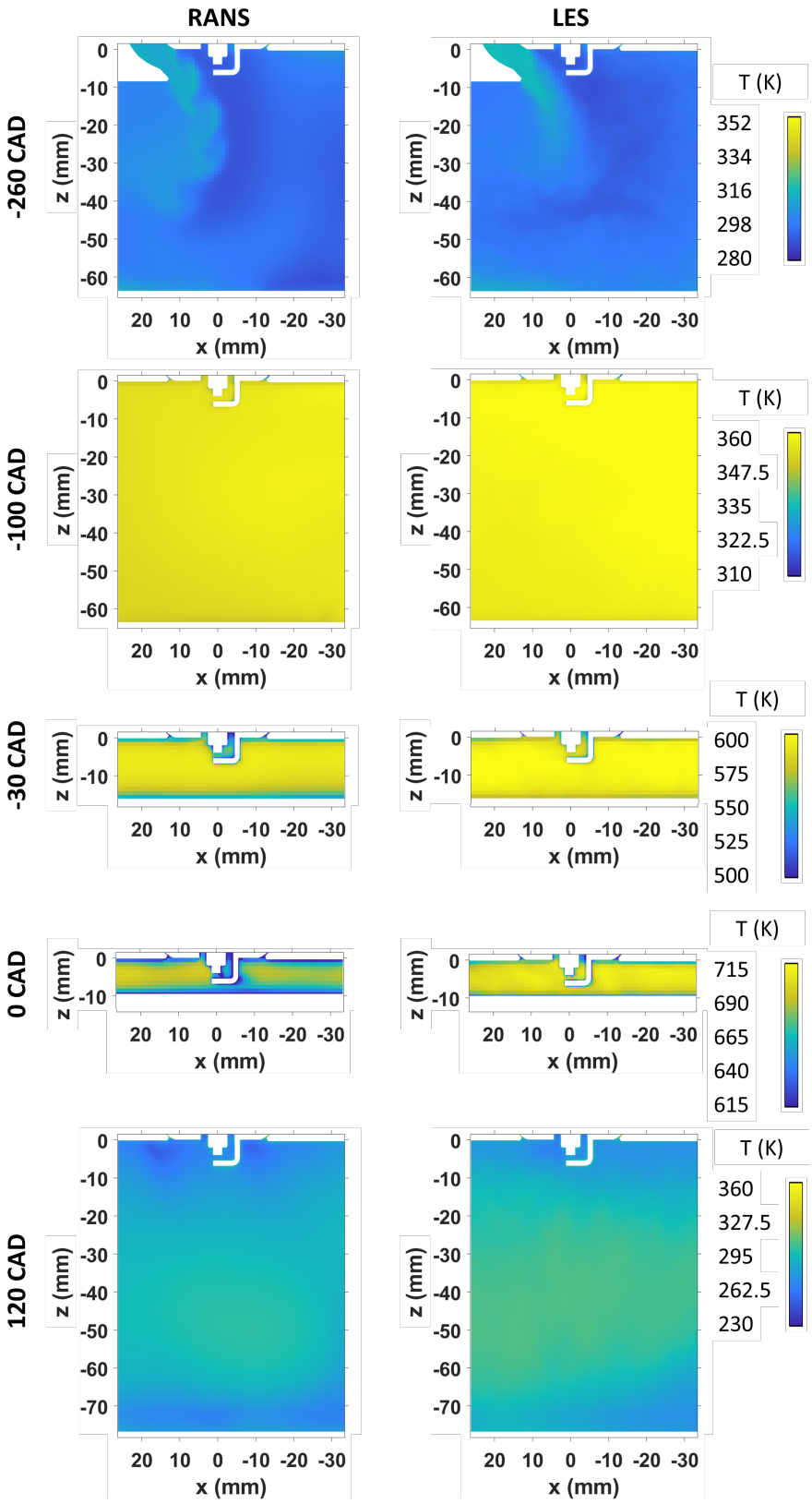

Figure 4.12. Bulk temperature field in the y=0 mm plane of Cases 1 and 2.

4.3.2 Near-Wall Velocity and Temperature Field

The near-wall velocity field was analyzed in Wu et al. [141, 142], as part of a collaborative effort between General Motors and the University of Michigan Collaborative Research Laboratory (UM-GM CRL). This analysis is repeated here for the near-wall PIV dataset S_2016_03_13_04, which has 141 imaged cycles in the ensemble average.

Compared to the bulk flow area which shows minimal influence from the wall model, the near-wall flow region tells a different story. As shown in Figures 4.13 to 4.16, the effects of the law of the wall model becomes more pronounced in both simulations. In Figure 4.13, the flow direction is well captured near the wall at -260 CAD aTDCc, as shown by the high RI values. The RI values decrease away from the wall. The velocity magnitude, on the other hand, is overestimated, especially in the RANS simulation. This overestimation is lower in the LES as evidenced by the lower KEI values with some areas that have KEI close to 1.

Figure 4.14 shows the near-wall velocity field at -100 CAD aTDCc. The RANS simulation can capture the flow direction correctly, while in the LES, the flow direction is opposite that of the PIV. In addition, the velocity magnitude is better captured by the RANS simulation than the LES with the LES having KEI values below 1 and the RANS having KEI values closer to 1.

Figure 4.15 shows the near-wall velocity field at -30 CAD aTDCc. In both simulations, the near-wall flow direction compares well to the PIV, but away from the wall, the flow is reversed. In the RANS simulation, a tumble-like structure appears on this plane at $y = 28$ mm, and its vortex center moves towards the head surface due to the upward piston motion. This causes the flow recirculation between z = -1 and -3 mm in Figure 4.15. In the LES, a weak jet-like structure from the head surface impinges with a much stronger flow near the piston surface, which is moving towards the exhaust valve, causing flow recirculation between z = 0 mm and -2 mm. The velocity magnitude is overpredicted to a larger extent in the RANS simulation than the LES, especially near the surface.

Figure 4.16 shows that as TDC is approached, the coherent structures from -30 CAD in the simulations are displaced due to convection, and the flow direction becomes similar to the measurement. Although the current field of view does not include the bulk flow region at $y = 28$ mm, the PIV measurements in the tumble plane revealed a tumble structure, with its core being displaced as TDC was approached [140]. The change in flow direction of the PIV measurement from -30 to 0 CAD aTDCc indicates the presence of a tumble structure with its center outside of

the field of view, while the simulations predict a tumble structure with a center that is different from the measurement. At this crank angle degree location, the velocity magnitude is overpredicted to a larger extent in the LES than in the RANS simulation.

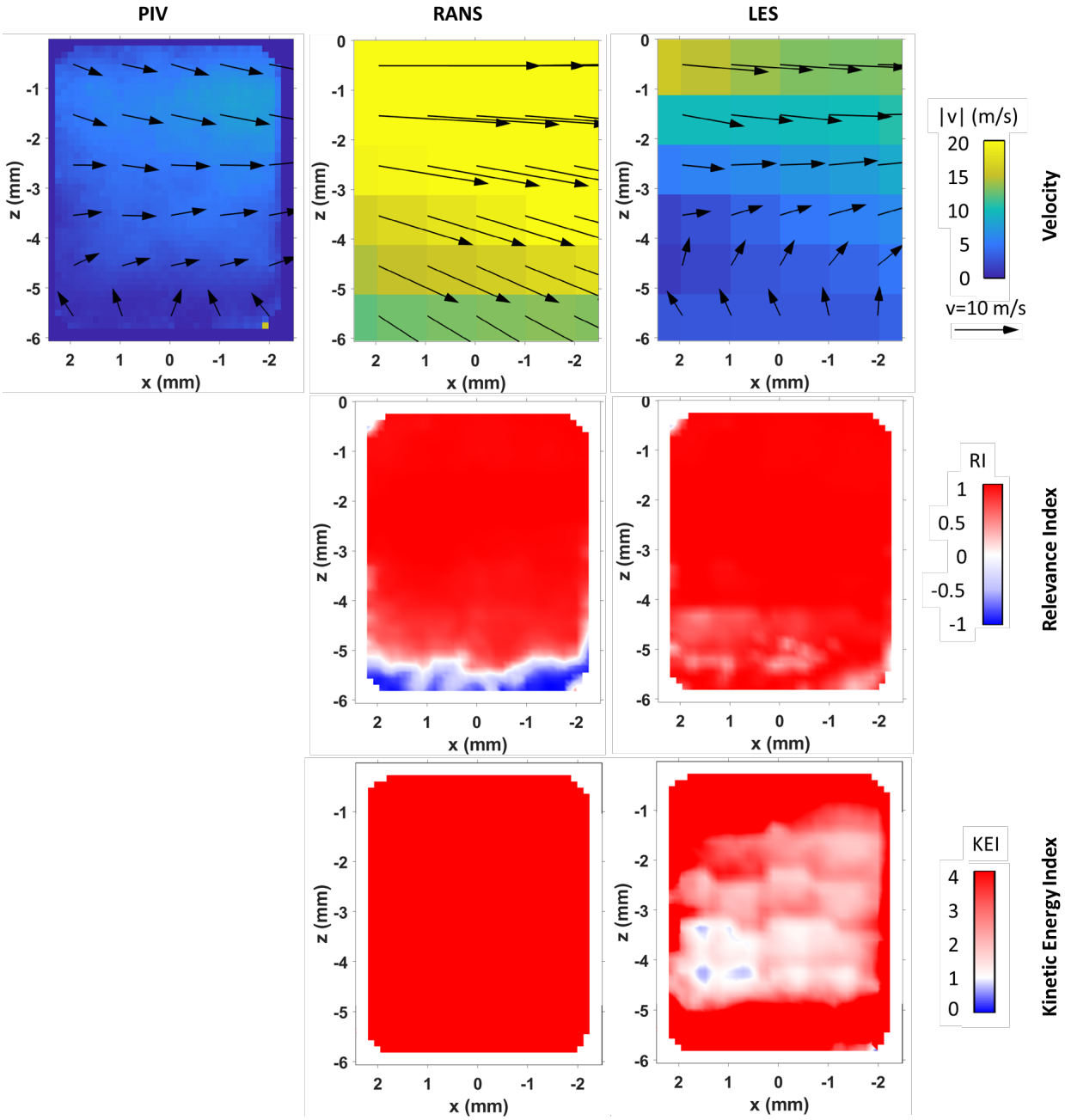

Figure 4.13. Near-wall velocity field validation of Cases 1 and 2 with PIV at -260 CAD aTDCc. Only every 8th vector in the PIV is shown.

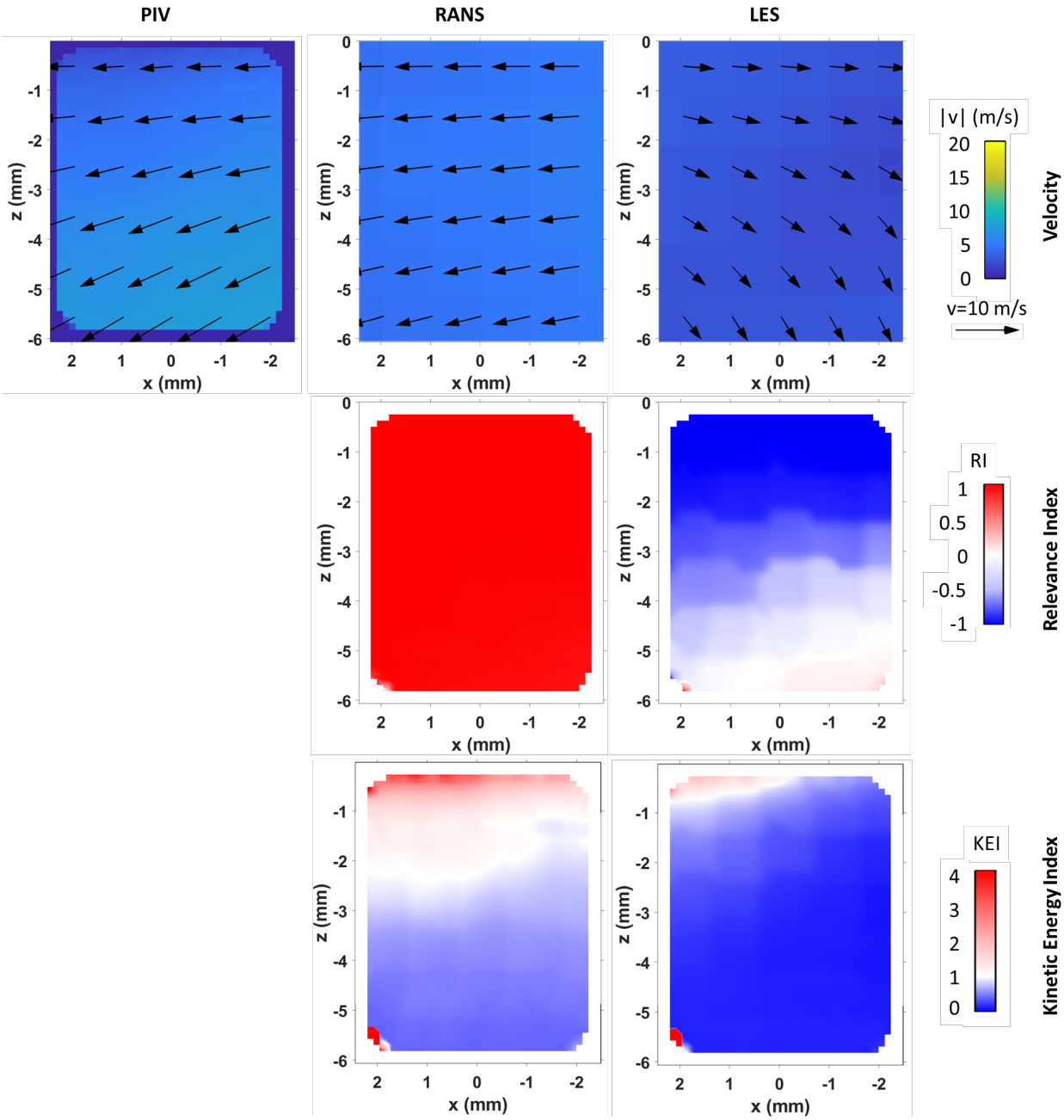

Figure 4.14. Near-wall velocity field validation of Cases 1 and 2 with PIV at -100 CAD aTDCc. Only every 8th vector in the PIV is shown.

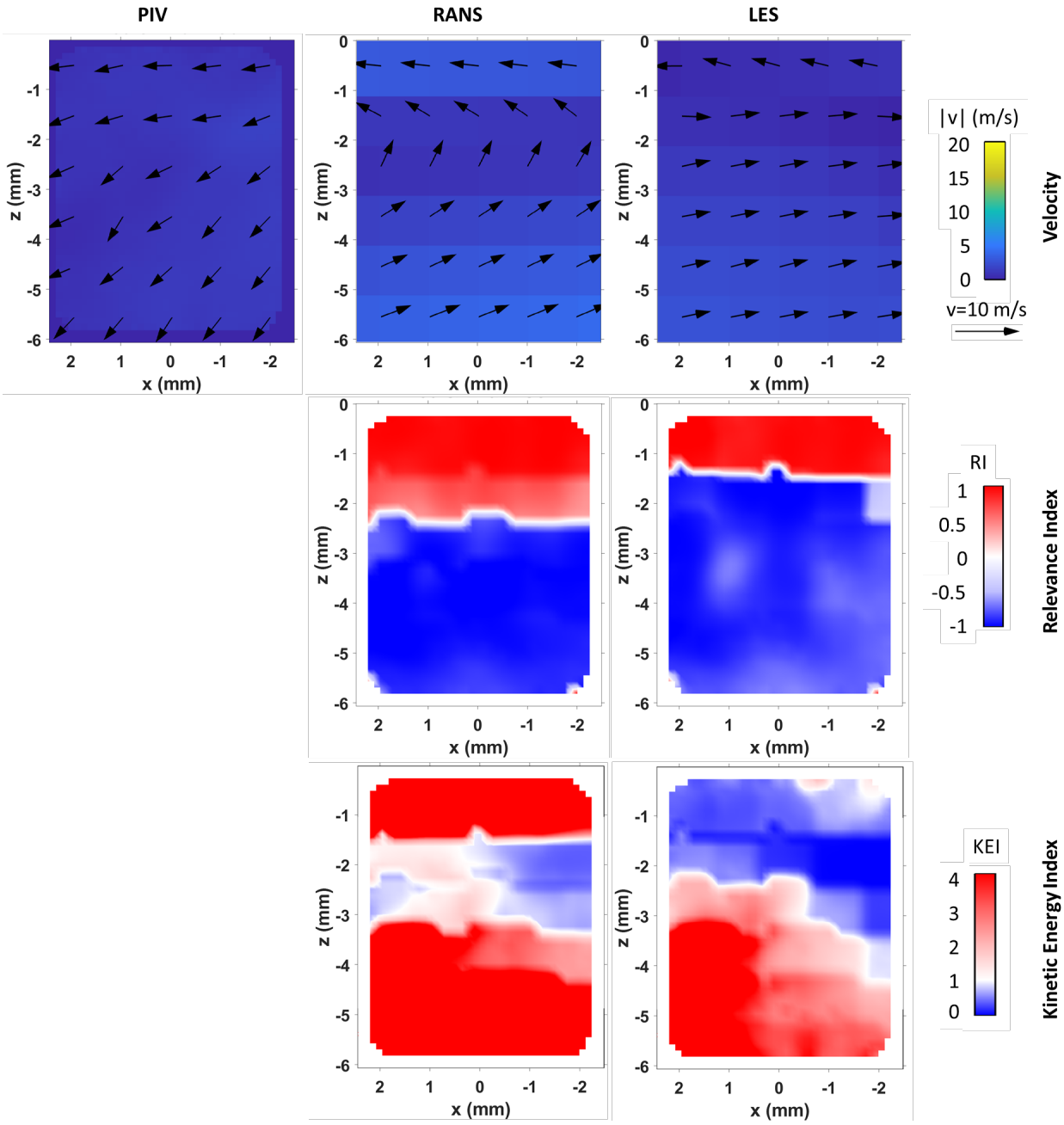

Figure 4.15. Near-wall velocity field validation of Cases 1 and 2 with PIV at -30 CAD aTDCc. Only every 8th vector in the PIV is shown.

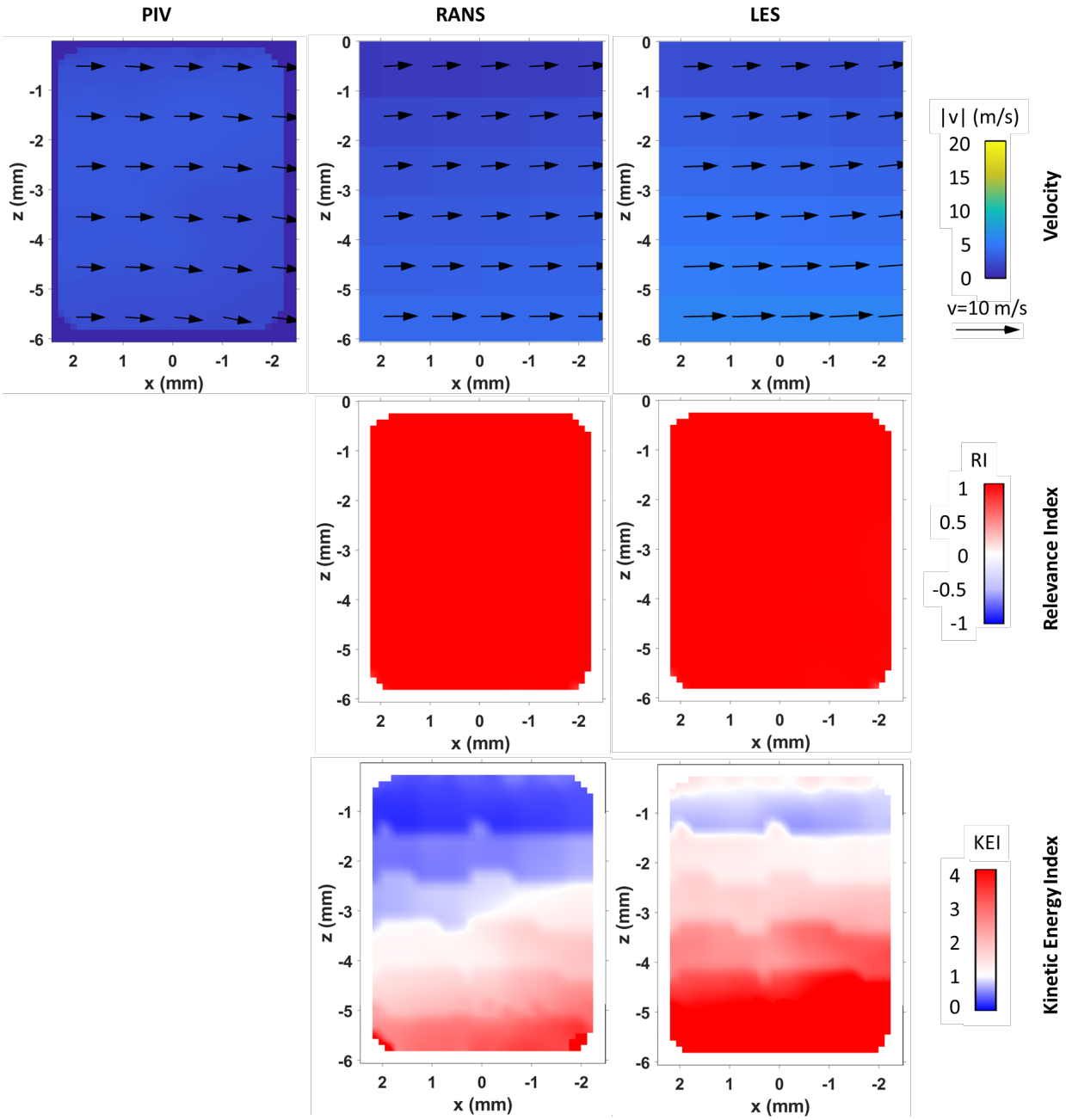

Figure 4.16. Near-wall velocity field validation of Cases 1 and 2 with PIV at 0 CAD aTDCc. Only every 8th vector in the PIV is shown.

The velocity components at $x = 0$ mm, as a function of wall distance z, are shown in Figure 4.17. The solid lines are the ensemble average velocity, while the shaded areas are the standard deviation of the ensemble-averaged velocity, and shows the CCV in the PIV and LES datasets. Only the fourth cycle of the RANS simulation is analyzed, therefore, no standard deviation in the RANS velocity field is provided.

The wall-parallel velocity component u is shown on the top row of Figure 4.17. At -260 CAD aTDCc, both simulations predict a much larger wall-parallel velocity u compared to the PIV, especially near the wall, with RANS predicting a more negative velocity than LES. With increasing wall distance, the LES velocity matches considerably well with that of the PIV, while the RANS velocity is slightly outside of the experimental velocity envelope. Both simulations predict a similar behavior of the velocity profile as a function of wall distance. CCV in the wall-parallel velocity is slightly underpredicted by the LES. At -100 CAD aTDCc, due to the flow direction mismatch between the LES and the PIV measurement, the wall-parallel velocity component of the LES is opposite that of the PIV. In contrast, the RANS predicts a wall-parallel velocity that is closer to the measured velocity and is within the experimental envelope. The LES predicts a smaller standard deviation than the measurement. At -30 CAD aTDCc, the LES predicts a wall-parallel velocity close to the wall that compares better with the measurement, while RANS overpredicts this value, but is within the experimental envelope. The standard deviation of the LES is comparable with that of the measurement. At TDC, the LES velocity matches considerably well with the measurement from z = -1 mm to -2 mm, while the RANS underpredicts the velocity. Away from the wall, $\bar{u}$ of both simulations do not match well with the measured value.

The wall-normal velocity component v is shown on the bottom row of Figure 4.17. From -260 to -30 CAD aTDCc, the LES predicts a velocity that is much closer to the measurement than the RANS model. The RANS simulation predicts a velocity that is within the experimental envelope. Closer to the wall, the RANS is able to capture the wall-normal velocity well, but with increasing wall distance, the prediction deteriorates. At TDC, the RANS predicts a wall-normal velocity that is closer to the experimental ensemble average than the LES. The CCV in the wall-normal velocity of the LES is smaller than that of the PIV.

The wall model is applied at the first connected to the surface and provides the wall shear stress as a boundary condition for the rest of the CFD domain. Figure 4.17 implies that the wall model has a larger influence on the wall-parallel velocity component than the wall-normal velocity component. This seems to be due to the law of the wall model being formulated with only the wall-parallel velocity component. As the wall distance increases, the wall model effects on the velocity predictions diminish.

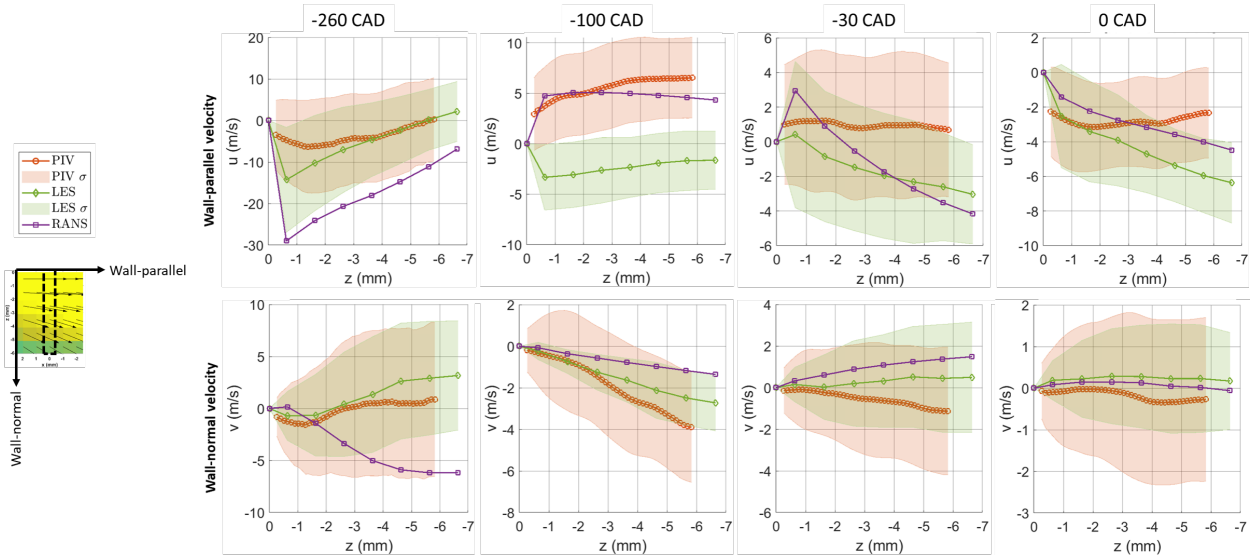

Figure 4.17. Near-wall velocity components compared with PIV.

Figure 4.18 shows the ensemble-averaged near-wall temperature field from PLIF thermometry, obtained by Alzuabi [39], from -100 to 0 CAD aTDCc. The PLIF measurement at TDC is at 0.1 CAD aTDCc, but for the analysis here it is assumed to be equal to TDC. The second and third rows are the temperature fields in the same region from the RANS and LES. The temperature scales are different for each CAD. These PLIF temperature fields were analyzed in Wu et al. [38]. The PLIF images show that there is some thermal stratification at -100 CAD aTDCc, and the stratification increases towards -35 CAD aTDCc with small hot and cold structures. In contrast, the temperature fields of both simulations are rather homogeneous and predicted a much lower temperature than the measurement. Also, the small structures are not seen in the simulations. At TDC, the PLIF measurement shows a more gradual increase in temperature from the surface to the bulk area.

To better compare the temperature fields and to remove the potential effects of the PLIF calibration or model parameters on the comparison, the spatial mean of the ensemble-averaged temperature field is subtracted from each image in Figure 4.18. The resulting relative temperature fields are shown in Figure 4.19. At -100 CAD aTDCc, the PLIF measurement has colder and hotter structures near the wall and in the bulk region away from the wall. These structures are also seen at -35 and 0 CAD aTDCc. In contrast, the relative temperatures in the simulations increase from negative to positive values with increasing wall distance. With compression, the magnitude of the relative temperatures increases in the simulations, whereas the relative temperatures of the PLIF

remain fairly similar throughout the compression stroke. The exception is the cold structure in the lower-left region of the PLIF images, which reduces in magnitude.

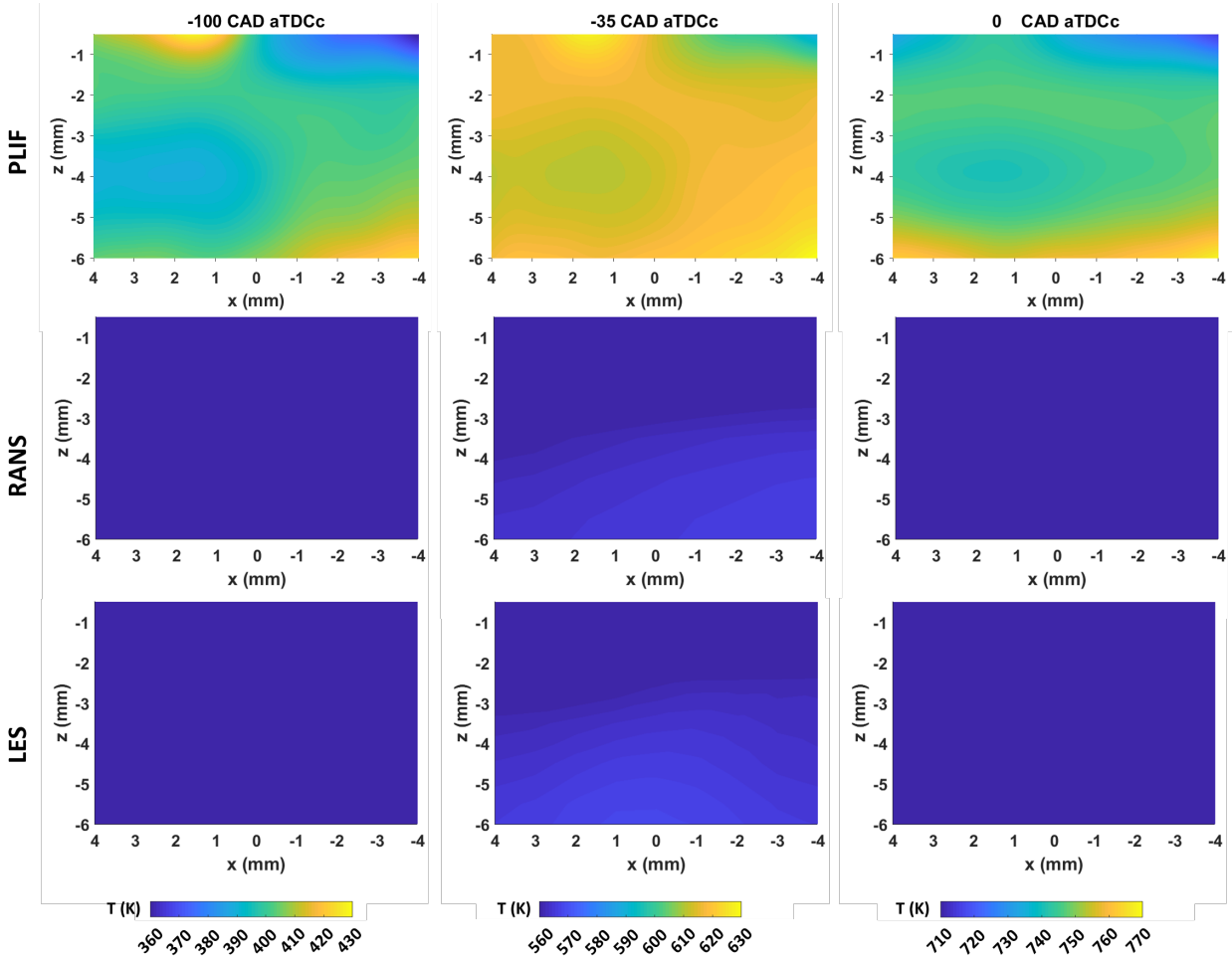

Figure 4.18. Near-wall temperature field validation of Cases 1 and 2 with temperature PLIF measurements.

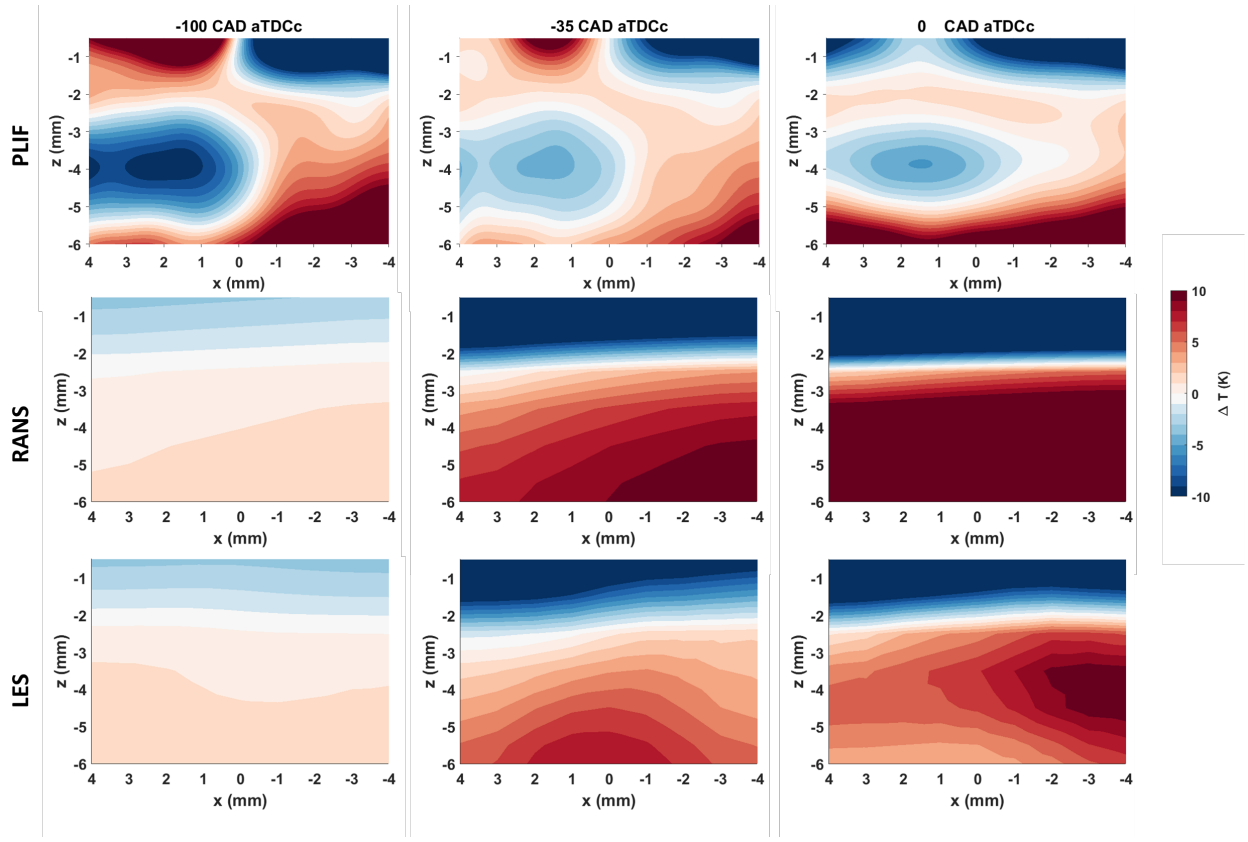

Figure 4.19. Relative near-wall temperature field, obtained from subtracting the ensemble average from the spatial mean, of Cases 1 and 2 compared with temperature PLIF measurements.

The temperature profiles at $x = 0$ mm as a function of wall distance is shown for Cases 1 and 2 and the PLIF measurement in Figure 4.20. Both models predict very similar temperature profiles. The LES predicts a slightly larger temperature near the wall. This leads to larger gas temperatures away from the wall in contrast with the RANS simulation. As expected, the gas temperature increases with compression due to compression heating. However, both simulations are unable to predict the measured PLIF due to the thermal boundary condition used, as Cases 1 and 2 both use an isothermal boundary condition of 318.16 K.

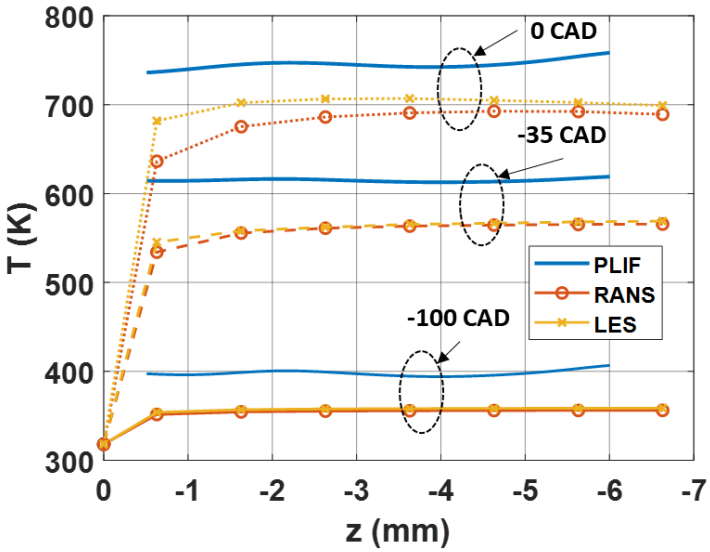

Figure 4.20. Temperature profiles from Cases 1 and 2 compared to temperature PLIF measurements from -100 to 0 CAD aTDCc.

The differences in the temperature profile could be attributed to the predicted surface heat flux by the two simulations. Shown in Figure 4.21 are the surface heat flux from Cases 1 and 2 compared against the measured heat flux. This surface heat flux was measured at the heat flux probe at the cylinder head, at x=12.1 mm and y=33.4 mm. Note that while the heat flux probe contains two thermocouples that have some finite surface area, this area small and comparable to a point location on the cylinder head. Therefore, the measured heat flux is compared to the simulated heat flux at the same location as the measurement probe.

The solid line is the ensemble average heat flux, and the shaded area is the standard deviation showing the CCV in heat flux in the measurement and LES. Note that the surface heat flux is measured at a location outside of the near-wall flow and temperature FoVs. A 100 Hz low-pass filter was applied to the measured heat flux to filter out the noise in the measurement. Note that low-pass filtering the measured heat flux tends to reduce the peak value, and the true measured peak heat flux is approximately 120 kW/m^{2}K, higher than shown in the figure.

The overall trend is captured by both simulations. The RANS peak heat flux matches well with the filtered measured peak heat flux. The RANS peak heat flux is approximately 104 kW/m^{2}K and compares well to the unfiltered peak heat flux of 120 kW/m^{2}K. The LES ensemble average peak heat flux is about 86 kW/m^{2}K, much smaller than the unfiltered peak heat flux. Also, the CCV in the LES heat flux is smaller than the experiment. There is relatively no CCV during the

intake, expansion, and exhaust strokes, and during early compression, but it increased towards TDC. Both RANS and LES capture a reversal of heat flux during the late expansion stroke, with a larger reversal being predicted by the RANS simulation. In the experiment, this reversal occurred earlier during the expansion stroke. In both simulations, the onset of negative heat flux occurred even when the bulk gas temperature was larger than the wall temperature. This is because the local near-wall gas temperature near the heat flux probe was lower than the wall temperature. This reversal of heat flux was observed by [122] and was attributed to unsteady effects, specifically, the pressure work in the energy equation.

The effects of the peak heat flux can be seen in the predicted in-cylinder pressures shown in Figure 4.5. The larger peak heat flux in RANS leads to increased heat transfer from the gases to the walls, and a smaller peak in-cylinder pressure is obtained which falls below the experimental pressure envelope. The LES predicts a smaller peak heat flux, leading to larger in-cylinder peak pressure. The CCV in heat flux also contributes to the CCV in the in-cylinder pressure.

The heat transfer model that was used in this dissertation was originally developed by Han and Reitz using a RANS turbulence model [77]. This heat transfer model, therefore, depends on RANS variables such as turbulent kinetic energy from the RNG k-ε model. When this heat transfer model is used with LES subgrid-scale models, such as the dynamic structure model, the subgrid-scale turbulent kinetic energy is used. The absolute value of this variable is much smaller in LES than RANS, which deteriorates the predicted heat flux. Recalibration of the Han and Reitz model for LES might improve LES predictions.

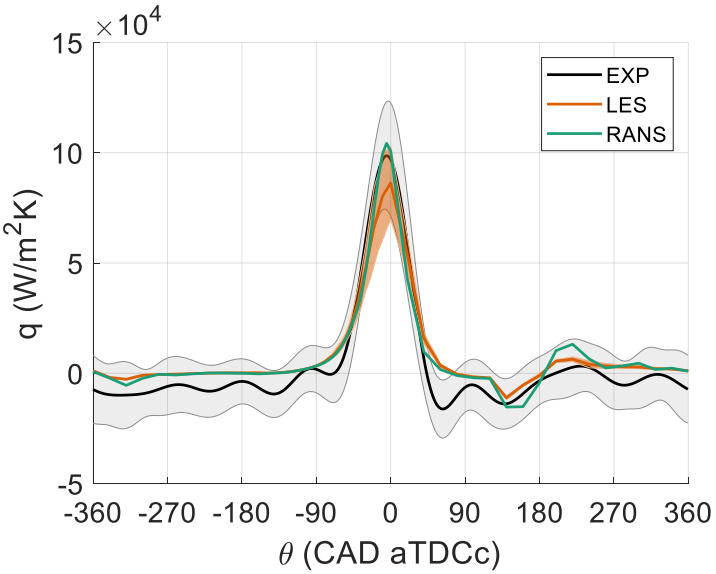

Figure 4.21. Surface heat flux profiles from Cases 1 and 2 compared against measured heat flux.

The use of the law of the wall model is widespread in the engine CFD community. However, measurements have shown that the law of the wall model is not applicable to engine CFD [72]. To show that this is the case for the PIV measurements analyzed here, the near-wall flow is normalized by standard wall units as follows. The conditionally sampled velocity components from the near-wall PIV measurement were ensemble-averaged, then spatially averaged over 8 columns to match the spatial resolution of 1 mm of the simulations. Linear regression through the origin [28, 72] was used to evaluate the velocity gradient $\frac{d\bar{u}}{dy}$ at the wall, using the no-slip condition and the first two non-zero velocities from the surface. From this, the shear stress was calculated using Equation 2.1. The dynamic viscosity μ_w used in Equation 2.1 was determined from Sutherland's law [143]

$$\mu_w = \mu_{ref}\left(\frac{T_s}{T_{ref}}\right)^{\frac{3}{2}}\frac{(T_{ref}+S)}{T_s+S} \tag{4.10}$$

Here, $T_{ref} = 273$ K, Sutherland's constant $S = 111$ K, and $\mu_{ref} = 1.716\times10^{-5}$ kg/m-s for air. The gas density ρ_w is evaluated with the ideal gas law using the measured in-cylinder pressure and the surface temperature T_s. The density and dynamic viscosity increase with compression and decrease again with expansion, as shown in Figure 4.22. This is due to compression heating and expansion cooling that leads to increasing and decreasing temperatures.

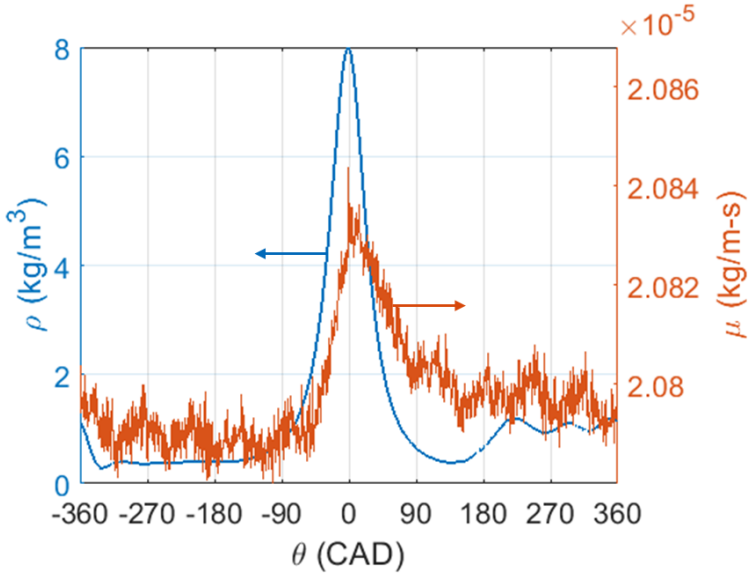

Figure 4.22. Density (blue) and dynamic viscosity (red) of the PIV measurement S_2016_03_13_04.

The shear velocity u_τ was then found using

$$u_\tau = \sqrt{\frac{\tau_w}{\rho_w}} \tag{4.11}$$

The wall-parallel velocity and the wall-distance were non-dimensionalized using Equations 2.2 and 2.3. Results are shown in Figure 4.23. Also plotted is the law of the wall and the Werner and Wengle wall models. It can be seen that throughout the compression stroke and into the expansion stroke, both wall models do not resemble the measured velocity profiles, confirming previous studies of the momentum boundary layer in ICEs [28, 30], especially with increasing wall distance. The measured velocity profiles do not collapse to a single line but instead depends on the crank angle degree location. If either wall models are used, their constants should vary throughout the engine cycle. This is currently not a feature in most commercial CFD software, including the CONVERGE package, and most likely a user-defined function needs to be implemented to apply a more accurate engine wall model.

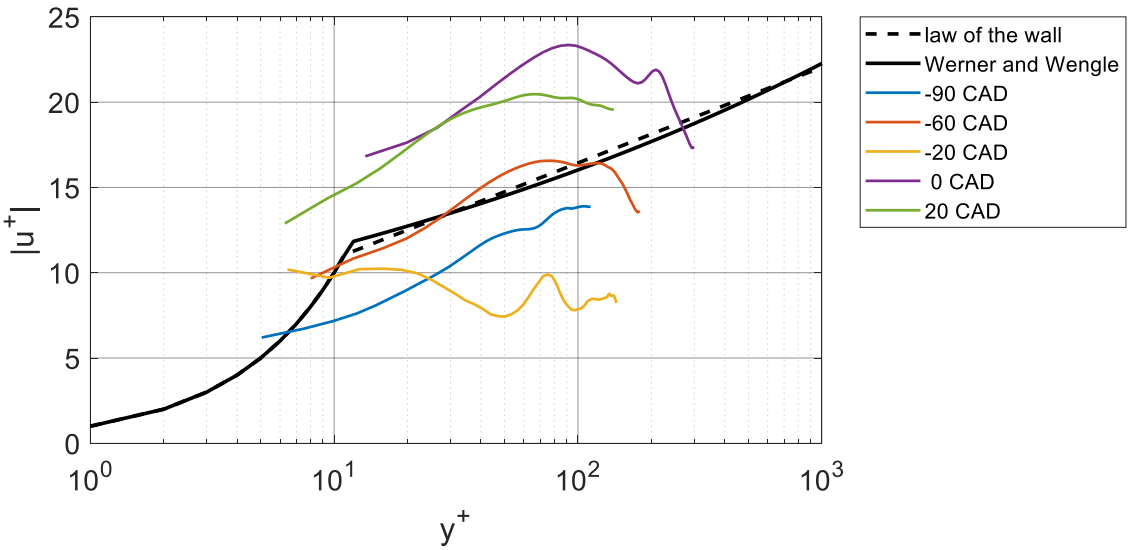

Figure 4.23. Ensemble-averaged wall-parallel velocity u from dataset S_2016_03_13_04, normalized by the shear velocity. The black dashed line is the law of the wall model with κ=0.41 and B=5.2. Figure updated from [142].

4.4 Effects of Mesh Refinement in LES

In the previous section, it was shown that the LES (Case 2) was unable to predict the correct near-wall velocity field, especially the wall-parallel velocity component. The mesh size is known to affect the resolved velocity field in LES [71, 132], especially near the walls [133], and surface heat flux [134]. Increasing the near-wall mesh could lead to better predictions in the velocity and

temperature fields. To assess the effects of the near-wall mesh on the LES predictions, the near-wall mesh was refined at several locations within the cylinder to 0.5 mm. The mesh was previously shown in Figure 3.11. This was then compared against the previous LES with a base near-wall mesh of 1 mm. 31 cycles were simulated with the refined mesh, and the first cycle was discarded from statistical analysis.

The in-cylinder pressure is shown in Figure 4.24. The base mesh model predicts a slightly higher in-cylinder peak pressure than the measurement, while the refined mesh peak pressure compares well with the measured peak pressure. However, the timing is slightly off as the measured peak pressure is advanced when compared to the simulations. The predicted CCV in the in-cylinder pressure is also small compared to the measurement.

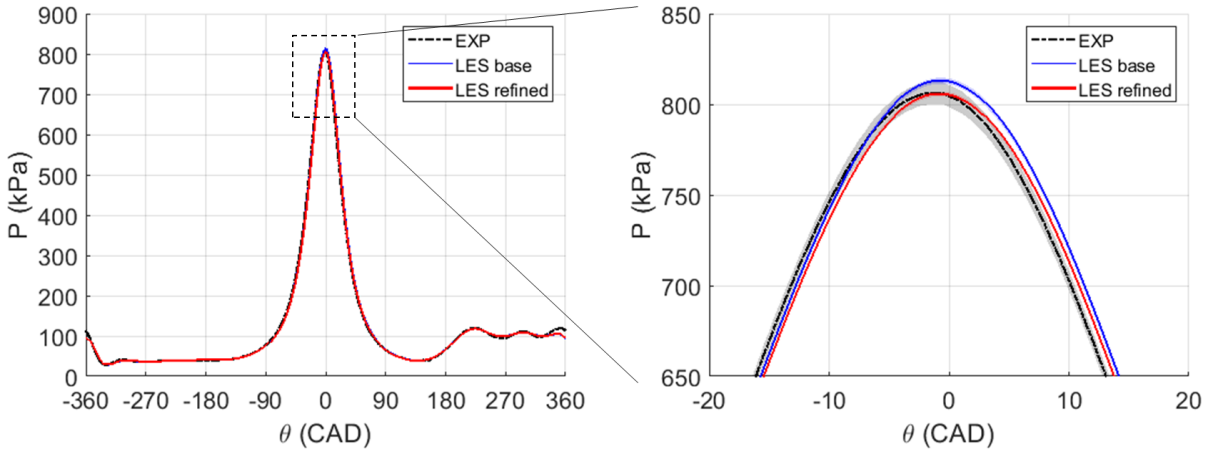

Figure 4.24. The dynamics of the in-cylinder pressure of Case 2 base and refined mesh simulations compare well to the experimental data. Figure updated from [142].

The near-wall velocity fields at -100 CAD aTDCc are shown in Figure 4.25 for the base and refined LES, compared against PIV measurements. Both models are unable to predict the flow direction correctly. With the refined mesh, the flow was better resolved and a larger velocity magnitude was obtained in the near-wall region as shown by the larger KEI values. This larger velocity magnitude will affect the heat transfer predictions as it leads to more convective heat transfer. Figure 4.26 shows that at -30 CAD, a flow reversal is seen in the base mesh but not in the refined mesh. This leads to the differences seen in the RI fields. Again, the velocity magnitude predicted by the refined mesh is larger than the base mesh. Finally, at TDC, Figure 4.27 shows that the flow direction is well predicted by both simulations, but velocity magnitude is still overpredicted by the refined mesh case.

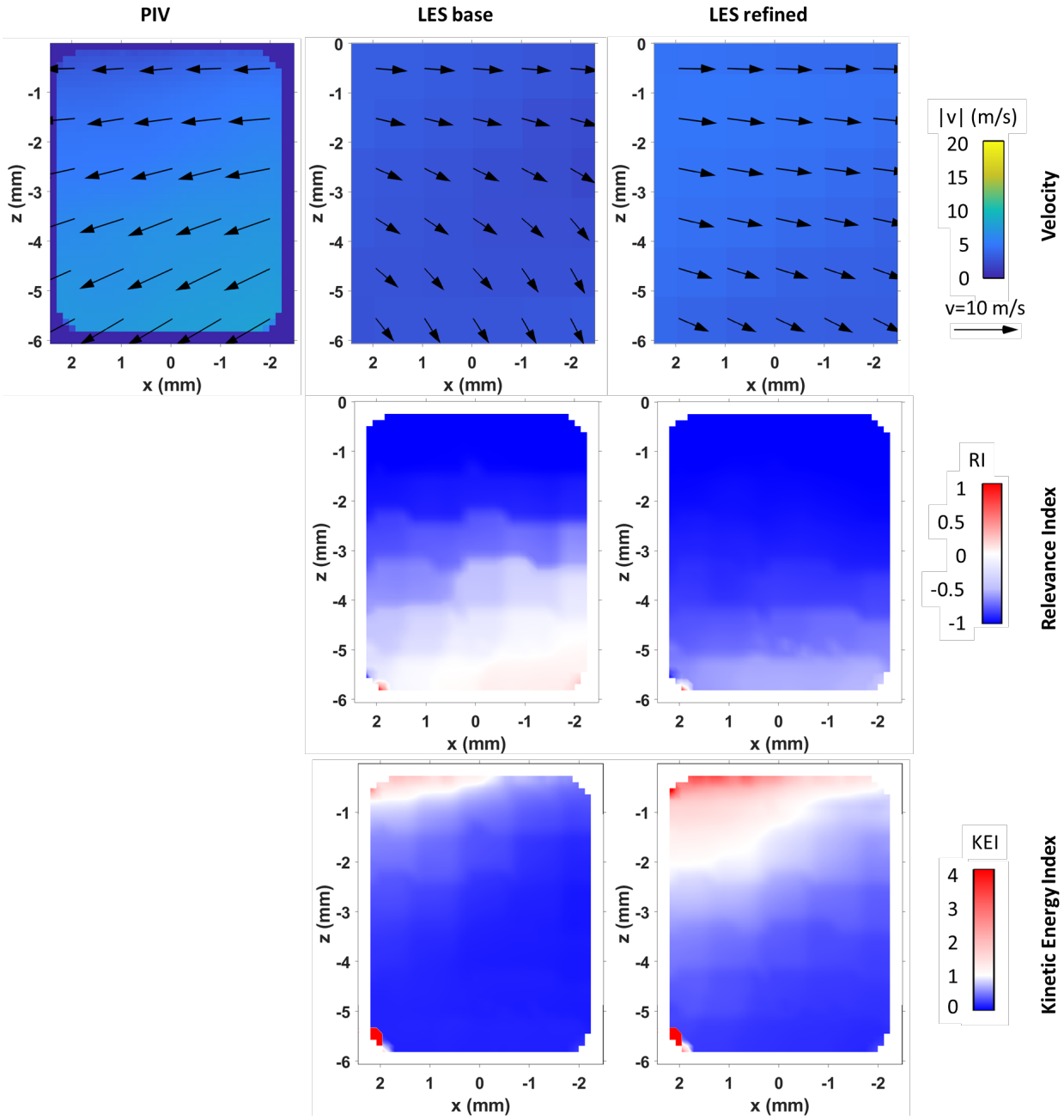

Figure 4.25. Near-wall velocity fields from Case 2 base and refined mesh simulations, compared against dataset S_2016_03_13_04, at -100 CAD aTDCc.

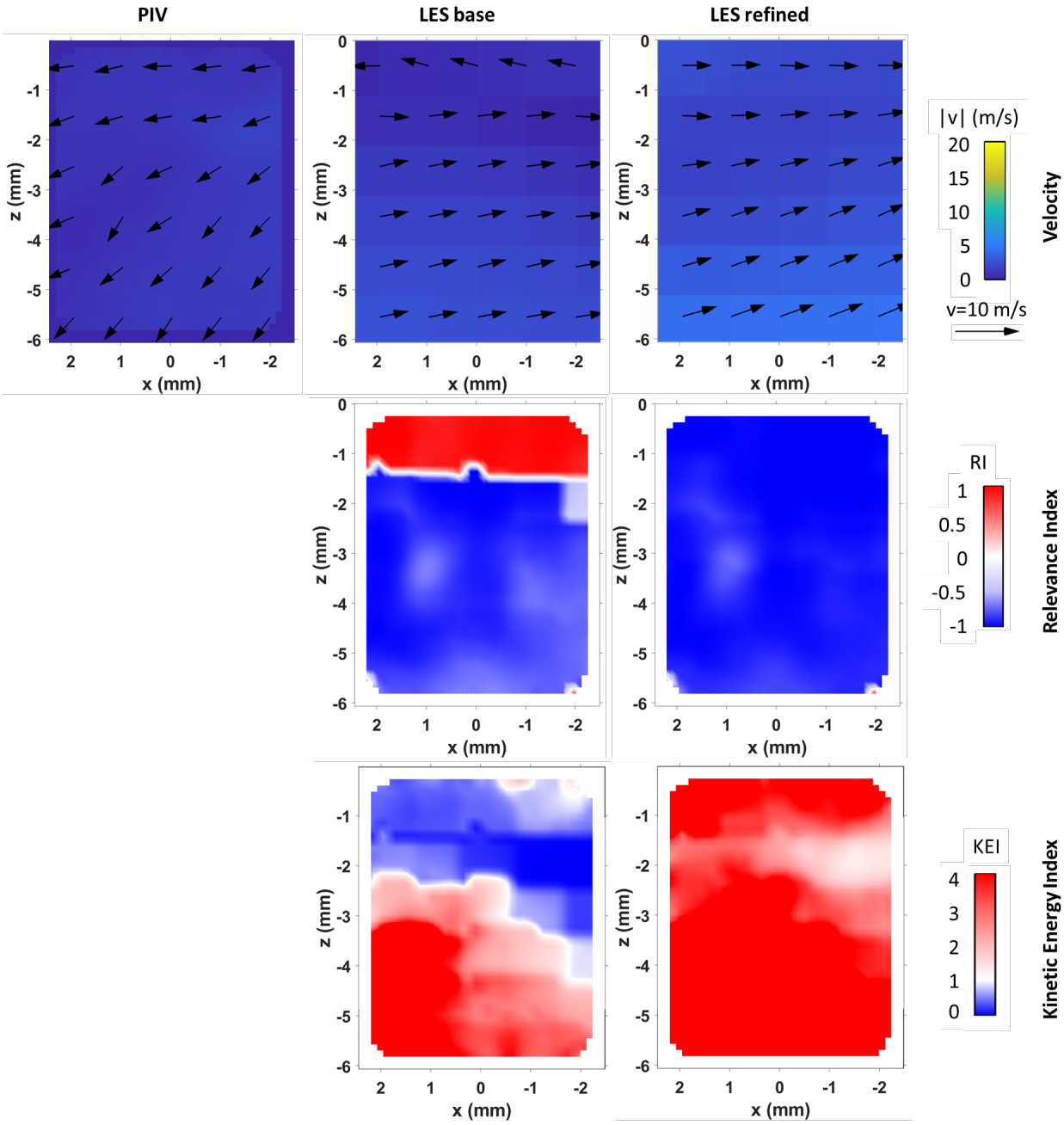

Figure 4.26. Near-wall velocity fields from Case 2 base and refined mesh simulations, compared against dataset S_2016_03_13_04, at -30 CAD aTDCc.

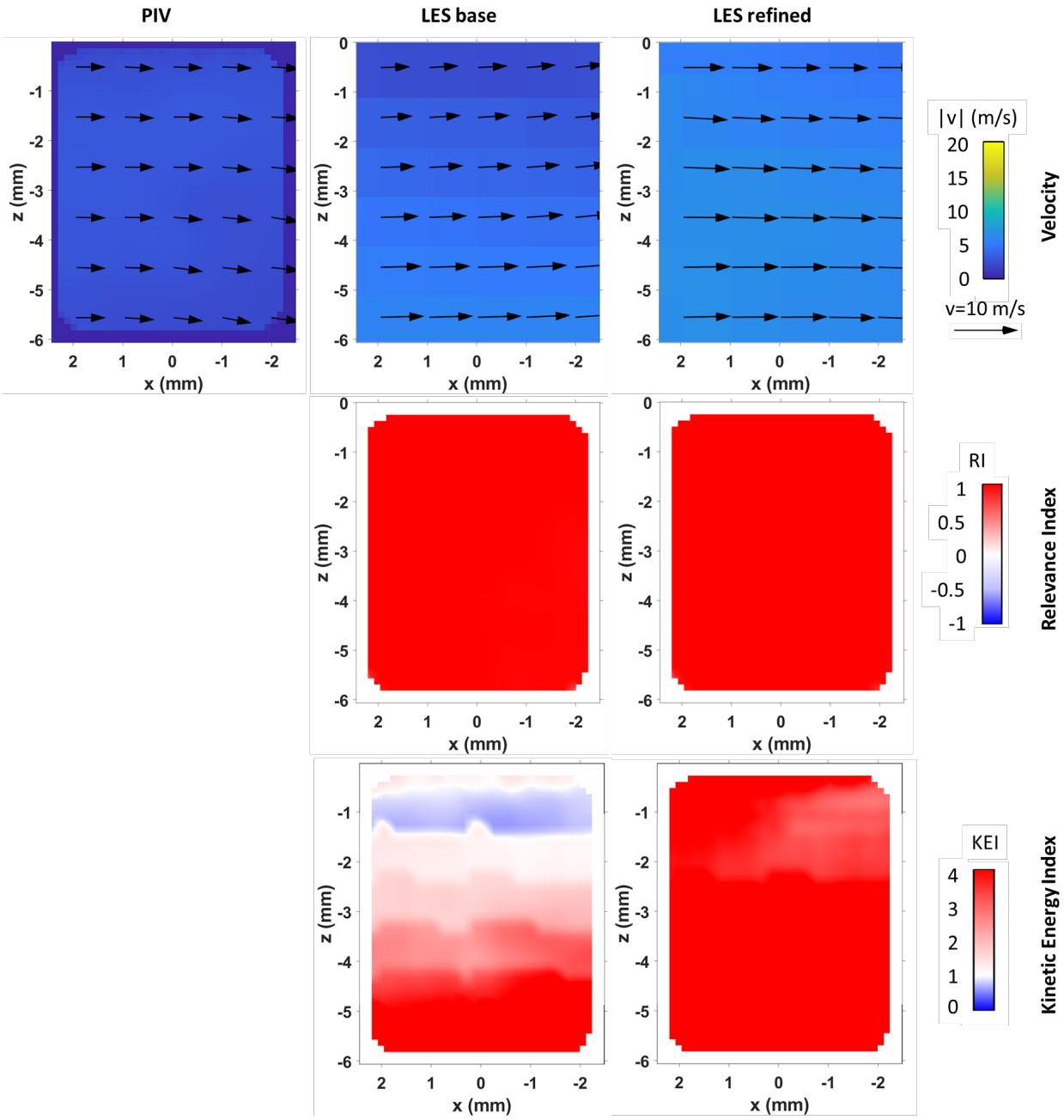

Figure 4.27. Near-wall velocity fields from Case 2 base and refined mesh simulations, compared against dataset S_2016_03_13_04, at 0 CAD aTDCc.

The ensemble average temperature fields are not shown here since both the refined mesh simulation predicted very similar temperature fields as the base mesh LES shown in Figure 4.18. The relative temperature fields in Figure 4.28 are very similar between the base and refined mesh simulations. This also shows that just refining the near-wall mesh does not lead to smaller structures in the simulations as found in the PLIF measurement. A refinement of the entire in-

cylinder mesh would be needed to resolve the smaller structures, which leads to computational costs that cannot be met with currently available computing resources.

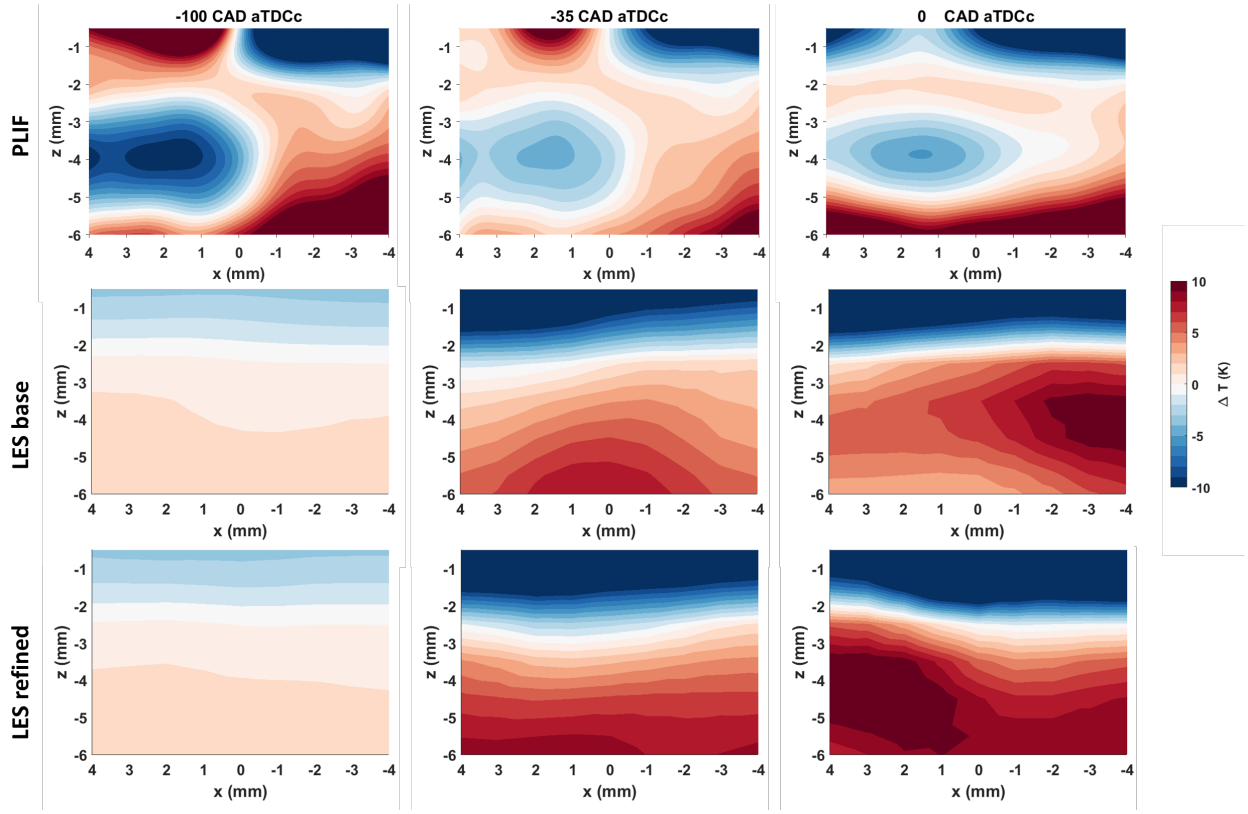

Figure 4.28. Relative near-wall temperature field, obtained from subtracting the ensemble average from the spatial mean, of Cases 2 base and refined mesh simulations compared with temperature PLIF measurements.

Refining the near-wall mesh leads to a more gradual change in the temperature profile as seen in Figure 4.29. The refined near-wall mesh leads to lower gas temperatures near the wall, but as wall distance is increased, the gas temperature of both simulations become very similar. This is because the smaller grid size near the wall allows for better resolving the temperature gradient, but the grid size away from the wall is the same between the two simulations. However, both models fail to predict the correct magnitude of the measured temperature.

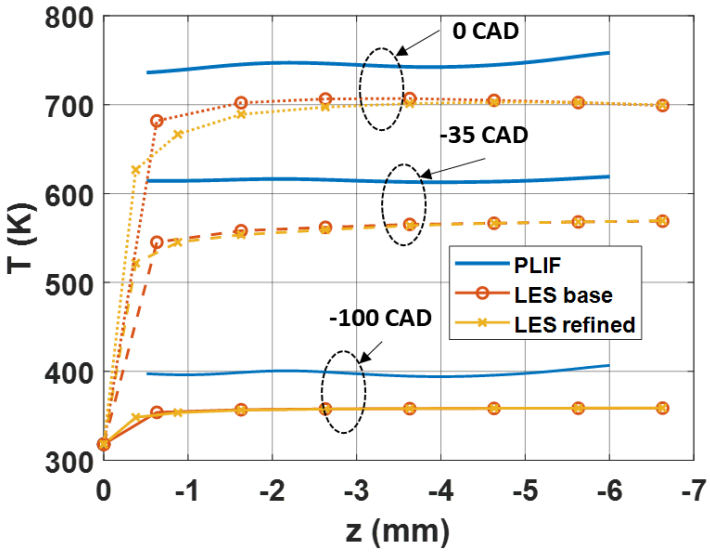

Figure 4.29. Temperature profiles from Case 2 base and refined mesh simulations compared to temperature PLIF measurements from -100 to 0 CAD aTDCc.

Figure 4.30 shows the effects of near-wall mesh refinement on surface heat flux predictions. Due to the increased near-wall velocity magnitude in the refined mesh, the convective heat transfer in the near-wall region is enhanced. This leads to larger peak heat fluxes in the refined mesh case. The peak heat flux of the refined mesh is approximately 113 kW/m^{2}K and is larger than the filtered measured peak heat flux. However, this peak value compares better with the unfiltered peak heat flux of 120 kW/m^{2}K than the base mesh case. In terms of the standard deviation, the base mesh simulation has a maximum standard deviation of 20 kW/m^{2}K, while the refined mesh has a maximum standard deviation of 23 kW/m^{2}K. The maximum standard deviation of the filtered heat flux is 26 kW/m^{2}K. Therefore, refining the near-wall mesh helps to improve heat transfer predictions of the LES in terms of CCV.

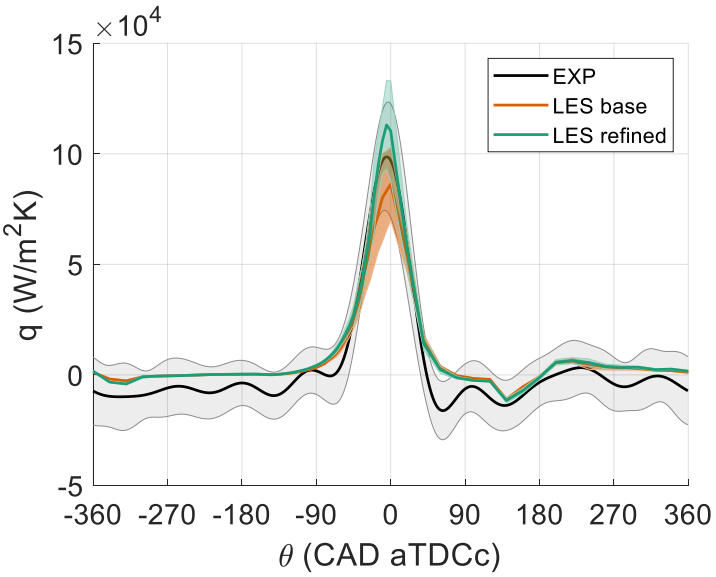

Figure 4.30. Heat flux profiles from the base and refined mesh of Case 2 and dataset S_2016_03_13_04.

4.5 Effects of the Wall Model in LES

Because the refined mesh leads to improved heat transfer predictions, the rest of the dissertation will use the 0.5 mm near-wall mesh. Here, the effects of the wall models in engine LES on the near-wall velocity and temperature fields are assessed. This was done because the Werner and Wengle wall model was developed specifically for LES [74], but the combination of an LES turbulence model and the law of the wall model is often used in engine CFD. The in-cylinder pressure is shown in Figure 4.31, and both simulations predict very similar in-cylinder pressures that are close to the measured pressure. The timing or dynamics of the pressure is not affected by the wall model used, and CCV is still underpredicted.

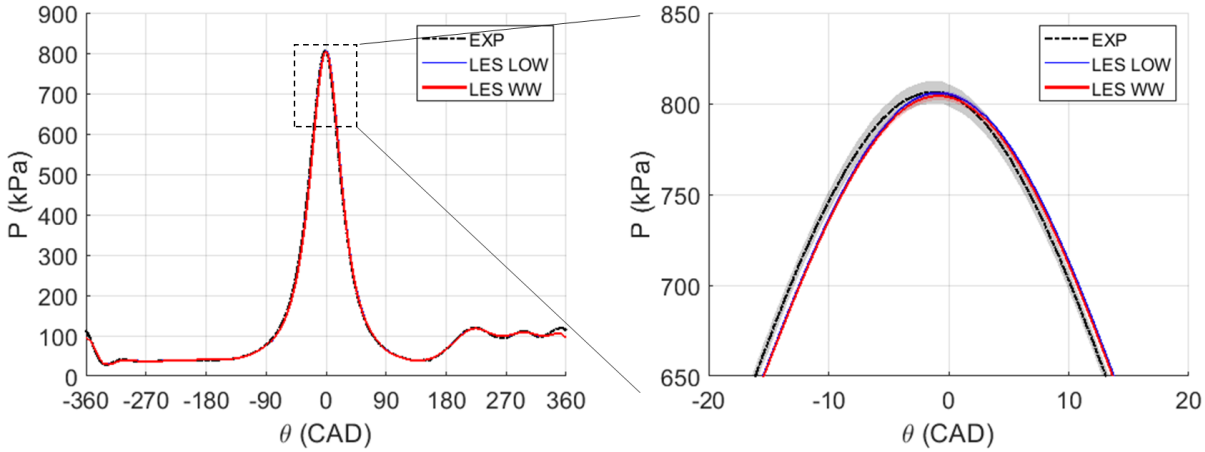

Figure 4.31. The in-cylinder pressures of Cases 2 and 3 compare well to the experimental data.

The near-wall velocity field at -100 CAD aTDCc is compared in Figure 4.32. The simulated flow directions of both cases are almost identical, with slight variations far away from the wall as indicated by the higher RI values in the LES with Werner and Wengle model. The LES does not simulate the correct near-wall flow direction regardless of the wall model used at this crank angle degree location. The velocity magnitude of the LES with Werner and Wengle model is also smaller than the LES with law of the wall, as indicated by the smaller KEI values, especially in the region away from the wall. In Figure 4.33, the flow directions at -30 CAD aTDCc of both simulations are similar, but again, the velocity magnitude of the LES with Werner and Wengle wall model is smaller. Figure 4.34 shows similar behavior at TDC, where the flow direction is the same between the two models, and the velocity magnitude is smaller with the Werner and Wengle model, especially near the wall. Therefore, it seems that the Werner and Wengle wall model does not lead to any differences in the ensemble average velocity field direction, but it does tend to

predict smaller velocity magnitudes in the near-wall region. This will ultimately affect the wall heat transfer.

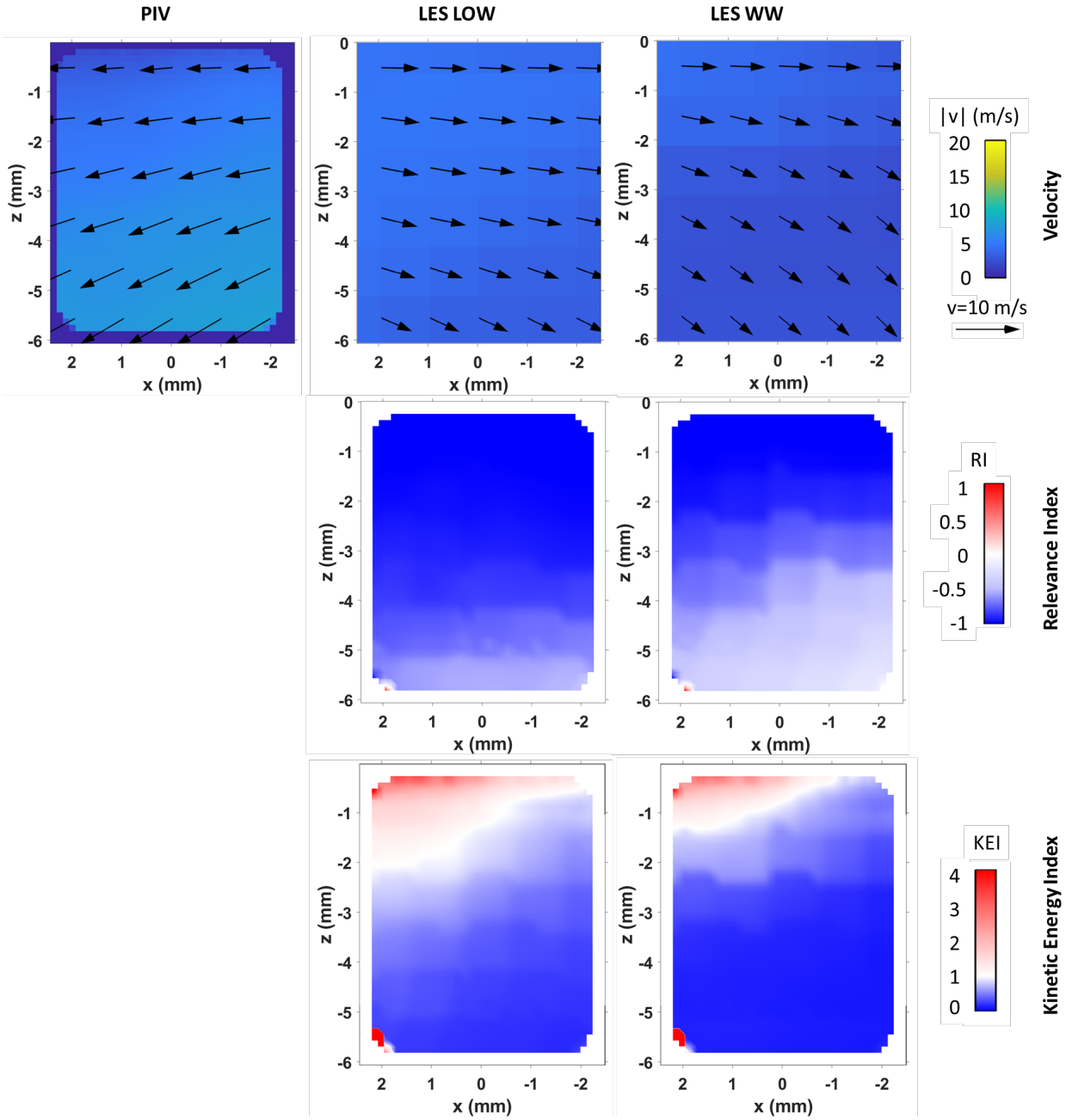

Figure 4.32. Near-wall velocity fields from Cases 2 and 3, compared against dataset S_2016_03_13_04, at -100 CAD aTDCc.

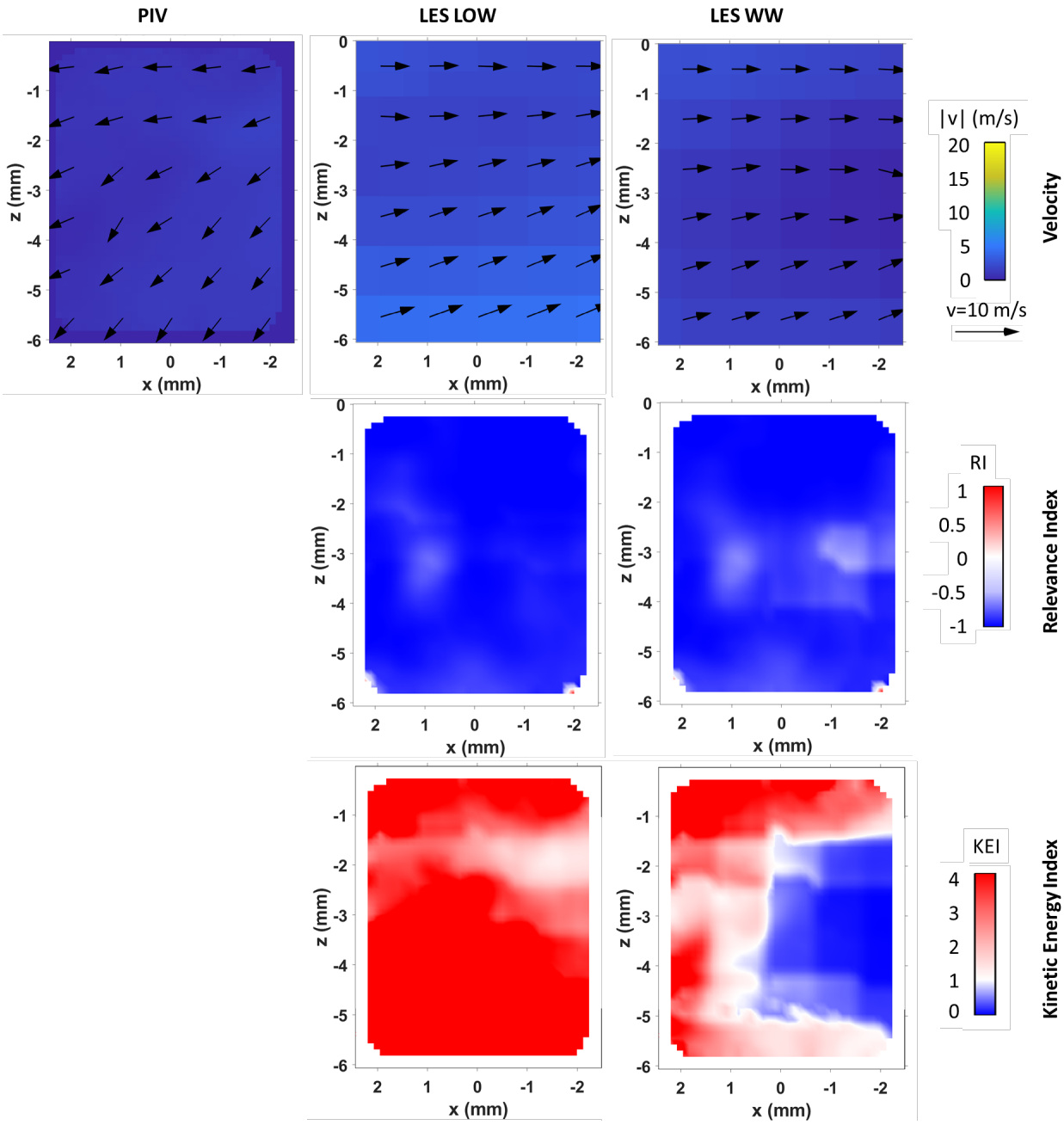

Figure 4.33. Near-wall velocity fields from Cases 2 and 3, compared against dataset S_2016_03_13_04, at -30 CAD aTDCc.

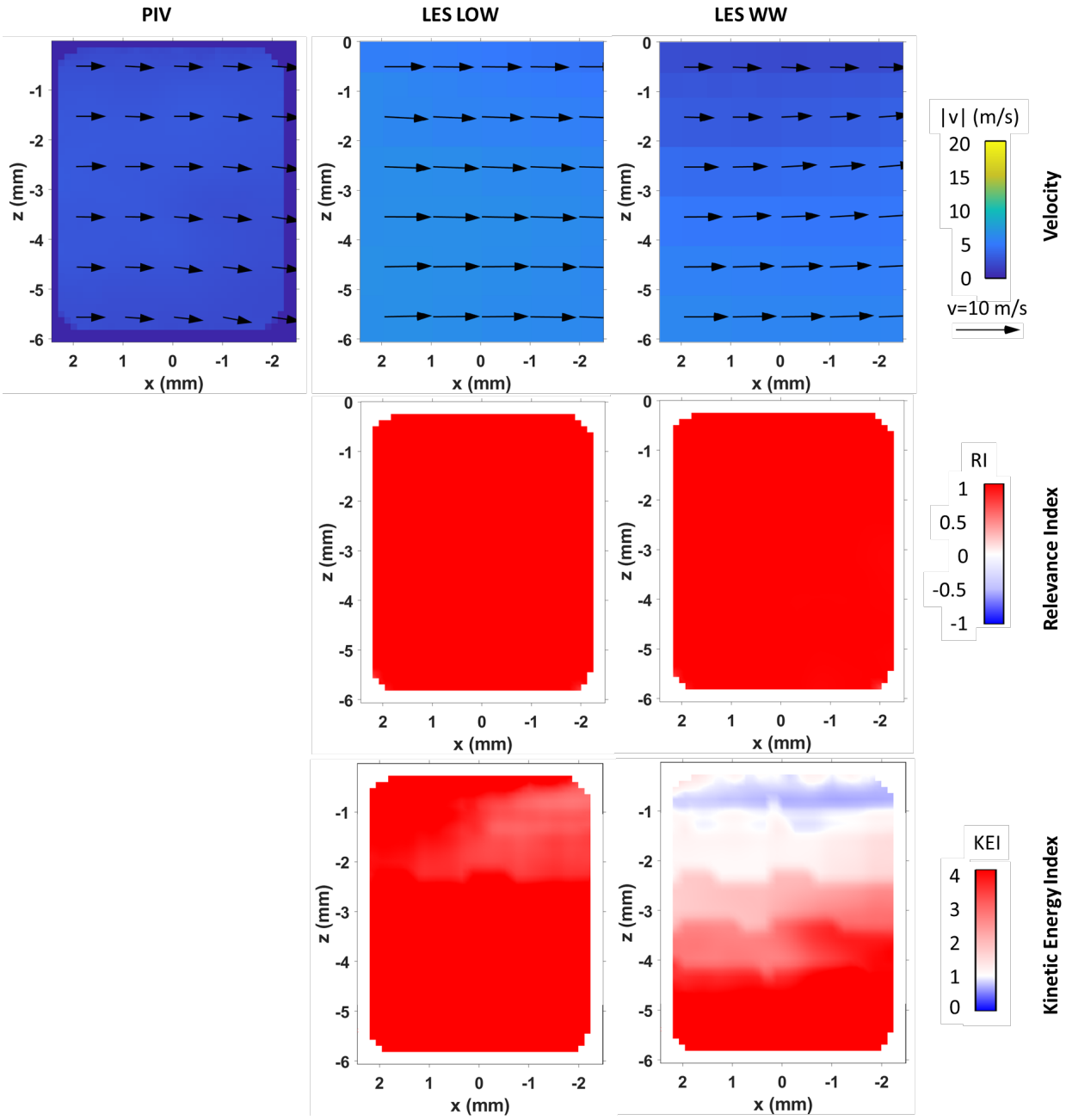

Figure 4.34. Near-wall velocity fields from Cases 2 and 3, compared against dataset S_2016_03_13_04, at 0 CAD aTDCc.

The ensemble average temperature fields are not shown here since both simulations predicted very similar temperature fields in the NWR as shown in Figure 4.18 regardless of the wall model used. Figure 4.35 shows the relative temperature fields of the two simulations with different wall models. The relative temperature fields are very similar between the two simulations. The relative temperature increases with increasing wall distance. Larger differences are seen at TDC away from the wall, in that there are two hot structures in the LES with Werner and Wengle

model, whereas the LES with law of the wall has one larger hot structure. Again, structures at the scale of the PLIF are not found in the simulations due to the in-cylinder mesh of 1 mm.

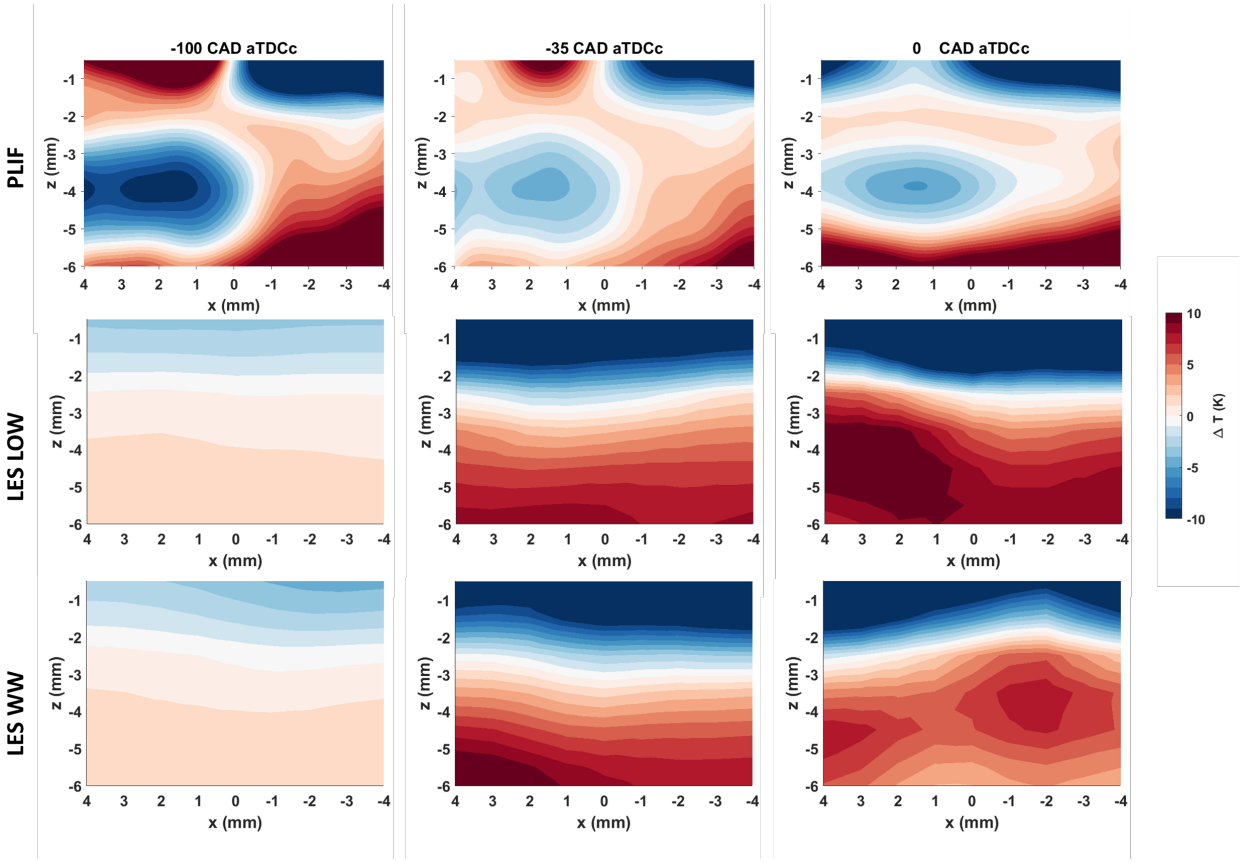

Figure 4.35. Relative near-wall temperature field, obtained from subtracting the ensemble average from the spatial mean, of Cases 2 and 3 compared with temperature PLIF measurements.

Figure 4.36 shows that the temperature profiles of the LES with the Werner and Wengle wall model are similar to those of the LES with law of the wall. The gas temperatures at the first cell are very similar at -100 CAD aTDCc in both models. At -35 CAD aTDCc, the gas temperature of the Werner and Wengle model simulation is slightly lower at the first cell. At TDC, the gas temperature of the Werner and Wengle model simulation is higher than the law of the wall simulation. Far away from the wall, the influence of the wall model diminishes and very similar gas temperatures are obtained. However, both models fail to predict the magnitude of the measured temperature.

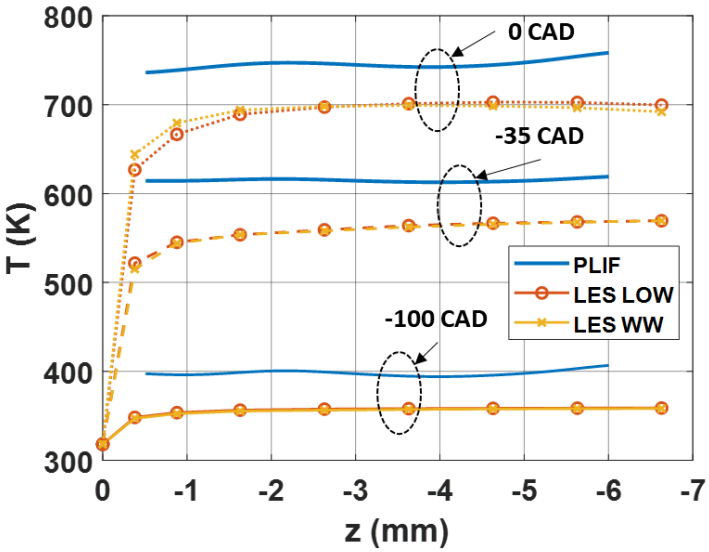

Figure 4.36. Temperature profiles from Cases 2 and 3 compared to temperature PLIF measurements from -100 to 0 CAD aTDCc.

The heat flux profile is shown in Figure 4.37. The law of the wall LES has slightly higher peak heat flux than the Werner and Wengle LES. The LES with Werner and Wengle wall model reached a peak value of 108 kW/m^{2}K, and LES with the law of the wall model reached a peak of 113 kW/m^{2}K. Compared to the unfiltered peak heat flux of 120 kW/m^{2}K, the law of the wall model provided a better heat transfer prediction. This is due to the larger velocity magnitudes obtained in the LES with law of the wall. The Werner and Wengle model has a maximum standard deviation of 24 kW/m^{2}K, while the law of the wall has a smaller standard deviation of 23 kW/m^{2}K. The maximum standard deviation of the filtered heat flux is 26 kW/m^{2}K. It is likely that because the Werner and Wengle wall model was developed with an LES subgrid-scale model for flows that demonstrate separation and reattachment characteristics, a larger CCV is obtained in the near-wall velocity field with this wall model configuration, leading to larger CCV in the heat flux.

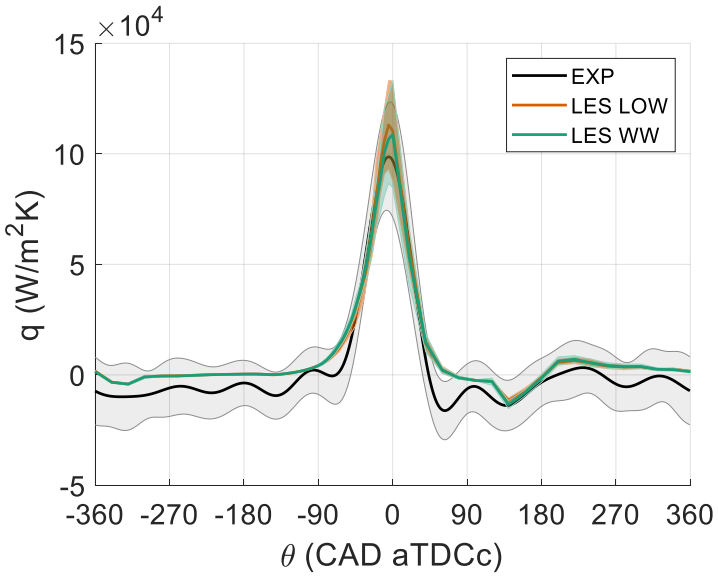

Figure 4.37. Heat flux profiles from Cases 2 and 3, and dataset S_2016_03_13_04.

4.6 Effects of the Uniform Thermal Boundary Condition

Since the Werner and Wengle wall model was developed to be used with LES, the rest of the simulations will use this wall model whenever LES was performed. The previous section showed that the Werner and Wengle wall model underpredicts the heat flux slightly. The heat transfer predictions can be affected by inaccurate thermal boundary conditions. For the next step, the surface temperature was increased to 353.16 K from 318.16 K, which is closer to the air heater and coolant temperature. All other models and model parameters were kept the same. The comparison here is between Cases 3 and 4, which are the LES with the Werner and Wengle wall model. The in-cylinder pressure for the two simulations are shown in Figure 4.38. The simulation with the higher surface temperature leads to lower in-cylinder pressures. This could be due to increased heat transfer from the gases to the walls.

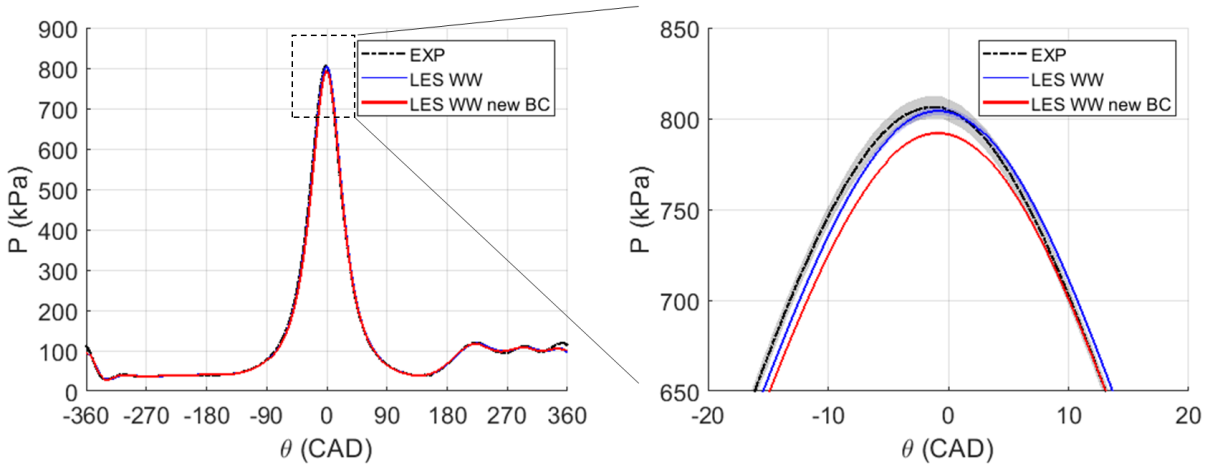

Figure 4.38. The in-cylinder pressure of Cases 3 and 4 compare well to the experimental data.

Figure 4.39 shows the near-wall velocity fields at -100 CAD aTDCc. Increasing the thermal boundary condition does not influence the velocity field direction or kinetic energy content much. Figure 4.40 shows that at -30 CAD aTDCc, similar results in the velocity field direction were obtained, but the velocity magnitude of the LES with the higher surface temperature is larger than the LES with the lower surface temperature. At TDC, Figure 4.41 shows a similar behavior as -30 CAD aTDCc.

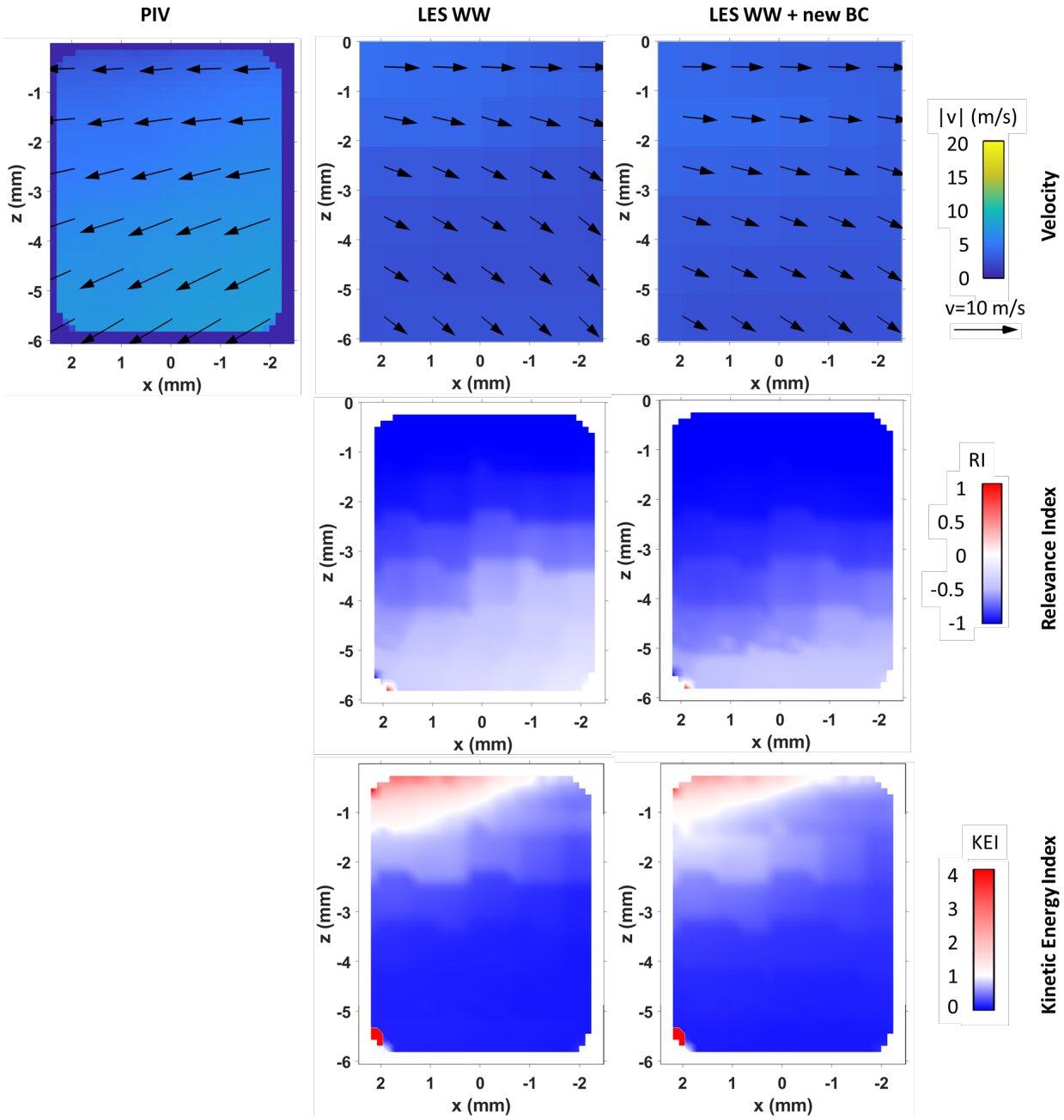

Figure 4.39. Near-wall velocity fields from Cases 3 and 4, compared against dataset S_2016_03_13_04, at -100 CAD aTDCc.

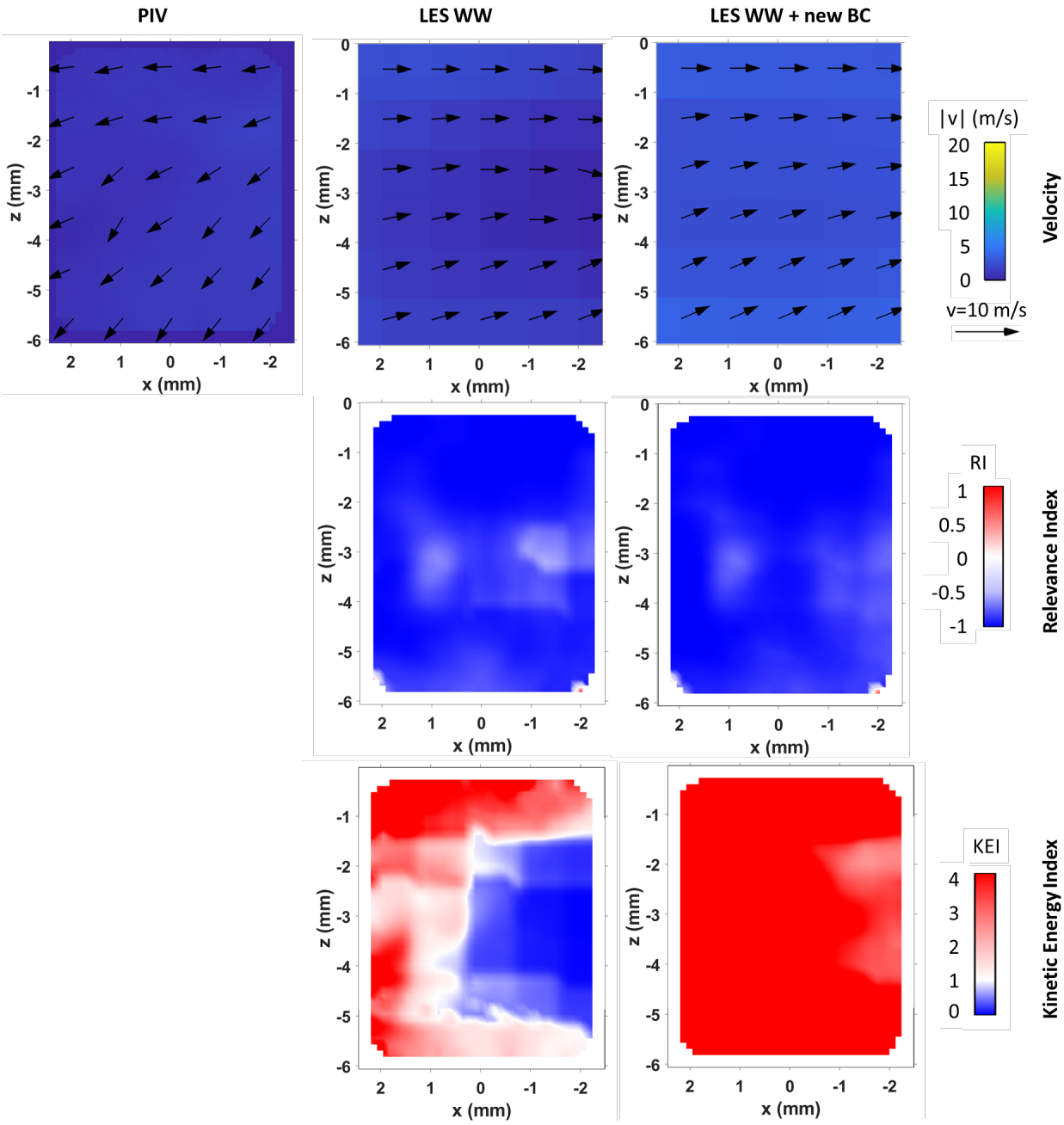

Figure 4.40. Near-wall velocity fields from Cases 3 and 4, compared against dataset S_2016_03_13_04, at -30 CAD aTDCc.

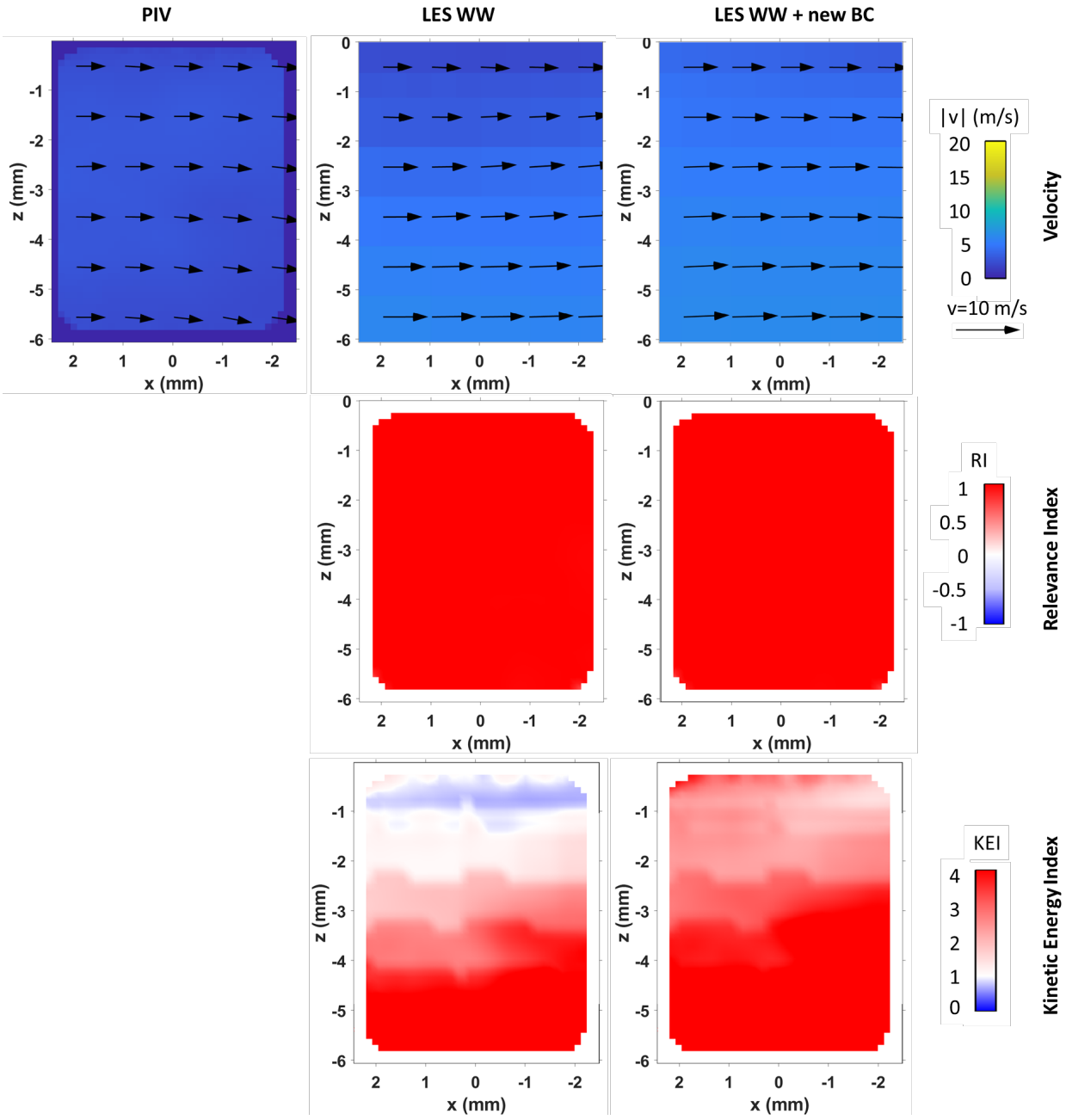

Figure 4.41. Near-wall velocity fields from Cases 3 and 4, compared against dataset S_2016_03_13_04, at 0 CAD aTDCc.

Figure 4.42 shows that the influence of the surface temperature boundary condition is more pronounced in the ensemble average temperature field, which could be due to the larger convective heat transfer coefficient due to increased velocity magnitudes in the near-wall velocity field. The gas temperature in the NWR increased with the increased surface temperature. While the simulation is still not able to capture the smaller thermal structures seen in the PLIF, the range of the simulated temperatures are now much closer to the measured temperatures.

Figure 4.43 shows the relative temperatures. At -100 CAD aTDCc, both simulations predict very similar relative temperature fields. As the piston moves towards TDC, however, the simulation with the higher surface temperature boundary condition has hotter structures far away from the wall. The near-wall cold structures, however, are unaffected by the increased thermal boundary condition.

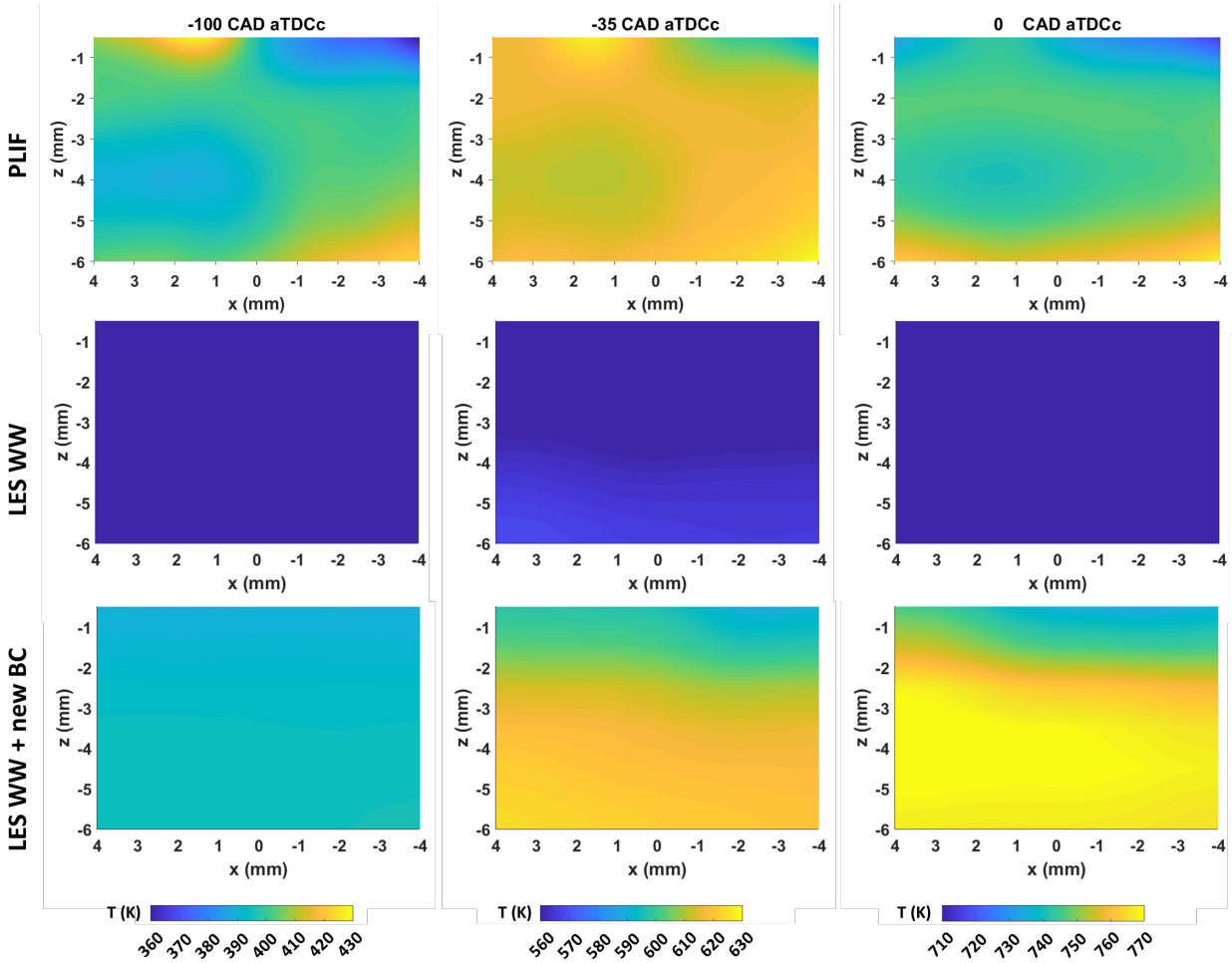

Figure 4.42. Near-wall temperature field validation of Cases 3 and 4 with temperature PLIF measurements.

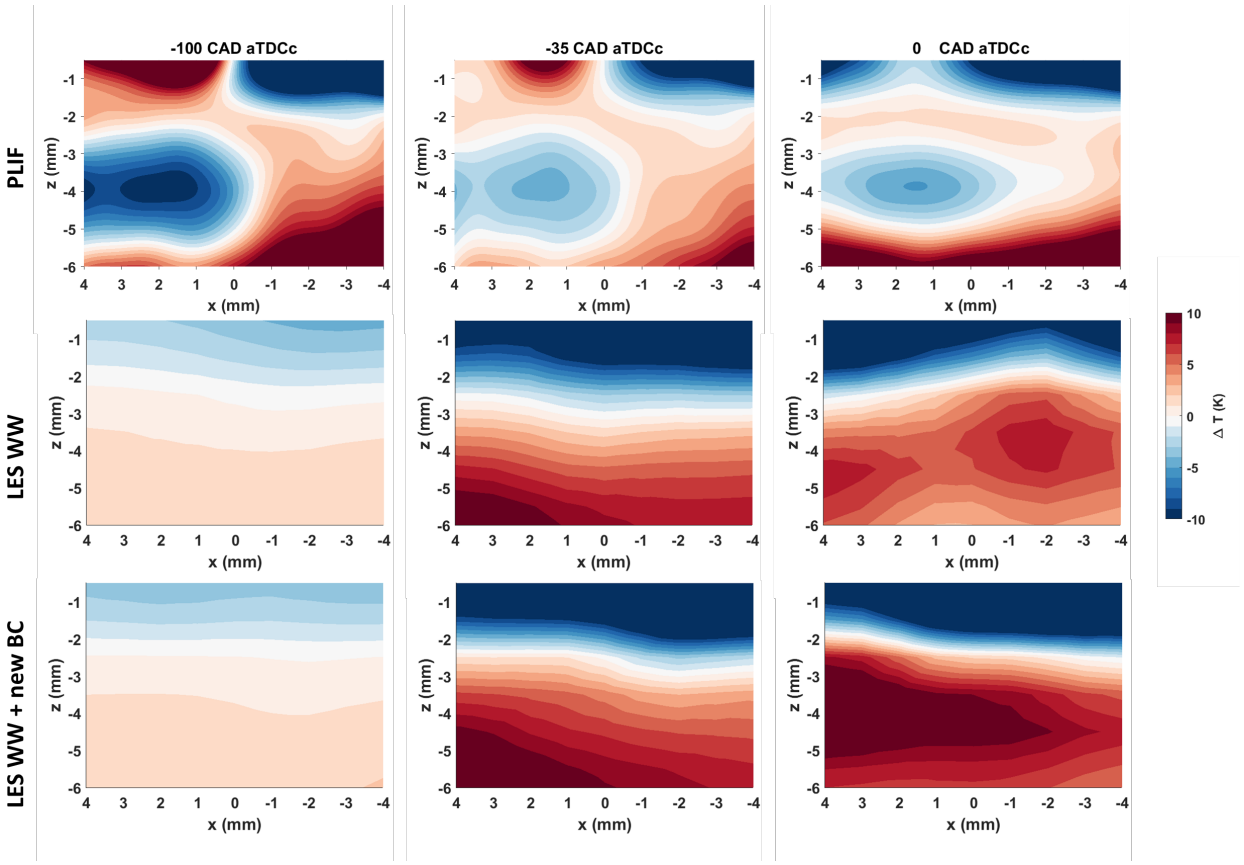

Figure 4.43. Relative near-wall temperature field, obtained from subtracting the ensemble average from the spatial mean, of Cases 3 and 4 compared with temperature PLIF measurements.

The temperature profiles in Figure 4.44 show that increasing the surface temperature leads to higher near-wall gas temperatures that are closer to the measured temperatures. Adding the surface temperature difference of 45 K to the simulation with the thermal boundary condition of 318.16 K leads to a collapse of the temperature profile, especially near the wall, as shown in Figure 4.45.

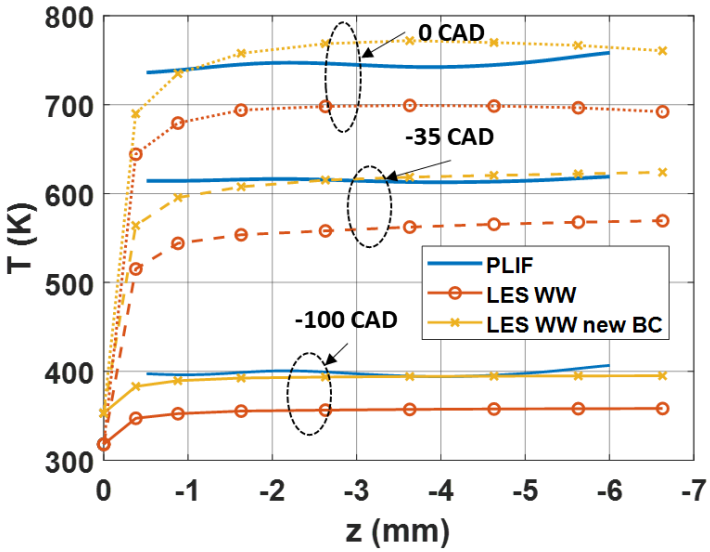

Figure 4.44. Temperature profiles from Cases 3 and 4 compared to temperature PLIF measurements from -100 to 0 CAD aTDCc.

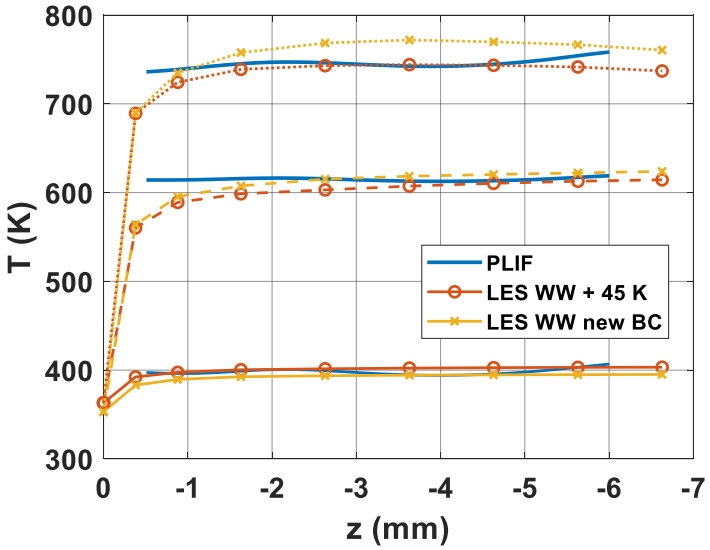

Figure 4.45. Temperature profiles from Cases 3 and 4 compared to temperature PLIF measurements from -100 to 0 CAD aTDCc, with 45 K added to Case 3.

The surface heat flux is shown in Figure 4.46. The simulation with the higher thermal boundary condition has a peak value of 113 kW/m^{2}K, while the simulation with the original thermal boundary condition has a peak value of 108 kW/m^{2}K. Compared to the unfiltered peak heat flux of 120 kW/m^{2}K, the higher surface temperature simulation leads to improved heat flux predictions. The lower surface temperature simulation has a maximum standard deviation of 24 kW/m^{2}K, while the higher surface temperature has a smaller standard deviation of 18 kW/m^{2}K.

The maximum standard deviation of the filtered heat flux is 26 kW/m^{2}K. Therefore, the simulation with the higher surface temperature has lower CCV than measured.

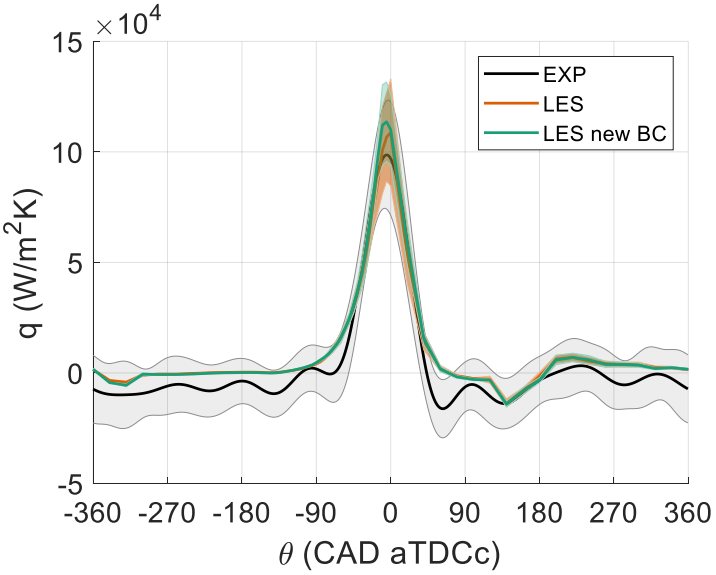

Figure 4.46. Heat flux profiles from Cases 3 and 4, and dataset S_2016_03_13_04.

4.7 Summary

In this chapter, the motored condition is examined for simulations using the uniform temperature models. RANS and LES models were compared to show the effect of the turbulence and subgrid-scale model on bulk flow, near-wall flow and temperature, and surface heat flux predictions. The intake jet in the bulk flow is shown to influence the location of large-scale vortex centers, and inaccurate predictions of the vortex centers lead to low RI and high KEI values. This indicates that improvements are needed in the simulation of the intake jet. The RANS model leads to overpredictions in the near-wall velocity which results in higher heat flux than LES. The flow was better resolved by decreasing the near-wall mesh in LES from 1 mm to 0.5 mm, resulting in larger near-wall velocities and higher heat flux. Changing the wall model in LES from law of the wall to Werner and Wengle wall model leads to smaller velocity magnitudes since the wall shear stress calculations are different. This leads to smaller heat flux, but since the Werner and Wengle wall model was specifically developed for LES, a larger CCV in the near-wall velocity is obtained, leading to larger CCV in the heat flux. Finally, the surface temperature was increased by 45 K to better match the coolant and intake temperatures. Increasing this surface temperature did not change the near-wall velocity field, but the near-wall temperature field predictions were improved.

Chapter 5 Motored Conjugate Heat Transfer Results

In this section, conjugate heat transfer is applied to the motored operating condition. Two simulations will be compared: Cases 4 and 6. Case 4 is the LES that uses a uniform temperature boundary condition of 353.16 K. Case 6 is the LES that uses CHT. Both simulations use the Werner and Wengle wall model, Han and Reitz model, and the refined near-wall mesh. Results show the differences in the predicted flow and temperature fields between the uniform surface temperature and CHT simulations, revealing the impact of the surface temperature on engine behavior.

11 cycles were simulated for Case 6, and the first cycle discarded to remove the initial condition bias. These cycles were compared to cycles 2-11 from Case 4. The simulation results were compared to PIV datasets S_2013_10_24_01, S_2016_03_13_04, and S_2016_03_13_08, and the motored PLIF temperature measurement. The analysis in this chapter is a collaborative effort with Mohammad Alzuabi [39] and has been published recently in Wu et al. [38, 121].

5.1 Convergence Criteria

The convergence study of the motored CHT case (Case 6) was originally published [121]. Similar to the convergence criteria for Case 4 in the previous chapter, the ensemble average and standard deviation of the velocity field were obtained for an increasing number of cycles (i.e. cycles 2-3, cycles 2-4, etc.), and then spatially averaged over the entire domain. The magnitude of the spatially averaged velocity vector was obtained. The results in Figure 5.1 show that satisfactory statistical convergence of the ensemble-averaged velocity is acquired after including 5 cycles (cycles 2-6) in the ensemble averaging process. At least 7 cycles (cycles 2-8) are needed for the standard deviation of the velocity to reach statistical convergence.

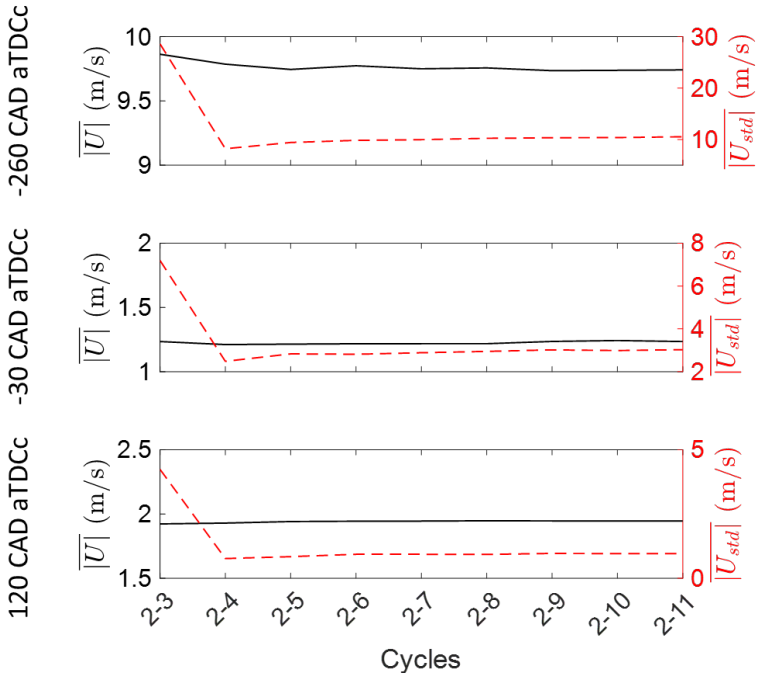

Figure 5.1. Convergence of the ensemble average and standard deviation of the velocity magnitude for Case 6, at three crank angle degree locations. The x-axis shows the cycles that are included in the statistical analysis. Figure extracted from [121].

Figure 5.2 shows the ensemble averaged in-cylinder gas temperature, spatially averaged over the entire cylinder domain, for an increasing number of cycles. The ensemble-averaged temperature reached statistical convergence after averaging cycles 2-3, while the standard deviation of the temperature becomes steady after cycles 2-8. It is also evident that the ensemble-averaged gas temperature of the CHT model is higher than the uniform temperature model in Figure 4.2.

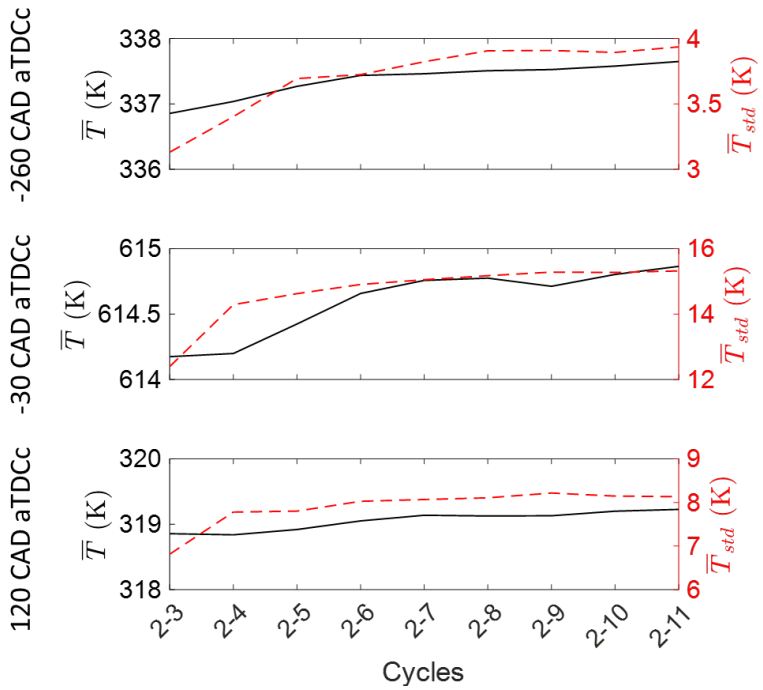

Figure 5.2. Convergence of the ensemble average and standard deviation of the in-cylinder gas temperature for Case 6, at three crank angle degree location. The x-axis shows the cycles that are included in the statistical analysis. Figure extracted from [121].

The quality index was also calculated for the CHT model over the engine cycle with increasing number of cycles in the ensemble averaging process and spatially averaged over the entire cylinder domain. The spatially averaged quality index $\overline{M}$ is shown in Figure 5.3. As the number of cycles in the ensemble averaging process increases, $\overline{M}$ decreases, i.e. the LES quality gets better. The exception is cycle 2-3 in the CHT model which has a low $\overline{M}$ value. This is most likely due to the initialization of the first LES CHT cycle, which uses the last iteration of Case 5, the RANS CHT model. This initialization could still have a large influence on the second LES CHT cycle. Once more cycles were added to the averaging process, $\overline{M}$ follows the same trend as the uniform temperature model in Figure 4.3. Statistical convergence occurs after including 6 cycles (cycles 2-7).

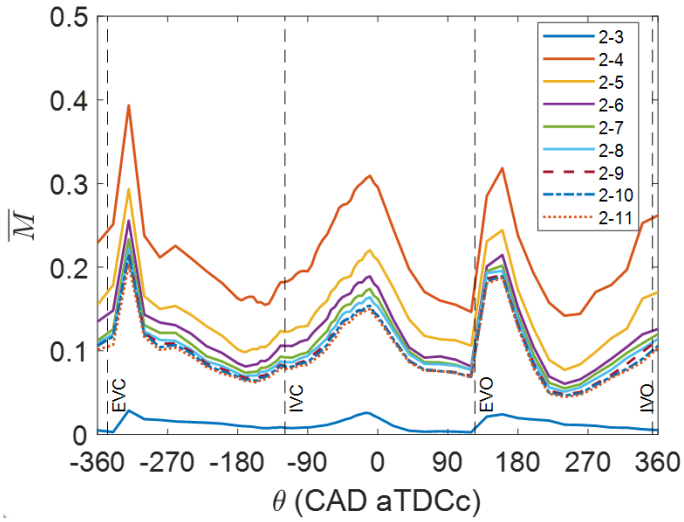

Figure 5.3. LES quality index $\overline{M}$ of Case 6, for increasing number of cycles in the ensemble averaging approach, over the entire engine cycle. Figure extracted from [121].

5.2 Bulk Velocity and Temperature Fields

After the convergence criteria is met, the first step to validate the simulations is to check the in-cylinder pressure. The shaded area is the standard deviation of the in-cylinder pressure and represents the experimental envelope. The ensemble averaged and standard deviation in-cylinder pressures are shown in Figure 5.4 for Cases 4 and 6. The histogram of peak pressures in Figure 5.5 clearly shows that the peak pressures are underestimated by both simulations but are within 3% of the experimental peak pressure. The CHT simulation obtained a slightly lower in-cylinder pressure than the uniform temperature simulation. The CCV of both simulations is small compared to the experimental CCV. This is mainly due to the limited number of simulated cycles in comparison to the 141 of the PIV cycles. It seems that even though statistical convergence is met with less than 10 cycles, the number of simulated cycles is too small to capture the measured CCV, and more LES cycles are needed to adequately capture the level of measured CCV. This was also seen in the study of Truffin et al. [42], where 10 cycles were simulated. They were able to estimate the ensemble-averaged pressure accurately but underestimated the level of CCV. Examples of multi-cycle LES of 60 or more cycles can be found in references [50, 56].

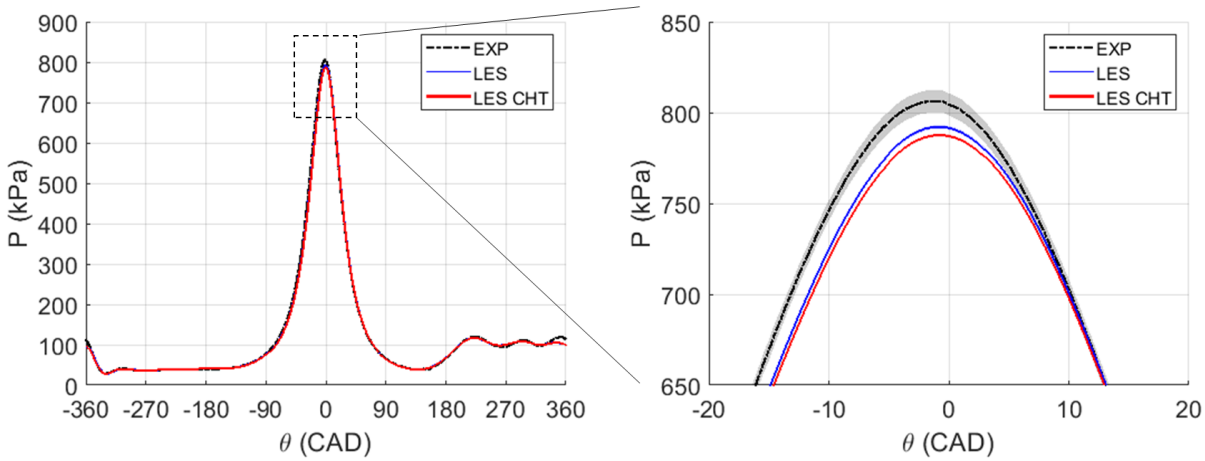

Figure 5.4. The dynamics of the in-cylinder pressure of Cases 4 and 6 compare well to the experimental data from S_2016_03_13_04 within 3%.

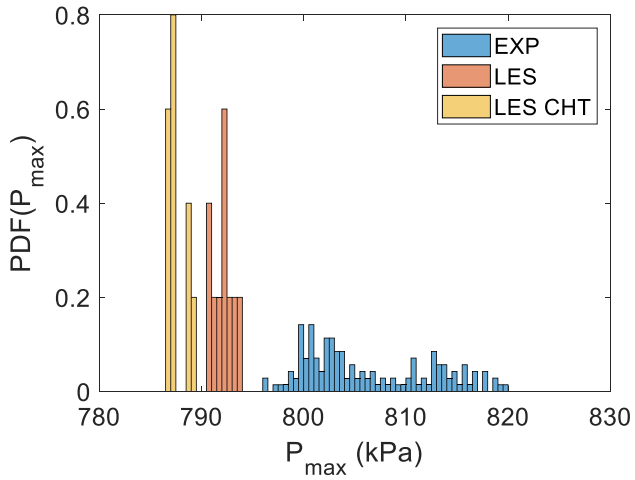

Figure 5.5. Histogram of motored peak in-cylinder pressures from experimental data (S_2016_03_13_04), uniform temperature LES, and LES CHT cases.

The ensemble-averaged bulk flow fields will be shown next for -260 CAD, -100 CAD, -30 CAD, and 120 CAD. -260 CAD was chosen as this was during the intake stroke when large-scale vortices are formed as the intake jet enters the combustion chamber. -100 CAD represents the early compression stroke after IVC, while -30 CAD represents the late compression stroke. 120 CAD is during the exhaust stroke to highlight the temperature field differences due to surface temperatures when both valves are closed and the flow fields are similar.

The ensemble-averaged bulk flow fields are shown in Figure 5.6 from the bulk PIV measurement and the simulations at -260 CAD aTDCc during the intake stroke. At this crank angle degree location, the spatially averaged LES quality index $\overline{M}$ values are equal to 0.10 for both models. This figure shows that the bulk flow is well captured by both models, but the modeled

intake jet needs improvement. The direction of the intake jet is well captured, and the entrainment of the flow on both sides of the intake jet is also seen in both simulations. However, differences in the bulk flow field between the simulations are evident. The flow entrainment on the left of the intake jet (region A) is much stronger in the CHT model compared to the uniform temperature model and compares quantitatively better with the magnitude of the flow in the measurement. The location of the vortex center on the right of the intake jet (region C) is better captured by the CHT model as well. These two regions coincide with vortices, which are created by the interaction of the intake jet with the engine surfaces as it enters the combustion chamber. The kinetic energy in the intake jet is overpredicted by both models. This leads to larger kinetic energy in the lower regions of the combustion chamber (regions B and D). But the kinetic energy predicted by the CHT model is closer to the measurement as shown by the smaller KEI values when compared to the uniform temperature model. The surface temperatures predicted by the CHT model are likely closer to the experimental surface temperature, and this leads to better predictions by the CHT model.

In Figure 5.6, regions A and C are marked by low RI values in both models. These regions contain the vortical structures near the intake jet. The low RI values indicate that the flow direction differs from measurement due to differences in the vortex centers. It can be seen that in the uniform temperature model, both regions encompass a larger area of low RI values compared to the CHT model. The flow direction in region D is better captured by the uniform temperature model. This is due to the flow entrainment on the left side of the intake jet, which is much weaker in the uniform temperature model. A larger part of the flow is entrained in the CHT model, and this causes flow in region D to move upwards. The RI values in region B is close to 1, indicating that the velocity direction is well captured by both models. The KEI values in the intake jet region is much larger in the uniform temperature model than the CHT model. This has implications on not only the formation of vortices in the combustion chamber, but also on heat transfer, as larger kinetic energy means higher velocities and therefore higher convective heat transfer. Therefore, improvements are needed in the simulation of the intake jet. Since the CHT likely predicts more accurate valve surface temperatures, this leads to better predictions in the intake jet region as evidenced by the lower KEI values.

Figure 5.7 shows that at -100 CAD aTDCc, the simulated velocity fields of both models compare well with the measurement, except in region A. The $\overline{M}$ value is 0.08 in both models. The

CHT model predicts a smoother velocity field near the cylinder head when compared to the uniform temperature model. The flow direction in Region A is then influenced by the flow direction near the cylinder head. In the PIV measurement, region A contains a vortical structure. This vortical structure is captured by the simulations, but the location of the vortex centers are below Region A in both simulations. This mismatch in vortex center location leads to low RI values near Region A. Vortex centers also have low kinetic energy content since the velocity is low. Therefore, the simulations overpredict the kinetic energy content as revealed by the high KEI value in Region A.

The ensemble averaged bulk flow fields at -30 CAD aTDCc are shown in Figure 5.8. The RI fields show that the velocity fields are very similar, except for the regions close to the spark plug (regions A and B). The kinetic energy is also overestimated in these two regions, with larger regions of high kinetic energy values in the uniform temperature model. This affects combustion simulations since the kinetic energy and the flow velocity are variables used in combustion modeling. At this crank angle degree location, the $\overline{M}$ values are equal to 0.14 for the CHT model and 0.17 for the uniform temperature model. The grid resolution may not be fine enough in regions A and B. Increasing the grid resolution in these regions will allow smaller flow structures to be resolved, leading to a possible reduction in the discrepancy of the flow direction and kinetic energy.

The ensemble averaged bulk flow fields at 120 CAD aTDCc is shown in Figure 5.9. At this CAD, the $\overline{M}$ values are equal to 0.07 for the CHT model and 0.09 for the uniform temperature model. This velocity field corresponds to right before EVO when the LES quality deteriorates quickly. The flow direction is well captured by both models with a better match between the CHT and the bulk flow measurements. Kinetic energy is better estimated by the CHT model since a large portion of the plane has KEI values close to 1.

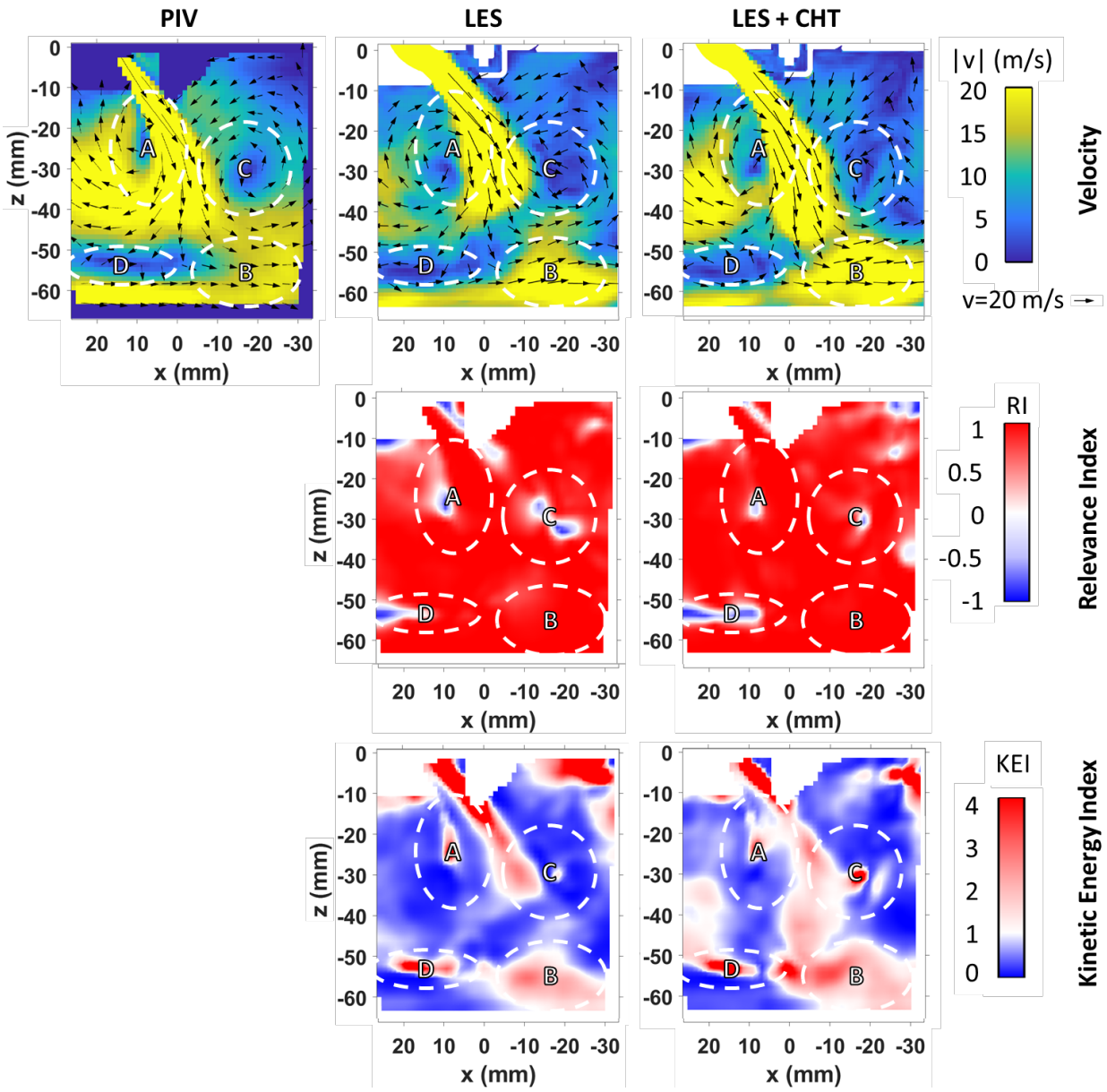

Figure 5.6. Average bulk flow field y=0 mm plane, at -260 CAD aTDCc compared to dataset S_2013_10_24_01. Figure updated from [121].

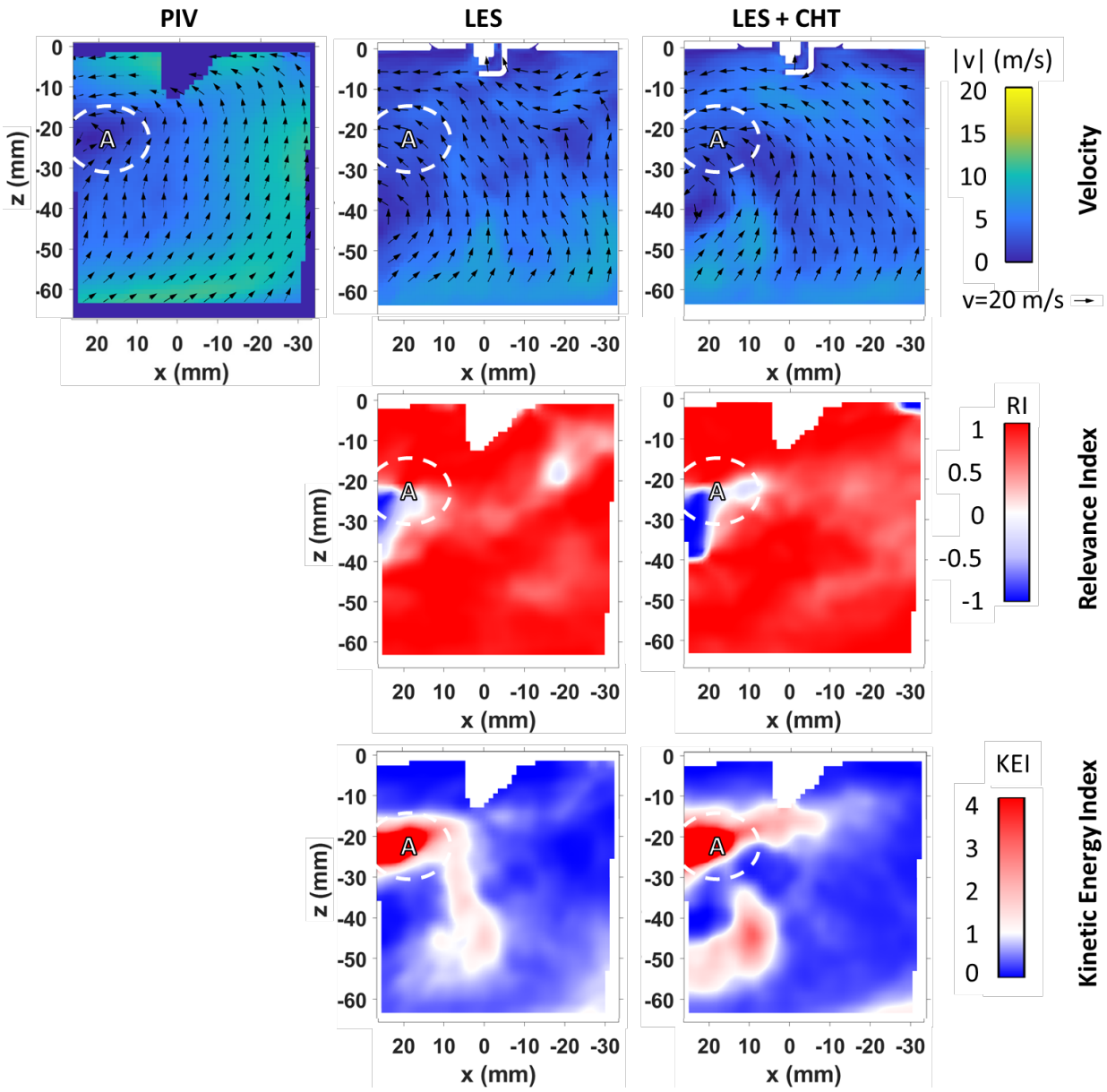

Figure 5.7. Average bulk flow field y=0 mm plane, at -100 CAD aTDCc compared to dataset S_2013_10_24_01.

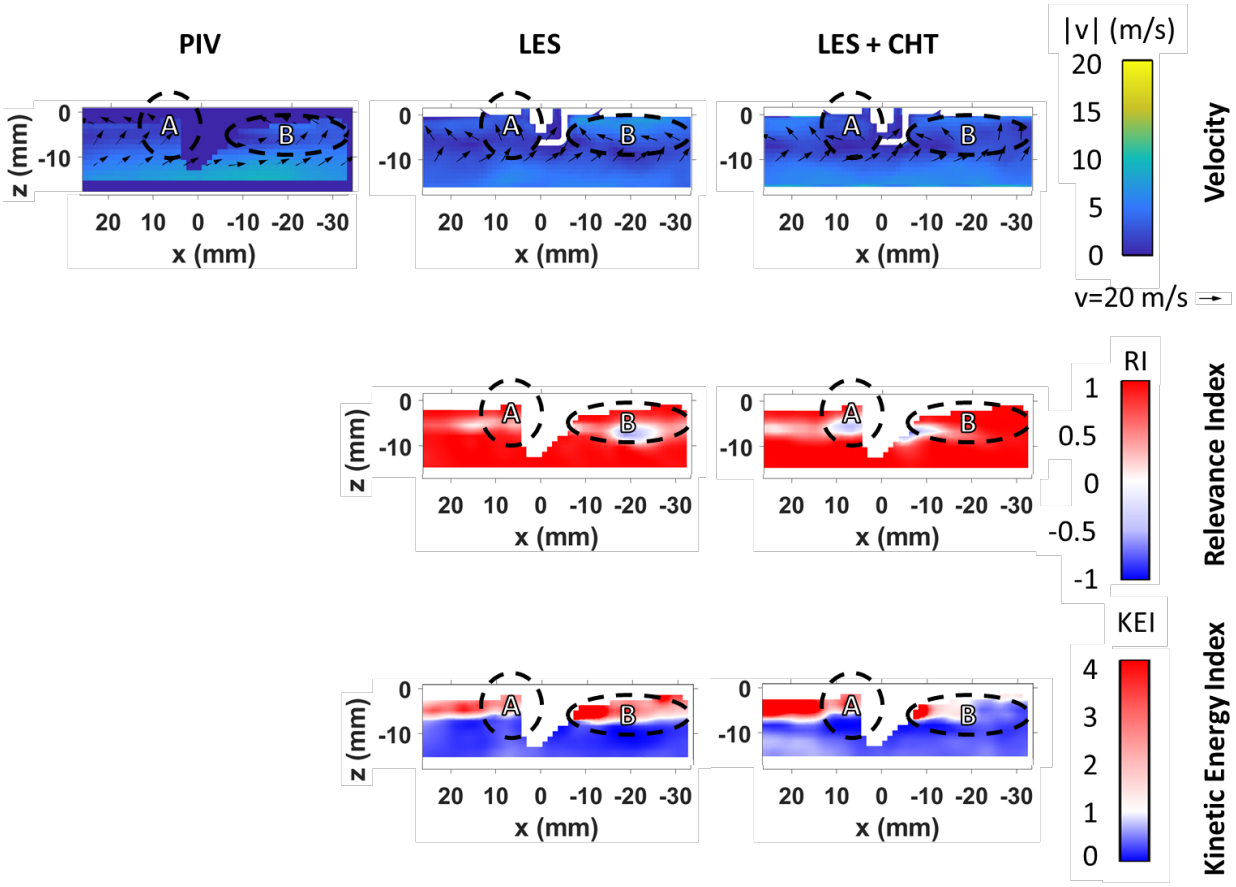

Figure 5.8. Average bulk flow field y=0 mm plane, at -30 CAD aTDCc compared to dataset S_2013_10_24_01. Figure updated from [121].

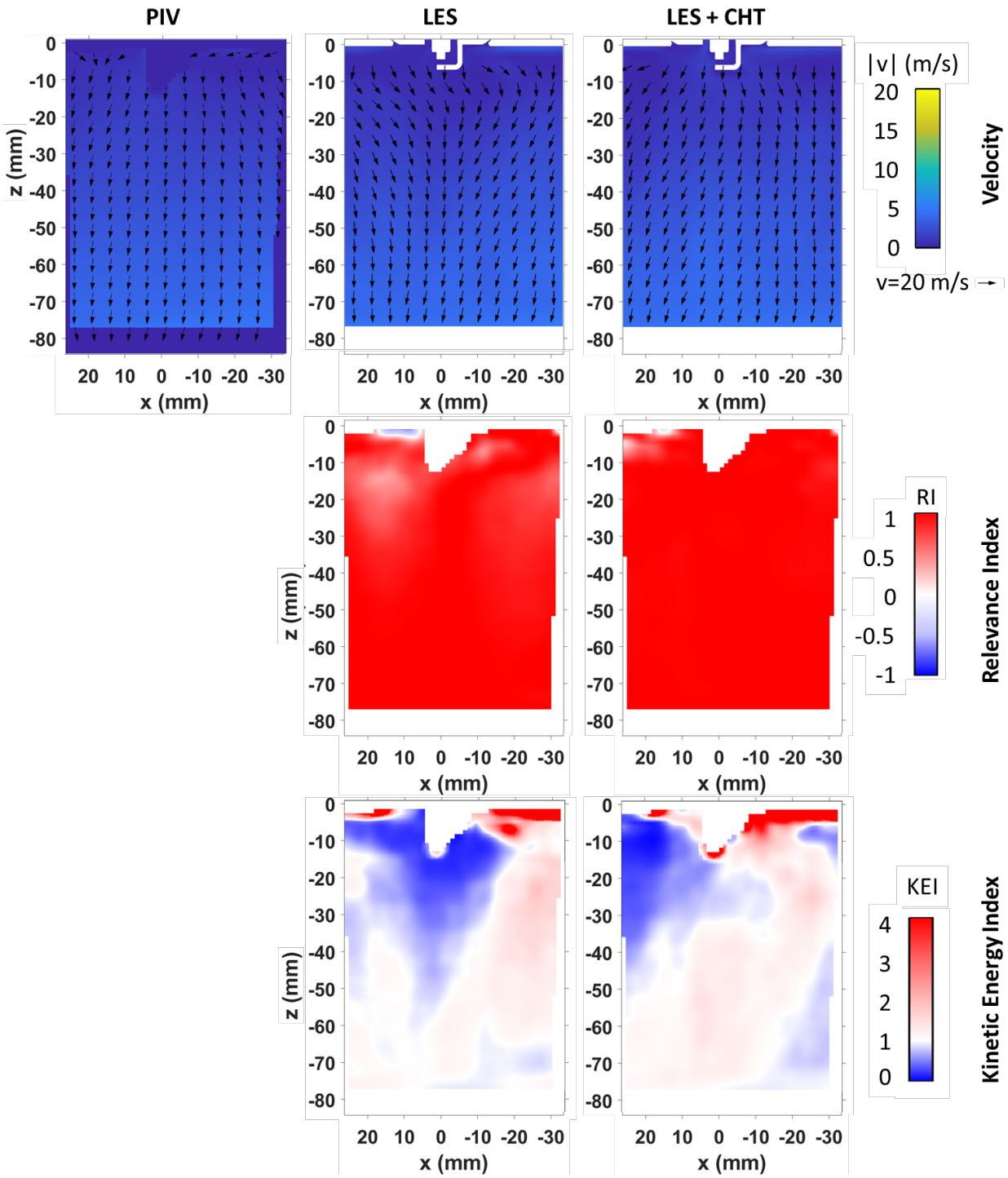

Figure 5.9. Average bulk flow field y=0 mm plane, at 120 CAD aTDCc compared to dataset S_2013_10_24_01. Figure updated from [121].

Figure 5.10 shows the temperature fields of the uniform temperature and CHT models. Experimentally determined bulk temperature fields are not yet available. Differences in the thermal boundary condition lead to differences in the gas temperature predictions. At -260 CAD aTDCc,

near the exhaust valve (region A), a hotter region exists in the CHT case compared to the uniform temperature model. This is due to the higher surface temperature of the exhaust valve predicted by the CHT model. Region B in the intake jet of the CHT case is also at a higher temperature compared to the uniform temperature model. Near the piston surface (region C), differences in the piston surface temperature also lead to different thermal behavior of the nearby gases in both models. In Section 5.5, Figure 5.23 shows the surface temperature of the spark plug at -20 CAD aTDCc for each cycle. The CHT model predicts a higher surface temperature than the prescribed temperature of the uniform temperature model at the ground strap. This leads to higher gas temperatures close to the spark plug, which will lead to differences in the flame kernel development in the CHT model due to changes in heat transfer. The differences in bulk gas temperature predictions lead to different gas density, hence the velocity fields are also affected by the thermal boundary condition, as shown in Figure 5.6. The temperature fields at -100 and -30 CAD aTDCc are comparable to each other, although the CHT model predicts slightly higher temperatures compared to the uniform temperature model. During the expansion stroke, at 120 CAD aTDCc, the effects of the surface temperature leads to bulk temperature field differences. For example, in regions D, a cooler region exists under the intake valve in the CHT model, and in region E the gas temperature is cooler than the uniform temperature model. The gas temperature around the piston surface is also higher in the CHT model than in the uniform temperature model.

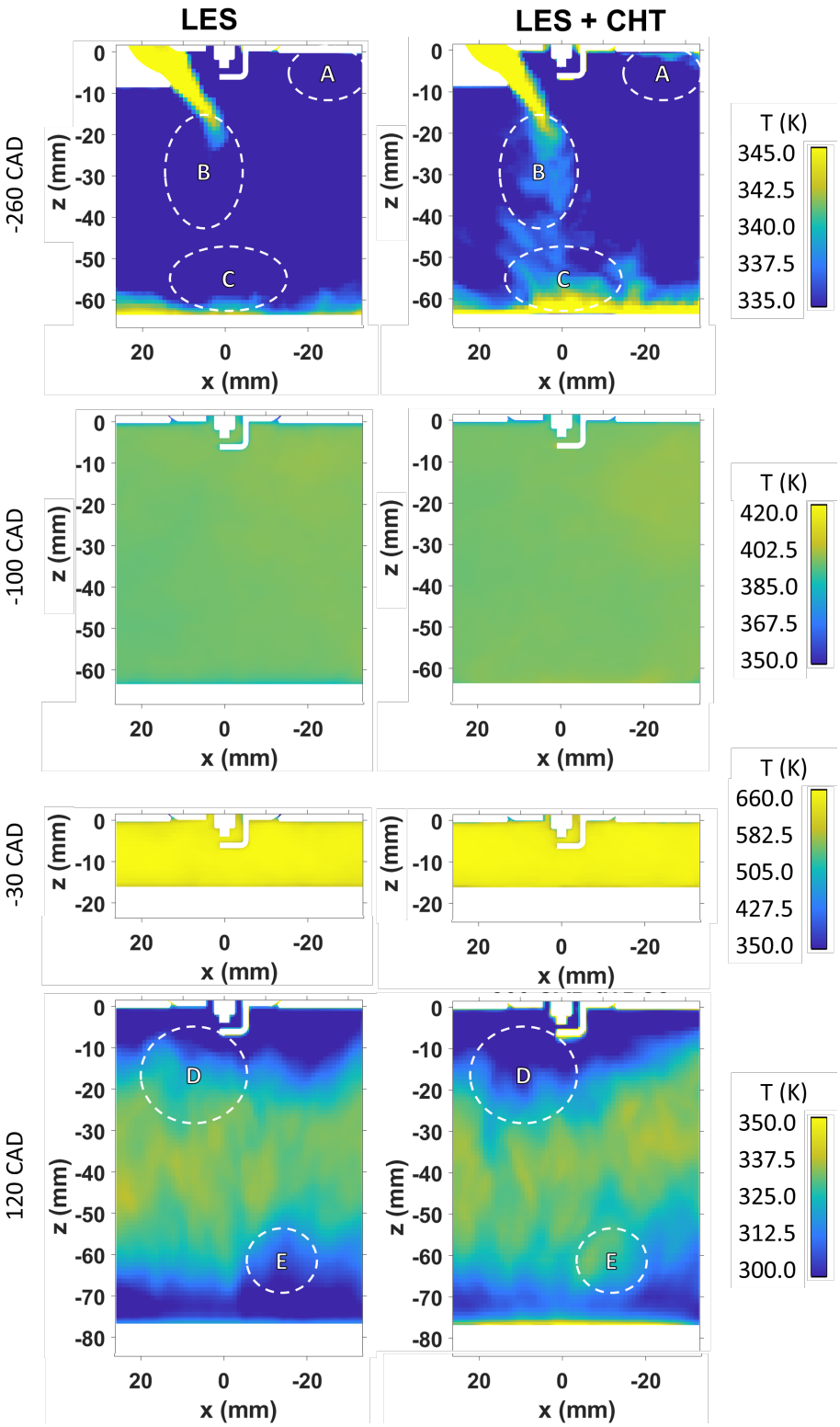

Figure 5.10. Average temperature fields at y=0 mm plane from -260 to 120 CAD aTDCc. Figure updated from [121].

5.3 Bulk Gas Temperature Region

The cooling effects of the near-wall gases on bulk temperature were demonstrated by [128]. The effects of the near-wall gas temperature on the bulk gas temperature were analyzed to determine the wall-distance at which the near-wall gases have minimal effects on the bulk gas temperature. This analysis also guided the choice of calibration location for the PLIF work, since PLIF signals were calibrated with in-cylinder temperatures from a GT-Power simulation [39]. The analysis was performed by taking a volume average of a cylindrical section in the combustion chamber that is at a distance δ away from the engine surfaces, using the data from LES CHT, as shown in Figure 5.11. The ensemble average temperature of the inner cylindrical volume is then calculated for δ from 0 mm to 4.5 mm. Results are shown in Figure 5.12. When the entire engine combustion chamber is included with $\delta = 0$ mm, the bulk gas temperature is higher since it includes the thermal boundary layers in the NWR. When $\delta = 1$ mm, the bulk gas temperature decreases, especially in the compression stroke. With $\delta > 1$ mm, the bulk gas temperature increases again.

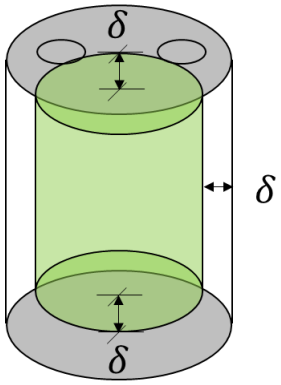

Figure 5.11. Inner cylindrical volume to obtain bulk gas temperature negating effects of the boundary layer. Figure extracted from [38].

The percent change of the bulk gas temperature as a function of CAD and δ is shown in Figure 5.13. As δ increases from 0 to 3 mm, the percent change in bulk gas temperature is significant. From 3 mm to 4 mm, the change in bulk gas temperature is essentially negligible. From 4 to 4.5 mm, there is a significant change in the bulk gas temperature, mainly due to reduced data points, especially at TDC as the clearance height is just 9.5 mm, which affected the bulk gas temperature calculation from the simulation. Therefore, a wall-distance of 4 mm was determined to be the extent of the influence from near-wall gases on the bulk gas temperature, while still containing enough data points for volumetric averaging. This analysis also provides an avenue of

separating the near-wall region ($z > -4$ mm) from the bulk gas region ($z \leq -4$ mm), which justifies the location of the PLIF calibration region.

The inner core temperature was also found to be affected by the relatively cooler boundary layer in Ref. [128]. The boundary layer thickness at the cylinder wall changes throughout the engine cycle and the thickness is different along the piston, cylinder liner, and the cylinder head [18, 31, 144]. Also, when the piston moves along the cylinder liner, the boundary layer gas is scraped off, causing vortices at the piston-cylinder liner corners [18, 31, 144]. These structures induce mixing of cooler and hotter gases. The effects of the thermal boundary layer and piston-induced vortices are removed when the inner-cylinder volume is decreased by increasing the wall distance δ.

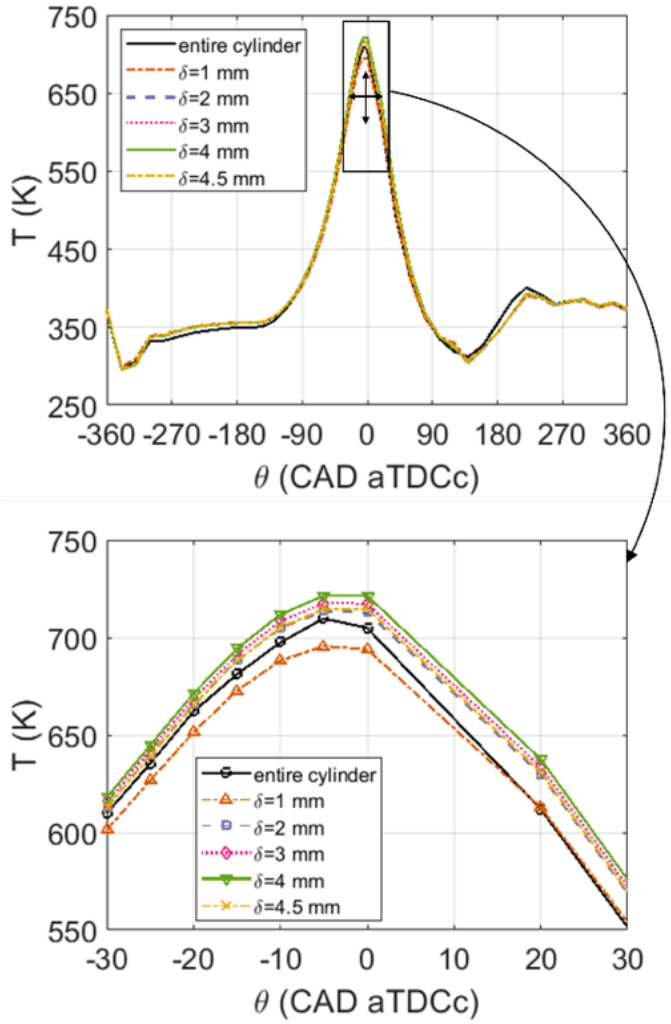

Figure 5.12. Ensemble-averaged bulk gas temperature of the inner cylinder region. Figure extracted from [38].

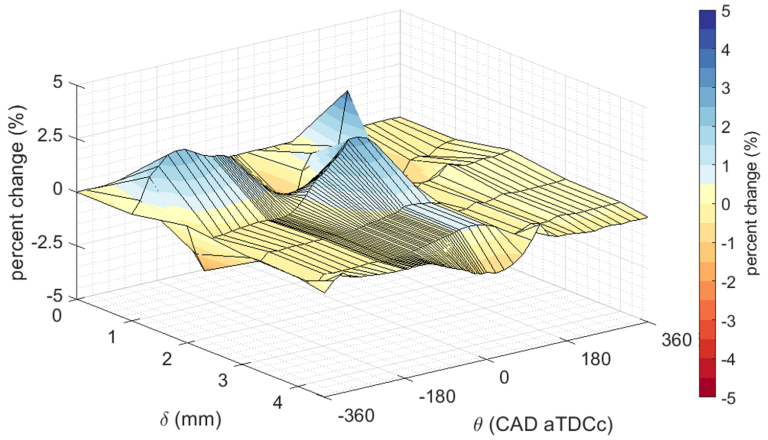

Figure 5.13. Percent change in bulk gas temperature with increasing distance δ from the engine walls. Figure was extracted from [38].

5.4 Near-Wall Flow and Temperature Predictions

The ensemble-averaged near-wall flow fields from the near-wall PIV and both simulations are shown in Figure 5.14 for -260 CAD aTDCc. Note that the first cells at the fluid-solid interfaces near $z = 0$ mm are not available for display from the CHT model due to data export routine limitations and are masked out. From the RI values, the uniform temperature model is able to capture the near-wall flow direction better than the CHT model. The kinetic energy is underpredicted by both models, with a larger region of small kinetic energy in the CHT model. With increasing distance from the cylinder head, the influence of the wall model on the flow predictions is reduced, and the direction of the flow in the CHT model aligns better with the measurement, in contrast with the uniform temperature model where the flow direction is mismatched far away from the wall.

The near-wall flow field at -100 CAD aTDCc is shown in Figure 5.15. The CHT simulation is able to predict the flow direction accurately, but underpredicts the velocity magnitude as shown by the low KEI values. In contrast, the flow direction of the uniform temperature model is opposite that of the PIV measurement in the near-wall region, while the velocity magnitude is larger in this same region compared to the CHT simulation.

Figure 5.16 shows the near-wall flow field at -30 CAD aTDCc. At this crank angle degree location, the CHT predictions are closer to the measurement than the uniform temperature model. The CHT model predicts a flow reversal near the surface so that the flow direction close to the surface is opposite that of the PIV measurement. As wall distance increases, the flow direction matches well, but the kinetic energy is underestimated. In contrast, the flow direction of the

uniform temperature model is opposite that of the experiment throughout the field of view, leading to negative RI values. Also, the uniform temperature model overpredicts the kinetic energy content of the field of view.

Figure 5.17 shows the near-wall flow field at TDC. The velocity field directions are well captured, while kinetic energy is overpredicted by the uniform temperature model. The kinetic energy is low in the CHT model near the surface, but as wall distance increased, the kinetic energy is overpredicted. Compared to the experimental flow field, both models do not predict the near-wall flow well.

These results show that the influence of the wall model on the near-wall predictions is large, as it leads to low RI and KEI values away from 1. This is because the wall model may not be valid in engine flows, especially in the outer layer as shown in Figure 4.23. At -100 and -30 CAD, the CHT model predicts a more accurate flow direction and kinetic energy compared to the uniform temperature model. These improved predictions of the flow could be due to more accurate thermal boundary conditions provided by the CHT model. Note that currently only 10 LES cycles have been ensemble-averaged compared to 141 PIV cycles. Including more cycles in the ensemble averaging process will lead to smoother velocity fields, and might impact the comparison between simulations and experiment.

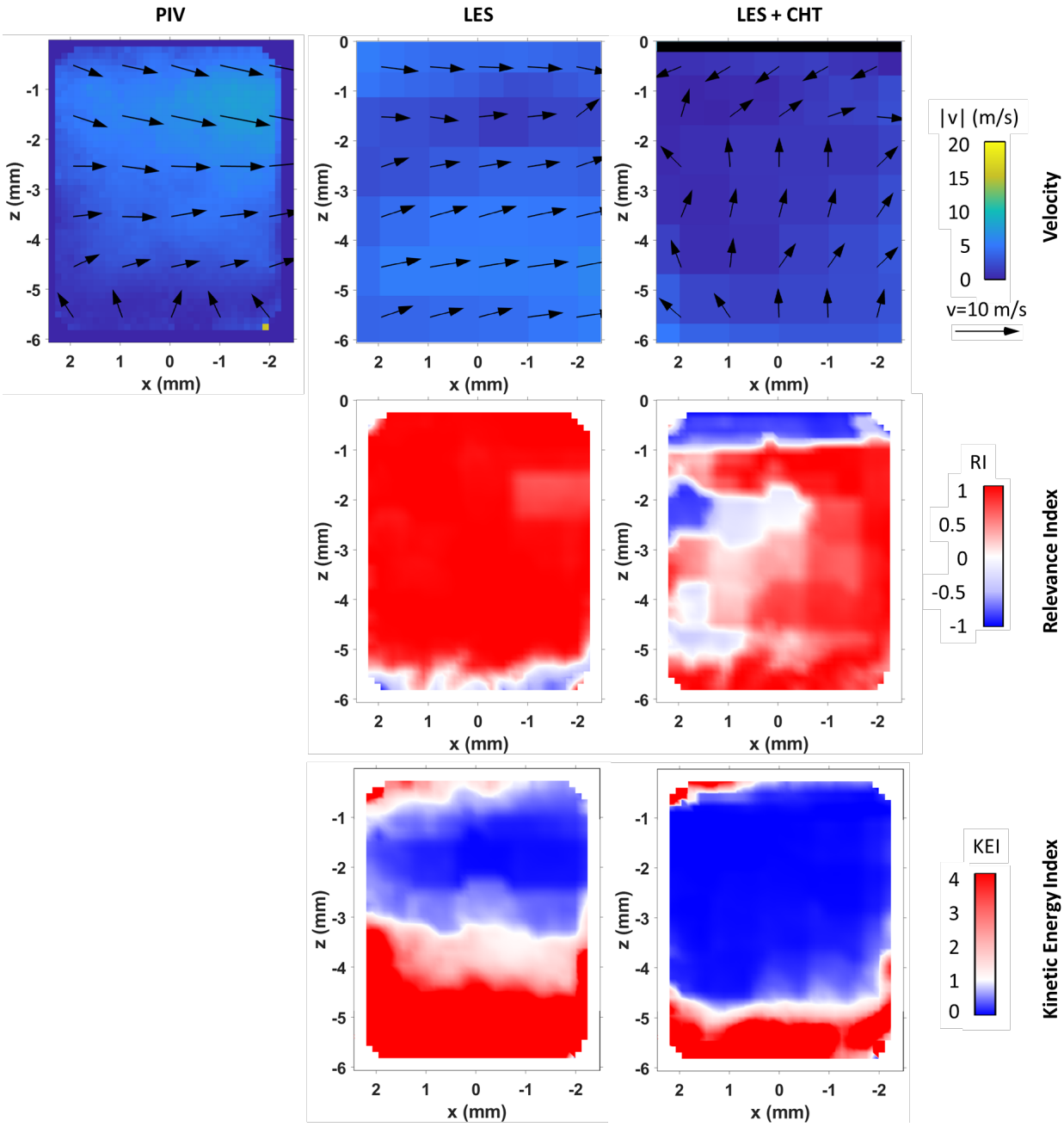

Figure 5.14. Average near-wall flow field, at -260 CAD aTDCc compared to dataset S_2016_03_13_04. Figure updated from [121].

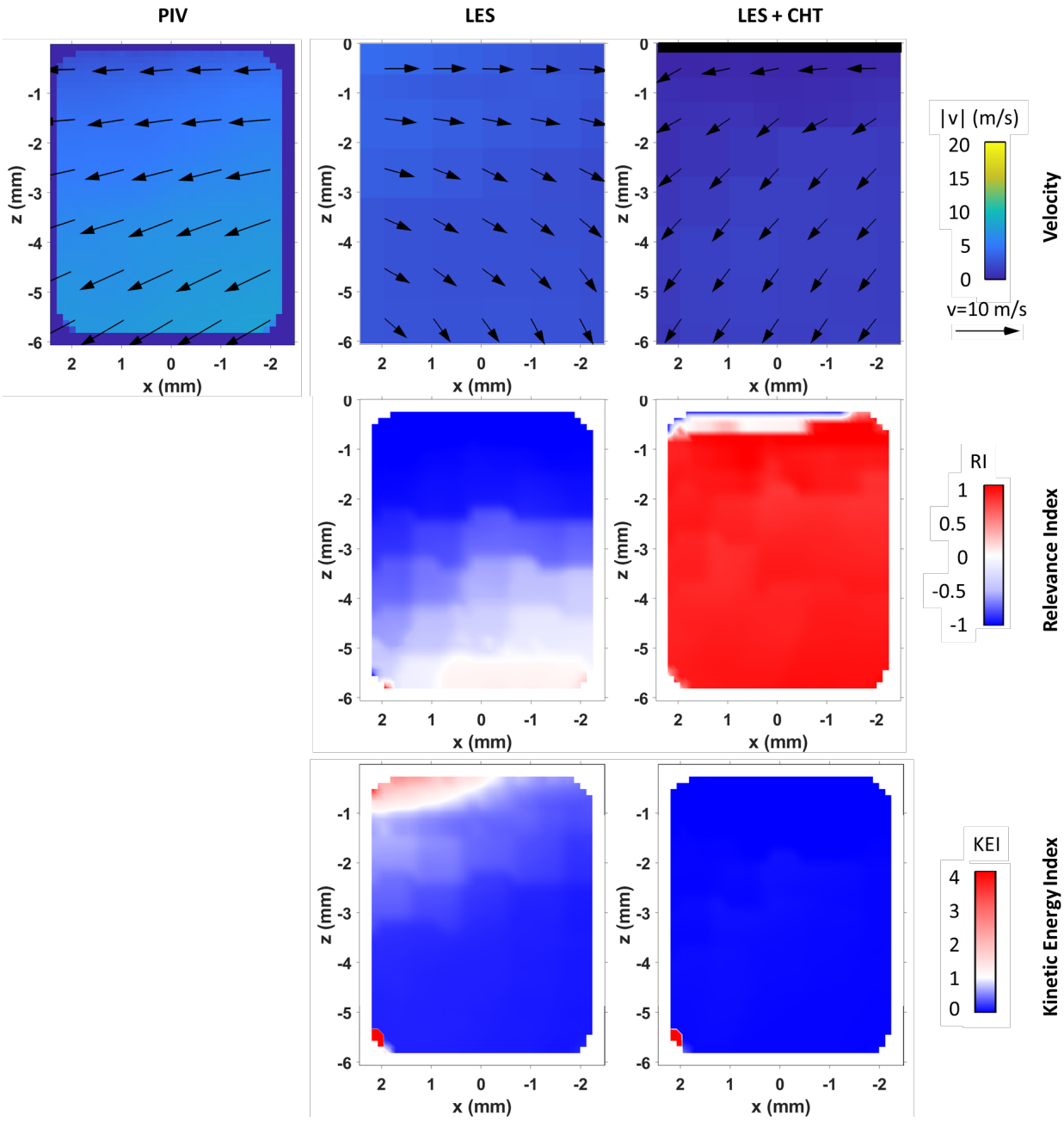

Figure 5.15. Average near-wall flow field, at -100 CAD aTDCc compared to dataset S_2016_03_13_04.

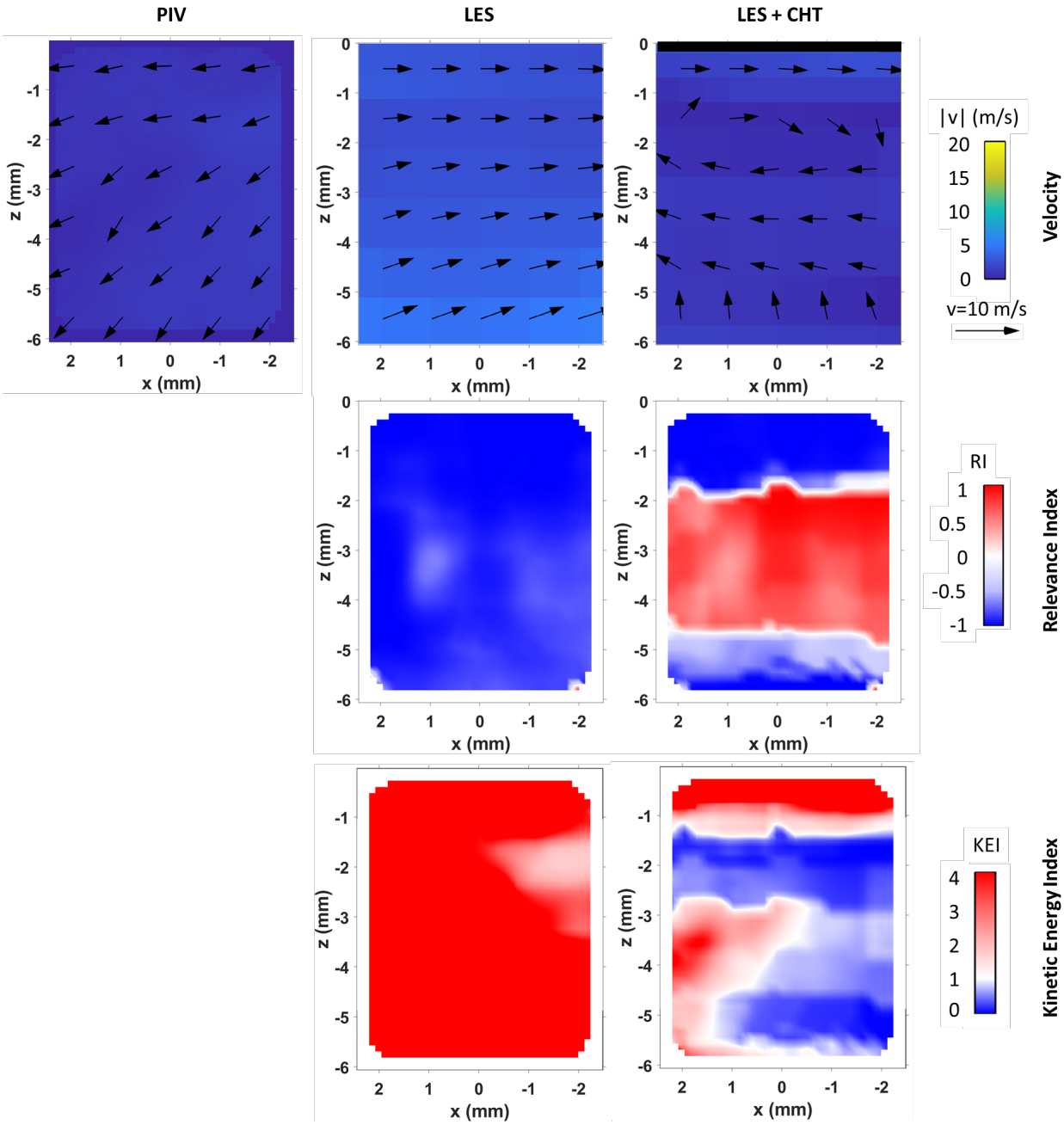

Figure 5.16. Average near-wall flow field, at -30 CAD aTDCc compared to dataset S_2016_03_13_04. Figure updated from [121].

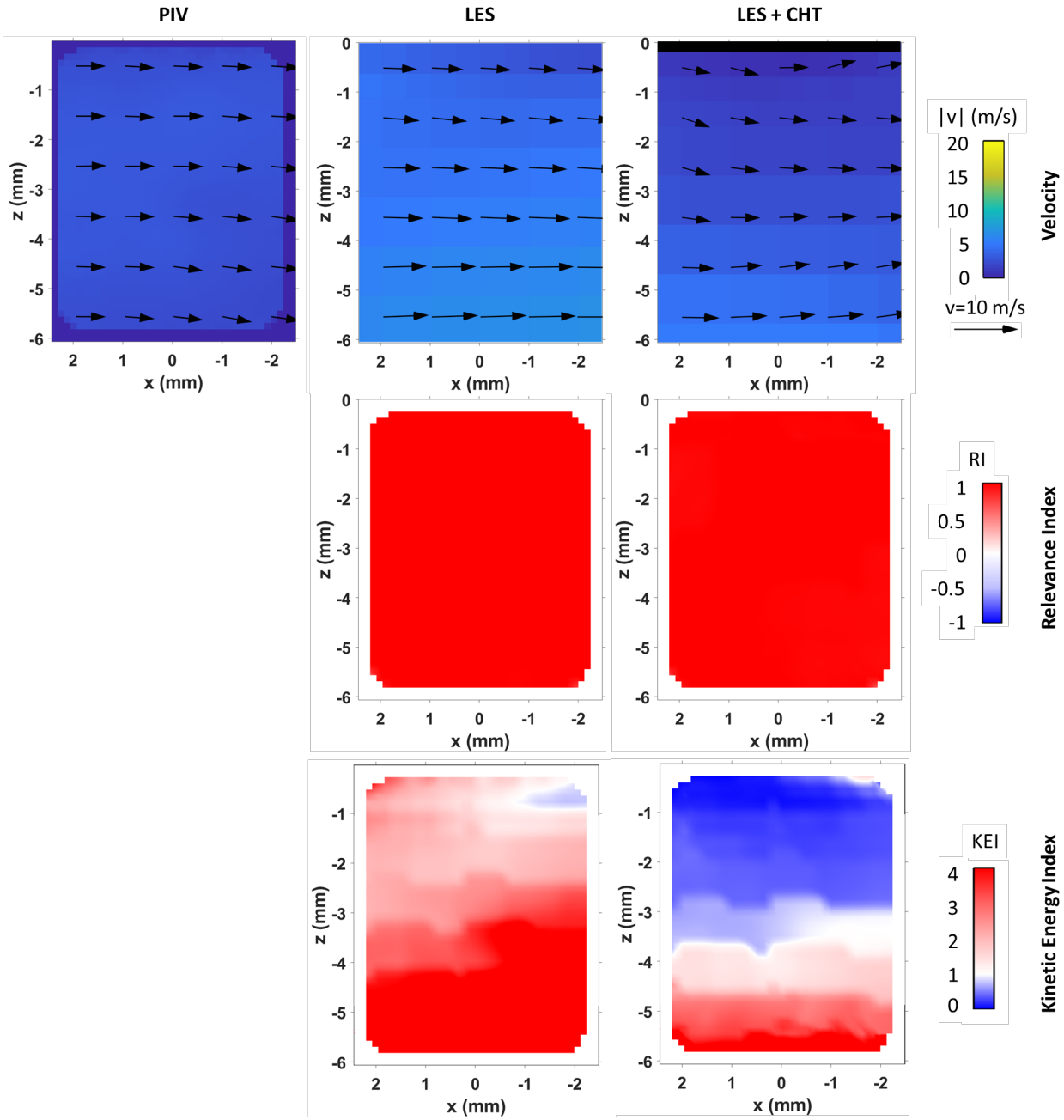

Figure 5.17. Average near-wall flow field at 0 CAD aTDCc compared to dataset S_2016_03_13_04. Figure updated from [121].

Next, the standard deviation of the velocity field is analyzed. For this analysis which was partially published in [38], the second set of motored near-wall PIV (S_2016_03_13_08) and near-wall PLIF data are used. The analysis is focused on -100, -35, and 0 CAD as these were the common crank angle degree locations between all datasets. This will aid in the understanding of near-wall thermal stratification and the influence of velocity fluctuations on heat transfer.

The standard deviation of the velocity field is shown in Figure 5.18. This standard deviation is about the ensemble average and it indicates the level of CCV in the flow field. The spatial average of the standard deviation is also shown in the figure as $\overline{v_{std}}$. The standard deviation of the velocity field in the measurement is slightly larger than that of both simulations. At -100 CAD aTDCc and at TDC, the distribution of the standard deviation is fairly homogeneous for the measurements and simulations. At -35 CAD aTDCc, the measurement and the CHT simulation show stratification in the standard deviation of the velocity field, with higher CCV near the surface of the CHT simulation. In contrast, the uniform temperature model still has a homogeneous distribution of the standard deviation of the velocity at -35 CAD aTDCc. The spatially averaged values of the standard deviation for both experiment and the CHT model show a similar increase from -100 CAD to -35 CAD, then decrease again at TDC. The spatially averaged values of the standard deviation of the uniform temperature model decreases with compression. This shows that the CHT model can capture the standard deviation of the velocity field more accurately than the uniform temperature model. This has implications on not only the cyclic variation in the velocity field, but also the CCV of temperature field, and results in improved levels of CCV in heat transfer than the uniform temperature model.

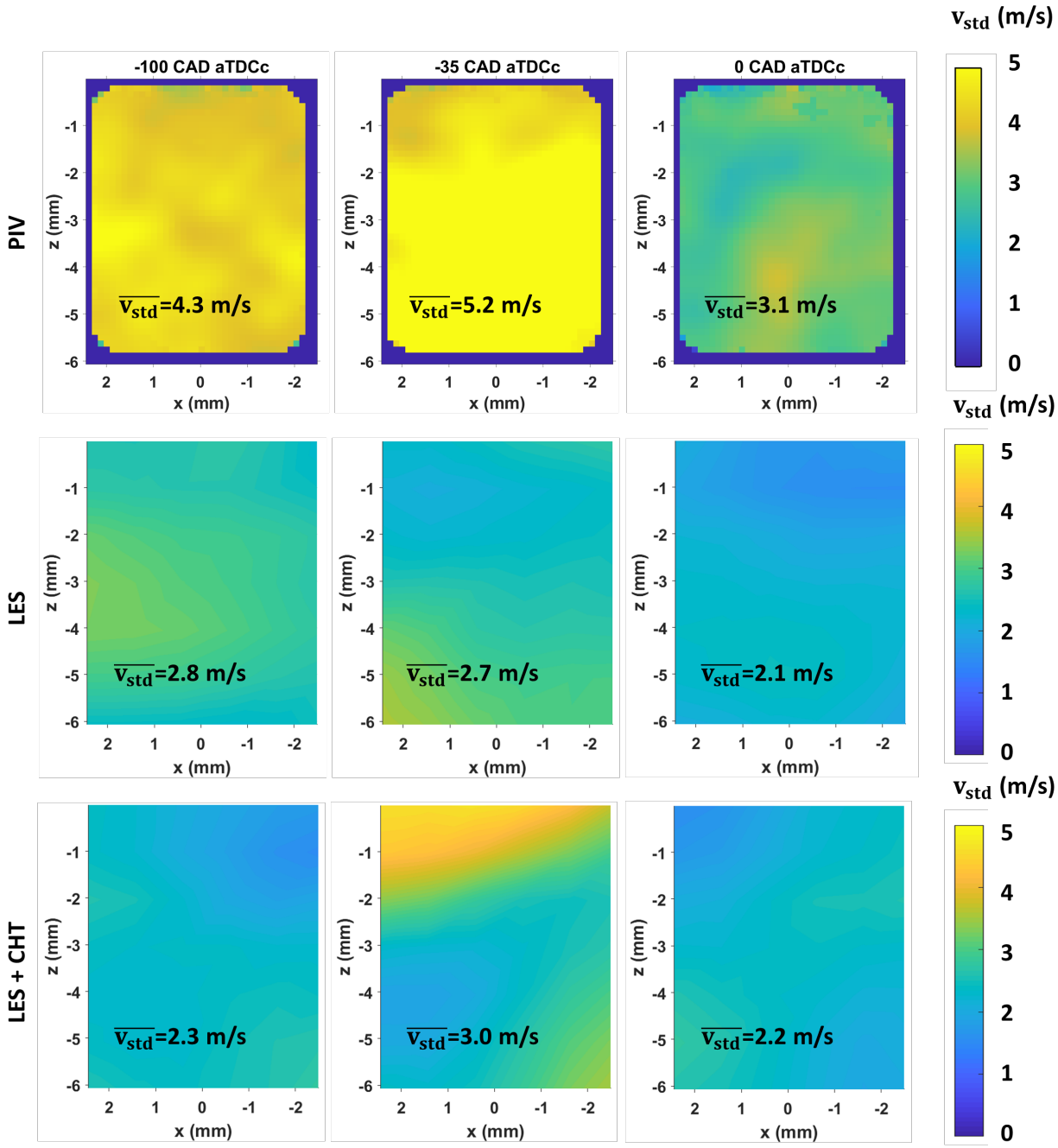

Figure 5.18. Standard deviation of the velocity fields, compared to dataset S_2016_03_13_08. Figure updated from [38].

Ensemble averaged temperature fields from PLIF and LES are shown in Figure 5.19 to provide insights into the temperature distribution in the NWR. The in-plane velocity field is imposed on top of the simulated temperature fields to shed light on the effects of the flow field on the temperature distribution. The spatial average temperature is indicated on each image as $\overline{T}$. The

differences that are seen in the figure arise from the differences in the surface temperature, which is used in the heat transfer model for the heat flux calculation at the first cell.

PLIF images show that some thermal stratification has already developed at -100 CAD aTDCc, and the stratification increases towards TDC with visible hot and cold structures. In contrast, the simulated temperature fields at -100 CAD aTDCc are rather homogeneous. This difference can be attributed to the mesh resolution being ten times larger than the PLIF resolution in the FoV. Structures smaller than the mesh resolution of the simulation cannot be resolved. At this piston position, both simulations predict a smaller velocity magnitude compared to the PIV, leading to lower convective heat transfer and thus a more homogeneously distributed temperature field.

At -35 CAD aTDCc, the PLIF measurement shows a more stratified temperature field with smaller cold and hot structures, which are not seen in the simulations. The increased stratification is due to a larger temperature difference between the gases and the surface. The simulations show a more gradual change in temperature from colder gases near the wall to hotter gases in the bulk region, whereas there are hot and cold structures near the surface in the measurement. The flow in the CHT simulation convects the hotter bulk gases towards the NWR. In addition, a recirculation zone forms, which leads to mixing of hot and cold gases in the same region. The uniform temperature model shows a more uniform, wall-parallel flow, which causes less mixing of the flow in the same region, and therefore, the colder gases of the NWR do not penetrate far into the bulk region. This leads to a smaller area of colder gases compared to the CHT simulation. Also, the surface temperatures of the CHT are higher than the surface temperature of the uniform temperature model. This explains the slightly higher spatial average temperature in the uniform temperature model compared to the CHT model.

At TDC, the simulated temperature field of both models are on average 10 K higher than the measured temperature field. The in-plane velocity fields from both simulations are mainly parallel to the wall. This parallel in-plane flow could be convecting the thermal stratification seen in both simulations into the field of view from somewhere else. The measured and simulated images show similar levels of stratification in the temperature fields.

Compared to the LES temperature fields in Figure 4.18, where a uniform temperature of 318.16 K was used, and the uniform temperature LES in Figure 5.19, which has a uniform temperature of 353.16 K, the LES CHT model predicts higher surface temperatures at the cylinder

head. At -100 CAD and TDC, the CHT model predicts a spatial average temperature that is closer to the measurement. However, the small structures found in the measurements are not captured due to the mesh resolution of 1 mm. This indicates that the mesh resolution will need to be refined, which will increase computation costs.

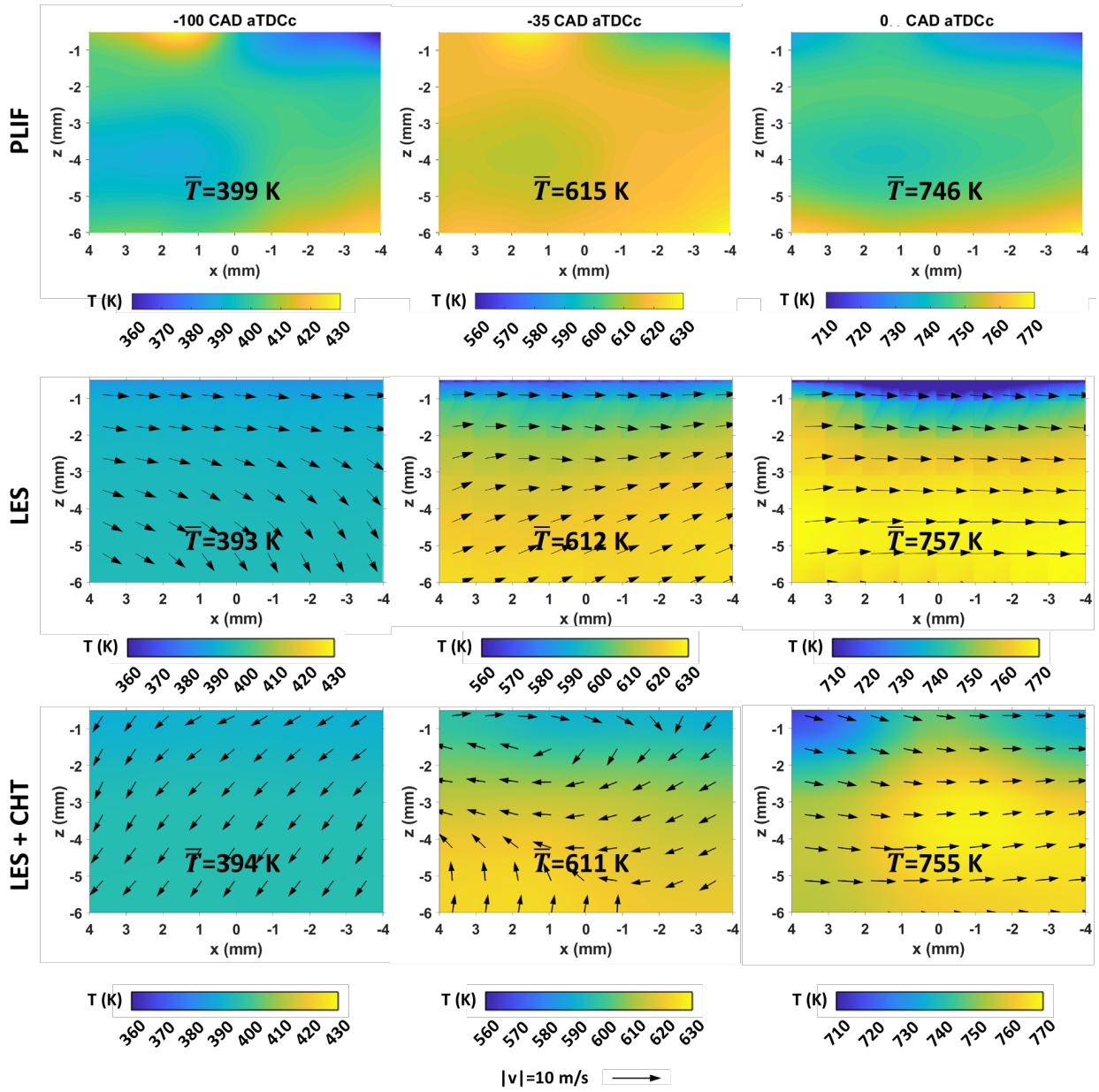

Figure 5.19. Ensemble averaged near-wall temperature field of Cases 4 and 6 and PLIF measurement. Figure updated from [38].

The standard deviation of temperature distributions is shown in Figure 5.20. Measured and simulated results indicate that the near-wall region exhibits larger CCV than the bulk gas region. In both simulations, this region of large CCV extends further into the bulk region than in the PLIF

images, where large CCV is mainly restricted to a wall distance of 1 mm. The spatially averaged values of the standard deviation also increase with compression in the simulation, while it is decreasing in the measurements. Both simulations are similar in the level of stratification in the standard deviation of the temperature field, but at TDC, there are two regions of high CCV in the uniform temperature model.

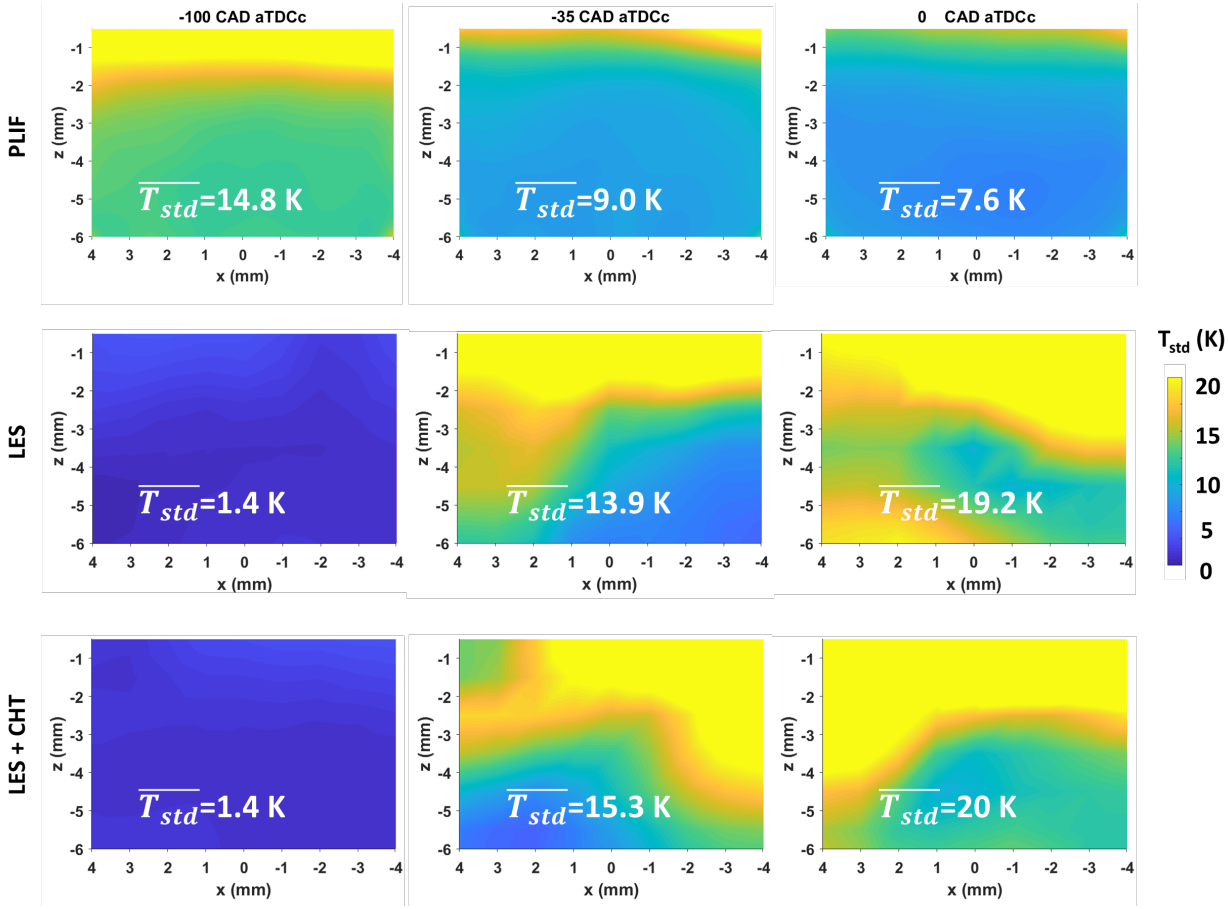

Figure 5.20. Standard deviation of the temperature fields Cases 4 and 6 and PLIF measurement. Figure updated from [38].

Relative temperature fields from subtracting the spatial mean of the ensemble average temperature fields are shown in Figure 5.21. The small structures seen in the PLIF measurement are not found in either simulation. The relative temperatures in the simulations increase from negative to positive values with increasing wall distance and are very similar to the relative temperature fields of the previous chapter. With compression, the magnitude of the relative temperatures increases in the simulations.

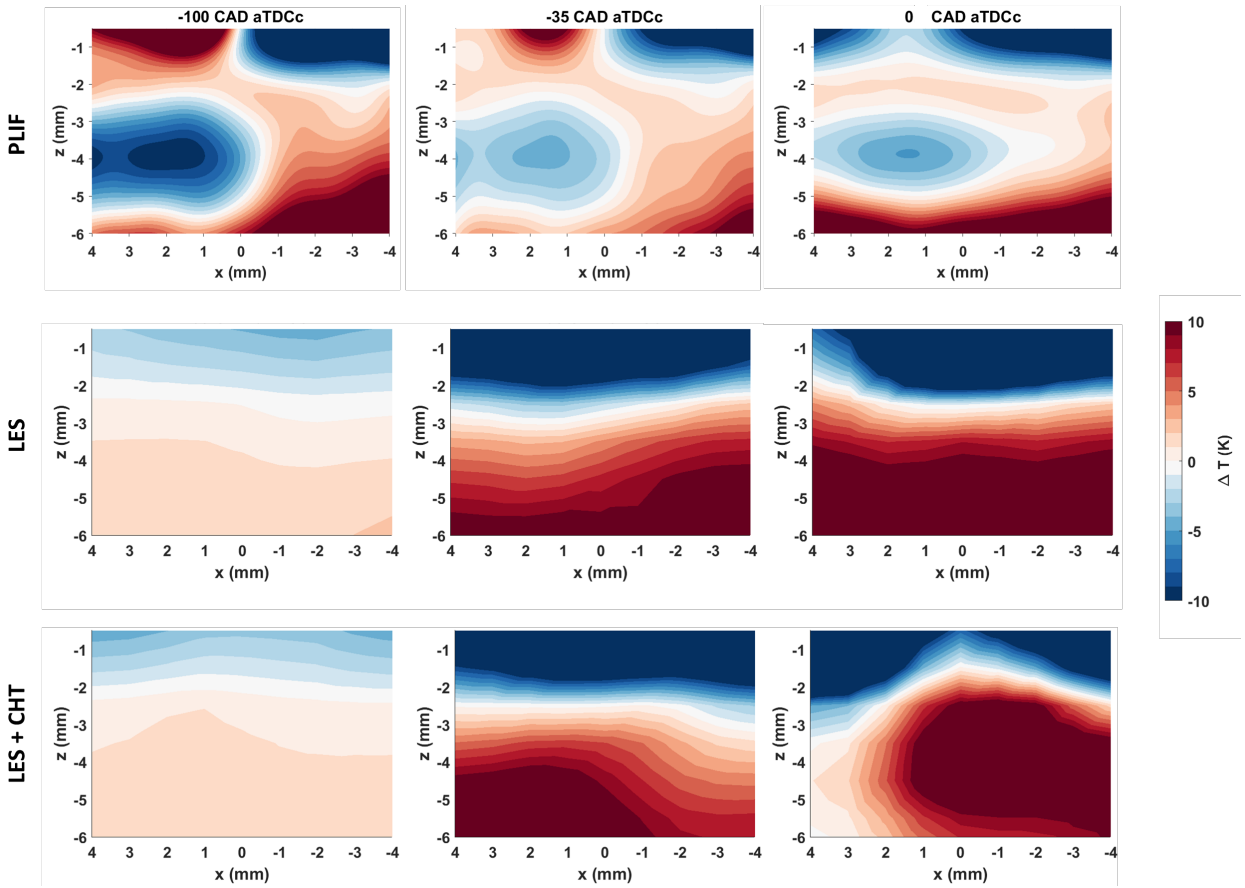

Figure 5.21. Relative near-wall temperature field validation of Cases 4 and 6 with temperature PLIF measurements.

5.5 Surface Temperature and Heat Flux Predictions

The heat flux probe provides surface temperature measurements over the entire engine cycle at the cylinder head. The measured and predicted surface temperatures from the CHT model are plotted in Figure 5.22(a). Note that a low-pass filter of 100 Hz was applied to the measured surface temperature to filter out the noise in the measurement. The shaded area represents one standard deviation from the ensemble average and indicates CCV of the surface temperature. The CHT model overestimates the surface temperature by 5 K or approximately 1.4%. This can be due to approximations in the thermal boundary conditions applied at the outer surfaces of the solid geometries, which were not all measured. In addition, the material properties could have been oversimplified as constant material properties were used in the CHT simulation. However, the temporal behavior of the surface temperature matches very closely with the measurement during compression. The increase in the surface temperature is captured, but the drop in the temperature happens earlier in the compression stroke compared to the measurements. The peak temperature

occurs at -5 CAD aTDCc in the simulation, while in the experiment the low-pass filtered surface temperature peaks at 14 CAD aTDCc. The unfiltered peak surface temperature occurs at -0.5 CAD aTDCc. The discrepancy in the CAD location of the peak temperature is likely due to the difference in the crank-angle resolution between the simulations (5 CAD) and the measurements (0.5 CAD) in the compression stroke. The simulated standard deviation is also smaller compared to the experiment, but an improvement on the constant surface temperature used in the uniform temperature models.

For easier assessment of the temperature prediction, Figure 5.22(b) shows the normalized temperature profile $\Theta = \frac{T_S}{\bar{T}_{S,[-270,-90]\,CAD}}$. The surface temperature is quasi-steady from -260 CAD to -90 CAD and the mean value from this interval is used to normalize the surface temperature. It can be seen that the surface temperature is underpredicted in the intake, expansion, and exhaust strokes. The normalized temperature reveals that the increase in the surface temperature in the compression stroke is well captured, but the surface temperature peak and subsequent decrease happens earlier in the simulation compared to the experiment.

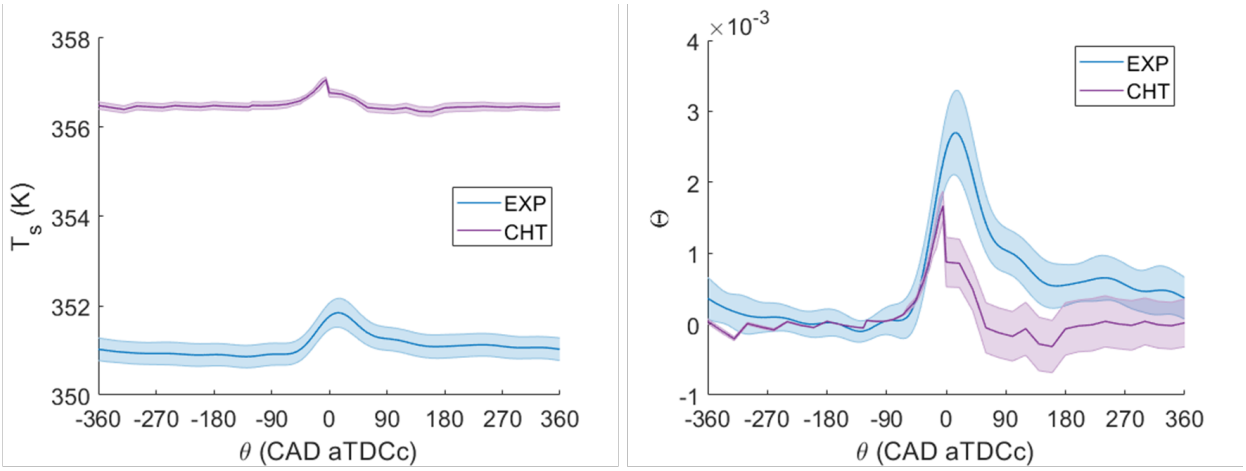

a) b)

Figure 5.22. a) Ensemble averaged surface temperature from the CHT simulation and measurement (S_2016_03_13_04) and b) normalized representation. The shaded area represents one standard deviation from the ensemble average.

The temperatures at the inner engine surfaces are difficult to measure. The LES CHT model is able to predict the temporal, spatial, and cyclic variation of the surface temperature, and therefore it can lead to more accurate engine heat transfer simulations. Figure 5.23 shows the surface temperature of the spark plug from cycle 2 to 11 at -20 CAD aTDCc. Noticeable is the surface temperature variation in the ground strap. This surface temperature is also higher for certain cycles,

for example cycles 6, 10, and 11. For the fired simulation, the CCV and spatial stratification of the surface temperature in the ground strap is larger, as will be shown in Chapter 6.

Figure 5.24 shows the surface temperature of the piston for cycles 2 to 11 for three different CAD. The piston consists of a metal crown that surrounds a cylindrical quartz window. The thermal conductivity of the quartz material is low compared to the metal crown, which results in a much higher surface temperature in the quartz window compared to the metal crown. The surface temperature is also non-uniform due to the asymmetry of the in-cylinder flow. As the piston comes to TDC, the surface temperature increases due to compression heating of the surrounding gas temperatures. Evident from Figure 5.24 is the CCV in the surface temperature. These results are in stark contrast with the conventional uniform wall temperature model, where a constant, uniform temperature of 353.16 K was applied to all engine surfaces.

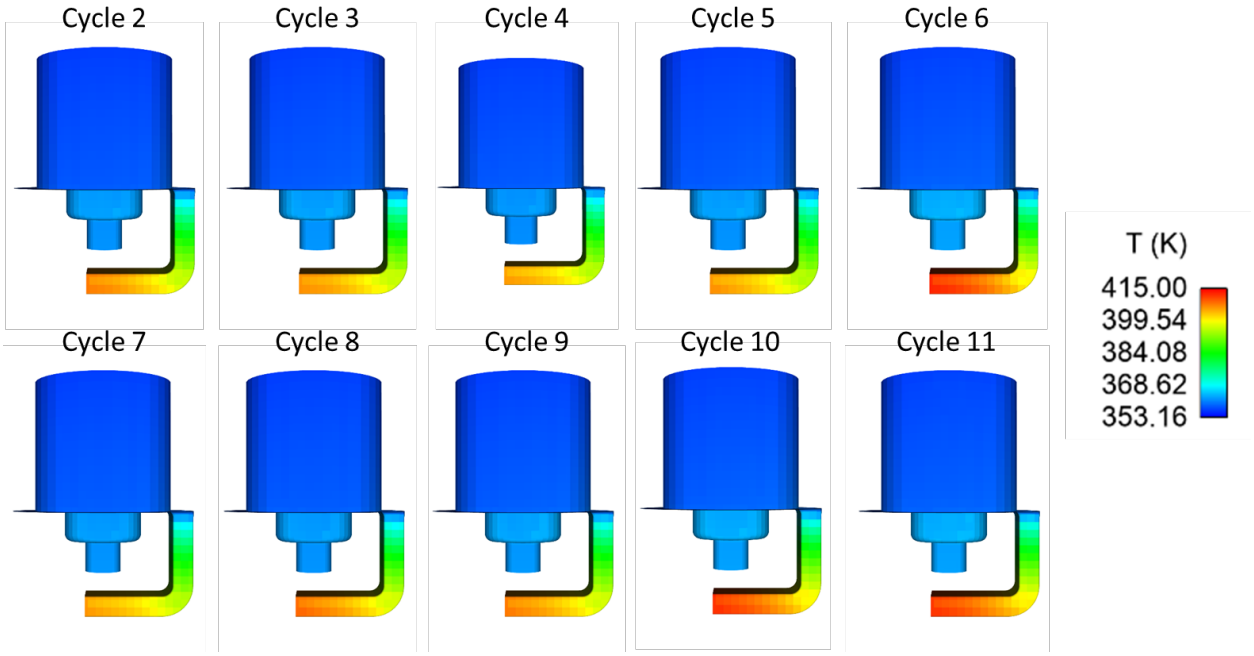

Figure 5.23. Cycle-to-cycle variation in the surface temperature of the spark plug at -20 CAD aTDCc of the LES CHT simulation.

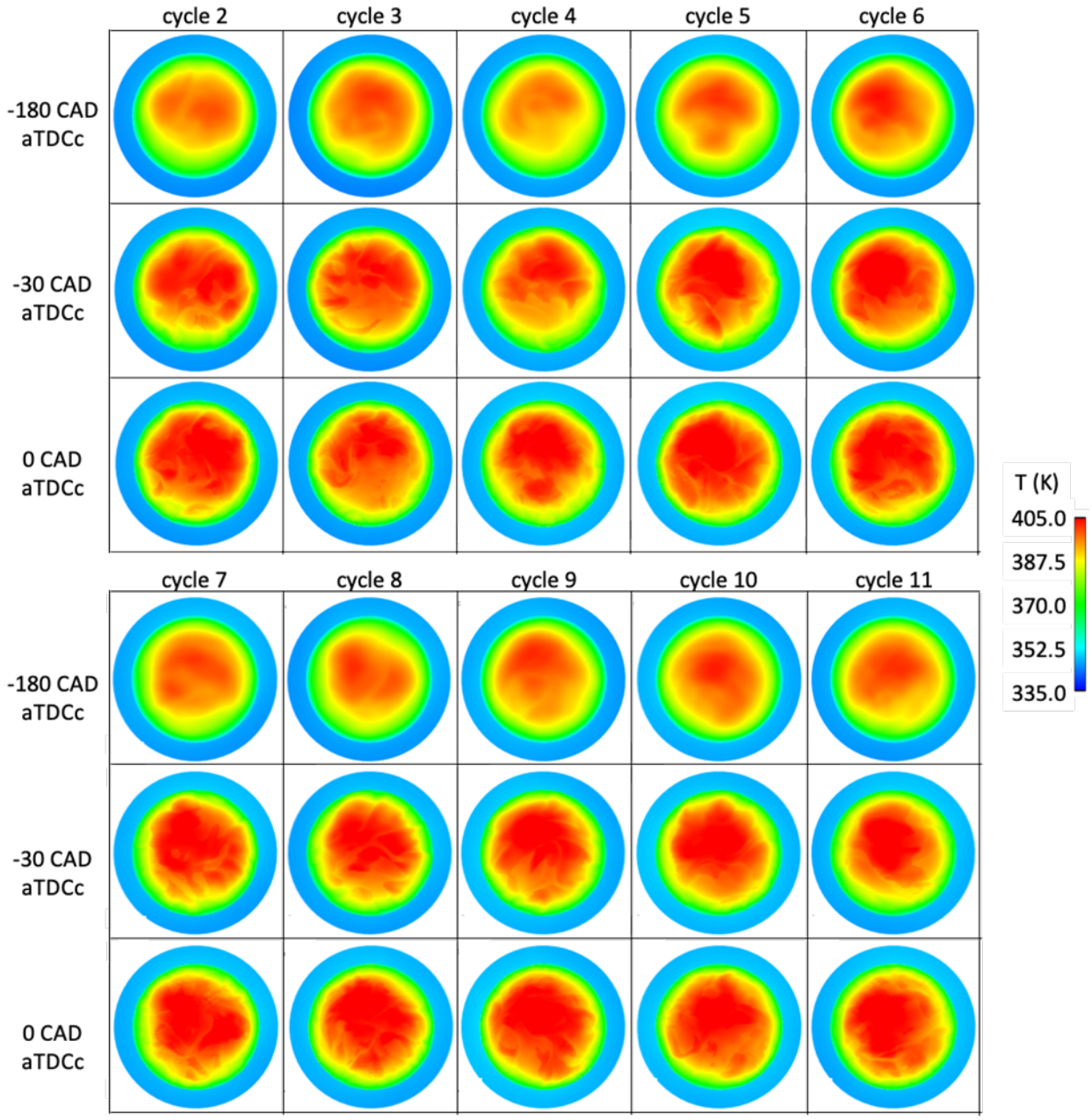

Figure 5.24. The LES CHT model predicts spatial, temporal, and cyclic variation in the piston surface temperature.

The surface temperatures from the piston, inner liner surface, and cylinder head are first ensemble averaged, then spatially averaged for the entire engine cycle in Figure 5.25 for each surface. The shaded area indicates one spatial standard deviation of the surface temperature, i.e., the level of stratification in the temperature distribution over the surfaces. The temporal variation of the surface temperature in the piston and cylinder liner over the engine cycle is much larger than that of the cylinder head. This is due to the cooling circuit in the cylinder head stabilizing the

cylinder head temperature. The cylinder head surface also has the smallest temperature stratification compared to the inner liner and the piston surfaces. The temperature stratification of the inner liner surface is large due to the scrubbing motion of the piston, which exposes the inner liner surfaces to different thermal boundary conditions during the cycle. The piston surface has the largest temperature stratification since it is composed of two different materials. This figure shows that the temperature at each surface is different and has significant spatial and temporal variation, which is in contrast with the uniform temperature assumption. Due to the inherent difficulty in measuring the temperatures at these engine surfaces, the CHT can provide more accurate thermal boundary conditions for engine simulations than only involving the gas-phase.

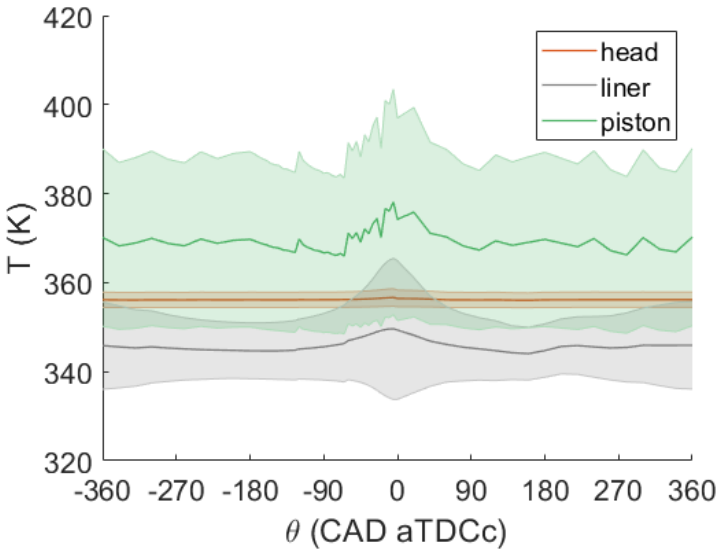

Figure 5.25. Spatial average of the ensemble-averaged surface temperatures of the cylinder head, liner, and piston, obtained from the motored LES CHT. The shaded area is one standard deviation of spatially averaged temperature, indicating the spatial stratification over the surface.

The surface heat flux was measured at the heat flux probe at the cylinder head, at $x = 12.1$ mm and $y = 33.4$ mm, and is shown in Figure 5.26 along with the results from the simulations. Both models predict the correct temporal behavior of the filtered surface heat flux. The peak location of the CHT heat flux compares well with that of the filtered heat flux as both peak at -5 CAD aTDCc. In contrast, the heat flux peaks at -10 CAD for the uniform temperature model. The CHT model has a peak value of 112 kW/m^{2}K, while the uniform temperature model has a peak of 118 kW/m^{2}K. The unfiltered experimental peak heat flux is 120 kW/m^{2}K. In terms of CCV, the maximum standard deviation of the filtered heat flux is 26 kW/m^{2}K. The uniform temperature maximum standard deviation is 18 kW/m^{2}K. The CHT simulation maximum standard deviation is

25 kW/m^{2}K. The experimental CCV is larger than both simulations, but the CHT model predicts larger CCV than the uniform temperature model with the same number of cycles due to it being able to predict variations in the surface temperatures. More than 10 cycles are likely needed to capture a larger CCV, even if statistical convergence is met.

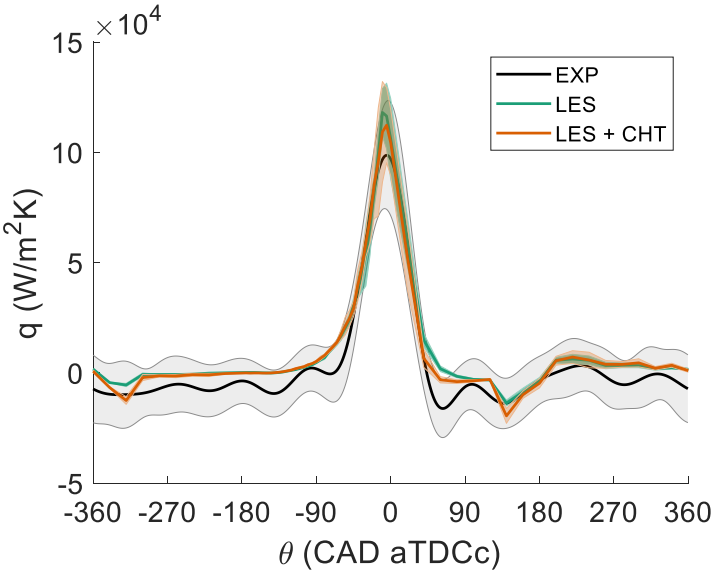

Figure 5.26. Ensemble averaged surface heat flux at the cylinder head of a) the uniform temperature model and b) the CHT model, compared with the ensemble averaged heat flux from S_2016_03_13_04. Shaded areas indicate one standard deviation from the ensemble average heat flux.

5.6 Sources of Discrepancy

It should be noted that the bulk flow has been validated previously by [60] and in Sections 4.3.1 and 5.2. The cause of LES not predicting the correct velocity magnitude and/or flow direction in the near-wall region can be due to many factors, including the use of the Werner and Wengle wall model, which could provide inaccurate wall shear stress boundary conditions to the rest of the CFD calculations. The use of the law-of-the-wall model has been investigated recently by [72] and shown to not accurately predict the shear velocity when the y^+ value of the first cell is outside of the viscous sublayer ($y^+ \leq 5$).

In Figure 5.27, the spatially averaged, ensemble averaged y^+ value is plotted for both simulations in the near-wall PIV FoV. The y^+ of 11.05 indicates the switching point in the Werner and Wengle model between viscous and outer layer for the calculation of u^+. The CHT model has $y^+ \leq 11.05$ for most of the engine cycle except for a brief period after EVO. In contrast, the uniform temperature model has $y^+ > 11.05$ after EVO for the duration of the exhaust stroke, for

brief periods after IVO during the intake stroke, and late compression and early expansion strokes. No discernable trends are observed in the y^+ and predicted velocity vectors in the first two near-wall cells. At -260 CAD aTDCc, both models fall within $y^+ \leq 11.05$ and the uniform temperature model predicts the velocity vector direction better than the CHT model in the first two near-wall cells. At -30 CAD aTDCc, $y^+ = 11.9$ in the uniform temperature model, and $y^+ = 5.6$ in the CHT model. Both models fail to predict the velocity direction in the first two near-wall cells. At 120 CAD, $y^+ = 6$ in the uniform temperature model, while $y^+ = 1.3$ in the CHT model. The velocity direction is well captured, while the velocity magnitude is over-estimated in the first two near-wall cells. On the other hand, from Figure 5.19, it can be seen that the temperature gradient in the first two near-wall cells is large and this leads to conclusions that the LES may be under-resolved. It may be necessary to increase the grid resolution near the wall to below $y^+ < 1$, which may not be feasible in practical engine simulations. These results suggest that more work is required to investigate the use of Werner and Wengle wall model in engine LES and the effects of y^+ values on near-wall flow and temperature predictions.

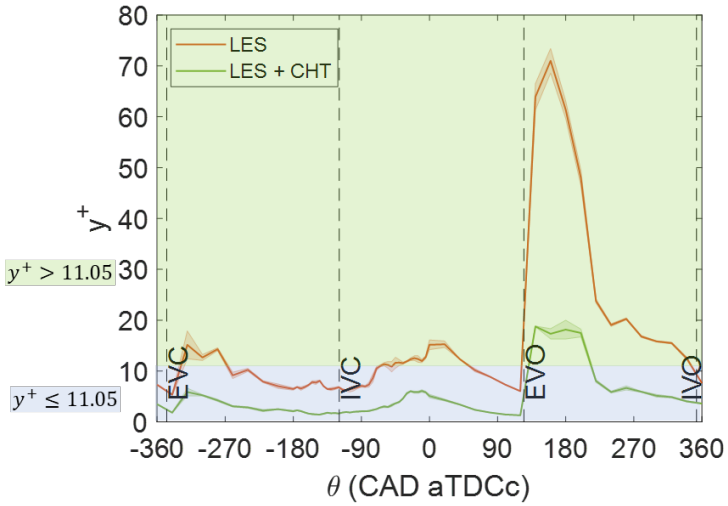

Figure 5.27. Ensemble average y^+, which is spatially averaged, in the near-wall PIV field of view. The shaded area represents one standard deviation in the spatial average value, indicating spatial variations of y^+ in the field of view. Figure extracted from [121].

The numerical scheme used could also affect resolved velocity predictions. Nichani et al. [61] found that the second-order central differencing scheme provides better predictions, especially for velocity fluctuations, due to reduced numerical viscosity. The first-order upwind scheme was found to underpredict peak velocities. While the second-order central differencing scheme can provide more accurate predictions, numerical stability is still an issue, and

CONVERGE and other commercial CFD codes will resort back to first-order upwind when velocity or density fields become nonmonotonic [123].

The choice of the subgrid-scale model and the grid resolution affect the subgrid kinetic energy and therefore the resolved velocity calculations [61]. The dynamic structure model is a non-viscosity based model that solves the transport equation of the subgrid kinetic energy. This model was specifically developed for ICE applications [45] and was found to predict the jet penetration depth well when compared to other subgrid-scale models [61]. However, the dynamic structure model underpredicts velocity fluctuations, especially in the shear layer of the intake jet. Nichani et al. [61] found that at -60 CAD aTDCc, the predictions become insensitive to the subgrid-scale model used, most likely due to lack of high-shear flow structures at this piston position. In regards to the grid resolution, the current simulation resolves 80% or more of the turbulent kinetic energy during most of the cycle as was shown in Figures 4.3 and 5.3. Only during IVO and EVO does the resolved kinetic energy drop below 80%, which could result in erroneous resolved velocities that can affect the results at later timesteps.

The simulated temperature fields show that the thermal boundary layer modeling method also needs to be improved. The Han and Reitz heat transfer model was developed with a RANS turbulence model. This model uses a single equation for T^+ for all y^+, but the turbulent Prandtl number in their formulation depends on y^+ [77]. In fact, the transition point y_0^+ from viscous sublayer to turbulent boundary layer for the calculation of the turbulent Prandtl number was not chosen based on experimental observation but was purely chosen for mathematical ease. It may be that the turbulent Prandtl number is calculated using the wrong formula or the wrong transition point y_0^+, which could lead to incorrectly predicted heat transfer values. In addition, the use of this heat transfer model with LES subgrid-scale modeling has not yet been validated and a parametric study may be needed of the model constants. Since the temperature field is coupled with the velocity field, any errors in temperature or velocity will inevitably affect the other variable.

Finally, the surface temperature predicted by the CHT model can also affect the temperature field in the near-wall region. A maximum difference of 1.4% between the measured and predicted surface temperature from LES CHT at the heat flux probe was found, which should not significantly impact the temperature predictions. However, a lack of a spatially resolved surface temperature measurement prevents the full validation of the LES CHT temperatures. Also, values of the solid material properties were taken from literature and not measured directly.

While there are more validation studies needed to improve the simulation side, the impact of experimental errors must also be taken into consideration. The near-wall PIV measurement has experimental errors that can affect comparisons to the LES results. These sources of error include the determination of the wall location, which leads to a 3% uncertainty in the wall-normal distance z for measurement locations closest to the surface. The laser-sheet thickness was chosen to allow a sufficient number of particle image pairs to be captured, but it also allows for greater out-of-plane motion of the particles within the sheet, leading to a larger error in the in-plane measurement. These and other errors were previously discussed in [29], and great care was taken to ensure the accuracy of the PIV measurement.

A primary error of the LIF temperature measurements is associated with the accuracy of the GT-Power model used to calibrate the LIF signal, which was tuned to match the experimental pressures within ± 5%. The predicted in-cylinder temperature from GT-Power was then correlated with the ensemble average LIF signal, extracted from a defined 1×1 mm^2 calibration region, to generate the LIF temperature calibration curve from intake valve closing to TDC. Any deviation between simulated and experimental pressures would affect the accuracy of the LIF temperature calibration and therefore comparisons to the LES results. The ensemble-averaged temperature of the calibration region was found to match the LES results within ± 2%.

Furthermore, the temperature measurements will exhibit inaccuracies if any local LIF signal variations are caused by inhomogeneous toluene mixture. The one-color detection technique utilized in this study is not able to distinguish between temperature variations and mixture inhomogeneities [35, 145]. Toluene was premixed with the intake air upstream of the intake plenum to deliver a homogeneous mixture to the cylinder, but the formation of heterogeneous toluene mixtures could happen during expansion due to local regions of condensation, which might leave deposits on surfaces or within crevices, affecting the mixture's homogeneity in the following cycles. Nevertheless, this was evaluated to have minimal impact on the one-color detection technique during compression [145].

Moreover, the post-processing steps to correct the LIF images affect the temperature calibration. In particular, the reflection correction step might have suppressed cycle-to-cycle temperature fluctuations towards TDC, leading to lower standard deviation values with increasing compression. Further improvements in the correction algorithms were deemed challenging because of the inability to isolate the background fluorescence signal due to reflections.

5.7 Fluctuating Velocity and Temperature PDFs

Histograms of the fluctuating velocities and temperature about their ensemble average values can show if the simulations are able to capture the CCV adequately and reveal the behavior of the measured CCV. The PDF of the wall-parallel and wall-normal fluctuating velocity components are shown in Figure 5.28 for the uniform temperature model, and Figure 5.29 for the CHT model. These are compared to the fluctuating velocities from the near-wall PIV dataset S_2016_03_13_08.

At -100 CAD aTDCc, the wall-parallel component is distributed more narrowly in the CHT simulation, with higher peak values of the PDF, than the PIV measurement. In contrast, the uniform temperature model has a wider distribution than the CHT simulation but still is narrower than the measurement. This indicates that the simulations are capturing less fluctuations than the PIV in the wall-parallel component. The range of values for this component is more evenly distributed about 0 m/s for the measurement. The PDFs of the CHT simulation and the PIV measurement broaden slightly at -35 CAD aTDCc, while the PDF of the uniform temperature model seems to become narrower. The peak PDF value from the CHT compares better with the PIV measurement, while the peak of the uniform temperature model is higher. At TDC, the PDFs become narrower, with comparable peak values albeit slightly higher in the simulations. The PDFs of the measurement indicate that the wall-parallel velocity fluctuations decrease with increasing compression, and the simulations can capture the effects of compression on the wall-parallel velocity fluctuations, with better agreement at TDC.

In terms of the wall-normal velocity fluctuations, both simulations predict peak values of the PDFs centered about 0 m/s with narrower distributions at the three crank angle degree locations when compared to the broadness of the measurement PDFs. Again, this indicates that the simulations are capturing less fluctuations in the wall-normal velocity than the PIV. At TDC, the peak values of the PDFs from CHT compare better with the measurement than the uniform temperature model.

Overall, the range of values that the wall-normal velocity fluctuations can take in the LES tends to be narrower compared to the wall-parallel velocity fluctuations. The distributions of the wall-normal fluctuating velocity from PIV are also narrower than the wall-parallel fluctuating velocity. At TDC, the ranges become similar between the simulations and the PIV measurement.

This indicates that the cyclic variation in the velocity is underestimated by either simulations, and more cycles need to be simulated to capture a larger range of the velocity fluctuations.

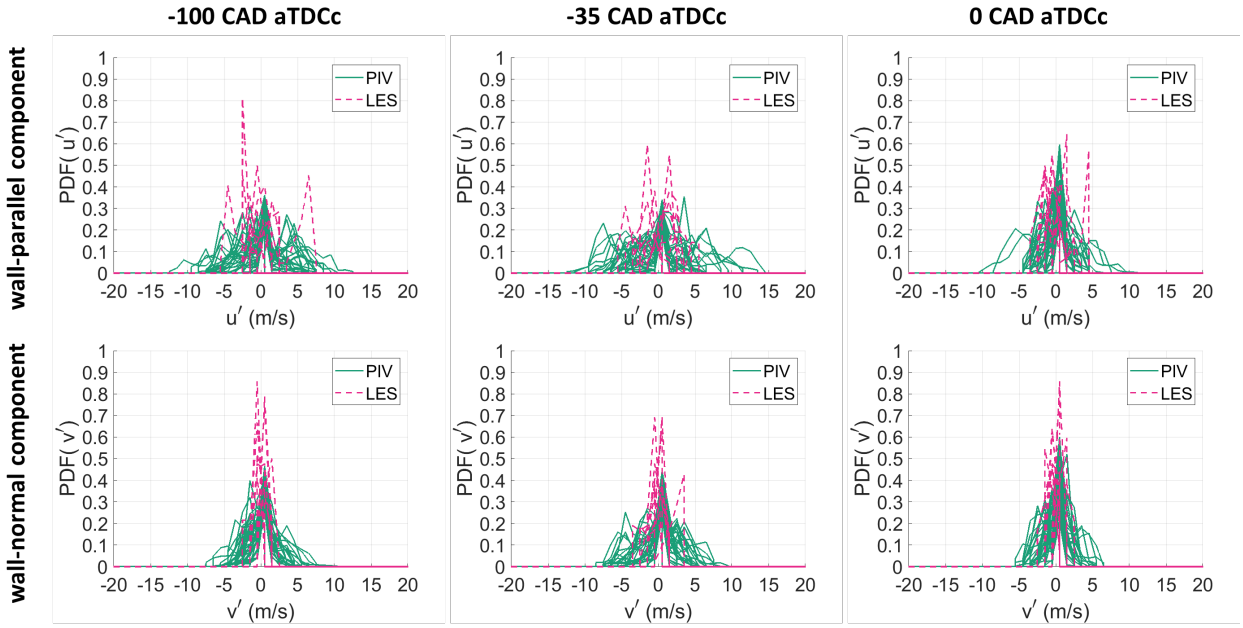

Figure 5.28. PDFs of fluctuating velocity fields from PIV (35 cycles) and uniform temperature LES (10 cycles). Upper rows are wall-parallel velocity fluctuations, while lower rows are the wall-normal velocity fluctuations. Each curve represents an individual cycle.

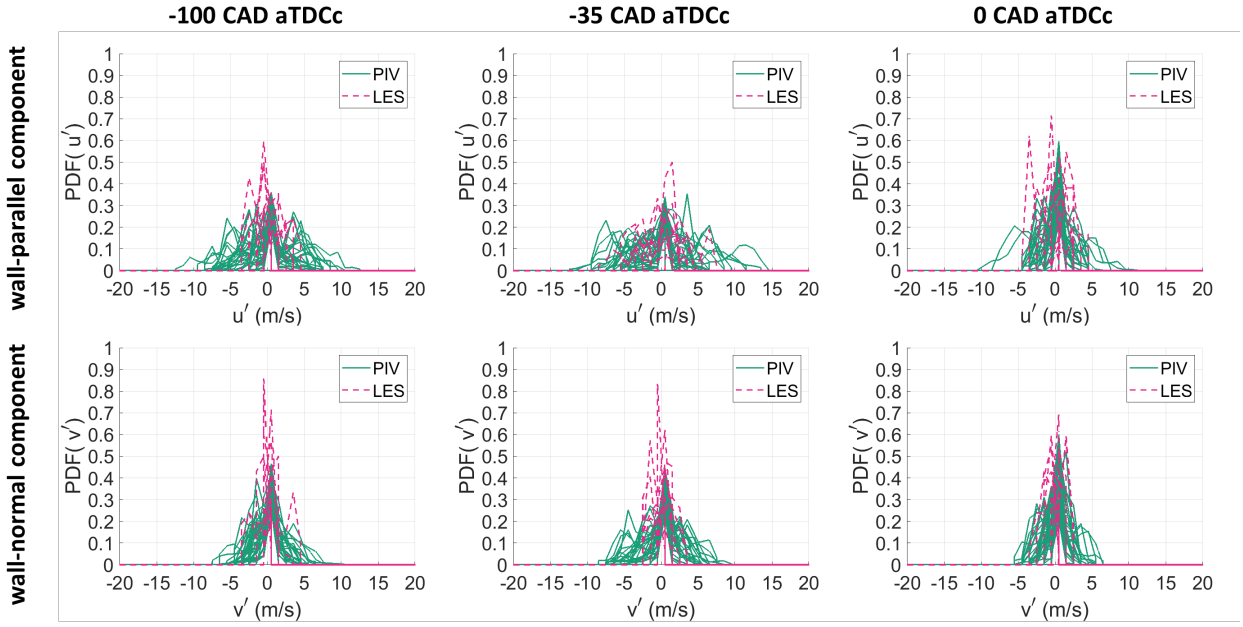

Figure 5.29. PDFs of fluctuating velocity fields from PIV (35 cycles) and LES CHT (10 cycles). Upper rows are wall-parallel velocity fluctuations, while lower rows are the wall-normal velocity fluctuations. Each curve represents an individual cycle.

Figure 5.30 shows the PDF of the temperature fluctuations. At -100 CAD aTDCc, the peak values of the LES PDFs are comparable to the PLIF measurement, but the range is much narrower in the LES than PLIF. This indicates much smaller and more repeatable temperature fluctuations in the simulations compared to the measurement, and again supports the need for more LES cycles. This was evident in Figure 5.20 where the standard deviation of temperature is much smaller than the measurement at -100 CAD aTDCc. At -35 CAD aTDCc, the range of the PDF curves from LES becomes similar to those of PLIF, with smaller peak values in the simulations than in the measurement. At TDC, both the range and peak values become very similar.

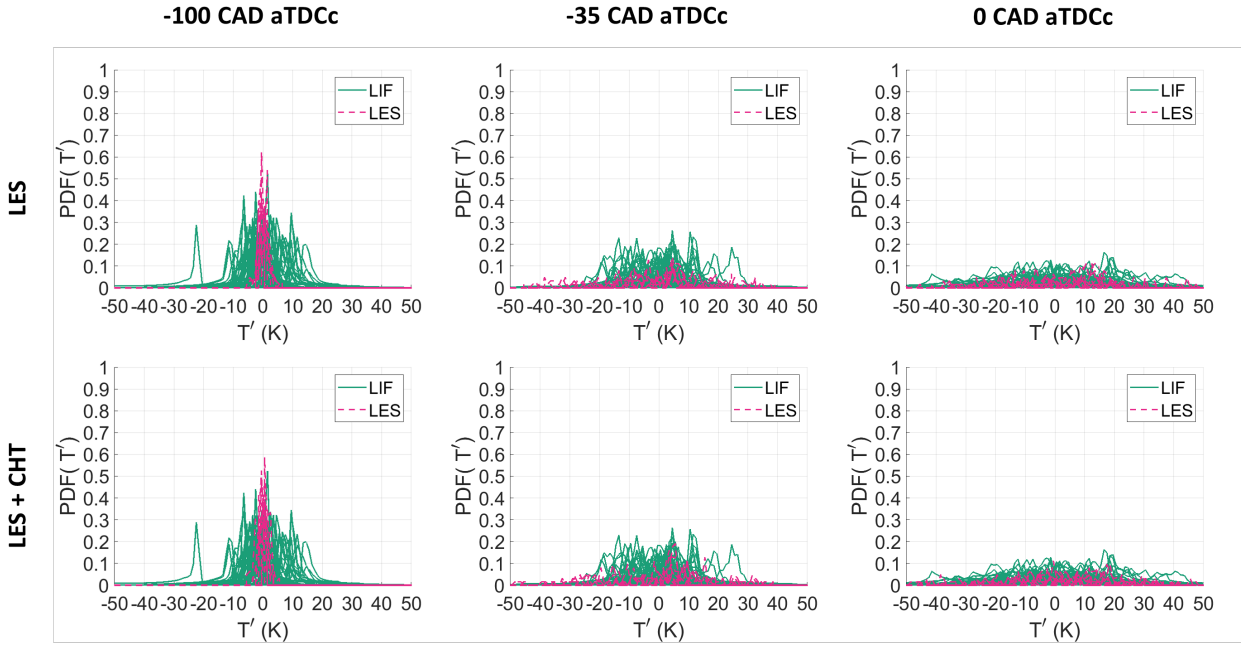

Figure 5.30. PDFs of fluctuating temperature fields from PLIF (73 cycles), uniform temperature LES, and LES CHT (10 cycles). Each curve represents an individual cycle.

5.8 Spatial Correlation Analysis

Spatial correlations provide additional insights into the structure of turbulence and heat transfer in engines, but they have not been investigated extensively in engine flows. Two-point velocity correlations can be integrated to provide an estimate of the longitudinal and transversal integral length scales. Their ratio indicates the level of anisotropy in the turbulent flow field, with a value of two in the ratio signifying an isotropic turbulent flow [106]. These length scales are important in engine heat transfer [146] and their distribution in the NWR could help improve the understanding of engine heat transfer and how it develops during the cycle, as smaller length scales coincide with larger thermal gradients and thus increased heat transfer.

Funk et al. [147] calculated the longitudinal integral length scales from two-point correlations under high and low swirl conditions. Compared with the low swirl case, smaller integral length scales are found in the high swirl flow, and their distribution is more inhomogeneous. In contrast, the low swirl case has a more homogeneously distributed field of the length scale since there is no organized flow redistributing the turbulent structures. Breuer et al. [148] argued that at least two integral length scales in two directions are needed to describe anisotropic flow adequately, such as those found in piston engines. They developed a model for the length scale and found that compression causes the length scale to change over time. Heim and Ghandhi [24] calculated two-point correlations and estimated longitudinal and transversal integral length scales, in the horizontal and vertical directions, for different engine speeds at TDC. They found that the length scales in these two directions are similar, indicating isotropy in the two directions. In addition, the longitudinal to transversal length scale ratio is close to two, further supporting their observation of an isotropic flow field. Two-point correlations of the near-wall flow were analyzed by Macdonald et al. [30]. The spatial correlation analysis allowed them to distinguish the near-wall flow from the bulk flow. However, length scales could not be estimated in this limited field of view since the spatial correlations did not cross the zero-line.

Temperature length scales have not been explored as extensively as turbulent length scales in engines. These temperature length scales directly affect the temperature gradients and engine heat transfer. Schmitt et al. [128] simulated an engine-like flow using DNS and showed that the temperature length scales decreased with compression, leading to smaller and hotter heat flux structures. Schmitt et al. [146] also calculated the temperature length scale distribution in the engine at TDC. They found that the length scale decreases towards the wall, i.e. the temperature gradients increased towards the wall, leading to increased heat transfer in the NWR.

Spatial correlations give an indication of the size of the turbulent structures over which the fluctuating quantities are strongly correlated with each other. The two-point, single-sided, spatial correlations of the fluctuating velocity fields were calculated using the method described in [30]:

$$R_{u_i u_i r} = \frac{\langle u_i'(r_o) u_i'(r_o + \Delta r) \rangle}{\sqrt{\langle u_i'^2(r_o) \rangle \langle u_i'^2(r_o + \Delta r) \rangle}} \tag{5.1}$$

Here, r_o is the correlation point, Δr is the correlation distance, u_i' is the fluctuating velocity component, and brackets denote ensemble averaging. The two-point spatial correlations in the x- and y-direction were calculated for all points in the field of view, for both velocity components to

obtain the longitudinal and transversal correlations. These correlations can be integrated to the zero-crossing line to provide an estimate for the integral length scales.

5.9 Velocity Fluctuation Spatial Correlations

The spatial correlations of the velocity fluctuations were computed for each direction x and z. Results are shown in Figure 5.31 for the x-direction at correlation point $x = x_o = 1.5\ mm$, and in Figure 5.32 for the z-direction at correlation point $z = z_o = -1$ mm.

The longitudinal correlation in the x-direction, $R_{uu,x}$, is shown in the top row of Figure 5.31. The bottom row shows the transversal correlation in the x-direction, $R_{ww,x}$. The line indicates the row-average of the correlation curves across all z. The shaded area indicates the spatial standard deviation in the z-direction, i.e. the stratification at $x_o = 1.5\ mm$ across all z. The fluctuation velocity in both simulations seem to be more strongly correlated than the PIV for both velocity components in the x-direction. The measurement's spatial correlation decreases for smaller correlation distance Δx than the simulations. This indicates a smaller length scale and larger velocity fluctuation gradient in the measurement than in the simulations. The measurement shows that the correlation curve of both velocity components initially is very strongly correlated for small correlation distance Δx, then drops significantly after increasing Δx, and then gradually flattens. This "reversed S-shaped" curve follows a stretched exponential decay function $f(r) = e^{-ar^b}$, but the measurement's correlation curves do not all asymptotically approach 0. This will prove to be a problem for estimating the measured integral length scales. The correlation curves of the simulations also follow a similar shape, but the initial drop happens at a larger Δx.

Differences can be seen between the correlation curves of the uniform temperature and the CHT simulations. At -100 CAD aTDCc, the longitudinal correlation curves are very similar, but the transversal correlation $R_{ww,x}$ is larger for the CHT than the uniform temperature model at the same correlation distance. This indicates that the CHT simulation has a larger transversal length scale at the correlation point $x_o = 1.5$ mm. The spatial standard deviation of $R_{uu,x}$ of the CHT simulation is larger than that of the uniform temperature model. On the other hand, the spatial standard deviation of $R_{ww,x}$ of the CHT simulation is smaller than that of the uniform temperature model.

With compression, differences in the longitudinal correlations increase. At -35 CAD aTDCc, the spatial average longitudinal correlation of the uniform temperature model is now larger

than that of the CHT model, especially with increased correlation distance, indicating larger longitudinal length scales in the uniform temperature model. In contrast, the transversal correlation of the CHT model is slightly larger for Δx from approximately 1 mm to 4 mm. The spatial standard deviation of the longitudinal correlation is larger for the CHT simulation, but that of the transversal correlation is larger for the uniform temperature model.

At TDC, the longitudinal correlation of the CHT model is larger than the uniform temperature model at the same correlation distance. The transversal correlation is larger for Δx up to approximately 3 mm for the CHT model. The spatial standard deviation of both correlation curves is smaller for the CHT model.

In general, the spatial standard deviation of the uniform temperature model's transversal correlation is larger than that of the CHT model. This indicates that there is more spatial stratification of the transversal integral length scale in the uniform temperature model at the correlation point $x_o = 1.5$ mm in the z-direction. On the other hand, the spatial standard deviation of the longitudinal correlation is comparable between both models at -100 CAD aTDCc, but with compression, the spatial standard deviation of the uniform model's longitudinal correlation seems to increase, while that of the CHT increases first from -100 to -35 CAD aTDCc, then decreases towards TDC. There is more spatial stratification in the longitudinal integral length scale of the uniform temperature model, especially with increasing compression, at the correlation point $x_o = 1.5$ mm in the z-direction. The CHT model has increased stratification from -100 to -35 CAD, and then the stratification reduces towards TDC.

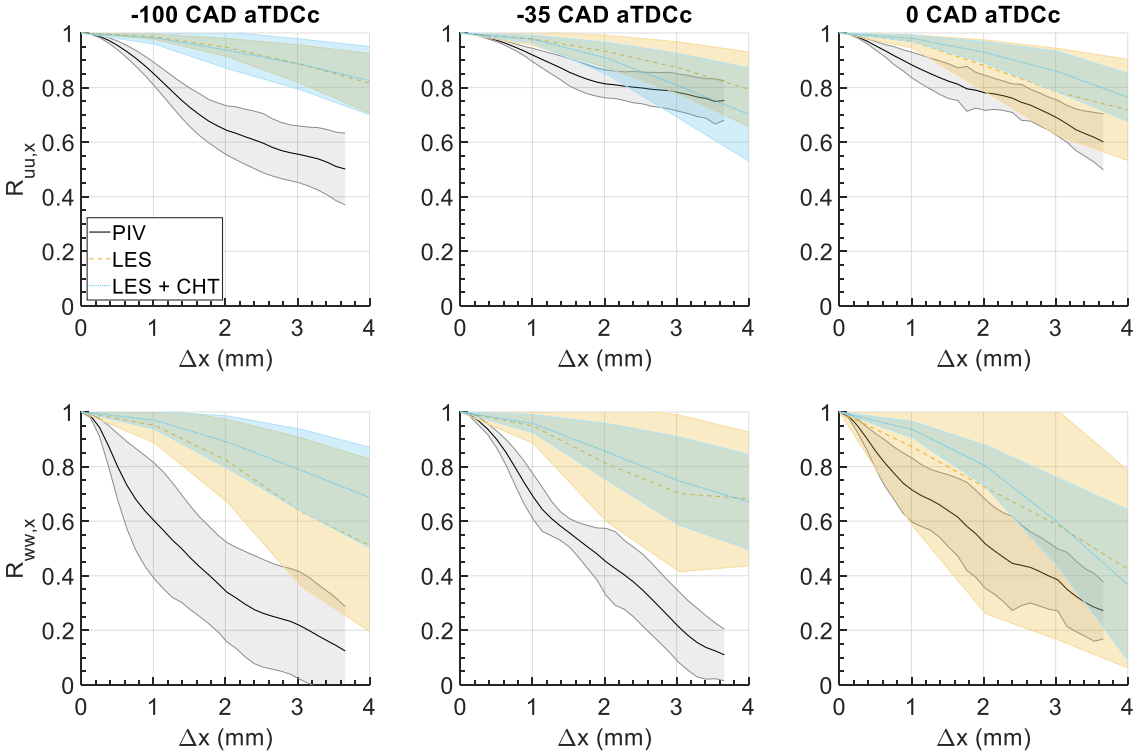

Figure 5.31. Spatial correlation of the velocity fluctuations u' and w' in the x-direction at $x = x_o = 1.5$ mm.

Correlation curves are shown in Figure 5.32 in the z-direction, with the transversal correlation in the top row, $R_{uu,z}$, and the longitudinal correlation, $R_{ww\,z}$, in the bottom row, at correlation point $z_o = -1$ mm.

The measured correlation curves follow the same "reversed S-shape" as those of Figure 5.31. For small correlation distances, the transversal correlations $R_{uu,z}$ match well between the simulations and measurement, but as correlation distance increases, the differences between simulations and measurement become larger. For example, at -35 CAD aTDCc, initially the curves match well for Δz below 0.5 mm, but the correlation of the measurement decreases Δz of 0.4 mm to 2 mm and gradually flattens out. In contrast, the correlation curves of both simulations show that the fluctuating velocity u' is strongly correlated until Δz of 1 mm, and then the correlation curves decrease towards 0 at larger Δz than the measurement. A similar observation can be made for the differences in the measured and simulated longitudinal correlations. Trend-wise, the correlation curves are similar between the simulations and the measurement. These correlation curves indicate that the experiments have smaller length scales and higher gradients of the velocity

fluctuations compared to the simulations. The effects of the core flow on the near-wall flow is evident from the flattening-out behavior of the measured correlation curves for larger correlation distances. This flattening-out happens as well for the simulations but at a larger correlation distance than that of the measurement.

While the simulated curves are similar to each other for small correlation distances, as the correlation distance increases, the differences become more evident. At -100 CAD aTDCc, the transversal correlation curve of the CHT simulation is a better match with the measured correlation curve than the uniform temperature model. The fluctuating velocity u' of the uniform temperature model is more strongly correlated at larger correlation distances than the CHT model. The same can be said of the longitudinal correlation curve at this crank angle degree location. The spatial standard deviation of both correlation curves of the CHT model is larger at this time as well.

At -35 CAD aTDCc, the uniform temperature model shows stronger correlations in the transversal and longitudinal components than the CHT model. The spatial standard deviation of the transversal correlation of the uniform temperature model increased, while that of the longitudinal correlation decreased. The spatial standard deviation of both correlation curves of the CHT model decreased.

At TDC, the uniform temperature model now shows weaker correlations in the transversal and longitudinal direction compared to the CHT model. The spatial standard deviation of both correlation curves of the CHT model decreased again. The spatial standard deviation of the transversal correlation curve of the uniform temperature model decreased, while that of the longitudinal correlation curve increased.

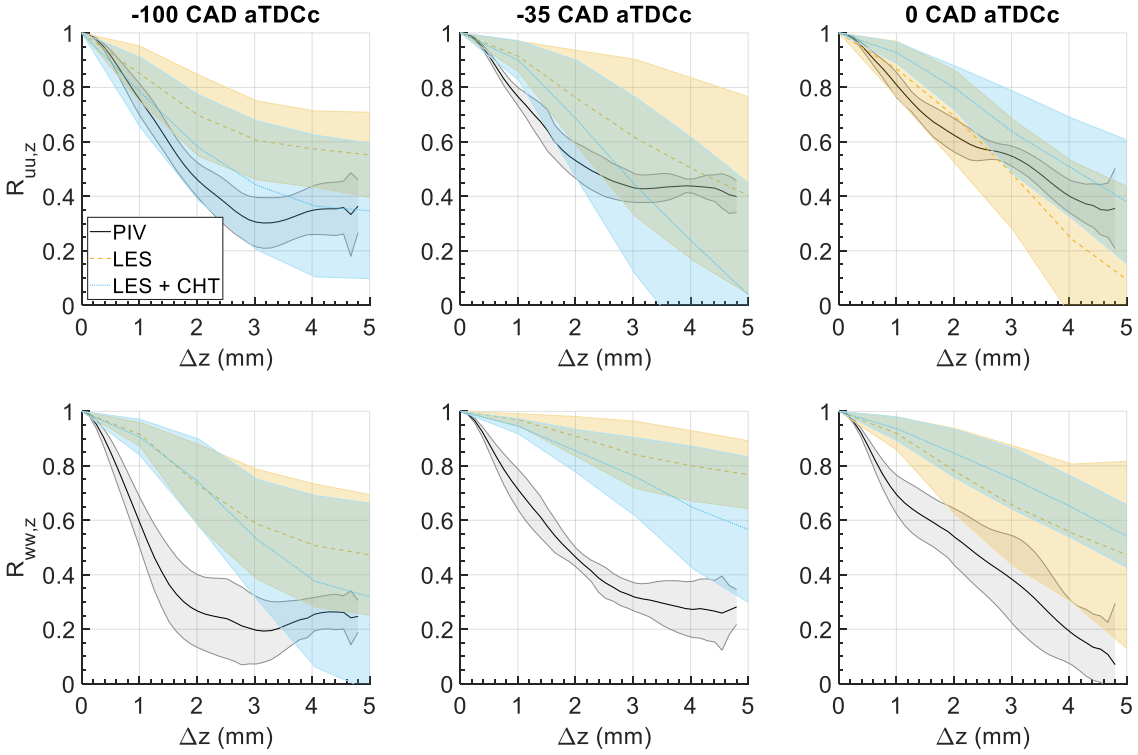

Figure 5.32. Spatial correlations of the velocity fluctuations u' and w' in the z-direction at $z = z_o$ = -1 mm.

5.10 Temperature Fluctuation Spatial Correlations

The spatial correlations of temperature fluctuations about the ensemble average are calculated using Equation 5.1, for both the x- and z-directions. The results are shown in Figure 5.33, with the top row being the correlations in the x-direction and the bottom row the correlations in the z-direction. Correlation curves are compared between the PLIF measurement and the simulations.

The curves follow the same "reversed S-shape" as those of the velocity fluctuations. In both directions, the spatial correlations of the measurement and simulations behave similarly. There is an initial drop in the spatial correlation from 1 for small correlation distances, then the temperature fluctuations stay strongly correlated as correlation distance increases as indicated by the flattening of the correlation curves. But, the measured temperature fluctuations are more strongly correlated than the simulations in both directions, and their spatial correlations do not cross the zero line in the measured FoV. The spatial correlations of both simulations asymptotically approach 0, sometimes within the FoV of the PLIF measurement. Compared to the measurements, smaller length scales are expected in the simulations at these correlation points. The PLIF field of

view is not large enough to capture the length scales, as the spatial correlation curves suggest length scales larger than 8 mm in the x-direction and 5.5 mm in the z-direction.

The correlations of the uniform temperature and the CHT models differ with increasing compression. This can be seen in the $R_{T,x}$ from -100 CAD to TDC. At -100 CAD aTDCc, the correlation curves are almost the same, but with increased compression, the correlation curve from CHT is larger at -35 CAD then smaller at TDC than the uniform temperature model. For the z-direction, the difference can be attributed to the correlation distance at which the correlation curves decrease. This correlation distance is smaller for the CHT simulation than the uniform temperature model. The spatial standard deviation of $R_{T,x}$ and $R_{T,z}$ decreased with compression for both models.

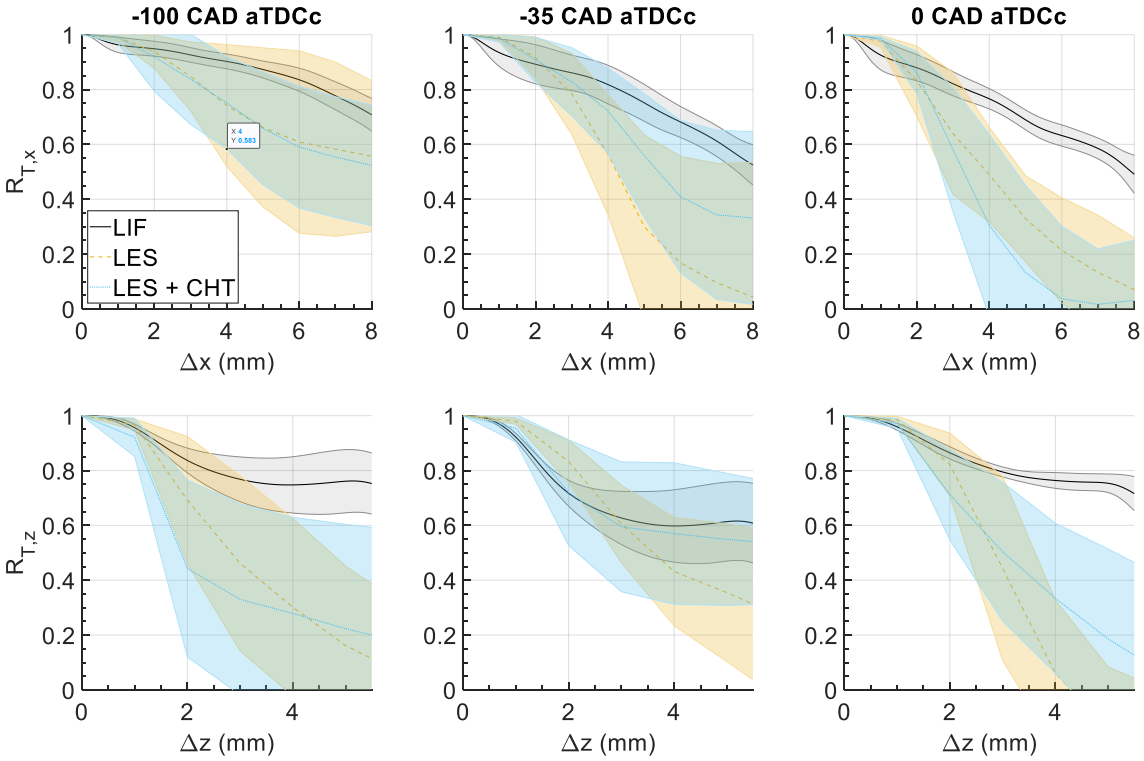

Figure 5.33. Spatial correlations of temperature fluctuations in the x-direction with correlation point $x = x_o$= 4 mm in the top row, and z-direction with correlation point $z = z_o = -0.5$ mm in the bottom row.

5.11 Integral Length Scales Using Fluctuating Values

The spatial correlations from LES were used to obtain the integral length scales since the correlations from the measurements did not cross the zero-line due to the small field of view, whereas the LES contains data points outside this FoV. The spatial correlations from LES were

calculated at each point in the field of view, with correlation distances Δx and Δz extending outside the field of view. In this manner, most of the spatial correlation curves in the simulation will approach or cross 0 without the need to extrapolate the data points.

Due to noise and sparse data points in the simulation, the spatial correlation curves were fit with a stretched exponential decay function with a nonlinear least square method:

$$f(r) = e^{-ar^b} \tag{5.2}$$

The problem using the stretched exponential fit function to curve fit the spatial correlations is that the spatial correlations oscillate with increasing correlation distances and do not all asymptotically approach zero. This can affect the curve fit especially when the oscillations are not about zero. When this oscillation occurs away from zero, the fit function performs poorly. The fit function seems to perform well when the correlation data either crosses the zero line, when no oscillation occurs, or when the oscillation is about zero. Such oscillations are also found in other engine flow measurements [140, 149]. Examples of good and bad fit of the fit function is shown in Figure 5.34.

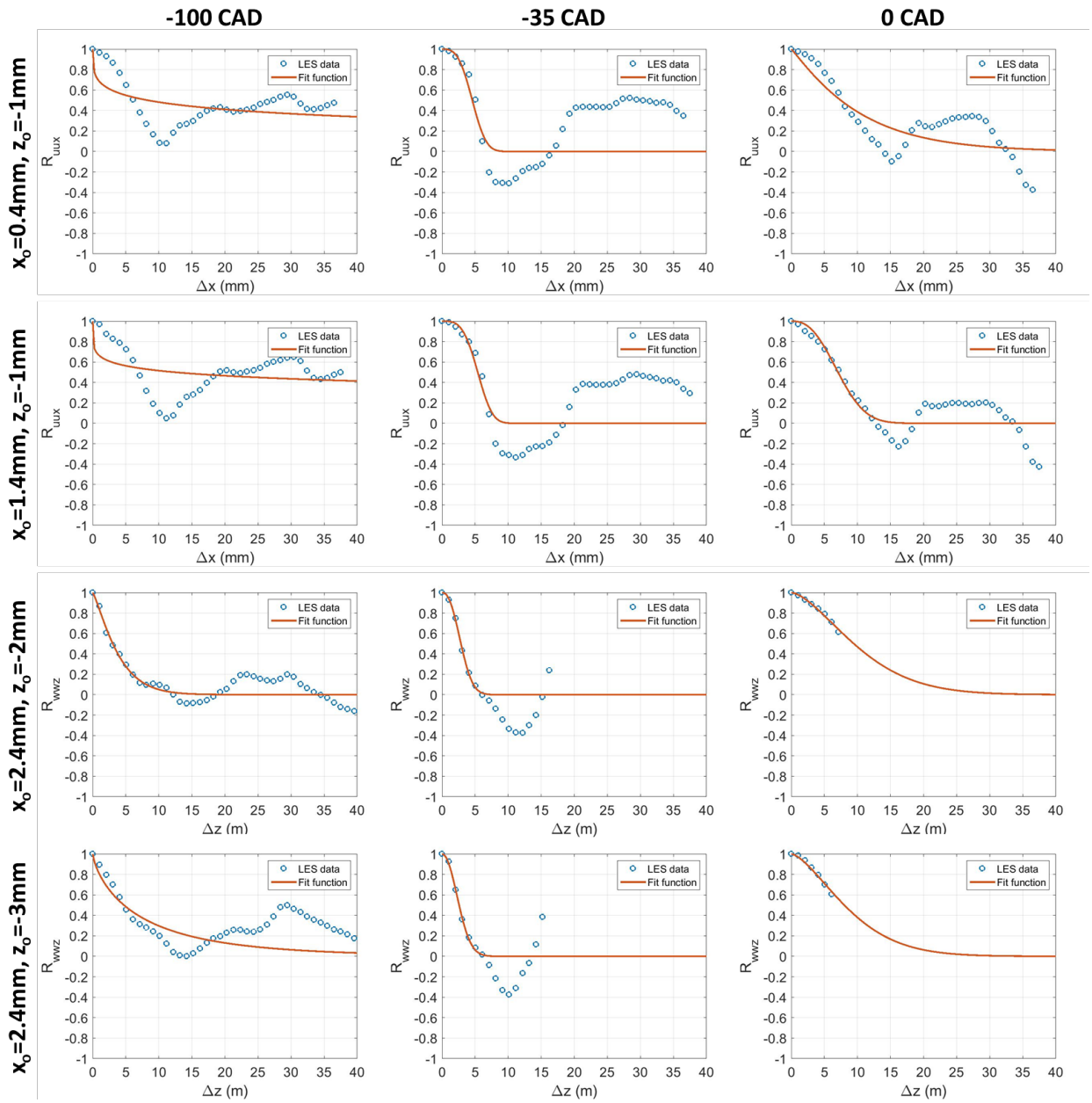

Figure 5.34. Spatial correlation curves at different correlation points are fitted with a stretched exponential decay function.

Knowing the limitations of the stretched exponential fit function, the curve fit was integrated to obtain the integral length scales:

$$L = \int_0^\infty f(r)dr \tag{5.3}$$

The trapezoidal method was used for numerical integration of the fit function. Despite poor fit at some correlation points, all length scale data is shown. Length scales larger than 20 mm should be

ignored as the correlations for such large length scales do not reach 0.2 within a correlation distance of 40 mm.

Since heat transfer is mainly influenced by the wall-normal components [73], the integral length scale analysis is performed only in the z-direction. Results are shown in Figure 5.35 for the integral length scales from the simulated wall-normal velocity fluctuations. Comparisons are made between the length scales from the uniform temperature and the CHT simulations. Length scales larger than 20 mm should be ignored due to curve fit issues.

At -100 CAD aTDCc, the spatial distribution of the length scales are very similar between the two simulations. Larger length scales can be seen in the upper left corner in the CHT model. The length scales decrease towards the wall in both simulations. At -35 CAD aTDCc, larger length scales are found away from the wall in both simulations, with decreasing length scales towards the wall. At TDC, the length scale distribution of the CHT simulation is more stratified than at -35 CAD aTDCc, with larger values in the near-wall region and the bulk region.

These results show that the spatial velocity length scales do not become more uniformly distributed with increased compression and that the length scales do not decrease monotonically with compression in this near-wall region. However, this decrease in length scale is expected as compression causes smaller length scales due to geometrical changes of the combustion chamber. The curve fit might affect the length scale calculations, especially with increased compression since fewer data points are available in the z-direction for the curve fit to work well.

Spatial variation in the length scale can be explained by effects from the cylinder head surface and the boundary layer development due to its proximity to the flow in this near-wall region. Changes in flow structures such as tumble breakdown in the bulk flow could also lead to smaller flow structures, which then interacts with the near-wall flow. Finally, flow property changes such as density can lead to changes in the length scales as well.

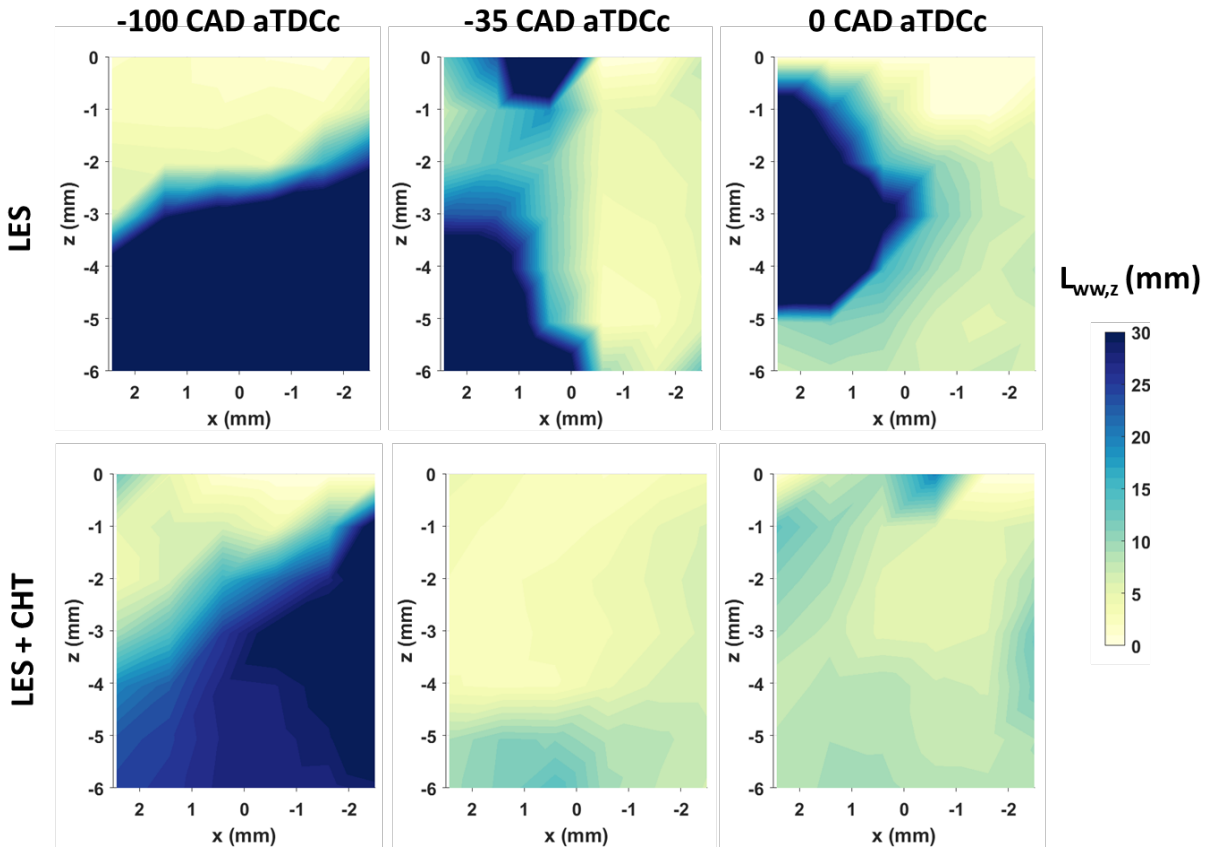

Figure 5.35. Velocity longitudinal integral length scales in the z-direction from Cases 4 and 6.

The temperature length scales are shown in Figure 5.36 in the z-directions in the PLIF field of view using LES results. Length scales larger than 20 mm should be ignored. At -100 CAD aTDCc, the uniform temperature model shows decreasing length scales towards the wall. The CHT simulation shows larger length scales in the near-wall region when compared to the uniform temperature model. At -35 CAD aTDCc, the uniform temperature model shows a more uniform distribution of the temperature length scale, while that of the CHT is more stratified. At TDC, the distribution of the length scales in the uniform temperature model is stratified again, while the CHT simulation distribution becomes more homogeneous.

The temperature and velocity length scales do not seem to be well correlated with each other. Large velocity length scales do not necessarily coincide with large temperature length scales. Schmitt et al. [146] performed an engine DNS study and found that the temperature length scales were larger than the turbulent kinetic energy length scales, which are related to the velocity length scales, due to thermal diffusion. This trend was not found in this analysis. However, it should be noted that the DNS study of [146] was performed in an engine-like geometry at 560 RPM for only one cycle, and the analysis was based on fluctuations about the spatial mean instead of the ensemble average.

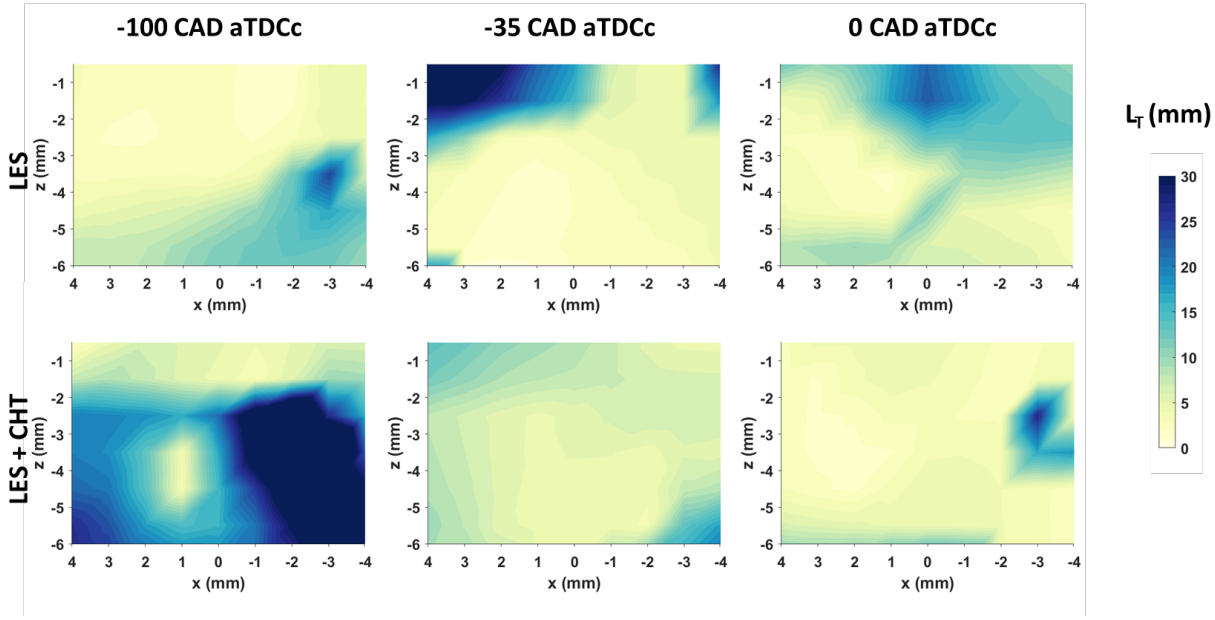

Figure 5.36. Temperature length scales in the z-directions for Cases 4 and 6.

5.12 Spatial Correlations Using Relative Values

Fluctuation values in engine research are typically obtained about the ensemble average values, but it is the instantaneous spatial gradients that drive heat transfer. Therefore, the relative velocity and temperature values were obtained about their spatial means within the imaging field of view. Then, the spatial correlations were obtained from the relative values. The correlation is performed in the z-direction for the relative wall-normal velocity and relative temperature.

Results of the velocity spatial correlations are shown in Figure 5.37 at correlation point z_o= -1 mm. The solid and dashed lines indicate column-average across the x-direction, while the shaded area indicates the spatial standard deviation in the x-direction. The figure shows that the simulations are more strongly correlated than the PIV relative velocities at this correlation point. The standard deviations of the simulations are also larger than the measurement. This means that the simulated relative velocity gradient is more spatially stratified than the measurement in the wall-parallel direction, especially at larger correlation distances i.e. in the bulk flow region. The spatial correlations of the measurement experience a substantial decrease over a shorter distance than those of the simulations, which indicates larger relative velocity gradients in the measurements than the simulations. From -100 CAD aTDCc to TDC, the relative velocity correlation becomes stronger in the simulations, while in the measurement the spatial correlation stays mostly the same.

Differences can be seen between the correlation curves for the two simulations. Noticeable is that the correlation of the relative wall-normal velocity is less strong for the CHT simulation at -100 CAD aTDCc than the uniform temperature model. But with increased compression, this correlation becomes stronger for the CHT simulation. This indicates that the integral length scale in the wall-normal direction becomes larger with increased compression for the CHT simulation at this correlation point. This integral length scale is smaller in the uniform temperature model at the same crank angle degree location. Spatial standard deviation is also larger for the uniform temperature model at TDC compared to the CHT simulation, meaning that there is more spatial stratification in the integral length scale in the uniform temperature model at TDC across all x values.

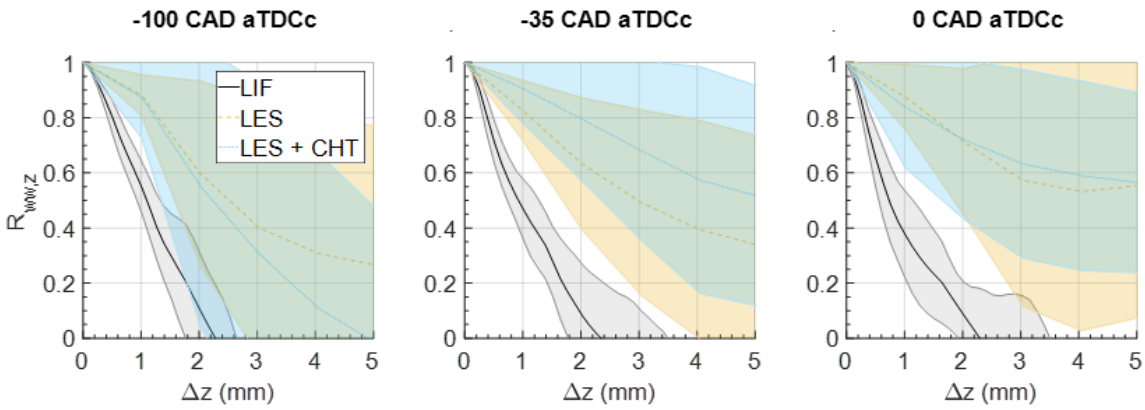

Figure 5.37. PIV and LES CHT relative velocity longitudinal spatial correlations.

The spatial correlations of the relative temperatures in the wall-normal direction at a correlation point z_o= -0.5 mm are shown in Figure 5.38. Results indicate that the CHT simulation can capture the behavior of the PLIF measurement at -100 CAD aTDCc, while the uniform temperature model overestimates the strength of the temperature correlation. At later crank angle degree locations, the strength of the correlations of both simulations increases. At -35 CAD aTDCc, the relative temperature of the CHT simulation is more strongly correlated than the measurement and the uniform temperature model. At TDC, both simulations have similar correlations, especially at small correlation distances. The standard deviation of the spatial correlation of both simulations, however, are much larger than the measurement at all CAD locations shown. This indicates that the relative temperature gradient varies significantly in the x-direction.

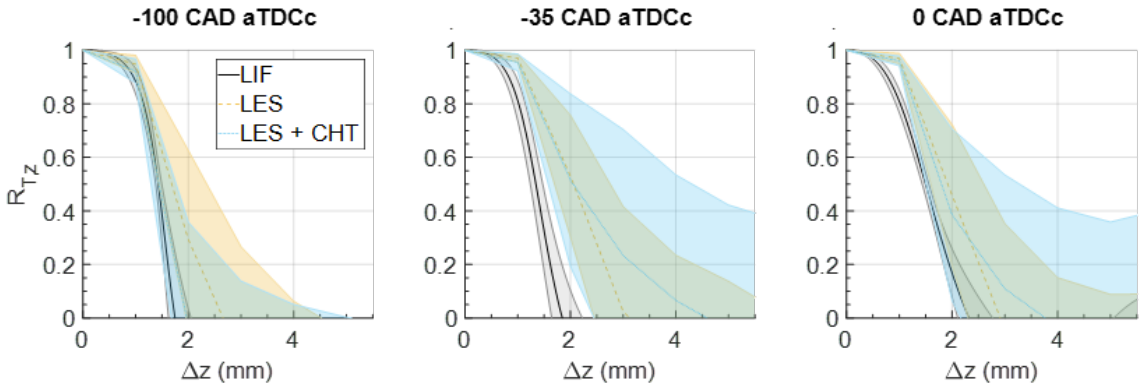

Figure 5.38. LIF and LES CHT relative temperature spatial correlations.

5.13 Integral Length Scales Using Relative Values

Integral length scales were calculated from the spatial correlations. The spatial correlations were curve-fit with the stretched exponential decay function from Equation 5.2. Correlations using the relative values decrease to zero within the FoV for the measurement, so the integral length scales are also obtained for the measurement. Examples of the curve fit at different correlation points are shown for the PIV dataset in Figure 5.39. Since the measurement data is limited to within the FoV window, the integral length scales are estimated up to a wall distance of z = -4 mm. Values beyond a wall distance of -4 mm are not shown since the number of statistically independent points are too low for estimation of the integral length scale.

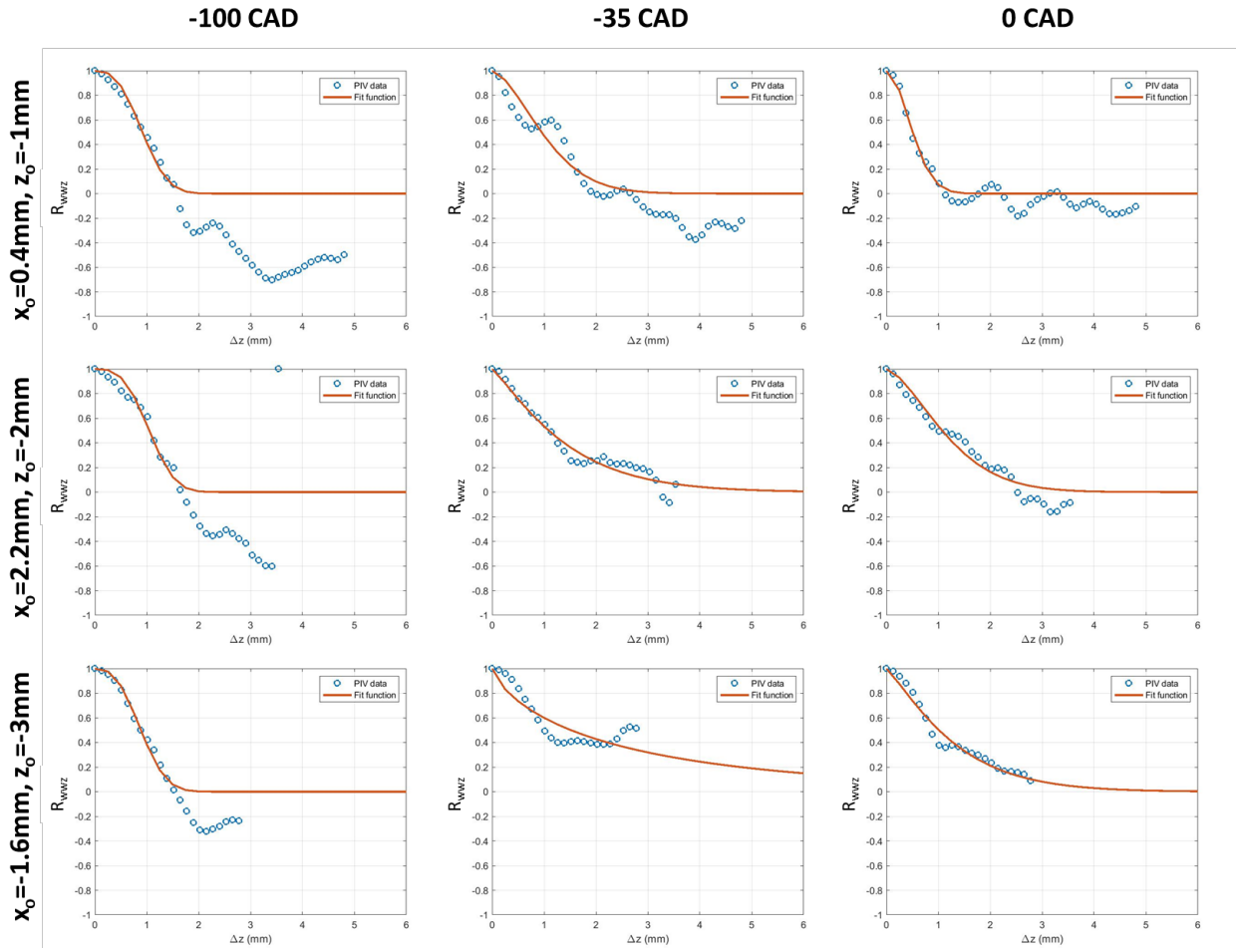

Figure 5.39. Spatial correlation curves from PIV dataset 2016_03_13_08 fitted with a stretched exponential decay function.

The velocity integral length scales in the wall-normal direction are shown in Figure 5.40. Results indicate that the length scales in the PIV are on the same order of magnitude as the simulations, but the simulations do have areas of larger length scales than the measurements. These

large length scales could be an artifact from the curve fit, especially length scales larger than 20 mm.

Larger length scales coincide with smaller velocity gradients. This shows that far away from the wall, the simulations predict a smaller velocity gradient than the experiment. This discrepancy could be due to many factors, including the use of the wall model, which is implemented in the first cell at the fluid-solid interface and provides boundary conditions for the rest of the computational domain. The mesh is also likely not fine enough to resolve the velocity gradient in the near-wall region. This can result in velocity gradients that do not match experiments. For example, at -100 CAD aTDCc, the length scales near $z = -4$ mm in the CHT simulation are larger than the PIV. While the uniform temperature model shows a similar trend, the very large length scales were most likely due to bad curve fitting. If length scales larger than 10 mm are ignored, the length scale distributions of both simulations become more homogeneous in two dimensions at -35 CAD and TDC.

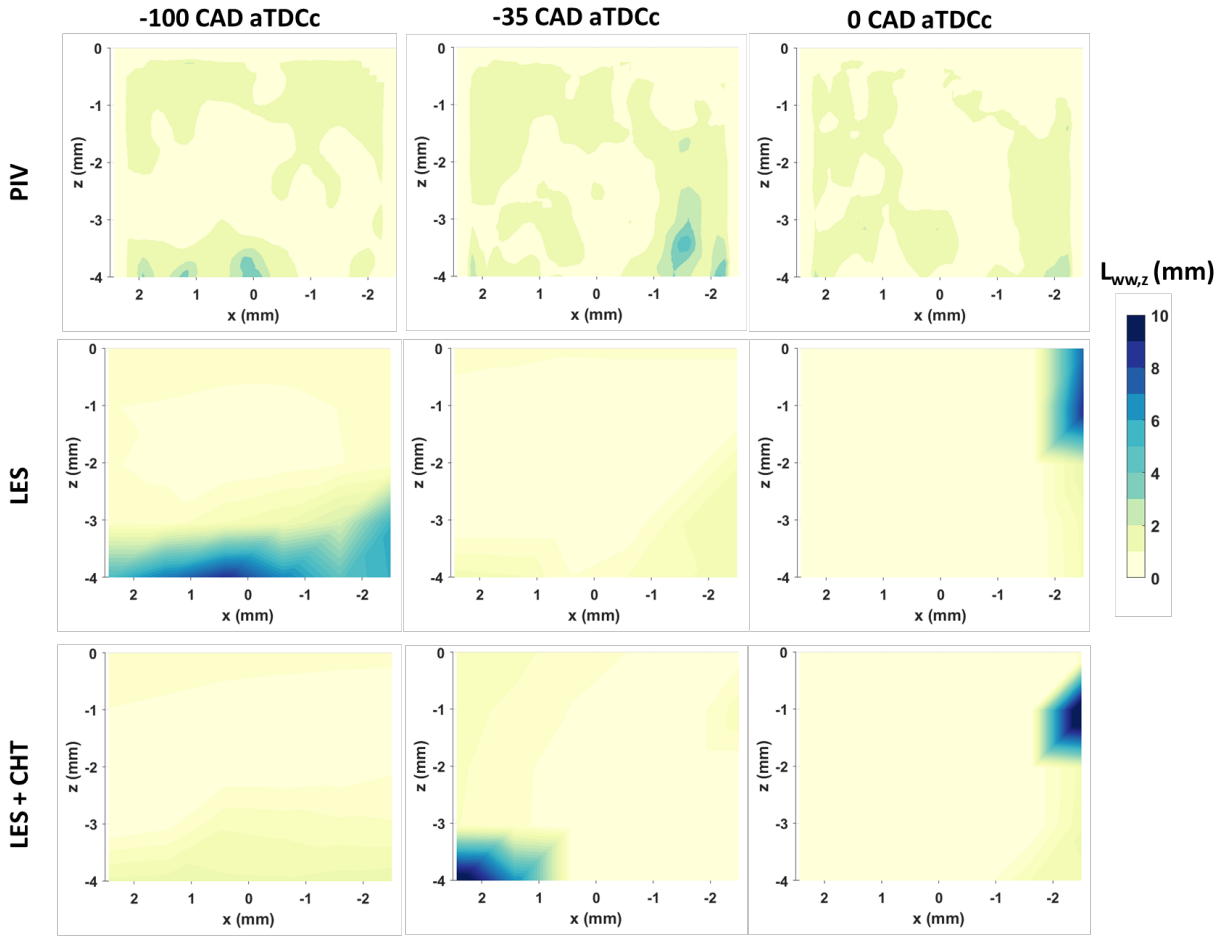

Figure 5.40. Integral longitudinal velocity length scales in z-direction.

The temperature length scales in the wall-normal (z) direction are shown in Figure 5.41. Results indicate that the temperature length scales decrease towards the wall in both simulations and the measurement. Smaller length scales result from larger temperature gradients, and therefore, heat transfer is increasing towards the wall due to increasing temperature gradients. With compression, the distribution of temperature length scales become more homogeneous, indicating that the heat transfer becomes more spatially uniform towards TDC. This behavior is observed in the simulations as well, with a more homogeneous distribution in the CHT model that better matches with the experimental observations.

From the simulation images, the distribution of the temperature length scale is very similar to the velocity length scale distribution. Areas of large temperature length scales coincide with that of the velocity length scales. The temperature length scales are larger than the velocity length scales in both the simulation and measurement. This was also observed in a DNS study, that showed that a larger temperature length scale at TDC than the turbulent kinetic energy length scale was attributed to thermal diffusion [146].

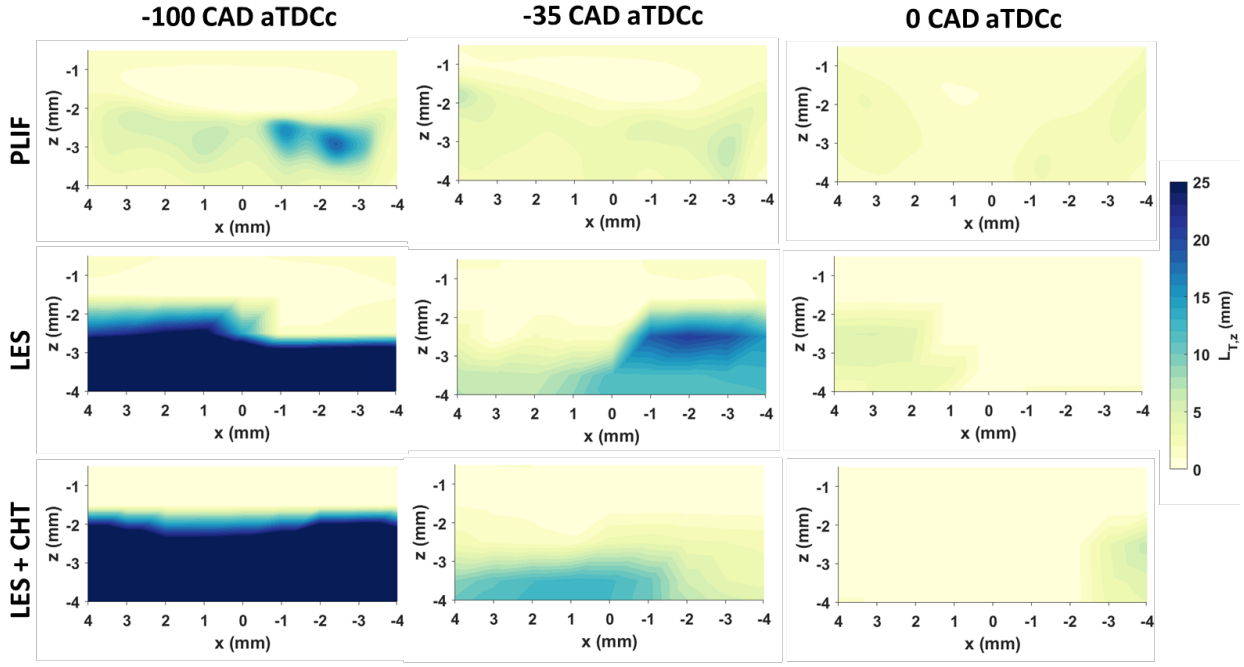

Figure 5.41. Integral temperature length scales in z-direction.

5.14 Summary

In this chapter, the conjugate heat transfer method was integrated with LES for a motored operating condition, and compared to a baseline uniform temperature LES. The CHT model predicted the surface temperature at the heat flux probe, located on the cylinder head surface,

within 5 K or 1.3% error. The CHT model is able to predict a larger CCV in the surface heat flux which is closer to the measured level of CCV compared to the uniform temperature model, as the CHT model predicts spatial, temporal, and cyclic variations in the surface temperature. There are still issues in the intake jet simulation, but the CHT model predicts a kinetic energy content that is closer to the measured values. Compared to the uniform temperature models, the LES CHT predicts a higher surface temperature and a spatial average temperature that is closer to that of the near-wall PLIF measurement. However, the mesh resolution is too large to resolve the small structures found in the measurement.

Spatial correlation analysis was performed using fluctuation values about the ensemble average and relative values about the spatial average. The spatial correlations of the measured fluctuations do not approach zero in the field of view and prevents a length scale analysis. In contrast, the spatial correlations of the measured relative values do approach or cross the zero line, allowing for length scale analysis of the relative velocity and relative temperature fields. This aids in heat transfer characterization, as heat transfer is driven by spatial gradients. It is shown that the distribution of velocity and temperature length scales are similar and that temperature length scales are larger than velocity length scales due to thermal diffusion. In addition, the temperature length scales are shown to decrease towards the wall. This indicates that temperature gradients increase towards the wall leading to increased heat transfer. The length scale distribution becomes more uniform with increased compression, indicating that heat transfer becomes more spatially uniform.

Chapter 6 Fired Conjugate Heat Transfer Results

In this section, CHT is applied to the fired operating condition of the TCC-III engine. The engine is operated at 1300 RPM, with a stoichiometric propane/air ratio, 40 kPa and 98 kPa intake and exhaust MAP, with spark timing set at -18 CAD aTDCc. Two simulations are compared: Cases 7 and 9. Case 7 is the LES that uses uniform temperature boundary conditions as shown in Figure 3.14 and was simulated using CONVERGE 2.4. Case 9 is the LES with CHT simulated in CONVERGE 3.0. Both simulations use the Werner and Wengle wall model and the refined near-wall mesh. Results show differences in the predicted combustion process, through analysis of the velocity, temperature, and heat transfer, revealing the impact of the surface temperature on combustion behavior. 11 cycles were simulated for both simulations, and the first cycle discarded to remove initial condition bias. The simulation results were compared to PIV datasets S_2013_11_07_03 and S_2016_03_25_09, and the fired PLIF temperature measurement.

The in-cylinder pressures are compared first in Figure 6.1, and histograms of the peak pressures are shown in Figure 6.2. The peak pressure of the uniform temperature model is closer to the measured peak pressure due to lower wall heat transfer. In contrast, the CHT underpredicts the peak in-cylinder pressure by about 130 kPa of -8% due to higher wall heat transfer. The b_1 values of the uniform temperature model and CHT model are 5.5 and 8, respectively. This b_1 value is used in the turbulent flame speed calculations, and increasing b_1 results in larger peak pressures. Different b_1 values were used since each model was simulated with a different Converge version. Using a b_1 of 5.5 in the CHT case would lead to more severe underprediction of the peak pressure. Increasing b_1 to 16 in the CHT leads to an overprediction of the peak in-cylinder pressure of about 150 kPa or about 9%. A parametric study of b_1 with multi-cycle fired LES is therefore still needed to improve the in-cylinder pressure predictions. The shaded areas represent one standard deviation about the ensemble average and indicate CCV. Both simulations underpredict the measured level of CCV and indicate that more cycles need to be simulated to capture the pressure envelope of the experiment.

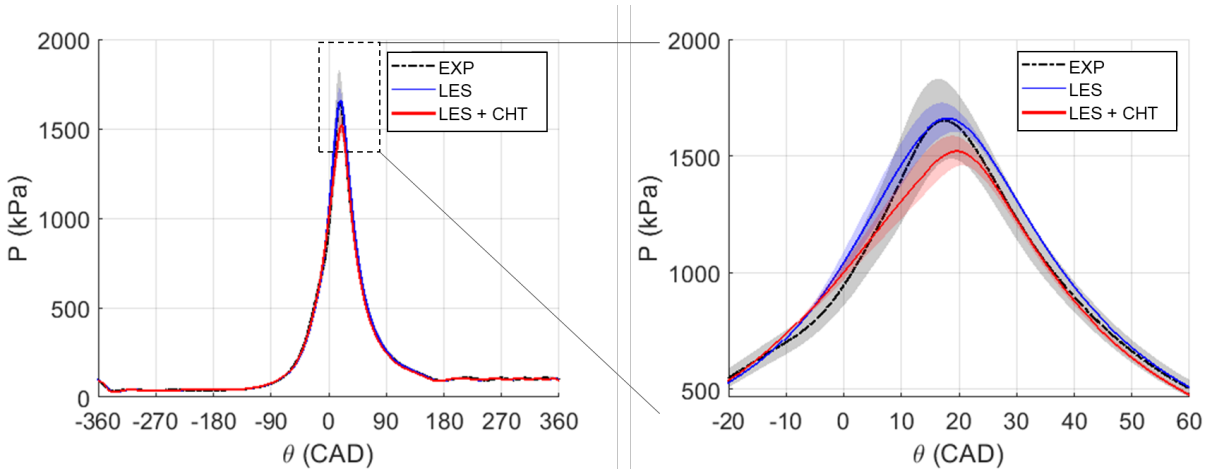

Figure 6.1. The dynamics of the in-cylinder pressure of Cases 7 and 9 compared against experimental data from S_2016_03_25_09. Simulation Case 9 (LES CHT) underpredicts the peak in-cylinder pressure by 8%, while simulation Case 7 (uniform temperature LES) compares well with the measured pressure.

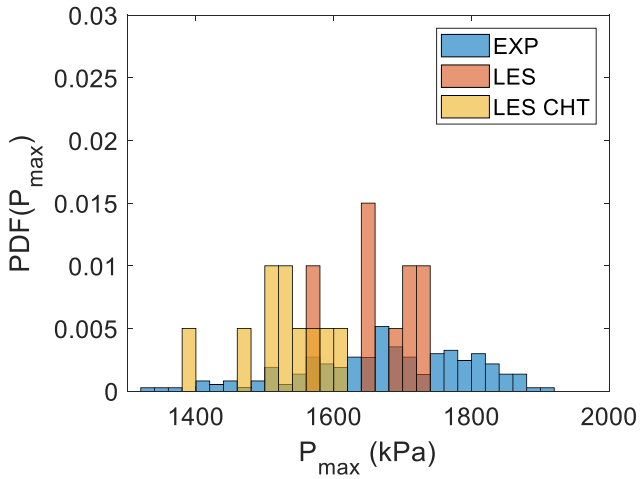

Figure 6.2. Histogram of fired peak in-cylinder pressures from experimental data (S_2016_03_25_09), uniform temperature LES, and LES CHT cases.

6.1 Bulk Velocity and Temperature Fields

The ensemble average bulk flow fields are compared next for -260 CAD, -100 CAD, -35 CAD, and -20 CAD aTDCc. These crank angle degree locations were selected as they were common amongst all velocity and temperature datasets.

The ensemble averaged bulk flow fields are shown in Figure 6.3 at -260 CAD aTDCc. Again, improvements are needed in the simulation of the intake jet, as its kinetic energy is overpredicted by both models. However, the intake jet of the CHT model has a smaller kinetic energy in the lower regions. The influence of the intake jet on the formation of vortices can be

seen. For example, because the intake jet is weaker in the CHT simulation than in the uniform temperature model, the entrainment of the flow on the right side leads to a more complex vortex structure in the CHT model than those found in the measurement or the uniform temperature model. This causes low RI values on the right side of the intake jet of the CHT model. Both models fail to predict the locations of the vortex centers accurately, leading to low RI values and high KEI values in the vortex regions.

With increased compression, the vortices introduced by the intake jet combine, and a large-scale tumble vortex is formed. Figure 6.4 shows that at -100 CAD aTDCc, the simulated velocity fields compare well with the measurement except for the low RI regions on the left side of the plane. This is due to a mismatch in the tumble vortex center. The predicted vortex centers also lead to overpredicted kinetic energy in the low RI regions.

Figure 6.5 shows the velocity field at -35 CAD aTDCc. The RI and KEI fields show very similar velocity fields, but the kinetic energy in the uniform temperature model matches that of the PIV better than the CHT model with KEI values close to 1. Left of the spark plug gap, the uniform temperature model overestimates the kinetic energy, which will later impact the combustion event. In contrast, the CHT model underpredicts the kinetic energy in the same region.

Figure 6.6 shows the velocity field at -20 CAD aTDCc right before the spark event at -18 CAD aTDCc. While the flow direction is well captured, the kinetic energy near the spark plug is now overestimated by more than a factor of 4 in the uniform temperature model, on the left side of the spark plug gap. The CHT model also predicts more the kinetic energy in this region than non-CHT, but it is to a smaller extent.

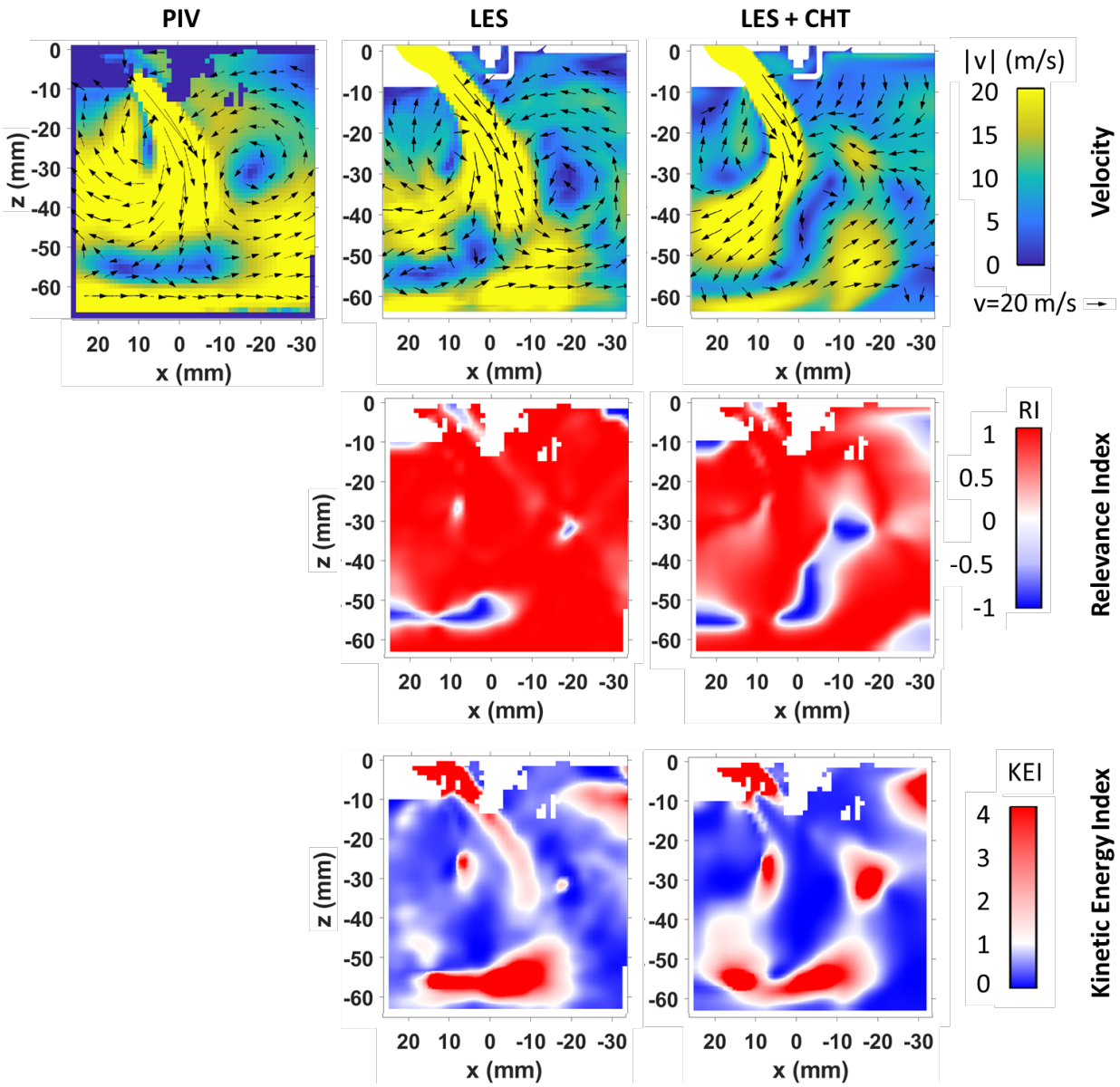

Figure 6.3. Average bulk flow field y=0 mm plane, at -260 CAD aTDCc compared to dataset S_2013_11_07_03.

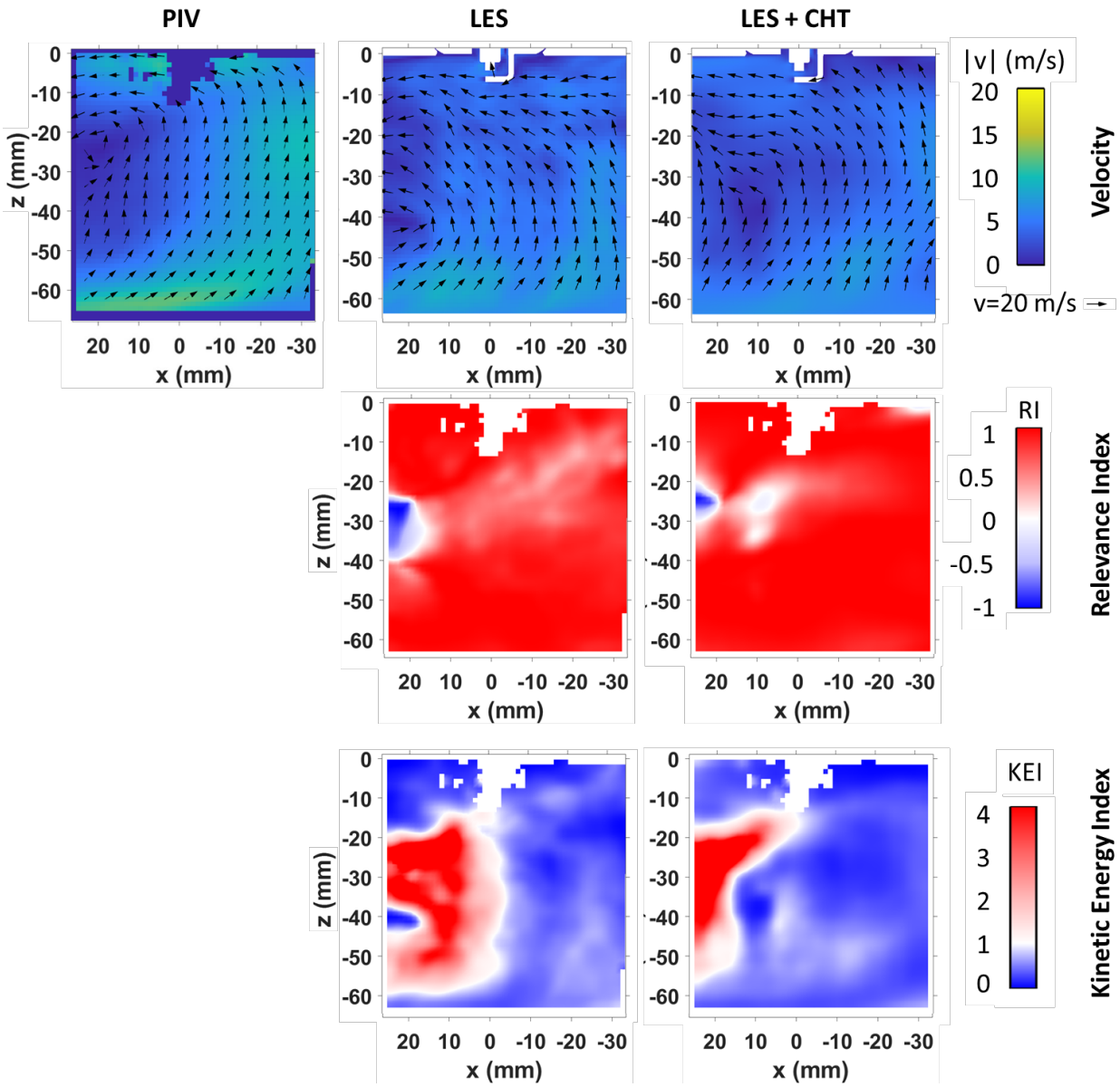

Figure 6.4. Average bulk flow field y=0 mm plane, at -100 CAD aTDCc compared to dataset S_2013_11_07_03.

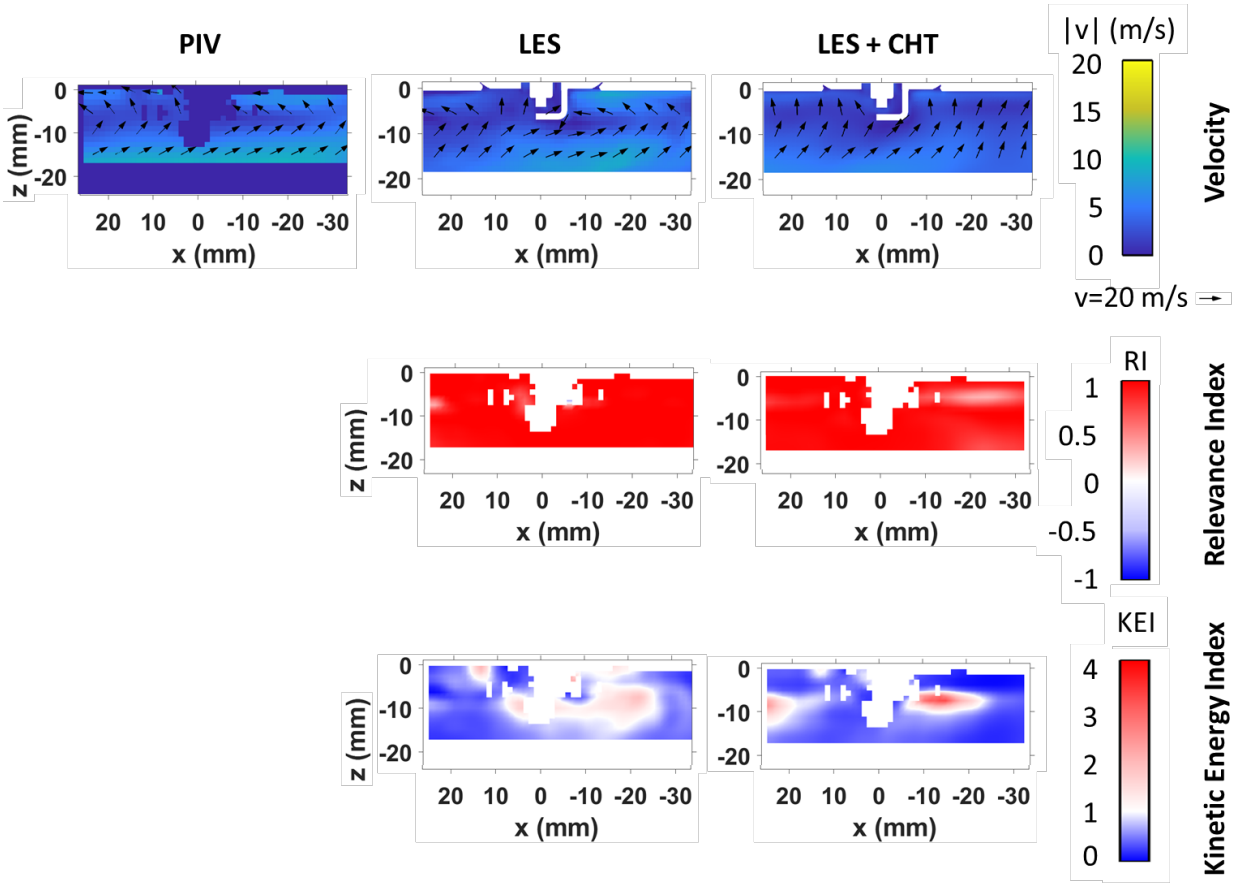

Figure 6.5. Average bulk flow field y=0 mm plane, at -35 CAD aTDCc compared to dataset S_2013_11_07_03.

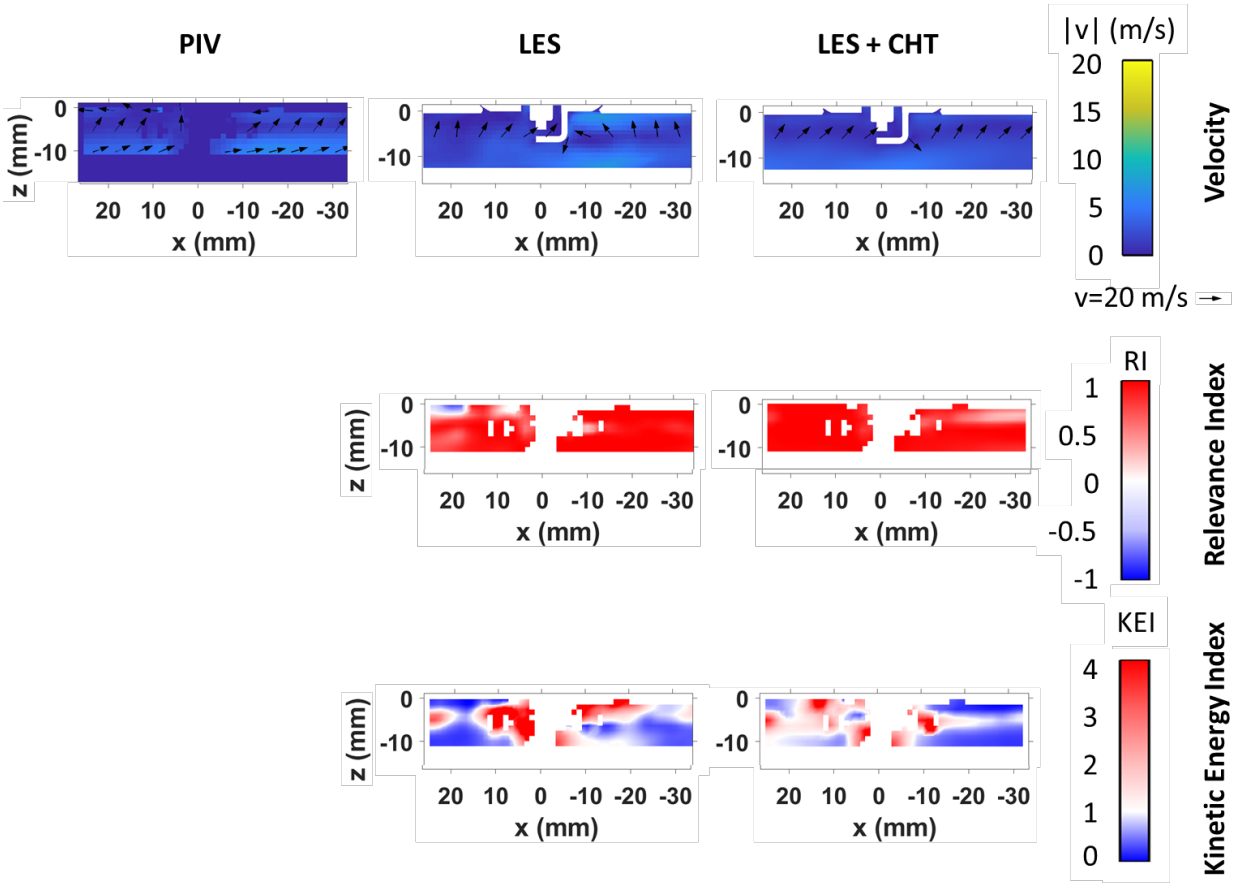

Figure 6.6. Average bulk flow field y=0 mm plane, at -20 CAD aTDCc compared to dataset S_2013_11_07_03.

Bulk temperature fields are shown in Figures 6.7 to 6.9 from -260 CAD to TDC. From the motored results, we have seen that the thermal boundary condition does affect the bulk temperature predictions and the level of thermal stratification, therefore, it is important to apply accurate thermal boundary conditions, which can be done using CHT. In Figure 6.7, the CHT results predict that the gases surrounding the spark plug's ground strap are much hotter than the gases around the core electrode. In contrast, in the uniform temperature model, a uniform surface temperature of 900 K was applied to the entire surface of the spark plug. This leads to more uniformly heated gases surrounding the spark plug. The surface temperature of the piston is also not spatially uniform in the CHT model, as will be shown in Section 6.3, leading to the surrounding gases around the piston to be heated more asymmetrically. As the intake jet enters the combustion chamber, the cooler air mixes with the hotter gases remaining inside the combustion chamber. At -100 CAD aTDCc, this results in a hotter mixture in the CHT model.

Figure 6.8 shows the progression of the bulk temperature field from -30 to -10 CAD aTDCc. At -30 CAD, the fuel-air mixture of the CHT model is overall hotter than that of the uniform temperature model. In contrast, the gases surrounding the spark plug is at a higher temperature than those of the CHT model. As the gases are further compressed, the bulk temperature increases. At -20 CAD aTDCc, the temperature field of the CHT is more stratified and at a higher temperature overall compared to the uniform temperature model. At -15 CAD, the flame kernel can be seen by the hot gases surrounded by the red contour of the flame front, which was plotted using the isosurface $G = 0$. This variable tracks the flame front. As can be seen, the flame structure is larger in the CHT simulation compared to the uniform temperature model, likely due to lower heat transfer from the flame to the spark plug or faster combustion rate in the CHT model. At -10 CAD aTDCc, the flame areas are similar between the uniform temperature model and the LES CHT, but the burnt gas temperature of the CHT case is more uniform and higher than that of the uniform temperature model. This is also seen at -5 and 0 CAD aTDCc in Figure 6.9. This will impact the heat transfer between the flame front and the engine surfaces as the flame increases in size and starts to interact with these surfaces. Note that the b_1 value of each simulation was different which will impact the turbulent flame speed model. This could explain the faster combustion rate in the CHT model, as it uses a larger b_1 value.

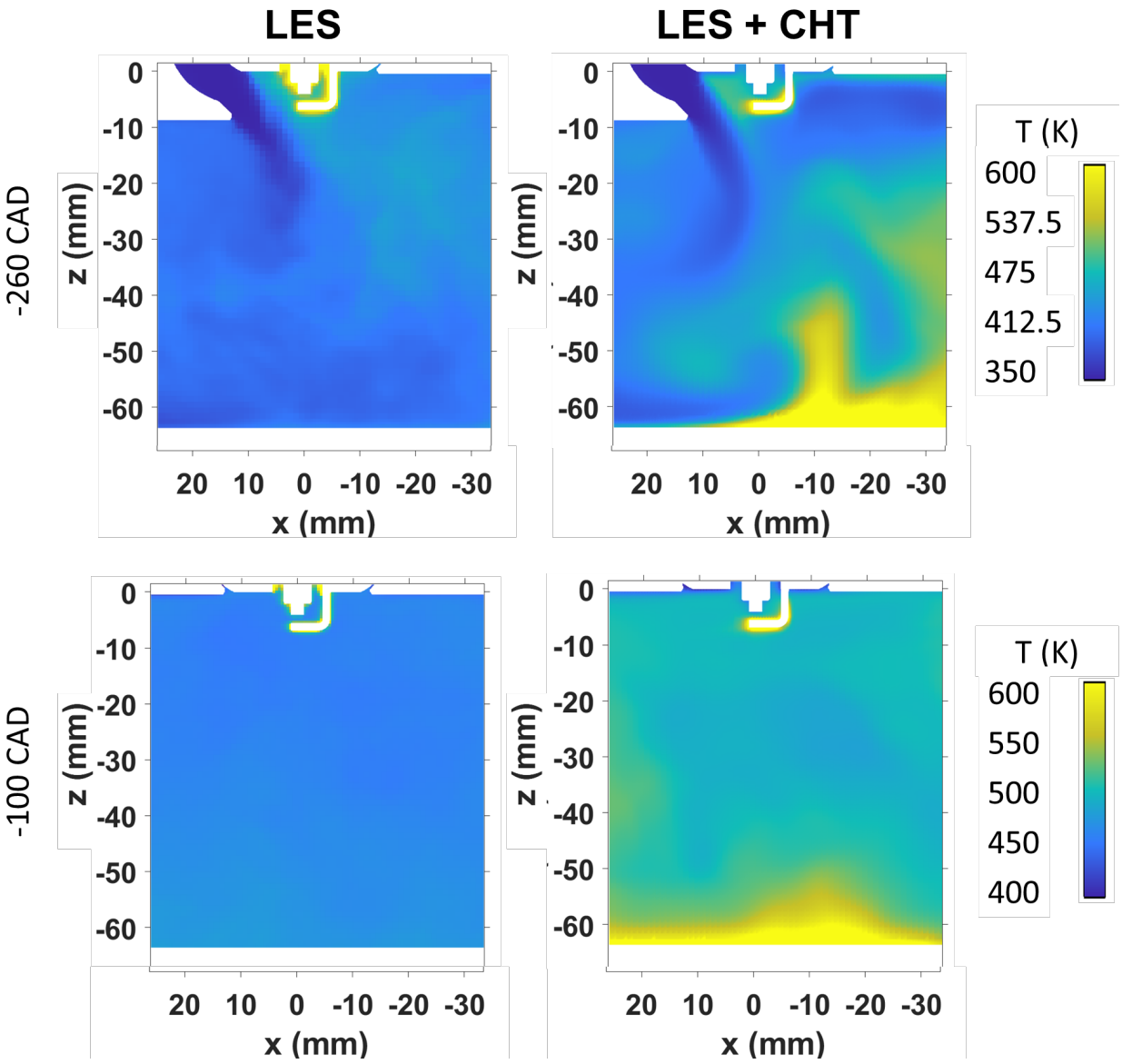

Figure 6.7. Average temperature fields at y=0 mm plane from -260 and -100 CAD aTDCc.

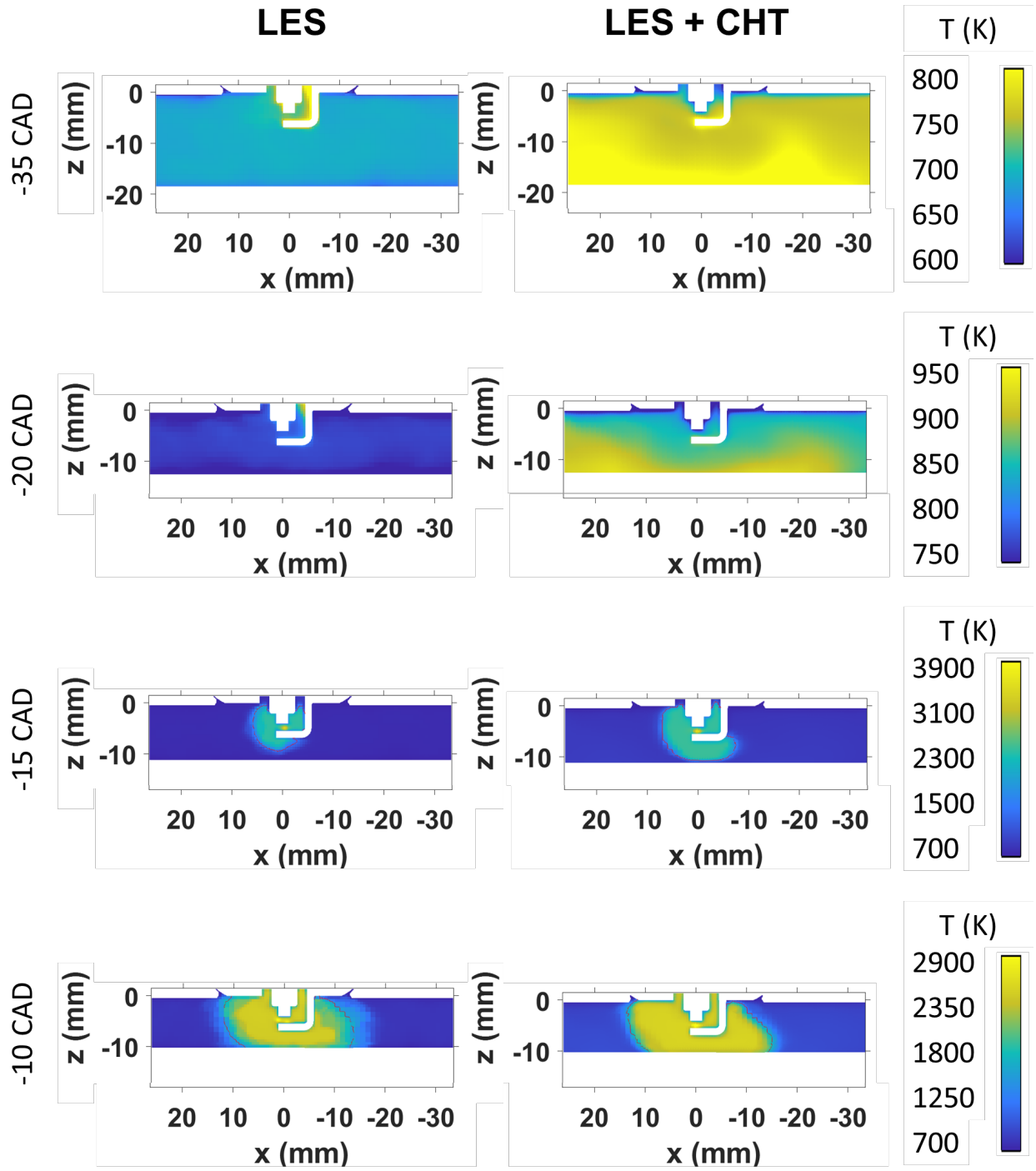

Figure 6.8. Average temperature fields at y=0 mm plane from -35 to -10 CAD aTDCc. The flame front is outlined at -15 and -10 CAD in red using isosurface G=0.

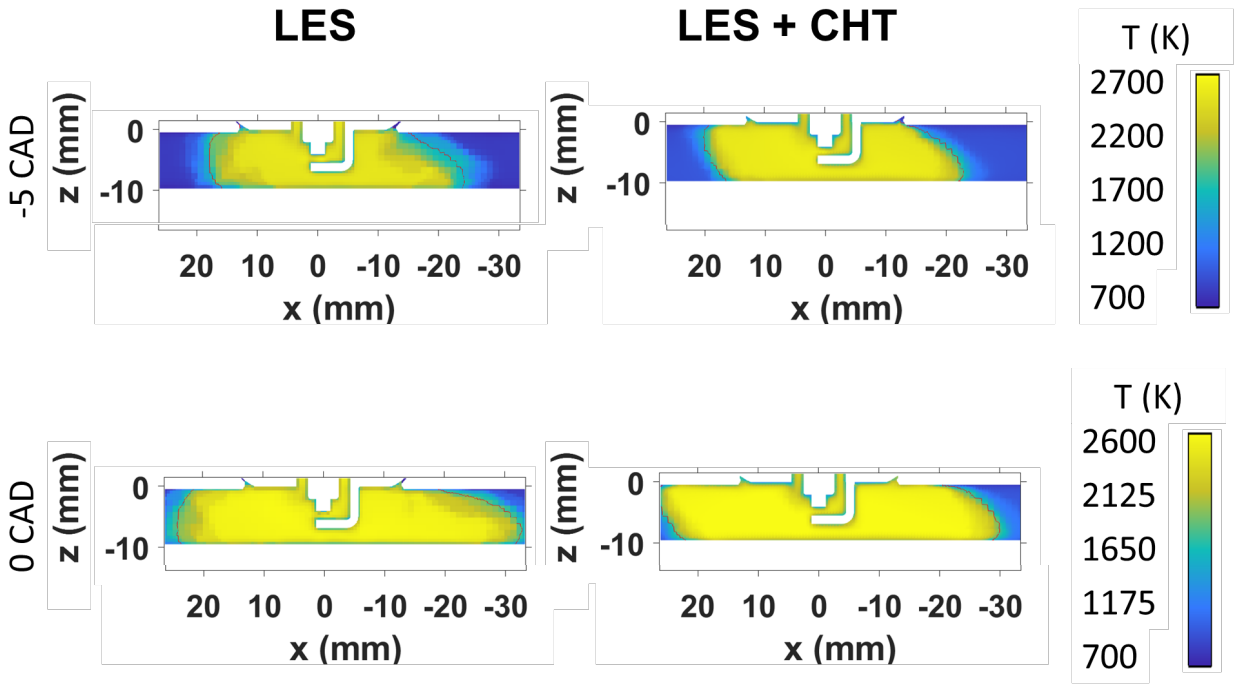

Figure 6.9. Average temperature fields at y=0 mm plane from -5 CAD aTDCc to TDC. The flame front is outlined at -5 CAD aTDCc and TDC in red using isosurface G=0.

6.2 Near-Wall Velocity and Temperature Fields

The near-wall velocity fields are shown in Figures 6.10 to 6.13 from -260 CAD to -20 CAD aTDCc. Again, these results indicate that there are improvements needed in the wall model as it causes inaccurate predictions in the velocity direction and magnitudes in the near-wall region.

Figure 6.10 shows that at -260 CAD aTDCc, the CHT model predicts most of the flow direction correctly, whereas the uniform temperature model predicts a flow that is directly orthogonal to the measured flow in most of the field of view. On the other hand, the velocity magnitude of the CHT model is much larger than the PIV measurement, while the velocity magnitude of the uniform temperature is higher on the left side of the field of view, and lower on the right side.

Figure 6.11 shows that at -100 CAD aTDCc, the CHT simulation is able to predict the flow direction accurately, but velocity magnitude is underpredicted as shown by the low KEI values. In contrast, the flow direction of the uniform temperature model is opposite that of the PIV measurement in the near-wall region, while the velocity magnitude is higher in this region compared to the CHT simulation.

At -35 CAD aTDCc, Figure 6.12 shows that the CHT model predicts the flow direction accurately while the flow in the uniform temperature model is still opposite that of the measurement. On the other hand, the velocity magnitude is underestimated by both models.

Figure 6.13 shows the near-wall flow field at -20 CAD aTDCc. The velocity field in the CHT model is opposite the measured flow in most of the field of view, whereas the velocity magnitude is closer to that of the measurement. The uniform temperature model predicts the velocity direction better in the bulk region of the field of view, but the velocity magnitude is overestimated.

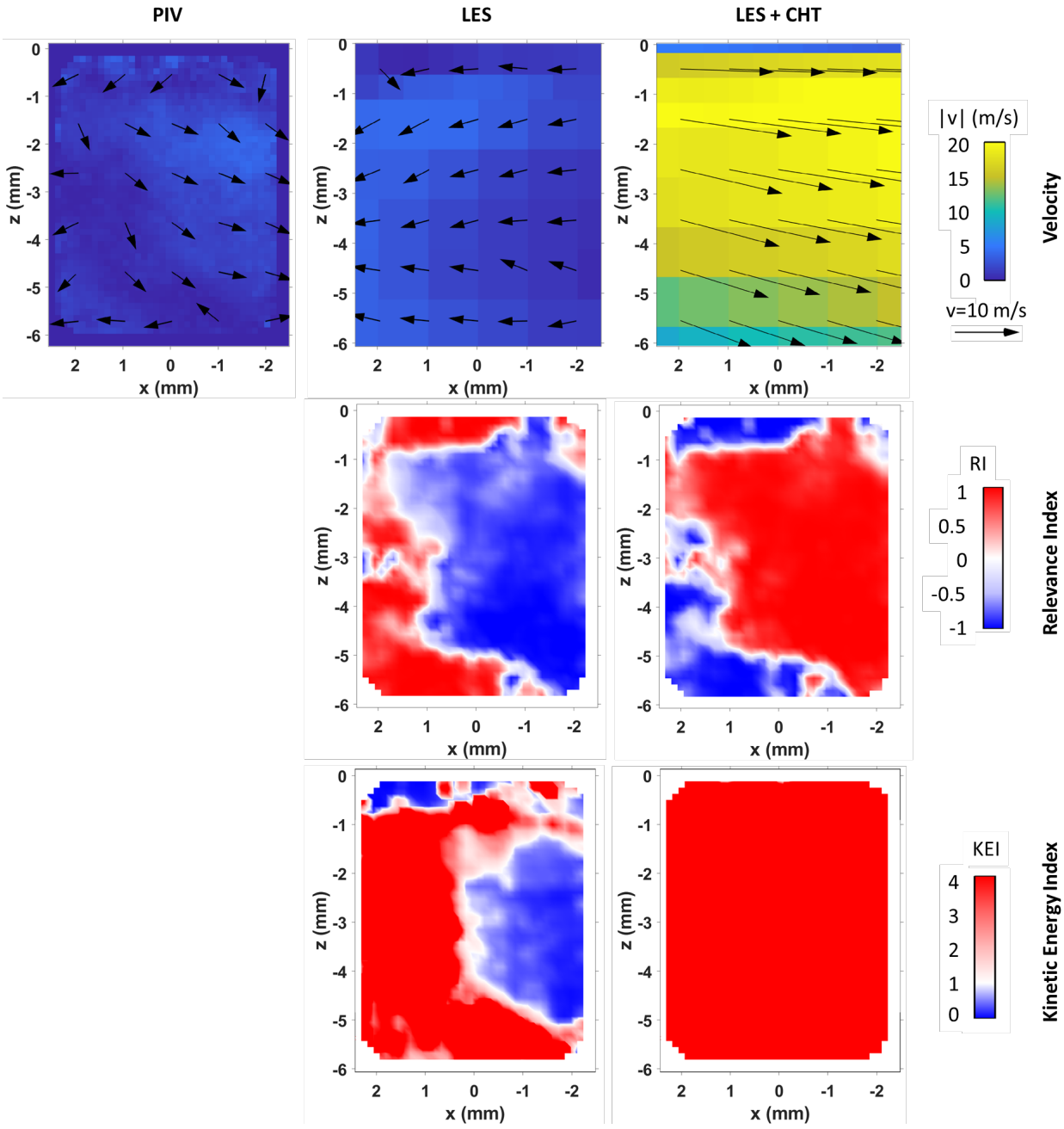

Figure 6.10. Average near-wall flow field, at -260 CAD aTDCc compared to dataset S_2016_03_25_09.

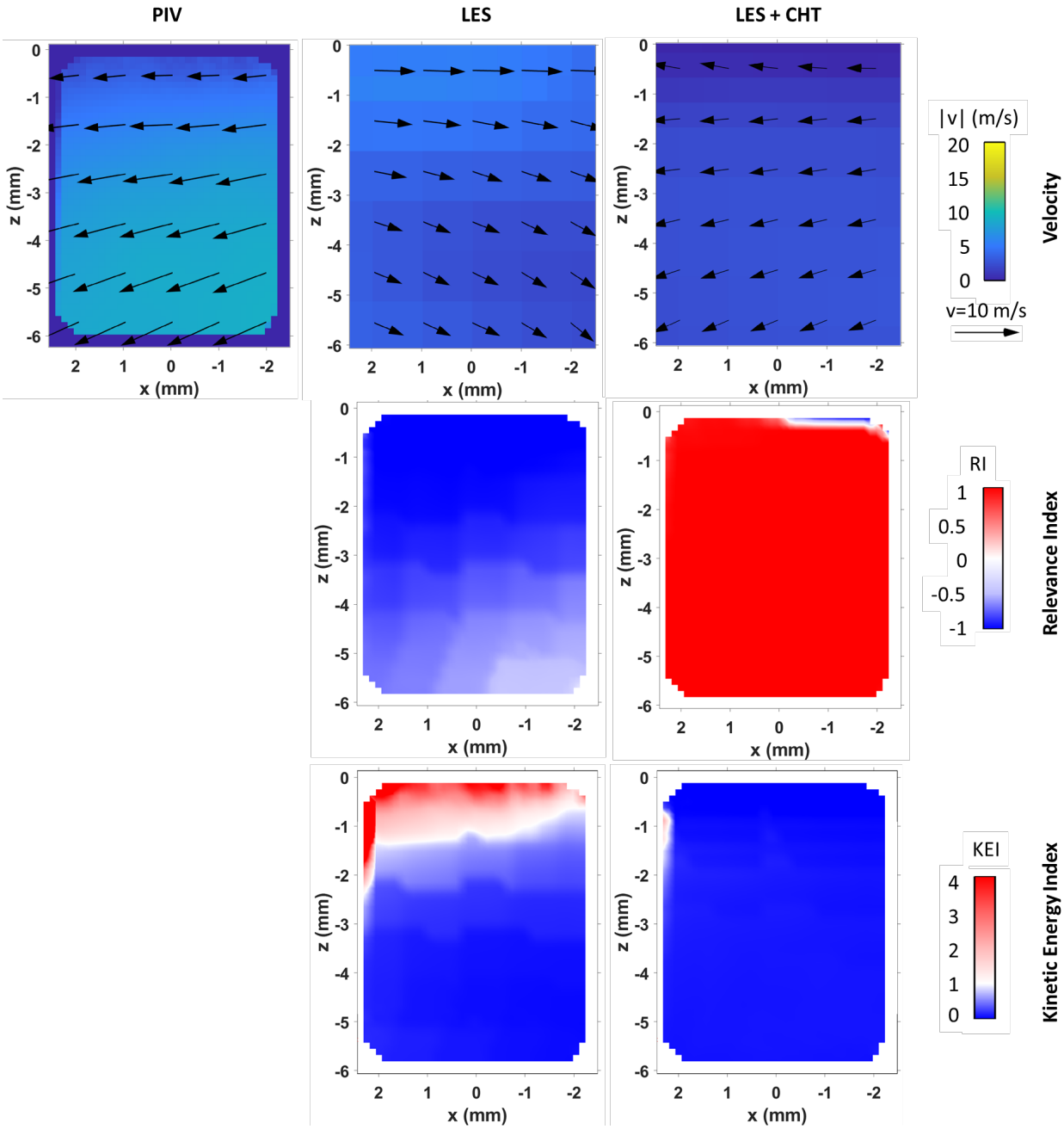

Figure 6.11. Average near-wall flow field, at -100 CAD aTDCc compared to dataset S_2016_03_25_09.

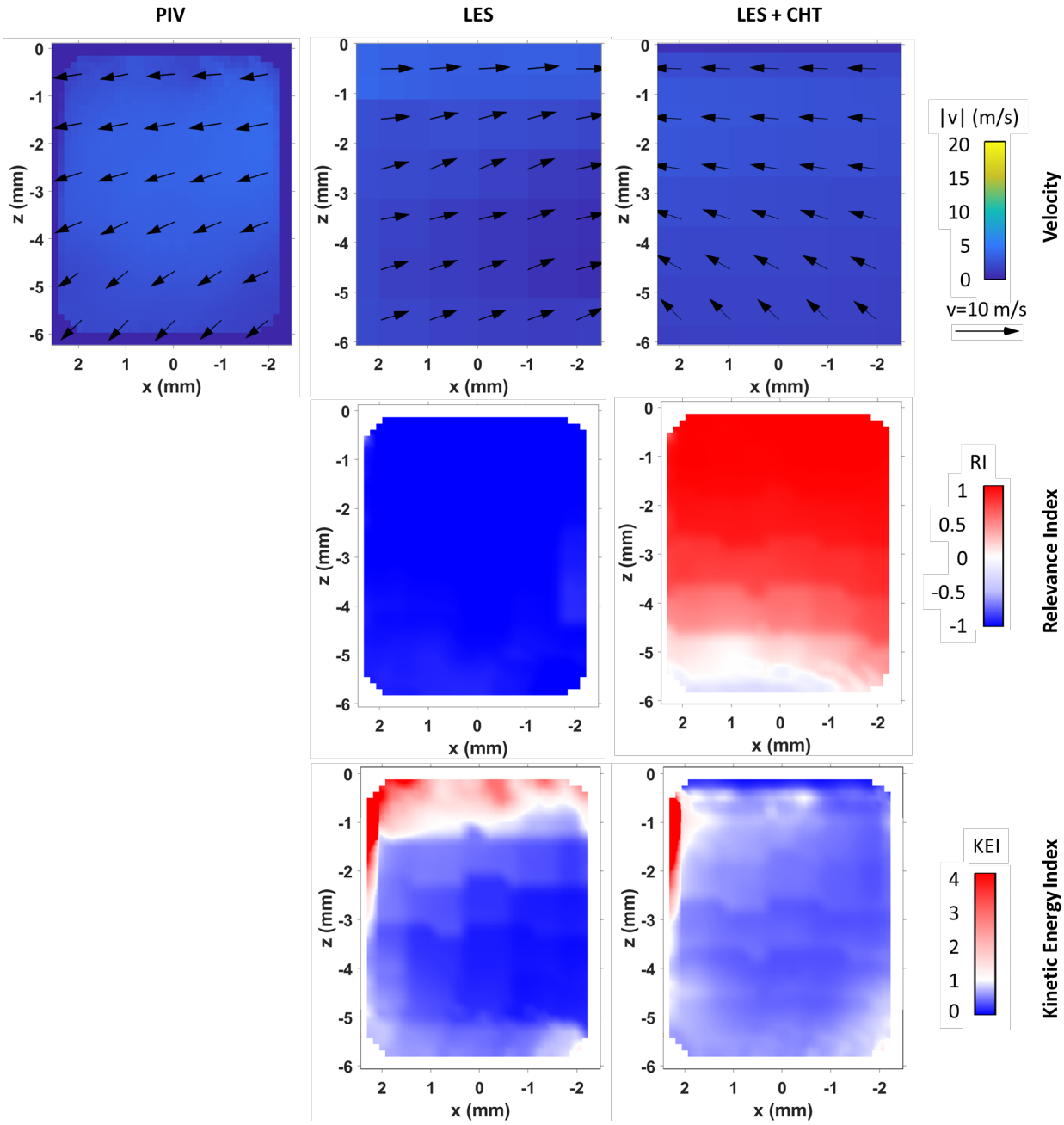

Figure 6.12. Average near-wall flow field, at -35 CAD aTDCc compared to dataset S_2016_03_25_09.

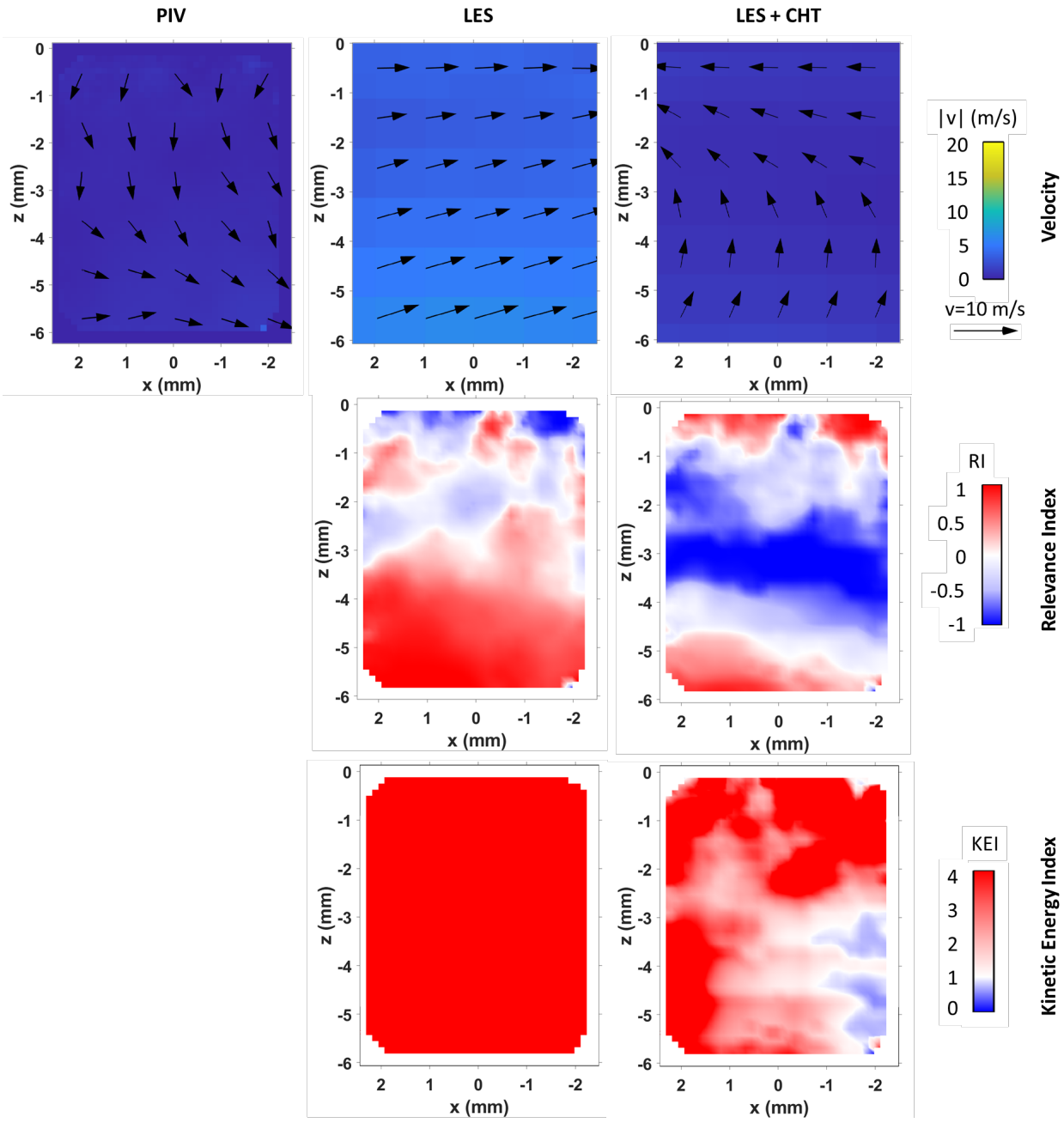

Figure 6.13. Average near-wall flow field, at -20 CAD aTDCc compared to dataset S_2016_03_25_09.

Next, the standard deviation of the velocity field is compared and is shown in Figure 6.14. The spatial average of the standard deviation is also shown in the figure as $\overline{v_{std}}$. Similar to the motored case, the measured standard deviation is larger than that of the simulations. This indicates that the simulations are not able to capture the measured level of CCV. In comparison to the uniform temperature model, the standard deviation of the velocity in the CHT model is lower. This implies that the CCV in heat transfer will be lower in the CHT model The distribution of velocity

standard deviation is such that there are lower values near the surfaces than in the bulk region for the measurement and the simulations, which indicates that there is less CCV in the regions close to the wall than in the bulk region.

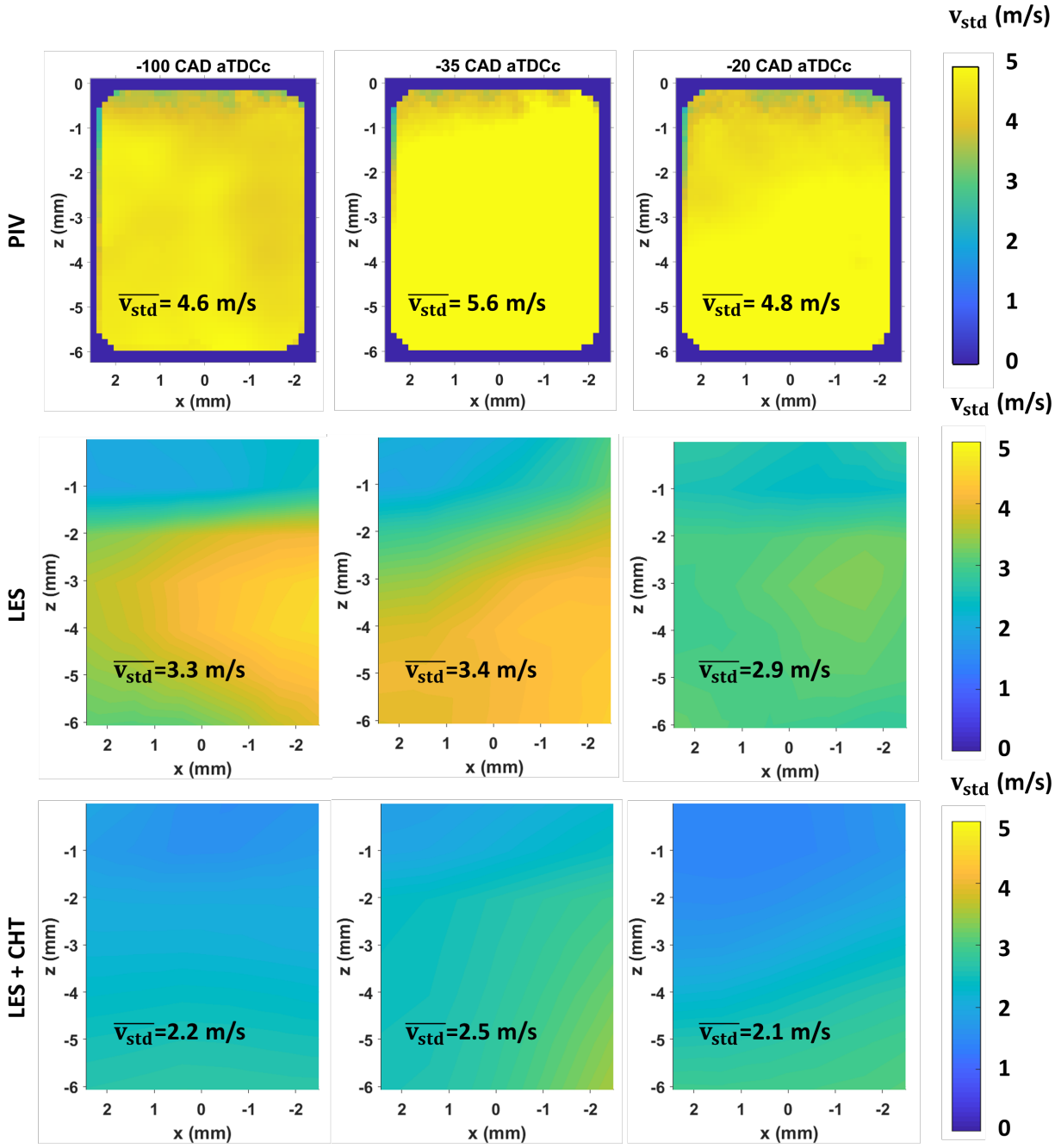

Figure 6.14. Standard deviation of the velocity fields, compared to dataset S_2016_03_25_09.

Ensemble averaged temperature fields from PLIF and LES are shown in Figure 6.15. The spatial average temperature is indicated on each image as $\bar{T}$. The simulations predict higher near-

wall temperatures than the measurement. At -100 CAD aTDCc, there is some stratification in the PLIF and the simulations. The uniform temperature model predicts a near-wall temperature field with decreasing temperatures from the bulk region to the upper left corner of the field of view. In contrast, the CHT model predicts a temperature field where the temperature decreases rather uniformly towards the wall. This temperature distribution does not change much with compression. In contrast, the measured temperature field does not uniformly increase with wall distance. The spatial average temperature of the uniform temperature model is higher than the CHT simulation and the PLIF measurement.

At -35 CAD aTDCc, compression heating leads to increased temperatures. The PLIF measurement has smaller colder and hotter structures and these are again not seen in the simulations. The simulations show a more gradual change in the gas temperature. The spatially averaged temperature of the CHT model is the highest compared to the PLIF and the uniform temperature model. This can be due to surface temperatures or bulk temperatures being overpredicted by the CHT.

At -20 CAD, the spatially averaged temperature of the CHT model is almost 80 K higher than that of the measurement. On the other hand, the uniform temperature model is about 30 K hotter than the measurement. This leads to increased heat transfer in the CHT model, and therefore a lower in-cylinder pressure in the CHT model as shown in Figure 6.1.

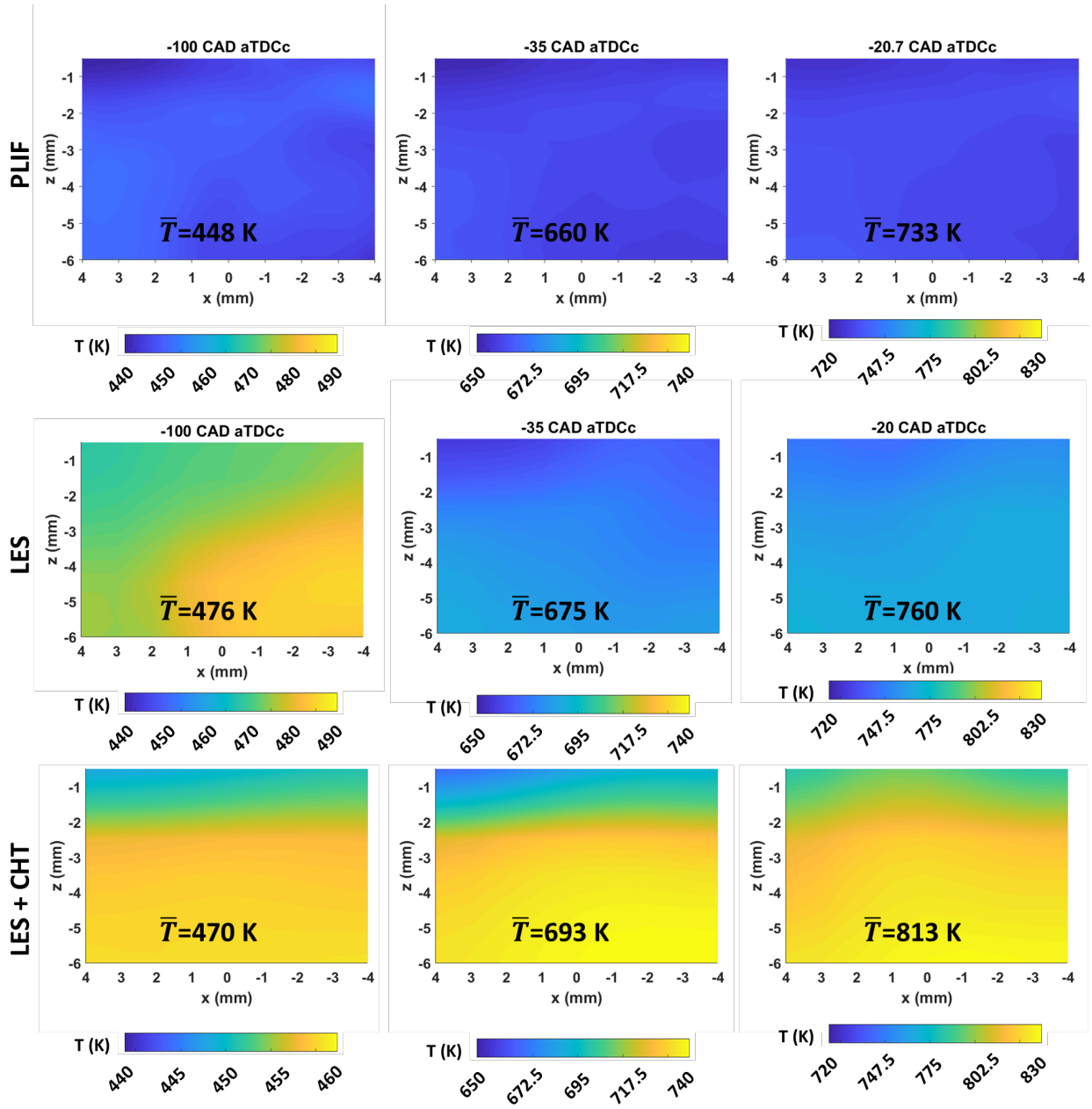

Figure 6.15. Ensemble averaged near-wall temperature field of Cases 7 and 9 and PLIF measurement.

The standard deviation of temperature distributions is shown in Figure 6.16. The measurement shows that, in the near-wall region, larger CCV in the gas temperature exists than in the bulk region from -100 to -20 CAD aTDCc. The uniform temperature model predicts the opposite at -100 CAD aTDCc, as the standard deviation is higher in the bulk region than in the near-wall region. From -35 to -20 CAD, the uniform temperature model predicts the correct behavior of the standard deviation of temperature. The CHT model accurately predicts the

behavior of the standard deviation of temperature at -100 and -35 CAD, where the standard deviation increases towards the wall. But, the CHT model overpredicts the standard deviation value. Also, large values of CCV are not restricted to regions close to the surface. In fact, at -20 CAD, the entire field of view of the CHT model has large standard deviation values of temperature. This is a consequence of the surface temperature predictions by the LES CHT model, which captures not only spatial variation but also temporal and cyclic variation in the surface temperature. In Section 6.3, it is shown that the CHT surface temperatures increased from cycles 2 to 4 as the engine surfaces warm up, after which they stabilized. This, combined with the predicted variations in the surface temperature, leads to larger CCV in the temperature field. Therefore, more than 10 cycles should be simulated with LES CHT and the initial four cycles should be discarded.

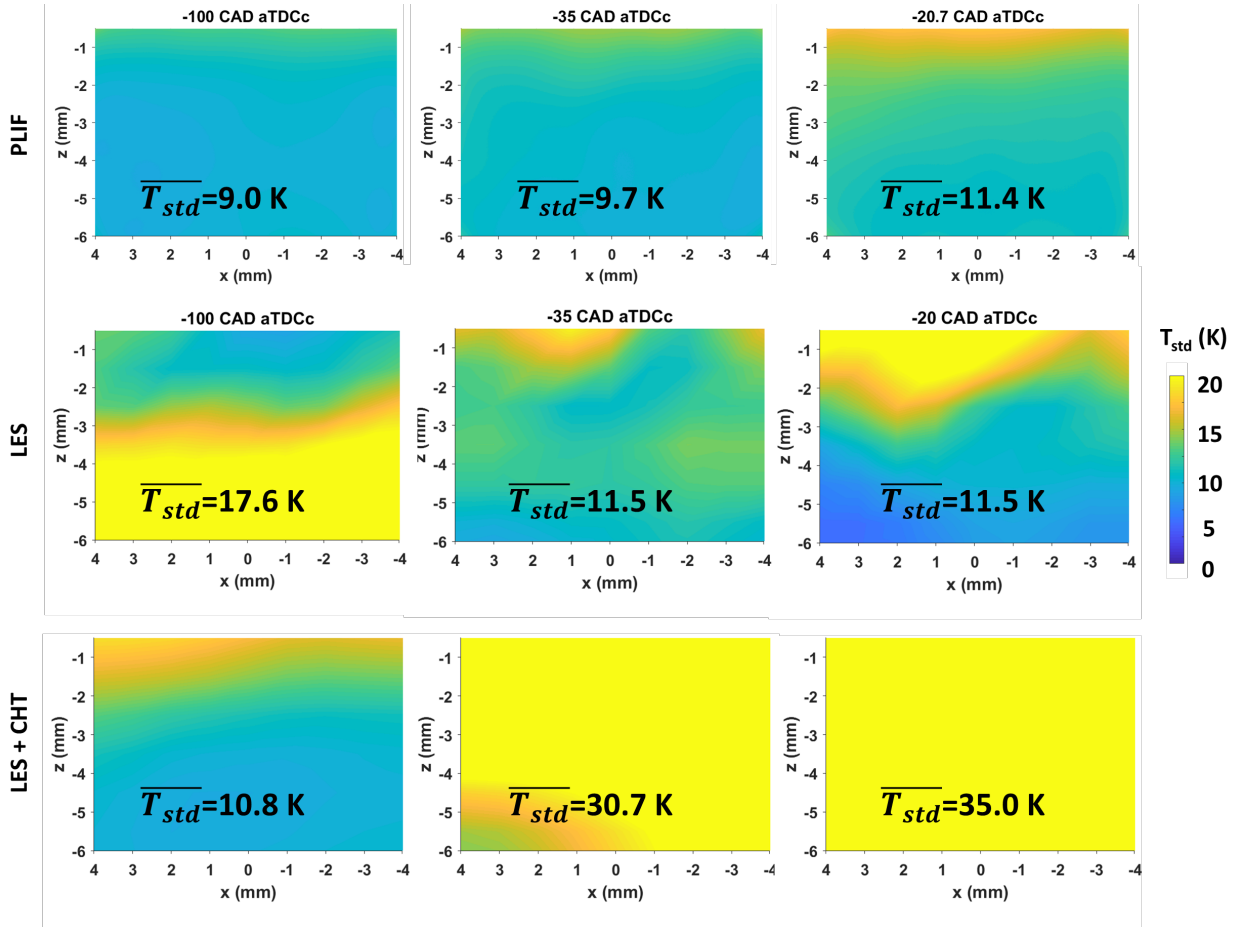

Figure 6.16. Standard deviation of the temperature fields Cases 7 and 9 and PLIF measurement.

Relative temperatures about the spatial means are shown in Figure 6.17. The results show that there are small structures in the PLIF measurement, and these are not captured by either simulations. The relative temperatures are also larger in magnitude in the simulations when

compared to the measurement. With compression, the magnitude of the relative temperatures increase in the simulations, with larger magnitudes in the CHT simulation.

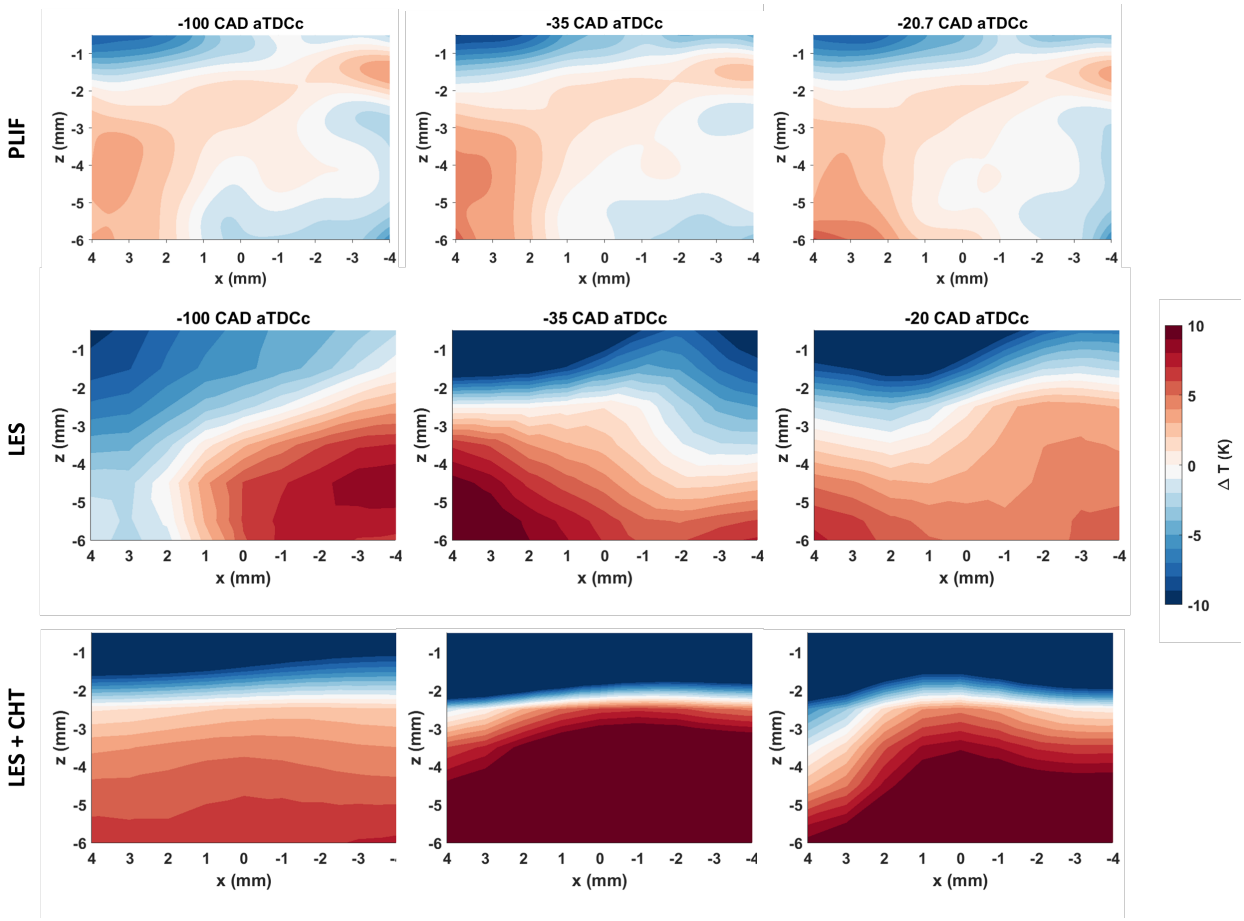

Figure 6.17. Relative near-wall temperature field validation of Cases 7 and 9 with temperature PLIF measurements.

PDFs of the fluctuating velocity components about the ensemble average values are shown in Figure 6.18 for the uniform temperature model. For all the crank angle degree locations examined, the uniform temperature model is unable to capture the range of fluctuating velocities found in the near-wall PIV measurement. Similar to the motored PDFs of the previous chapter, the wall-normal velocity fluctuations span a narrower range than the wall-parallel velocity fluctuations. With increased compression, the range of the measured fluctuations become narrower.

Figure 6.19 shows the PDFs of the fluctuating velocity components for the CHT model. Compared to the uniform temperature model, the CHT model captures a smaller range of wall-parallel velocity fluctuations from -100 to -20 CAD. The range of the wall-normal velocity fluctuations are larger at -100 CAD in the CHT model, but smaller at -35 and -20 CAD. These

results indicate that, although the statistical convergence is met for both simulations, more cycles are likely needed to capture the range of fluctuation velocities.

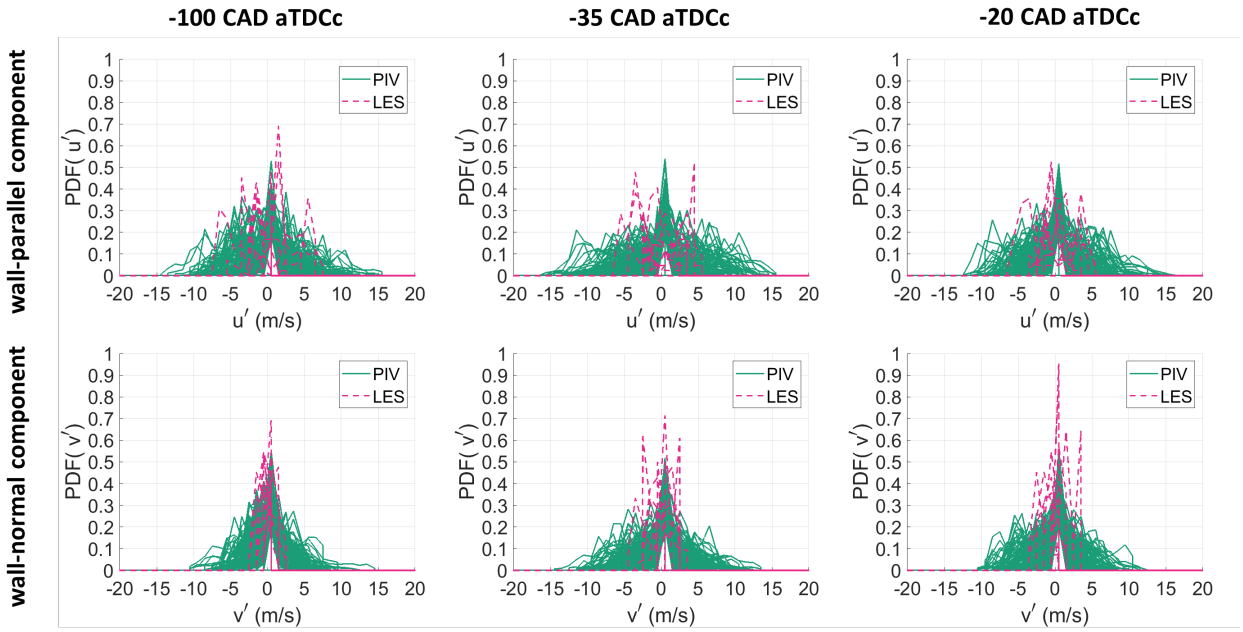

Figure 6.18. PDFs of fluctuating velocity fields from PIV (184 cycles) and uniform temperature LES (10 cycles). Upper rows are wall-parallel velocity fluctuations, while lower rows are the wall-normal velocity fluctuations. Each curve represents an individual cycle.

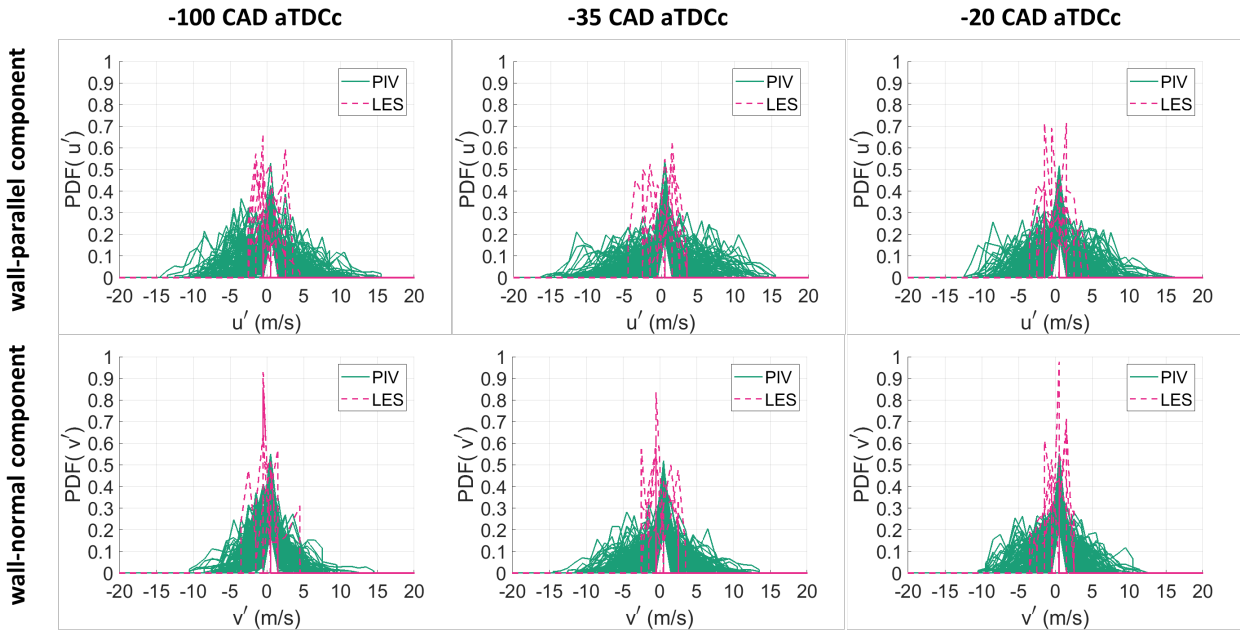

Figure 6.19. PDFs of fluctuating velocity fields from PIV (184 cycles) and LES CHT (10 cycles). Upper rows are wall-parallel velocity fluctuations, while lower rows are the wall-normal velocity fluctuations. Each curve represents an individual cycle.

PDFs of the simulated fluctuating temperatures about the ensemble average are shown in Figure 6.20. They indicate that for the uniform temperature model, at -100 CAD aTDCc, the simulation is able to capture the broadness of the fluctuations, but not the peak values of the measured PDF. This is likely due to the limited number of data points available in the PLIF field of view of the simulation. On the other hand, the CHT model does not capture as wide of a range of fluctuating temperatures as the uniform temperature model at this crank angle degree location. With compression, the range of fluctuating temperatures of the uniform temperature model narrows at -35 and -20 CAD and is narrower than the measured PDFs. The CHT model shows an increase in the range of temperature fluctuations at -35 and -20 CAD aTDCc that better match with the experimental range.

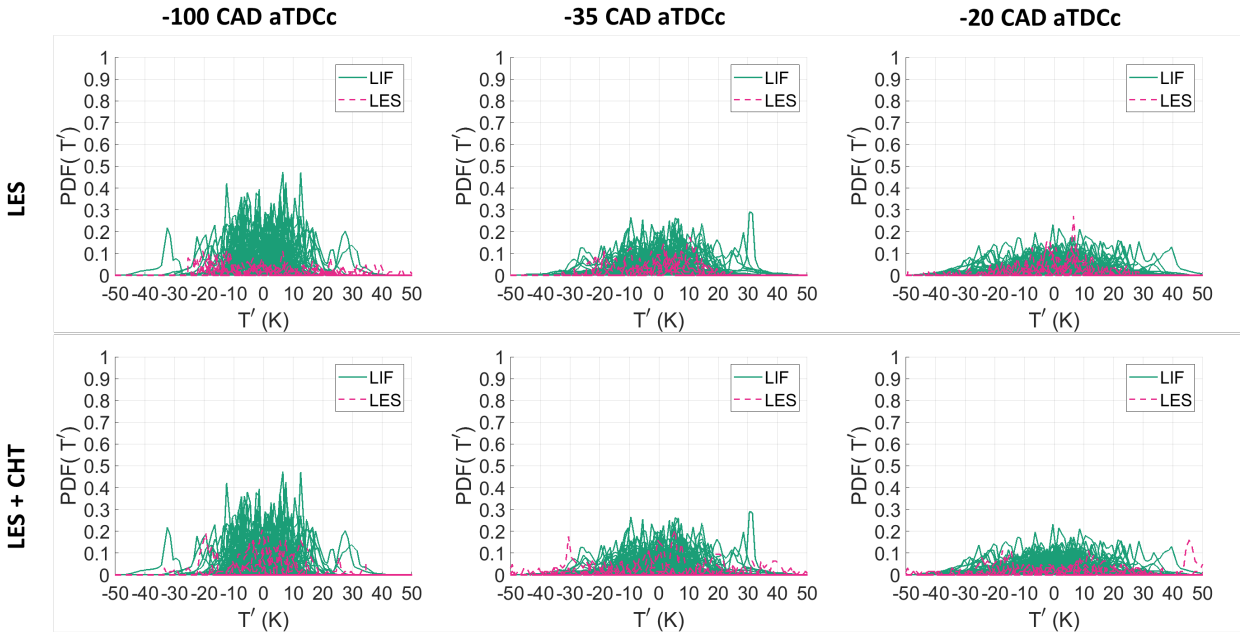

Figure 6.20. PDFs of fluctuating temperature fields from PLIF (145 cycles), and uniform temperature and CHT simulations (10 cycles each). Each curve represents an individual cycle.

6.3 Surface Temperature and Engine Heat Flux

The surface temperature at the heat flux probe is shown in Figure 6.21. The LES CHT underpredicts this surface temperature measurement by about 13 K or about 3%. The CCV in the surface temperature during late compression and early expansion stroke is well captured as shown by the shaded area which represents one standard deviation from the ensemble average. After 40 CAD aTDCc, the CCV of the CHT simulation is larger than the measured CCV in the surface temperature. The surface temperature was non-dimensionalized in a similar manner as Figure

5.22(b) and the non-dimensional surface temperature of the simulation peaks earlier than that of the measurement. The non-dimensionalized CCV is also smaller than the measurement, but as the surface temperature peaks, the CCV in the surface temperature also increases similarly as that of the measurement. After 40 CAD aTDCc, the CCV in the simulated surface temperature is overpredicted.

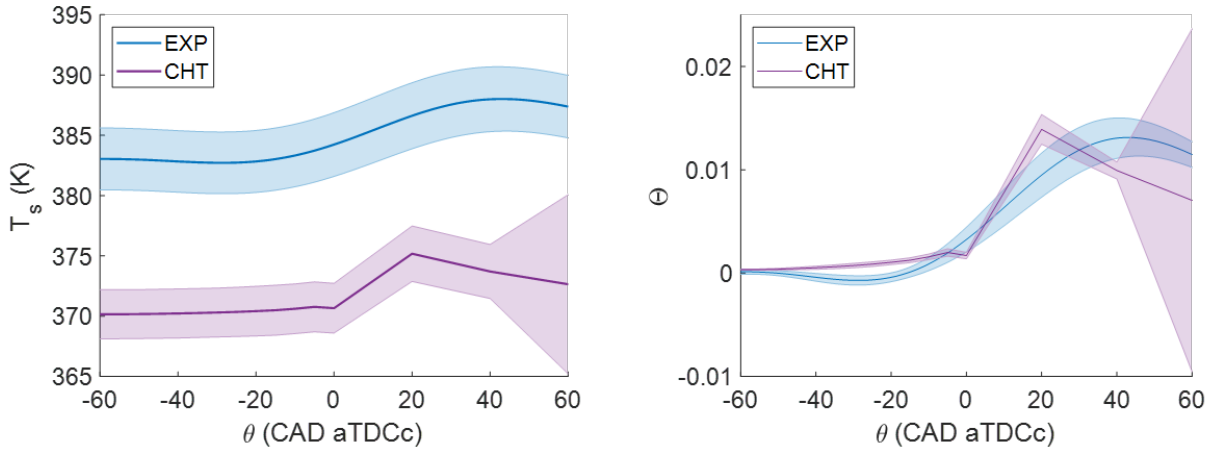

Figure 6.21. (a) Surface temperature, and (b) non-dimensionalized surface temperature at the heat flux probe from the LES CHT model, compared against measurement. The LES CHT underpredicts the surface temperature by about 13 K.

Surface temperatures at the spark plug from the CHT simulation are shown in Figure 6.22 from -20 CAD to TDC for each cycle. The surface temperature varies significantly in the ground strap from 350 K to over 1000 K. This is larger than the surface temperature range of the motored engine in Chapter 5. The surface temperature also increases over time, as the engine warms up during the simulation and as the flame structure develops throughout the combustion event, which then interacts with the spark plug. The surface temperature decreased in cycle 11, possibly due to flow variability or low wall heat transfer in the spark plug region in this cycle. There is also some CCV in the spatial distribution of the ground strap temperature.

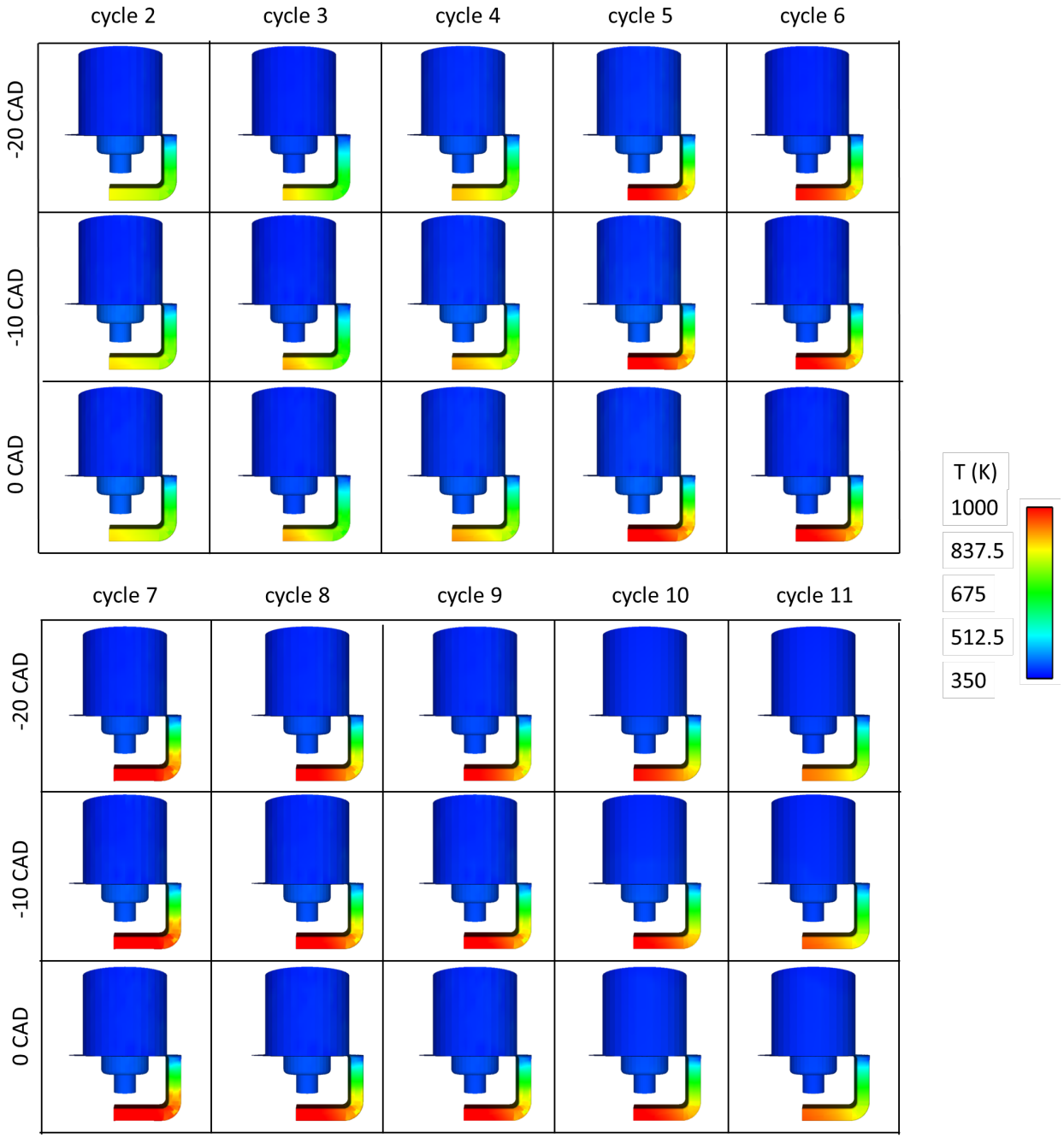

Figure 6.22. Surface temperature of the spark plug as predicted by the fired LES CHT model. It predicts transient, spatial, and cyclic varying surface temperatures. In addition, the spark plug surface warms up with increasing number of cycles.

The surface temperatures of the piston are shown in Figure 6.23. The surface temperature of the piston in the second cycle is lower than the rest of the simulation as the piston surface is still warming up. After the spark event at -18 CAD aTDCc, the flame structure arrives at the piston surface and can be seen at -10 CAD aTDCc as it heats a portion of the piston quartz. With

compression, the area of higher surface temperature on the quartz increases as the flame surface area increase and is compressed. In cycle 3, at -180 CAD aTDCc, the piston quartz surface is still hot from the previous cycle. The residual gas is cooled down by the intake jet, leading to lower quartz surface temperatures, until combustion happens and the flame structure arrives again at the piston surface at -10 CAD aTDCc. As the flame structure enlarges and is further compressed, a larger portion of the quartz surface becomes hot. The piston crown is also getting hotter. After cycle 3, the piston crown surface temperatures stabilize, and the quartz surface remains hot.

The surface temperature of a metal piston in an HCCI engine was measured previously by [150]. Their measurements show that the piston surface temperature ranges from approximately 420 K to 430 K for a clean piston surface, and for a piston covered in soot deposit, the temperature ranges from about 430 K to 440 K. This is lower than the surface temperatures in the piston metal crown obtained by the LES CHT model, with temperatures of about 700 to 750 K. It should be noted that the engines and operating conditions are different between our study and that of [150]. Their piston has a bowl shape and no quartz component, and fuel is injected instead of premixed with air as in the TCC-III engine. Also, the heat transfer characteristics of HCCI engines are very different than SI engines, with less spatial variation since autoignition in HCCI engines leads to more uniform combustion in the cylinder.

When compared to the uniform temperature model, the LES CHT model shows that there is still significant spatial, temporal, and cyclic variation in the surface temperature. It also shows that there is a transient phase in the surface temperature as the engine surfaces warm up before reaching a thermal equilibrium. The surface temperature stabilizes after cycle 4 for the piston surface and spark plug. In the uniform temperature model, we assumed that the surface temperature is 468 K for the entire piston surface, which is much lower than the predicted surface temperature by the CHT model, as the quartz surface temperature can reach above 1000 K with increasing engine cycles. The spark plug surface was assumed to be at a uniform 900 K, but the CHT simulation shows that the spark plug experiences a large range of temperatures from 350 K to above 1000 K in the ground strap. This surface temperature will affect not only the combustion event through heat transfer exchange with the developing flame structure, but will also affect emissions and engine performance, as was seen in the in-cylinder pressure in Figure 6.1.

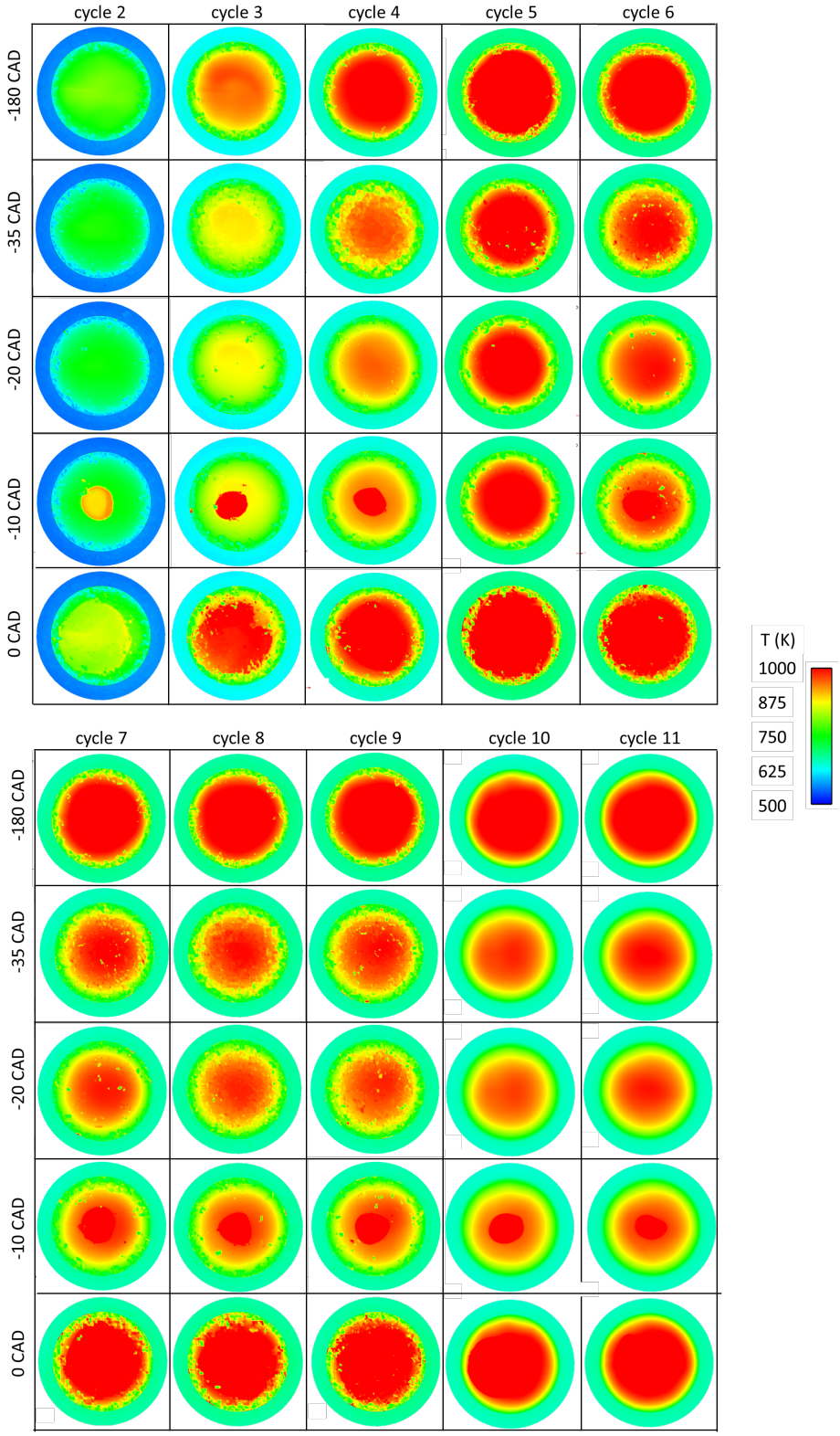

Figure 6.23. The fired LES CHT predicts spatial, transient, and cycle-to-cycle variations in the piston surface temperature. This contrasts with the uniform temperature LES where a uniform piston temperature of 468 K was assumed.

Figure 6.24 shows the spatial average of the ensemble average surface temperatures of the piston, inner liner surface, cylinder head, and spark plug. The shaded area indicates one spatial standard deviation of the surface temperature, i.e., the level of stratification in the temperature distribution over the surfaces. This figure shows that the temperature at each surface is different and experiences different levels of temporal and spatial variations, in contrast with the uniform temperature assumptions. As in the motored case, the cylinder head surface has the smallest temperature stratification compared to the other surfaces due to the coolant circuit within the head. The liner experiences large temperature stratification due to the scrubbing motion of the piston. The piston and spark plug are made of different materials, and this leads to large spatial stratification. The spark plug experiences the highest level of spatial stratification since it is composed of different materials with vastly different thermal conductivities. Time averaging the surface temperatures of Figure 6.24 leads to different values than the uniform temperature assumptions of Figure 3.14. For example, the head surface was assumed to be at 458 K which is higher than the temperature of 376 K as calculated by the CHT simulation. The spark plug temperature was assumed to be 900 K, but the CHT simulation resulted in an average of 525 K.

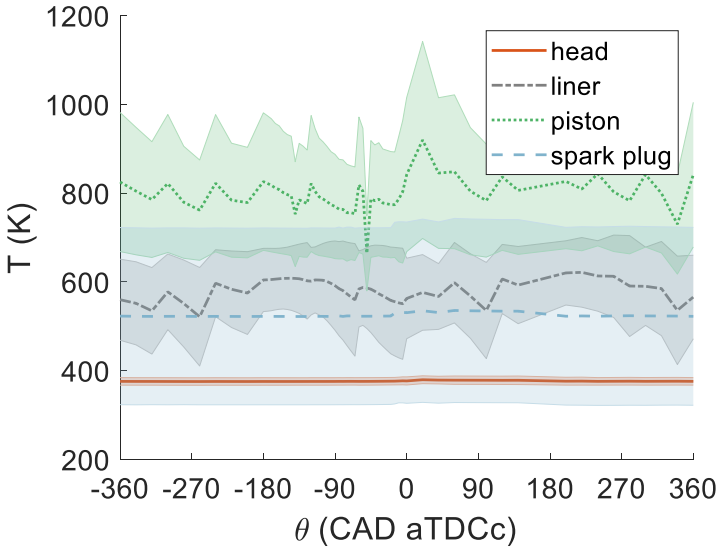

Figure 6.24. Spatial average of the ensemble-averaged surface temperatures of the cylinder head, liner, and piston, obtained from the fired LES CHT. The shaded area is one standard deviation of spatially averaged temperature, indicating the spatial stratification over the surface.

The effects of the surface temperature on emissions is shown in Figure 6.25. The mass of each species in grams was normalized by the total fuel mass per cycle of 12 mg. The shaded area represents one standard deviation from the ensemble average. Because the CHT model predicts

larger in-cylinder temperatures and a larger standard deviation of the temperature than the uniform temperature model, it leads to larger amounts of NOx. Also, larger CCV in the surface and gas temperature in the CHT simulation leads to larger CCV in the NOx formation. Hydrocarbon levels are lower in the CHT model due to higher temperatures leading to more hydrocarbons being burnt up. This also leads to lower oxygen content in the CHT model. CO and CO_2 were found in the burnt gas region behind the flame. In the CHT model, the flame is larger at the same crank angle degree location as seen in Figure 6.8. This is likely the cause of higher CO levels in the CHT model. This, combined with less oxygen available, leads to lower CO_2 levels. It should be noted that the reaction mechanism and NOx model used could lead to uncertainties with the emissions predictions.

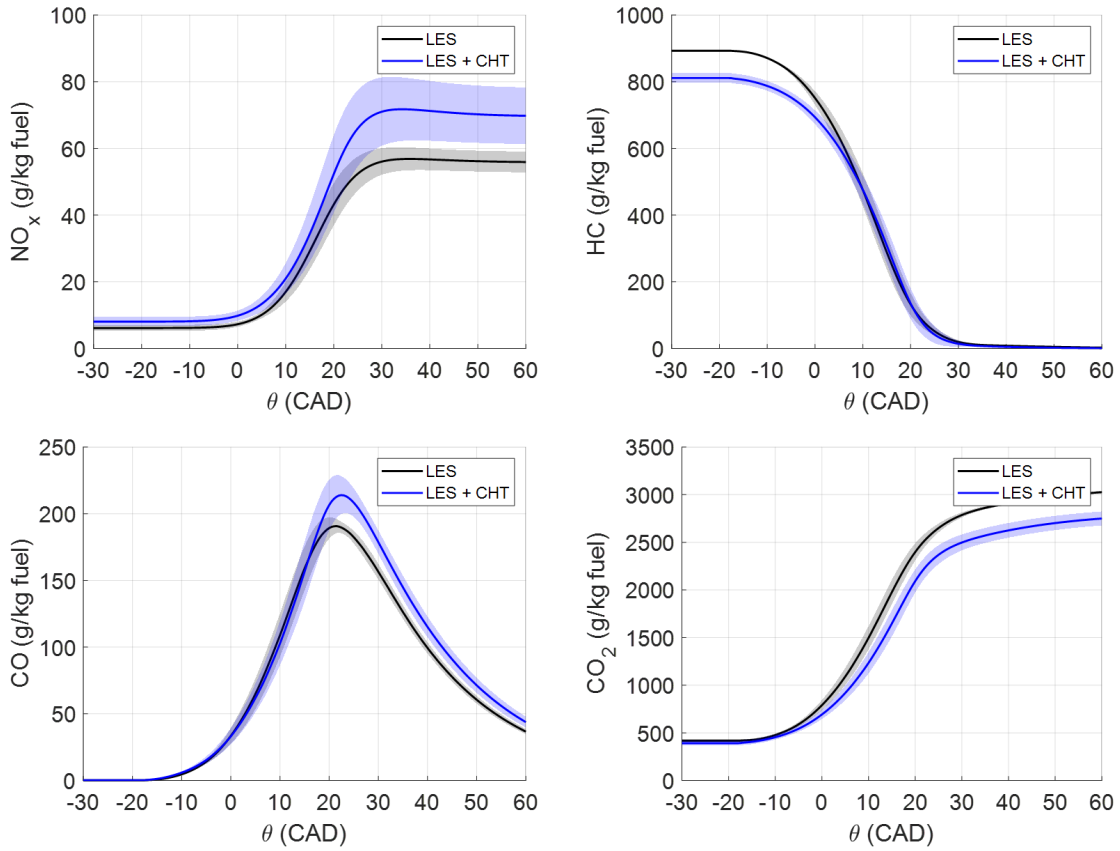

Figure 6.25. NO_x, hydrocarbon, CO, and CO_2 emissions of uniform temperature and CHT models.

The surface heat flux was measured at the heat flux probe at the cylinder head, at x=12.1 mm and y=33.4 mm, and is shown in Figure 6.26. The unfiltered peak heat flux from measurement is 990 kW/m^{2}K. Compared to the measured peak heat flux, the CHT peak heat flux is 1191 kW/m^{2}K, an overprediction of about 20%. The uniform temperature peak heat flux is 949

kW/m^{2}K, an underprediction of about 4%. The CHT model predicts higher bulk gas temperatures and lower head surface temperatures than the uniform temperature model, and this could lead to locally large temperature differences between the gas and solid. This leads to the higher heat transfer at the heat flux probe location in the CHT model, and therefore a low peak pressure in Figure 6.1. In terms of CCV, the maximum standard deviation of the filtered measured heat flux is 109 kW/m^{2}K. The uniform temperature model has a maximum standard deviation of 484 kW/m^{2}K and the CHT model 222 kW/m^{2}K, which is closer to the measurement CCV. This can be due to the combined effect of large CCV in surface temperature and near-wall temperatures, as was shown in Figure 6.16, resulting in a smaller ΔT range in the CHT model that is more consistent from cycle to cycle.

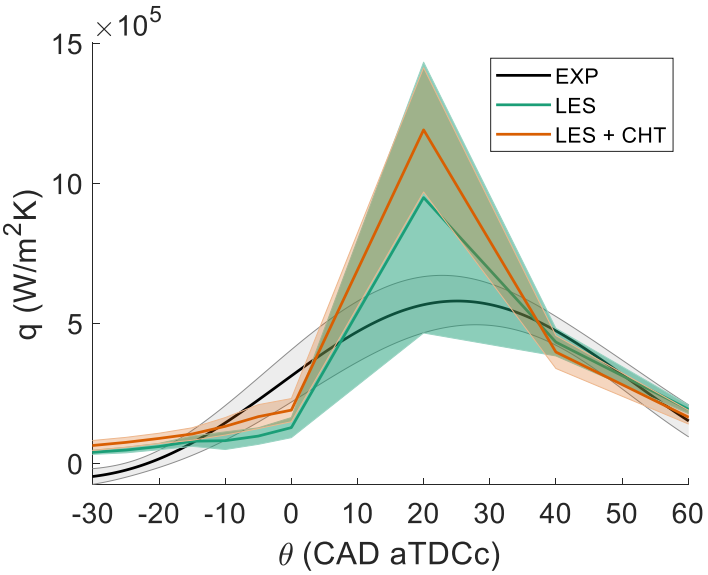

Figure 6.26. Surface heat flux of the simulation Cases 4 and 6 compared against filtered experimental heat flux of PIV dataset S_2016_03_25_09. The shaded areas indicate one standard deviation of the heat flux.

6.4 Spatial Correlations Using Fluctuating Values

Spatial correlations were assessed using the fluctuating velocities about the ensemble average. Results are shown in Figure 6.27 for the wall-normal velocity fluctuations in the wall-normal direction at correlation point $z_o = -1$ mm. Trend-wise, the simulated spatial correlations match the shape of the measured correlation curves. However, the velocity fluctuations are more strongly correlated in the simulations compared to the measurement. These correlations indicate that the experiments have smaller length scales and higher gradients of the velocity fluctuations

compared to the simulations at this correlation point. With increased compression, the correlations become stronger for the measurement and the simulations.

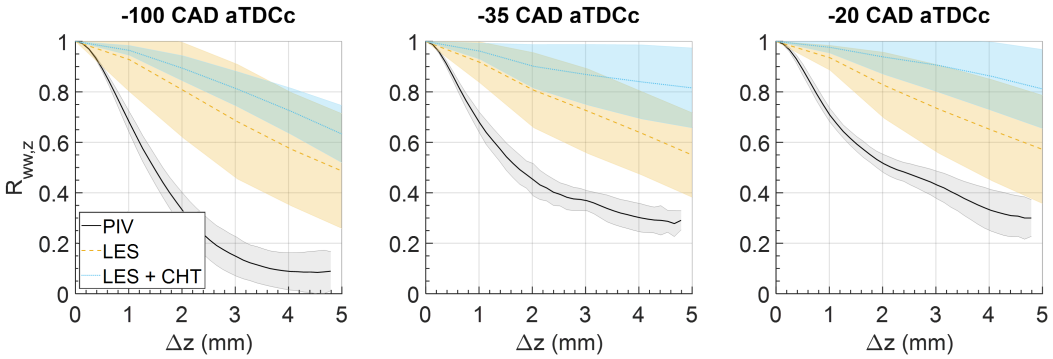

Figure 6.27. Spatial correlations of the wall-normal velocity fluctuations in the z-direction for the simulations and PIV measurement.

Spatial correlations assessed using the fluctuating temperature about the ensemble are shown in Figure 6.28 for the wall-normal direction at correlation point $z_o = -1$ mm. The fired PLIF measurement is more strongly correlated than the simulations, showing that at this location, the simulations predict a smaller integral length scale than the measurement. The standard deviation in the spatial correlation is shown by the shaded areas and indicates the stratification of the spatial correlations in the x-direction. It can be seen that the simulations overpredict the stratification of the spatial correlation at this location.

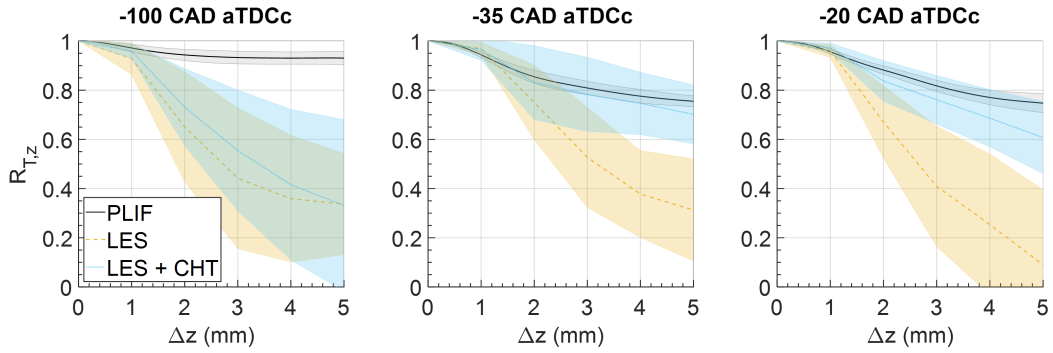

Figure 6.28. Spatial correlations of temperature fluctuations of PLIF measurement compared against uniform temperature and CHT models.

6.5 Integral Length Scales Using Fluctuating Values

Integral length scales were obtained from the spatial correlations of the fluctuating values about the ensemble average. Results are shown in Figure 6.29 for the integral length scales from the simulated wall-normal velocity fluctuations in the z-direction. Comparisons are made between

the length scales from the uniform temperature and the CHT simulations. Length scales larger than 20 mm should be ignored due to curve fit issues.

At -100 CAD aTDCc, no viable length scales could be obtained for the CHT model due to the curve fitting issue. The spatial distribution of the uniform temperature model is inhomogeneous. At -35 and -20 CAD aTDCc, length scales are increasing towards the wall for both simulations. This is in contrast with the motored results of Section 5.11, where length scales were decreasing towards the wall. The spatial velocity length scales also do not become more uniformly distributed with increased compression as there is still a level of stratification in the length scales in both models.

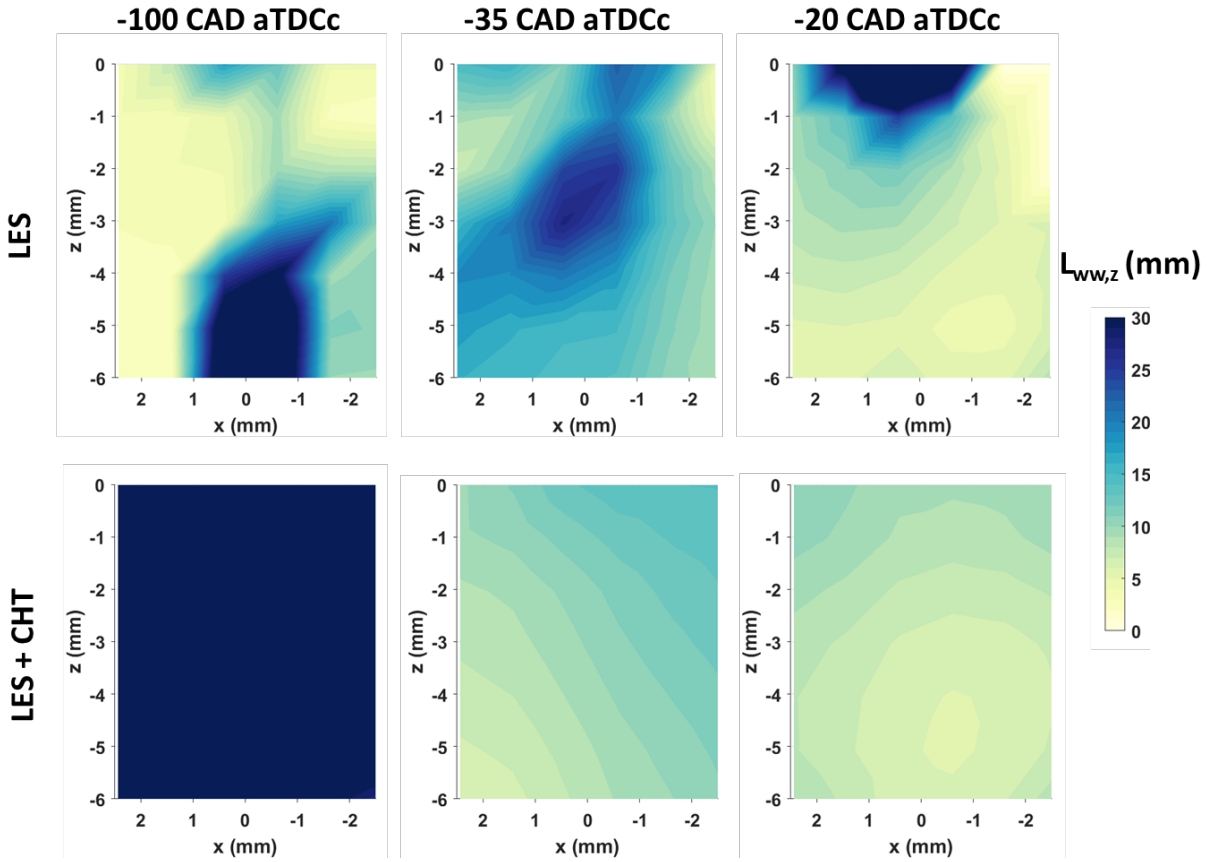

Figure 6.29. Integral length scales of velocity fluctuations about the ensemble average in the z-direction for the uniform temperature and CHT models.

The temperature length scales are shown in Figure 6.30 in the z-directions in the PLIF field of view using LES results. Length scales larger than 20 mm should be ignored. At -100 CAD aTDCc, no viable length scales were obtained for the CHT model. The uniform temperature model shows increasing length scales towards the wall. At -35 CAD aTDCc, the temperature length scales

decrease towards the wall in the uniform model, while the CHT model shows length scales are increasing towards the wall. At TDC, the distribution of both simulations become uniform.

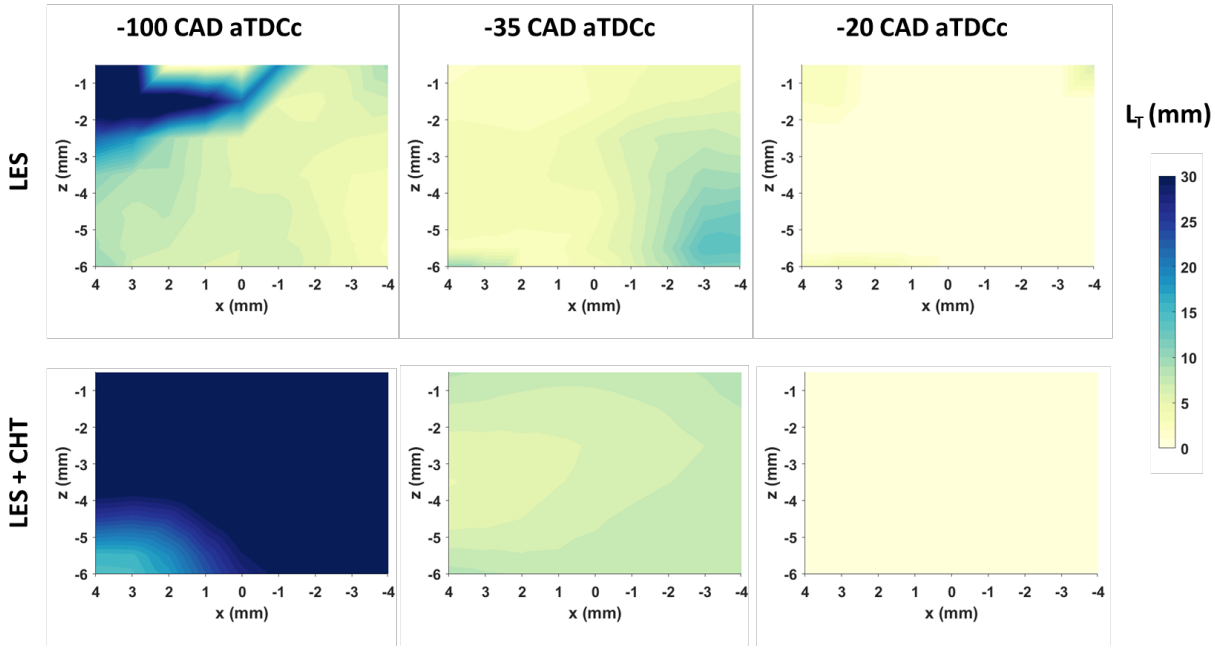

Figure 6.30. Temperature length scales in the z-direction of the temperature fluctuations for the uniform temperature and CHT models.

6.6 Spatial Correlations Using Relative Values

Spatial correlations were also obtained using the relative values about their spatial means. The correlation is performed in the z-direction for the relative wall-normal velocity and relative temperature. Results of the velocity spatial correlations are shown in Figure 6.31 at correlation point z_o= -1 mm. The solid and dashed lines indicate column-average across the x-direction, while the shaded area indicates the spatial standard deviation in the x-direction.

Compared to the PIV measurement, the simulations are more strongly correlated. The standard deviation of the spatial correlations of the simulations is also larger. This is similar to the motored results of Section 5.12. The simulated relative velocity gradient is more spatially stratified than in the measurement in the x-direction, especially in the bulk flow region at large correlation distances. The spatial correlations decrease at a shorter correlation distance than those of the simulations, again indicating that there is a larger relative velocity gradients in the PIV measurement than the simulations. From -100 CAD aTDCc to TDC, the relative velocity correlation becomes stronger in the simulations, while in the measurement the spatial correlation stays mostly the same.

Differences can be seen between the simulations in their correlation curves. The relative wall-normal velocity is less strongly correlated in the CHT simulation at -100 CAD, but the correlation becomes stronger for the CHT model with increasing compression. This is similar to the motored results. Again, this indicates that the integral length scale in the wall-normal direction becomes larger with increased compression for the CHT simulation at this correlation point. This integral length scale is smaller in the uniform temperature model at the same crank angle degree location with increased compression. On the other hand, the spatial standard deviation is larger for the CHT simulation, indicating that there is more spatial stratification in the integral length scale in the CHT model across all x values.

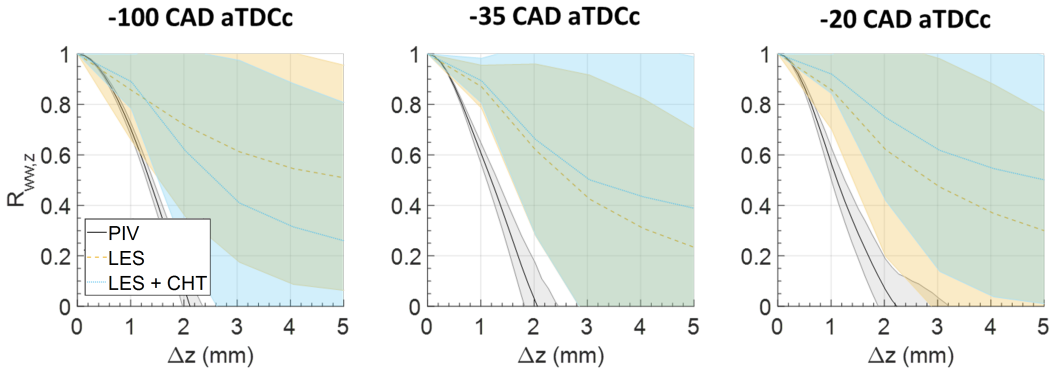

Figure 6.31. Spatial correlations of relative velocities about the spatial means in the z-direction.

Spatial correlations of the relative temperature about the spatial means from PLIF and the simulations are shown in Figure 6.32. The results show that the CHT model can more accurately capture the spatial correlation curve of the measurement at -100 CAD aTDCc, with a close match in the spatial mean and the spatial standard deviation of the spatial correlation. The uniform temperature model predicts a stronger spatial correlation and a larger standard deviation, which indicates larger temperature length scales at this correlation point. At -30 and -20 CAD, the spatial mean correlations of both simulations match the measured correlation well. The spatial standard deviation of the CHT model is larger than that of the uniform temperature model, and both are larger than the measured spatial standard deviation.

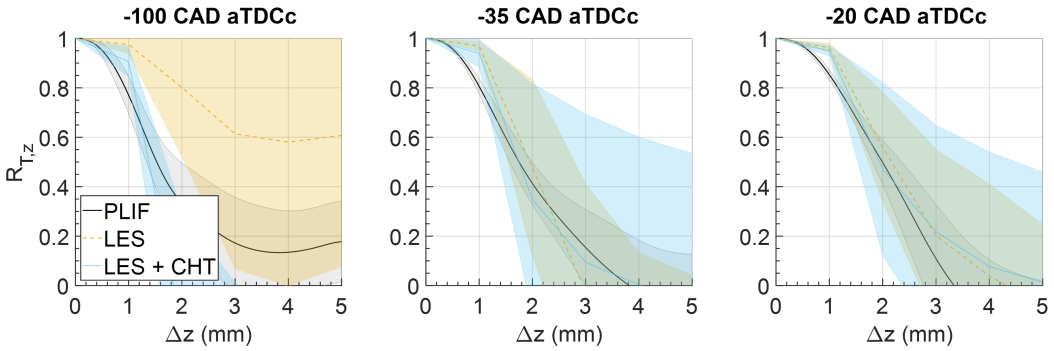

Figure 6.32. Spatial correlations of relative temperatures about the spatial means in the z-direction.

6.7 Integral Length Scales Using Relative Values

The velocity integral length scales in the wall-normal direction are shown in Figure 6.33. Results show that there are areas in the simulations where large length scales were obtained, mostly due to bad curve fit leading to length scales larger than 20 mm. However, in the near-wall region, length scales are obtained in the simulations on the order of those of the measurement.

As a reminder, larger length scales coincide with small velocity gradients. This shows that near the wall, approximately the same velocity gradients are obtained in the simulations as those of the measurement. The length scales in the PIV measurement decrease from the wall to the middle of the field of view, then increase again with increasing wall distance. This pattern can be seen in the simulations at -100 and -35 CAD aTDCc, but not at TDC.

The spatial distribution of the length scales at -100 CAD aTDCc are somewhat similar between the simulations and the measurement, with the uniform temperature model being able to capture the small region of small length scales in the middle of the field of view. In contrast, the CHT model has a larger region of small length scales that span across the middle of the field of view. At -35 CAD aTDCc, a larger portion of the field of view has small length scales in both simulations which do not compare well with the measurement. At TDC, the length scales become more homogeneous in the simulations, but the length scales in the measurement are still spatially distributed. This indicates that the turbulence becomes more homogeneous with increased compression in the simulations than in the measurement.

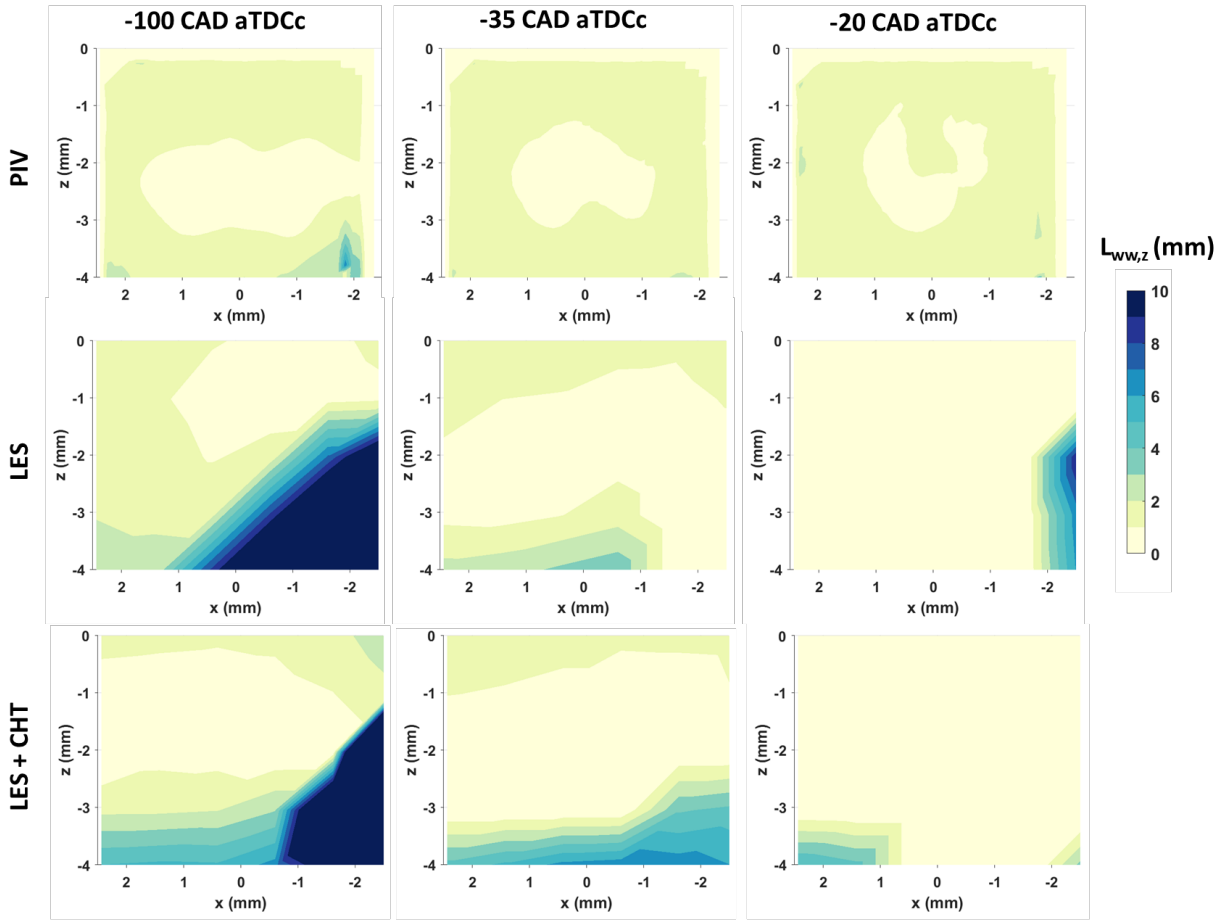

Figure 6.33. Integral length scales of relative velocity about the spatial means.

The temperature length scales in the wall-normal direction are shown in Figure 6.34. Length scales larger than 20 mm should be ignored. Results indicate that the temperature length scales decrease towards the wall in the measurement. This behavior is also seen in the simulations at -35 CAD and -20 CAD aTDCc. Smaller length scales coincide with larger temperature gradients, and therefore, heat transfer is increasing towards the wall due to increasing gradients. The spatial distribution of length scales become more homogeneous with increased compression, which can be seen in both simulations and measurement. This indicates that the heat transfer becomes more uniform with increased compression. The behavior of the heat transfer in the fired condition is very similar to that of the motored condition before combustion.

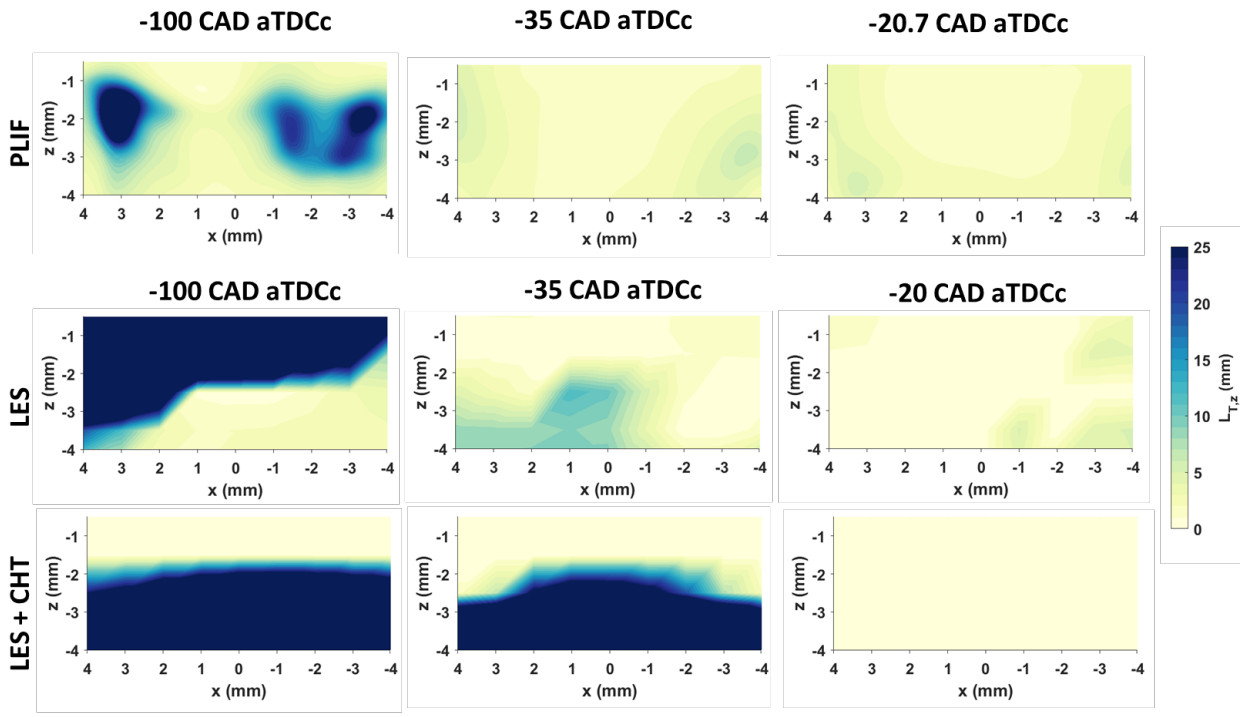

Figure 6.34. Integral length scales of relative temperature about the spatial means.

6.8 Summary

The fired operating condition was simulated in this chapter using uniform temperature boundary conditions and contrasted with the fired LES CHT. The bulk flow fields show similar issues with the intake jet simulations as those of the motored cases. The kinetic energy is overpredicted in the intake jet, leading to vortex centers that do not match with measured locations. The bulk temperature fields show that the spatial distribution in the surface temperature obtained by the CHT simulation leads to changes in the early flame kernel development. The burnt gas temperature in the CHT simulation is more uniform than the uniform temperature model, and the combustion rate was faster in the CHT simulation.

The near-wall velocity predictions show that improvements are needed in the wall models, as was the case for the motored flow. The simulations predicted larger near-wall temperatures than the fired PLIF measurement. In addition, the standard deviation of the temperature field was much larger in the CHT simulation. The standard deviation of the temperature in the CHT model increased towards the wall, and this behavior was found in the PLIF measurement. In contrast, the uniform temperature model did not capture this spatial behavior.

The LES CHT predicts large spatial and cyclic variations in the surface temperatures of the spark plug, with a wide temperature distribution range from 350 K to 1000 K. The same variations

were found on the piston surface. In addition, the surface temperature increased gradually from cycles 2 to 4 as the engine surfaces warmed up during the simulation, showing that there is a transient phase in the surface temperature before thermal equilibrium was reached. Note that super-cycling was used in the simulation which reduces the number of cycles needed for the solid components to reach thermal equilibrium. Combined with the larger standard deviation of the near-wall temperature field and the CCV in the surface temperature, the CHT predicts temperature differences between the gases and surfaces that are most likely more consistent from cycle to cycle, as evident by the lower CCV in heat flux obtained by the LES CHT case, which compares better with the experiment than the uniform temperature model. The uniform temperature model severely overpredicts the CCV in the heat flux, since the surface temperature is constant but the near-wall temperature fields change from cycle to cycle. This leads to a more inconsistent temperature differences from cycle to cycle.

Spatial correlation analysis using the relative values about the spatial means was performed, and integral length scales were obtained in the near-wall region. The temperature length scales of the fired condition increase towards the wall in a similar manner as those of the motored conditions. This indicates that heat transfer increases towards the wall. Measurements show that the velocity and temperature length scales become more homogeneous with increased compression. This indicates that the turbulence and heat transfer become more spatially uniform with increased compression.

Chapter 7 Conclusions and Future Work

7.1 Contributions

Engine heat transfer affects the internal combustion engine's efficiency, performance, and emissions. To improve the accuracy of engine simulations, engine heat transfer needs to be simulated correctly. This requires that we capture the temporal, spatial, and cycle-to-cycle variations (CCV) in engine heat transfer. In conventional engine CFD, the surface temperature is often assumed to be constant and uniform. Conjugate heat transfer couples the heat transfer solution between fluid and solid domains, and can provide more accurate thermal boundary conditions. In this dissertation, CHT was integrated with LES with moving valves and piston for improved heat transfer predictions for motored and fired operating conditions, using a commercial CFD software. These simulations were compared to baseline uniform temperature LES to show improvements in engine heat transfer predictions using CHT. The quality of the engine simulations was evaluated against bulk flow, near-wall flow, and near-wall temperature measurements performed by the Quantitative Laser Diagnostics Laboratory (QLDL) group at the University of Michigan. Such a comparison to the near-wall flow and temperature fields have not been available to date and are described here for the first time.

In the first part of the study, the motored operating condition was simulated with uniform temperature boundary conditions, and modeling methods were analyzed that improved heat transfer predictions, including turbulence models, wall models, near-wall mesh resolution, and temperature boundary conditions. Bulk flow analysis shows that the simulation of the intake jet largely impacted the predicted vortex center locations and heat transfer. Near-wall flow analysis shows that improvements in the wall models are needed. The RANS turbulence model results in an overprediction of the near-wall velocity magnitudes, causing higher surface heat flux that better match with the experimental data. Refining the LES near-wall mesh from 1 mm to 0.5 mm allowed the flow to be better resolved, resulting in larger near-wall velocity magnitudes which improved surface heat flux predictions. Changing the LES wall model from the law of the wall to the Werner and Wengle wall model which is recommended for LES, reduced the near-wall velocity magnitudes and surface heat flux, but improved the CCV in the surface heat flux. Finally,

increasing the surface temperature by 45 K to match the coolant and intake air temperatures resulted in improved near-wall temperature predictions.

In the second part of the study, CHT was integrated with LES. The LES CHT was validated with measured surface temperature within 1.4% and 3% error for the motored and fired operating conditions, respectively. The LES CHT predicted spatial, temporal, and CCV in the surface temperatures. The results show the impact of surface temperature on the predicted flow and temperature fields. For example, the spark plug surface temperature varied from 350 to 1000 K, which has a significant impact on the heat transfer from the flame to the spark plug and the early combustion process.

The CHT work was performed in a parallel effort with Alzuabi [39], who measured the near-wall temperature field using PLIF thermometry. The LES CHT work guided the choice of the calibration region of the PLIF measurements by identifying the bulk gas temperature region where near-wall temperature effects were minimized. This collaborative effort was performed to assess the LES CHT predictive capability in the near-wall temperature field. Length scale analysis was performed in the wall-normal direction to provide insights into the spatial scales that are important in engine heat transfer. Results show that the length scales decrease towards the wall, indicating that temperature gradients increased towards the wall leading to increased heat transfer. Their distribution also became more homogeneous towards TDC, and therefore, heat transfer becomes more spatially uniform with increased compression. These results were found in both the measured and simulated temperature fields.

A key question when using LES for CCV studies is the number of LES cycles that are needed to reach statistical convergence, but also reduce the computational costs associated with simulating an excessive number of cycles. A statistical convergence criteria was developed with the well-known LES quality index. It was shown that this quality index converges for increasing number of cycles, and statistical convergence was met by the motored LES after 10 cycles. However, statistical convergence does not mean that the simulations capture the measured level of CCV, as the motored simulations typically show lower levels of CCV compared to the measurement. Histograms of fluctuating velocities and temperatures show that the simulations capture a limited level of CCV compared to the measured fluctuations with only 10 cycles. For the fired simulations, a higher level of CCV was obtained due to a transient phase in the surface temperatures as predicted by the LES CHT from cycle 2 to 4 as the engine warmed up from the

combustion process. Therefore, more LES cycles are likely needed to capture the measured level of CCV.

Disagreements between near-wall measurements and the simulations were attributed to several causes, including wall model and subgrid-scale model effects. Specifically, the wall model constants may need to be recalibrated and allowed to vary with crank angle degree location. While the LES quality index shows that the current simulations resolve 80% and more of the turbulent kinetic energy, the grid resolution within the combustion chamber needs to be refined to capture smaller scales. However, this might not be feasible in practical engine simulations. The numerical scheme affected the resolved velocity predictions, and a higher-order differencing scheme such as second-order central differencing should be used to improve velocity predictions. While the LES CHT reduces the uncertainty in the surface temperature at the fluid-solid boundary interface, the thermal boundary conditions on the exterior surfaces of the engine were estimated. Also, there is a lack of spatially-resolved surface temperature measurements which prevents the full validation of the LES CHT temperatures.

On the experimental side, measurement uncertainties and noise can have a large impact on the results and conclusions of quantitative comparisons. For example, the wall location determination in the near-wall flow measurement leads to a 3% uncertainty in the wall-normal distance for measurement locations closest to the surface. The PLIF measurement was calibrated with a GT-Power model, and therefore bias errors in the temperature measurement can be caused by the accuracy of the GT-Power model. Finally, noise and uncertainty in the heat flux probe measurement will impact surface heat flux comparisons with the simulations.

7.2 Future Work

Improvements are needed in the simulations, especially in the high-shear intake jet region. As the intake jet interacts with the engine surfaces and the in-cylinder flow, vortices are created. It was shown that the velocity magnitude in the intake jet was overpredicted. This has implications not only in the vortex center predictions but also in heat transfer, as larger velocities lead to larger convective heat transfer, especially in the valve region and jet impingement regions. Comparisons of the near-wall flow and temperature fields show the need for improved wall models. The momentum and heat transfer models were developed for steady, wall-parallel flows with assumptions that do not apply to engine flows, which are highly three-dimensional, non-uniform, and unsteady, with non-negligible pressure gradients. Measurements show the dependence of the

velocity profiles on crank angle degree location. This drives the need for LES-based wall models with temporally-varying constants. The combustion modeling in CONVERGE is sensitive to the turbulent flame speed constant b_1 and the Converge version used. A parametric study needs to be performed with LES CHT to find $b_1$value that follows experimental turbulent flame speed measurements and that accurately captures the peak pressure, which can in turn help improve the surface temperature and heat flux predictions. Finally, engine simulations will likely need to be simulated with higher-order differencing schemes to improve velocity predictions.

While the LES reached statistical convergence after 10 cycles, there is an underestimation of the cyclic variation. The LES CHT model helps to improve this by predicting cyclic variation in the surface temperatures, but more LES cycles will likely be needed to capture the level of CCV in the experiments. However, LES combined with CHT will increase computational expenses. To decrease such computational expenses, one suggestion is to apply the spatially and temporally varying surface temperatures predicted by LES CHT on multi-cycle LES without CHT.

Bulk temperature field measurements are needed to validate the temperature fields of the simulations and to assess the predictive capability of the LES CHT. Currently, the surface temperature and heat flux of the LES CHT was validated at a single location on the engine head surface. To fully validate the LES CHT, spatially-resolved surface temperature and heat flux measurements are needed at multiple locations within the combustion chamber, such as the spark plug and the piston quartz and metal crown surfaces. In addition, measuring the temperature on the outer surfaces will provide more accurate outer thermal boundary conditions at these locations. Finally, the near-wall velocity and temperature measurements were performed in a plane parallel to the tumble plane. Such measurements can be performed in a perpendicular plane to further characterize the near-wall behavior of the highly three-dimensional engine flows. Simultaneous measurements of the near-wall velocity and temperature fields could also enable the full characterization of the engine boundary layer.

On the analysis side, the three-dimensional data from LES CHT can be used to provide a better understanding of the engine turbulence and heat transfer, as currently only in-plane data was analyzed. Also, the turbulent heat flux correlation $\langle \mathrm{v}'T' \rangle$ can be analyzed to study the effects of relative velocity on heat transfer. Finally, the spatial correlation and length scale analysis using relative values can be extended to the wall-parallel direction to fully characterize the heat transfer in that direction.

Bibliography

[1] "International energy statistics." U.S. Energy Information Administration. https://www.eia.gov/beta/international/data/browser/ -/?c=410000000200006000000000000g000200000000000000001&vs=INTL.44-1-AFRC-QBTU.A&vo=0&v=H&end=2016 (accessed 01/28/2019.

[2] "U.S. energy consumption rose slightly in 2016 despite a significant decline in coal use." https://www.eia.gov/todayinenergy/detail.php?id=30652 (accessed 01/28/2019.

[3] "U.S. energy facts explained." U.S. Energy Information Administration. https://www.eia.gov/energyexplained/index.php?page=us_energy_home (accessed 9/18/2018.

[4] L. Capuano, "International Energy Outlook 2018," 2018.

[5] "Sources of greenhouse gas emissions." U.S. Environmental Protection Agency. https://www.epa.gov/ghgemissions/sources-greenhouse-gas-emissions (accessed 09/18/2018.

[6] G. Borman and K. Nishiwaki, "Internal-combustion engine heat transfer," Progress in Energy and Combustion Science, vol. 13, no. 1, pp. 1-46, 1987.

[7] L. Henrion et al., "Characterization of radiative heat transfer in a spark-ignition engine through high-speed experiments and simulations," Oil Gas Sci. Technol. – Rev. IFP Energies nouvelles, 10.2516/ogst/2019030 vol. 74, 2019.

[8] C. Paul, S. Ferreyro Fernandez, D. C. Haworth, S. Roy, and M. F. Modest, "A detailed modeling study of radiative heat transfer in a heavy-duty diesel engine," Combustion and Flame, vol. 200, pp. 325-341, 2019/02/01/ 2019, doi: https://doi.org/10.1016/j.combustflame.2018.11.032.

[9] J. P. Myers and A. C. Alkidas, "Effects of combustion-chamber surface temperature on the exhaust emissions of a single-cylinder spark-ignition engine," SAE paper 780642, 1978.

[10] A. C. Alkidas and J. P. Myers, "Transient heat-flux measurements in the combustion chamber of a spark-ignition engine," Journal of Heat Transfer, vol. 104, no. 1, pp. 62-67, 1982, doi: 10.1115/1.3245069.

[11] Y. Harigaya, F. Toda, S. Ohyagi, and H. Tsuji, "Surface temperature and wall heat flux in a spark-ignition engine under knocking and non-knocking conditions," SAE paper 891795, 1989: SAE International, doi: https://doi.org/10.4271/891795.

[12] O. Ezekoye, R. Greif, and R. F. Sawyer, "Increased surface temperature effects on wall heat transfer during unsteady flame quenching," Symposium (International) on Combustion, vol. 24, no. 1, pp. 1465-1472, 1992, doi: https://doi.org/10.1016/S0082-0784(06)80171-2.

[13] X. Wang, P. Price, C. R. Stone, and D. Richardson, "Heat release and heat flux in a spray-guided direct-injection gasoline engine," Proceedings of the Institution of Mechanical Engineers, Part D: Journal of Automobile Engineering, vol. 221, no. 11, pp. 1441-1452, 2007, doi: 10.1243/09544070jauto586.

[14] J. E. Dec, "Advanced compression-ignition engines—understanding the in-cylinder processes," Proceedings of the Combustion Institute, vol. 32, no. 2, pp. 2727-2742, 2009, doi: https://doi.org/10.1016/j.proci.2008.08.008.
[15] J. Chang et al., "New heat transfer correlation for an HCCI engine derived from measurements of instantaneous surface heat flux," SAE paper 2004-01-2996, 2004, doi: https://doi.org/10.4271/2004-01-2996.
[16] "Mazda's new SKYACTIV gasoline and diesel engines are steps on the road to its "Ideal Engine"; focus on compression ratio." https://www.greencarcongress.com/2011/08/skyactiv-20110804.html (accessed 2018).
[17] J. L. Lumley, Engines: An introduction. Cambridge; New York: Cambridge University Press, 1999.
[18] J. B. Heywood, Internal combustion engine fundamentals (McGraw-Hill series in mechanical engineering). New York: McGraw-Hill Inc., 1988.
[19] M. J. Hall and F. V. Bracco, "Cycle-resolved velocity and turbulence measurements near the cylinder wall of a firing S.I. engine," SAE paper 861530, 1986, doi: 10.4271/861530.
[20] D. E. Foster and P. O. Witze, "Velocity measurements in the wall boundary layer of a spark-ignited research engine," Fuels and Lubricants, vol. 96, no. 7, pp. 534-547, 1987, doi: 10.4271/872105.
[21] D. L. Reuss, R. J. Adrian, C. C. Landreth, D. T. French, and T. D. Fansler, "Instantaneous planar measurements of velocity and large-scale vorticity and strain rate in an engine using particle-image velocimetry," Detroit, MI, 1989, SAE 890616.
[22] P. Schiffmann, S. Gupta, D. Reuss, V. Sick, X. Yang, and T. W. Kuo, "TCC-III engine benchmark for large-eddy simulation of IC engine flows," Oil Gas Sci. Technol. – Rev. IFP Energies nouvelles, vol. 71, no. 3, 2016, doi: 10.2516/ogst/2015028.
[23] E. Baum, B. Peterson, B. Böhm, and A. Dreizler, "On the validation of large-eddy simulation applied to internal combustion engine flows: Part 1: Comprehensive experimental database," Flow, Turbulence and Combustion, vol. 92, no. 1-2, pp. 269-297, 2014, doi: 10.1007/s10494-013-9468-6.
[24] D. Heim and J. Ghandhi, "A detailed study of in-cylinder flow and turbulence using PIV," SAE International Journal of Engines, vol. 4, no. 1, pp. 1642-1668, 2011, doi: 10.4271/2011-01-1287.
[25] F. Zentgraf, E. Baum, B. Bohm, A. Dreizler, and B. Peterson, "On the turbulent flow in piston engines: Coupling of statistical theory quantities and instantaneous turbulence," Physics of Fluids, vol. 28, no. 4, 2016, doi: 10.1063/1.4945785.
[26] P. H. Pierce, J. B. Ghandhi, and J. K. Martin, "Near-wall velocity characteristics in valved and ported motored engines," presented at the SAE International Congress & Exposition, 1992, SAE 920152.
[27] A. Y. Alharbi and V. Sick, "Investigation of boundary layers in internal combustion engines using a hybrid algorithm of high speed micro-PIV and PTV," Experiments in Fluids, vol. 49, no. 4, pp. 949-959, 2010, doi: 10.1007/s00348-010-0870-8.
[28] C. Jainski, L. Lu, A. Dreizler, and V. Sick, "High-speed micro particle image velocimetry studies of boundary-layer flows in a direct-injection engine," (in English), International Journal of Engine Research, vol. 14, no. 3, pp. 247-259, 2013, doi: 10.1177/1468087412455746.

[29] M. Greene, "Momentum near-wall region characterization in a reciprocating internal-combustion engine," PhD, Mechanical Engineering, University of Michigan, Ann Arbor, MI, 2017.
[30] J. R. MacDonald, C. M. Fajardo, M. Greene, D. Reuss, and V. Sick, "Two-point spatial velocity correlations in the near-wall region of a reciprocating internal combustion engine," presented at the SAE World Congress Experience, 2017, SAE 2017-01-0613.
[31] E. Lyford-Pike and J. B. Heywood, "Thermal boundary layer thickness in the cylinder of a spark-ignition engine," International Journal of Heat and Mass Transfer, vol. 27, no. 10, pp. 1873-1878, 1984.
[32] R. P. Lucht and M. A. Maris, "CARS measurements of temperature profiles near a wall in an internal combustion engine," Reciprocating Engines - Spark Ignition and Diesel, vol. 96, no. 4, pp. 468-474, 1987, doi: https://doi.org/10.4271/870459.
[33] J. Snyder, N. Dronniou, J. E. Dec, and R. Hanson, "PLIF measurements of thermal stratification in an HCCI engine under fired operation," SAE International Journal of Engines, vol. 4, no. 1, pp. 1669-1688, 2011, doi: https://doi.org/10.4271/2011-01-1291.
[34] J. E. Dec and W. Hwang, "Characterizing the development of thermal stratification in an HCCI engine using planar-imaging thermometry," SAE Int. J. Engines, vol. 2, no. 1, pp. 421-438, 2009, doi: https://doi.org/10.4271/2009-01-0650.
[35] S. A. Kaiser, M. Schild, and C. Schulz, "Thermal stratification in an internal combustion engine due to wall heat transfer measured by laser-induced fluorescence," Proceedings of the Combustion Institute, vol. 34, no. 2, pp. 2911-2919, 2013, doi: https://doi.org/10.1016/j.proci.2012.05.059.
[36] M. E. Cundy and V. Sick, "An approach to identify boundary layer temperature field structures in internal combustion engines," in CI/CS Spring Technical Meeting, Toronto, CA, 2012, pp. 02-001.
[37] B. Peterson, E. Baum, B. Böhm, V. Sick, and A. Dreizler, "High-speed PIV and LIF imaging of temperature stratification in an internal combustion engine," Proceedings of the Combustion Institute, vol. 34, no. 2, pp. 3653-3660, 2013, doi: https://doi.org/10.1016/j.proci.2012.05.051.
[38] A. Wu, M. K. Alzuabi, and V. Sick, "Spatial correlation and length scale analysis of the near-wall flow and temperature distribution of an internal combustion engine," presented at the SAE World Congress, Detroit, MI, 2020, SAE Paper 2020-01-1106.
[39] M. K. Alzuabi, "Imaging of temperature variations in the near-wall region of an optical reciprocating engine using laser-induced fluorescence," PhD, Mechanical Engineering, University of Michigan, Ann Arbor, 2020.
[40] F. Nicollet et al., "A PIV-guided large-eddy simulation of in-cylinder flows," Oil Gas Sci. Technol. – Rev. IFP Energies nouvelles, 10.2516/ogst/2017022 vol. 72, no. 5, 2017.
[41] B. Enaux et al., "LES study of cycle-to-cycle variations in a spark ignition engine," Proceedings of the Combustion Institute, vol. 33, no. 2, pp. 3115-3122, 2011, doi: 10.1016/j.proci.2010.07.038.
[42] K. Truffin, C. Angelberger, S. Richard, and C. Pera, "Using large-eddy simulation and multivariate analysis to understand the sources of combustion cyclic variability in a spark-ignition engine," Combustion and Flame, vol. 162, no. 12, pp. 4371-4390, 2015, doi: 10.1016/j.combustflame.2015.07.003.
[43] T. Wang, W. Li, M. Jia, D. Liu, W. Qin, and X. Zhang, "Large-eddy simulation of in-cylinder flow in a DISI engine with charge motion control valve: Proper orthogonal

decomposition analysis and cyclic variation," Applied Thermal Engineering, vol. 75, pp. 561-574, 2015, doi: 10.1016/j.applthermaleng.2014.10.081.
[44] Z. Han, R. D. Reitz, P. J. Claybaker, C. J. Rutland, J. Yang, and R. W. Anderson, "Modeling the effects of intake flow structures on fuel/air mixing in a direct-injected spark-ignition engine," 1996, SAE 961192.
[45] C. J. Rutland, "Large-eddy simulations for internal combustion engines - a review," International Journal of Engine Research, vol. 12, no. 5, pp. 421-451, 2011, doi: 10.1177/1468087411407248.
[46] R. Scarcelli, K. Richards, E. Pomraning, P. K. Senecal, T. Wallner, and J. Sevik, "Cycle-to-cycle variations in multi-cycle engine RANS simulations," 2016, SAE 2016-01-0593.
[47] M. M. Ameen, M. Mirzaeian, F. Millo, and S. Som, "Numerical prediction of cyclic variability in a spark ignition engine using a parallel large eddy simulation approach," Journal of Energy Resources Technology, vol. 140, no. 5, pp. 052203-052203-10, 2018, doi: 10.1115/1.4039549.
[48] F. Fontanesi, A. d'Adamo, F. Rulli, S. Breda, and F. Berni, "Understanding the origin of engine CCV via LES: Strengths, weaknesses and needs," ed: Virtual Engine Research Institute and Fuels Initiative (VERIFI) Workshop, 2017.
[49] M. Ghaderi Masouleh, K. Keskinen, O. Kaario, H. Kahila, Y. M. Wright, and V. Vuorinen, "Flow and thermal field effects on cycle-to-cycle variation of combustion: scale-resolving simulation in a spark ignited simplified engine configuration," Applied Energy, vol. 230, pp. 486-505, 2018/11/15/ 2018, doi: https://doi.org/10.1016/j.apenergy.2018.08.046.
[50] V. Granet, O. Vermorel, C. Lacour, B. Enaux, V. Dugu, and T. Poinsot, "Large-eddy simulation and experimental study of cycle-to-cycle variations of stable and unstable operating points in a spark ignition engine," Combustion and Flame, vol. 159, no. 4, pp. 1562-1575, 2012, doi: 10.1016/j.combustflame.2011.11.018.
[51] R. Tatschl et al., "LES simulation of flame propagation in a direct-injection SI-engine to identify the causes of cycle-to-cycle combustion variations," SAE paper 2013-01-1084, 2013, doi: 10.4271/2013-01-1084.
[52] D. C. Haworth, "Large-eddy simulation of in-cylinder flows," Oil & Gas Science and Technology, vol. 54, no. 2, pp. 175-185, 1999.
[53] D. Goryntsev, A. Sadiki, M. Klein, and J. Janicka, "Large eddy simulation based analysis of the effects of cycle-to-cycle variations on air–fuel mixing in realistic DISI IC-engines," Proceedings of the Combustion Institute, vol. 32, no. 2, pp. 2759-2766, 2009/01/01/ 2009, doi: https://doi.org/10.1016/j.proci.2008.06.185.
[54] M. S. Toledo, L. Le Penven, M. Buffat, A. Cadiou, and J. Padilla, "Large eddy simulation of the generation and breakdown of a tumbling flow," International Journal of Heat and Fluid Flow, vol. 28, no. 1, pp. 113-126, 2007/02/01/ 2007, doi: https://doi.org/10.1016/j.ijheatfluidflow.2006.03.029.
[55] C. Hasse, V. Sohm, and B. Durst, "Detached eddy simulation of cyclic large scale fluctuations in a simplified engine setup," International Journal of Heat and Fluid Flow, vol. 30, no. 1, pp. 32-43, 2009, doi: https://doi.org/10.1016/j.ijheatfluidflow.2008.10.001.
[56] P. Abraham, K. Liu, D. Haworth, D. Reuss, and V. Sick, "Evaluating large-eddy simulation (LES) and high-speed particle image velocimetry (PIV) with phase-invariant proper orthogonal decomposition (POD)," Oil and Gas Science and Technology, vol. 69, no. 1, pp. 41-59, 2014, doi: 10.2516/ogst/2013126.

[57] B. Enaux et al., "Large eddy simulation of a motored single-cylinder piston engine: numerical strategies and validation," Flow, Turbulence and Combustion, vol. 86, no. 2, pp. 153-177, 2011/03/01 2011, doi: 10.1007/s10494-010-9299-7.
[58] C. Pera and C. Angelberger, "Large eddy simulation of a motored single-cylinder engine using system simulation to define boundary conditions: Methodology and validation," SAE International Journal of Engines, vol. 4, no. 1, pp. 948-963, 2011, doi: 10.4271/2011-01-0834.
[59] M. Baumann, F. Di Mare, and J. Janicka, "On the validation of large eddy simulation applied to internal combustion engine flows part II: Numerical analysis," Flow, Turbulence and Combustion, vol. 92, no. 1-2, pp. 299-317, 2014, doi: 10.1007/s10494-013-9472-x.
[60] T. W. Kuo, X. Yang, V. Gopalakrishnan, and Z. Chen, "Large eddy simulation for IC engine flows," Oil and Gas Science and Technology, vol. 69, no. 1, pp. 61-81, 2014, doi: 10.2516/ogst/2013127.
[61] V. H. Nichani, R. Jaime, S. Singh, X. Yang, and V. Sick, "Influence of discretization schemes and LES subgrid models on flow field predictions for a motored optical engine," 2018, SAE 2018-01-0185.
[62] V. Dugué, N. Gauchet, and D. Veynante, "Applicability of large eddy simulation to the fluid mechanics in a real engine configuration by means of an industrial code," 2006, SAE 2006-01-1194.
[63] O. Vermorel, S. Richard, O. Colin, C. Angelberger, A. Benkenida, and D. Veynante, "Multi-cycle LES simulations of flow and combustion in a PFI SI 4-valve production engine," 2007, SAE 2007-01-0151.
[64] O. Vermorel, S. Richard, O. Colin, C. Angelberger, A. Benkenida, and D. Veynante, "Towards the understanding of cyclic variability in a spark ignited engine using multi-cycle LES," Combustion and Flame, vol. 156, no. 8, pp. 1525-1541, 2009, doi: 10.1016/j.combustflame.2009.04.007.
[65] C. Hasse, V. Sohm, and B. Durst, "Numerical investigation of cyclic variations in gasoline engines using a hybrid URANS/LES modeling approach," Computers & Fluids, vol. 39, no. 1, pp. 25-48, 2010, doi: https://doi.org/10.1016/j.compfluid.2009.07.001.
[66] P. Janas, I. Wlokas, B. Böhm, and A. Kempf, "On the evolution of the flow field in a spark ignition engine," Flow, Turbulence and Combustion, vol. 98, no. 1, pp. 237-264, 2017/01/01 2017, doi: 10.1007/s10494-016-9744-3.
[67] V. Moureau, I. Barton, C. Angelberger, and T. Poinsot, "Towards large eddy simulation in internal-combustion engines: simulation of a compressed tumble flow," SAE International, no. 724, pp. 1-10, 2004, doi: 10.4271/2004-01-1995.
[68] Z. Yue, K. D. Edwards, C. S. Sluders, and S. Som, "Prediction of cyclic variability and knock-limited spark advance in a spark-ignition engine," Journal of Energy Resources Technology, vol. 141, no. 10, pp. 102201-102201-8, 2019, doi: 10.1115/1.4043393.
[69] H. Schlichting, Boundary-layer theory, 7th ed. (McGraw-Hill series in mechanical engineering). New York: McGraw-Hill, 1979.
[70] F. Brusiani, C. Forte, and G. M. Bianchi, "Assessment of a numerical methodology for large eddy simulation of ICE wall bounded non-reactive flows," 2007, SAE 2007-01-4145.

[71] M. Schmitt, R. N. Hu, Y. M. Wright, P. Soltic, and K. Boulouchos, "Multiple cycle LES simulations of a direct injection natural gas engine," (in English), Flow Turbulence and Combustion, vol. 95, no. 4, pp. 645-668, 2015, doi: 10.1007/s10494-015-9625-1.
[72] P. C. Ma et al., "Development and analysis of wall models for internal combustion engine simulations using high-speed micro-PIV measurements," Flow Turbulence and Combustion, vol. 98, no. 1, pp. 283-309, 2016, doi: https://doi.org/10.1007/s10494-016-9734-5.
[73] M. Schmitt, "Direct numerical simulations in engine-like geometries," Dr. sc., ETH Zurich, Zürich, Switzerland, 2014.
[74] H. Werner and H. Wengle, "Large-eddy simulation of turbulent flow over and around a cube in a plate channel," in Turbulent Shear Flows 8, Berlin, Heidelberg, F. Durst, R. Friedrich, B. E. Launder, F. W. Schmidt, U. Schumann, and J. H. Whitelaw, Eds., 1993: Springer Berlin Heidelberg, pp. 155-168, doi: https://doi.org/10.1007/978-3-642-77674-8_12.
[75] P. C. Ma, M. Greene, V. Sick, and M. Ihme, "Non-equilibrium wall-modeling for internal combustion engine simulations with wall heat transfer," International Journal of Engine Research, vol. 18, no. 1-2, pp. 15-25, 2017.
[76] C. Angelberger, T. Poinsot, and B. Delhay, "Improving near-wall combustion and wall heat transfer modeling in SI engine computations," presented at the SAE International Fuels & Lubricants Meeting & Exposition, 1997, SAE 972881.
[77] Z. Han and R. D. Reitz, "A temperature wall function formulation for variable-density turbulent flows with application to engine convective heat transfer modeling," International Journal of Heat and Mass Transfer, vol. 40, no. 3, pp. 613-625, 1997, doi: https://doi.org/10.1016/0017-9310(96)00117-2.
[78] S. Keum, H. Park, A. Babajimopoulos, D. N. Assanis, and D. Jung, "Modelling of heat transfer in internal combustion engines with variable density effect," International Journal of Engine Research, vol. 12, no. 6, pp. 513-526, 2011, doi: 10.1177/1468087411410015.
[79] F. Berni, G. Cicalese, and S. Fontanesi, "A modified thermal wall function for the estimation of gas-to-wall heat fluxes in CFD in-cylinder simulations of high performance spark-ignition engines," Applied Thermal Engineering, vol. 115, pp. 1045-1062, 2017, doi: https://doi.org/10.1016/j.applthermaleng.2017.01.055.
[80] S. Šarić and B. Basara, "A hybrid wall heat transfer model for IC engine simulations," SAE International Journal of Engines, vol. 8, no. 2, pp. 411-418, 2015, doi: https://doi.org/10.4271/2015-01-0388.
[81] S. Šarić, B. Basara, and Z. Žunič, "Advanced near-wall modeling for engine heat transfer," International Journal of Heat and Fluid Flow, vol. 63, pp. 205-211, 2017, doi: https://doi.org/10.1016/j.ijheatfluidflow.2016.06.019.
[82] M. A. Nuutinen, O. T. Kaario, V. A. Vuorinen, P. N. Nwosu, and M. J. Larmi, "Imbalance wall functions with density and material property variation effects applied to engine heat transfer computational fluid dynamics simulations," International Journal of Engine Research, vol. 15, no. 3, pp. 307-324, 2013, doi: 10.1177/1468087413481779.
[83] W. J. D. Annand and T. H. Ma, "Second paper: Instantaneous heat transfer rates to the cylinder head surface of a small compression-ignition engine," Proceedings of the Institution of Mechanical Engineers, vol. 185, no. 1, pp. 976-987, 1970, doi: 10.1243/PIME_PROC_1970_185_110_02.

[84] D. A. Blank, "Conjugate conduction-convection heat transfer model for the valve flow-field region of four-stroke piston engines," Numerical Heat Transfer, vol. 18, no. 3, 1990.
[85] Y. Liu and R. D. Reitz, "Modeling of heat conduction within chamber walls for multidimensional internal combustion engine simulations," International Journal of Heat and Mass Transfer, vol. 41, no. 6, pp. 859-869, 1998, doi: https://doi.org/10.1016/S0017-9310(97)00178-6.
[86] J. Xin, S. Shih, E. Itano, and Y. Maeda, "Integration of 3D combustion simulations and conjugate heat transfer analysis to quantitatively evaluate component temperatures," presented at the SAE Powertrain & Fluid Systems Conference & Exhibition, Pittsburgh, PA, 2003, SAE 2003-01-3128.
[87] E. Urip and S.-L. Yang, "An efficient IC engine conjugate heat transfer calculation for cooling system design," 2007, SAE 2007-01-0147.
[88] E. Urip, K. H. Liew, and S. L. Yang, "Modeling IC engine conjugate heat transfer using the KIVA code," Numerical Heat Transfer, Part A: Applications, vol. 52, no. 1, pp. 1-23, 2007, doi: 10.1080/10407780601112803.
[89] M. Nuutinen, O. Kaario, and M. Larmi, "Conjugate heat transfer in CI engine CFD simulations," 2008, SAE 2008-01-0973.
[90] S. Fontanesi, G. Cicalese, A. D'Adamo, and G. Pivetti, "Validation of a CFD methodology for the analysis of conjugate heat transfer in a high performance SI engine," presented at the SAE 10th International Conference on Engines & Vehicles, 2011, SAE 2011-24-0132.
[91] Y. Li and S.-C. Kong, "Coupling conjugate heat transfer with in-cylinder combustion modeling for engine simulation," International Journal of Heat and Mass Transfer, vol. 54, no. 11, pp. 2467-2478, 2011, doi: https://doi.org/10.1016/j.ijheatmasstransfer.2011.02.015.
[92] Z. Dong, G. Chen, Y. Jiang, and C. Wang, "Modeling of transient heat transfer for the 3-D coupling components in an internal-combustion engine," 2012, SAE 2012-01-1759.
[93] O. Iqbal, S. Jonnalagedda, K. Arora, L. Zhong, and S. Gaikwad, "Comparison of 1-D vs 3-D combustion boundary conditions for SI engine thermal load prediction," presented at the ASME 2013 Internal Combustion Engine Division Fall Technical Conference, 2013, ICEF2013-19227.
[94] S. Fontanesi, G. Cicalese, G. Cantore, and A. D'Adamo, "Integrated in-cylinder/CHT analysis for the prediction of abnormal combustion occurrence in gasoline engines," 2014, SAE 2014-01-1151.
[95] O. Iqbal, K. Arora, and M. Sanka, "Thermal map of an IC engine via conjugate heat transfer: Validation and test data correlation," SAE International Journal of Engines, vol. 7, no. 1, pp. 366-374, 2014, doi: https://doi.org/10.4271/2014-01-1180.
[96] G. Cicalese, F. Berni, and S. Fontanesi, "Integrated in-cylinder/CHT methodology for the simulation of the engine thermal field: An application to high performance turbocharged disi engines," SAE International Journal of Engines, vol. 9, no. 1, pp. 601-617, 2016-04-05 2016, doi: https://doi.org/10.4271/2016-01-0578.
[97] P. Kundu et al., "Modeling heat loss through pistons and effect of thermal boundary coatings in diesel engine simulations using a conjugate heat transfer model," 2016, SAE 2016-01-2235.
[98] G. Cicalese, F. Berni, S. Fontanesi, A. D'Adamo, and E. Andreoli, "A comprehensive CFD-CHT methodology for the characterization of a diesel engine: from the heat transfer

prediction to the thermal field evaluation," presented at the SAE International Powertrains, Fuels & Lubricants Meeting, 2017, SAE 2017-01-2196.
[99] M. Leguille, F. Ravet, J. Le Moine, E. Pomraning, K. Richards, and P. K. Senecal, "Coupled fluid-solid simulation for the prediction of gas-exposed surface temperature distribution in a SI engine," presented at the SAE World Congress Experience, 2017, SAE 2017-01-0669.
[100] M. Wu et al., "Study on methods of coupling numerical simulation of conjugate heat transfer and in-cylinder combustion process in GDI engine," presented at the SAE World Congress Experience, 2017, SAE 2017-01-0576.
[101] A. Broatch, P. Olmeda, X. Margot, and J. Escalona, "New approach to study the heat transfer in internal combustion engines by 3D modelling," International Journal of Thermal Sciences, vol. 138, pp. 405-415, 2019, doi: https://doi.org/10.1016/j.ijthermalsci.2019.01.006.
[102] A. Misdariis, O. Vermorel, and T. Poinsot, "LES of knocking in engines using dual heat transfer and two-step reduced schemes," Combustion and Flame, vol. 162, no. 11, pp. 4304-4312, 2015, doi: https://doi.org/10.1016/j.combustflame.2015.07.023.
[103] A. Robert, K. Truffin, N. Iafrate, S. Jay, O. Colin, and C. Angelberger, "Large-eddy simulation analysis of knock in a direct injection spark ignition engine," International Journal of Engine Research, vol. 20, no. 7, pp. 765-776, 2018, doi: 10.1177/1468087418796323.
[104] Y. A. Cengel, J. M. Cimbala, and R. H. Turner, Fundamentals of thermal-fluid sciences, 5th ed. New York, NY: McGraw-Hill Education, 2012.
[105] A. A. Amsden, P. J. O'Rourke, and T. D. Bulter. L. A. N. Laboratory. (1989). KIVA-II: A computer program for chemically reactive flows with sprays.
[106] S. B. Pope, Turbulent flows. Cambridge: Cambridge University Press, 2000.
[107] R. Ruderich and H. H. Fernholz, "An experimental investigation of a turbulent shear flow with separation, reverse flow, and reattachment," Journal of Fluid Mechanics, vol. 163, pp. 283-322, 1986, doi: 10.1017/S0022112086002306.
[108] W. Annand, "Heat transfer in the cylinder of reciprocating internal engines," Proc. Instn Mech. Engrs., vol. 173, no. 36, pp. 973-990, 1963.
[109] G. Woschni, "A universally applicable equation for the instantaneous heat transfer coefficient in the internal combustion engine," 1967, SAE 670931.
[110] G. Woschni, "Die berechnung der wandverluste und der thermischen belastung der bauteile von dieselmotoren," Motortechnishe Zeitschrift, vol. 30, no. 12, pp. 491-499, 1970.
[111] G. F. Hohenberg, "Advanced approaches for heat transfer calculations," 1979, SAE 790825.
[112] A. C. Alkidas and I.-S. Suh, "The effects of intake-flow configuration on the heat-release and heat-transfer characteristics of a single-cylinder four-valve S.I. engine," 1991, SAE 910296.
[113] A. C. Alkidas, "Heat transfer characteristics of a spark-ignition engine," Journal of Heat Transfer, vol. 102, no. 2, pp. 189-193, 1980, doi: 10.1115/1.3244258.
[114] K. W. Cho, D. Assanis, Z. Filipi, G. Szekely, P. Najt, and R. Rask, "Experimental investigation of combustion and heat transfer in a direct-injection spark ignition engine via instantaneous combustion chamber surface temperature measurements," Proceedings

of the Institution of Mechanical Engineers, Part D: Journal of Automobile Engineering, vol. 222, no. 11, pp. 2219-2233, 2008, doi: 10.1243/09544070JAUTO853.
[115] T. LeFeuvre, P. S. Myers, and O. A. Uyehara, "Experimental instantaneous heat fluxes in a Diesel engine and their correlation," 1969, SAE 690464.
[116] J. C. Dent and S. J. Sulaiman, "Convective and radiative heat transfer in a high swirl direct injection Diesel engine," SAE Transactions, vol. 86, pp. 1758-1783, 1977.
[117] P. Bradshaw and G. P. Huang, "The law of the wall in turbulent flow," Proceedings: Mathematical and Physical Sciences, Volume 451, Issue 1941, pp. 165-188, vol. 451, pp. 165-188, 1995, doi: 10.1098/rspa.1995.0122.
[118] B. E. Launder and D. B. Spalding, "The numerical computation of turbulent flows," Computer Methods in Applied Mechanics and Engineering, vol. 3, no. 2, pp. 269-289, 1974/03/01/ 1974, doi: https://doi.org/10.1016/0045-7825(74)90029-2.
[119] G. Decan, S. Broekaert, T. Lucchini, G. D'Errico, J. Vierendeels, and S. Verhelst, "Evaluation of wall heat flux models for full cycle CFD simulation of internal combustion engines under motoring operation," presented at the SAE 13th International Conference on Engines & Vehicles, 2017, SAE 2017-24-0032.
[120] P. Schiffmann, D. L. Reuss, and V. Sick. "TCC collection." https://deepblue.lib.umich.edu/data/collections/8k71nh59c (accessed 2018).
[121] A. Wu, S. Keum, and V. Sick, "Large eddy simulations with conjugate heat transfer (CHT) modeling of internal combustion engines (ICEs)," Oil Gas Sci. Technol. – Rev. IFP Energies nouvelles, vol. 74, no. 51, 2019, doi: https://doi.org/10.2516/ogst/2019029.
[122] D. J. O. Nijeweme, J. B. W. Kok, C. R. Stone, and L. Wyszynski, "Unsteady in-cylinder heat transfer in a spark ignition engine: experiments and modelling," Proceedings of the Institution of Mechanical Engineers, Part D: Journal of Automobile Engineering, vol. 215, no. 6, pp. 747-760, 2001, doi: 10.1243/0954407011528329.
[123] K. Richards, P. K. Senecal, and E. Pomraning, CONVERGE v2.4 manual. Madison, WI: Convergent Science, Inc., 2018.
[124] V. Yakhot and S. A. Orszag, "Renormalization group analysis of turbulence. I. Basic theory," Journal of Scientific Computing, vol. 1, no. 1, pp. 3-51, 1986, doi: 10.1007/BF01061452.
[125] E. Pomraning and C. J. Rutland, "Dynamic one-equation nonviscosity large-eddy simulation model," AIAA Journal, vol. 40, no. 4, pp. 689-701, 2002, doi: 10.2514/2.1701.
[126] R. I. Issa, "Solution of the implicitly discretised fluid flow equations by operator-splitting," Journal of Computational Physics, vol. 62, no. 1, pp. 40-65, 1986, doi: https://doi.org/10.1016/0021-9991(86)90099-9.
[127] M. Schmitt, C. E. Frouzakis, Y. M. Wright, A. G. Tomboulides, and K. Boulouchos, "Direct numerical simulation of the compression stroke under engine-relevant conditions: Evolution of the velocity and thermal boundary layers," International Journal of Heat and Mass Transfer, vol. 91, pp. 948-960, 2015, doi: https://doi.org/10.1016/j.ijheatmasstransfer.2015.08.031.
[128] M. Schmitt, C. E. Frouzakis, Y. M. Wright, A. G. Tomboulides, and K. Boulouchos, "Investigation of wall heat transfer and thermal stratification under engine-relevant conditions using DNS," International Journal of Engine Research, vol. 17, no. 1, pp. 63-75, 2015, doi: 10.1177/1468087415588710.

[129] N. Peters, Turbulent combustion. Cambridge, UK ; New York: Cambridge University Press, 2000.
[130] Ö. L. Gülder, "Correlations of laminar combustion data for alternative S.I. engine fuels," 1984, SAE 841000.
[131] H. Pitsch, "A G-equation formulation for large-eddy simulation of premixed turbulent combustion," Center for Turbulence Research Annual Research Briefs, vol. 4, 2002.
[132] F. di Mare, R. Knappstein, and M. Baumann, "Application of LES-quality criteria to internal combustion engine flows," Computers and Fluids, vol. 89, pp. 200-213, 2014, doi: 10.1016/j.compfluid.2013.11.003.
[133] M. M. Ameen, X. Yang, T.-w. Kuo, Q. Xue, and S. Som, "LES for simulating the gas exchange process in a spark ignition engine," presented at the ASME 2015 Internal Combustion Engine Division Fall Technical Conference, Houston, Texas, 2015, ASME ICEF2015-1002.
[134] C. D. Rakopoulos, G. M. Kosmadakis, and E. G. Pariotis, "Critical evaluation of current heat transfer models used in CFD in-cylinder engine simulations and establishment of a comprehensive wall-function formulation," Applied Energy, vol. 87, no. 5, pp. 1612-1630, 2010, doi: https://doi.org/10.1016/j.apenergy.2009.09.029.
[135] P. M. Lillo, H. Zhuang, and V. Sick, "Topological development of homogeneous-charge and spray-guided stratified-charge flames in an internal combustion engine," International Journal of Engine Research, vol. 0, no. 0, 2017, doi: 10.1177/1468087417727192.
[136] B. Sagot, G. Antonini, A. Christgen, and F. Buron, "Jet impingement heat transfer on a flat plate at a constant wall temperature," International Journal of Thermal Sciences, vol. 47, no. 12, pp. 1610-1619, 2008, doi: https://doi.org/10.1016/j.ijthermalsci.2007.10.020.
[137] K. Liu and D. C. Haworth, "Development and assessment of POD for analysis of turbulent flow in piston engines," 2011, SAE 2011-01-0830.
[138] H. Chen, H. Zhuang, D. L. Reuss, and V. Sick, "Influence of early and late fuel injection on air flow structure and kinetic energy in an optical SIDI engine," 2018, SAE 2018-01-0205.
[139] S. B. Pope, "Ten questions concerning the large-eddy simulation of turbulent flows," New Journal of Physics, vol. 6, no. 1, 2004, doi: 10.1088/1367-2630/6/1/035.
[140] P. Schiffmann, "Root causes of cycle-to-cycle combustion variations in spark ignited engines," PhD, Mechanical Engineering, University of Michigan, Ann Arbor, MI, 2016.
[141] A. Wu, S. Keum, M. Greene, D. Reuss, and V. Sick, "Comparison of near-wall flow and heat transfer of an internal combustion engine using particle image velocimetry and computational fluid dynamics," presented at the ASME 2018 Internal Combustion Engine Division Fall Technical Conference, San Diego, CA, 2018, ICEF-9676.
[142] A. Wu, S. Keum, M. Greene, D. Reuss, and V. Sick, "Comparison of near-wall flow and heat transfer of an internal combustion engine using particle image velocimetry and computational fluid dynamics," Journal of Energy Resources Technology, vol. 141, no. 12, 2019, doi: 10.1115/1.4044021.
[143] W. Sutherland, "LII. The viscosity of gases and molecular force," The London, Edinburgh, and Dublin Philosophical Magazine and Journal of Science, vol. 36, no. 223, pp. 507-531, 1893, doi: 10.1080/14786449308620508.
[144] N. Dronniou and J. E. Dec, "Investigating the development of thermal stratification from the near-wall regions to the bulk-gas in an HCCI engine with planar imaging

thermometry," SAE Int. J. Engines, vol. 5, no. 3, pp. 1046-1074, 2012, doi: https://doi.org/10.4271/2012-01-1111.
[145] B. Peterson, E. Baum, B. Böhm, V. Sick, and A. Dreizler, "Evaluation of toluene LIF thermometry detection strategies applied in an internal combustion engine," Applied Physics B, vol. 117, no. 1, pp. 151-175, 2014, doi: 10.1007/s00340-014-5815-0.
[146] M. Schmitt, C. E. Frouzakis, A. G. Tomboulides, Y. M. Wright, and K. Boulouchos, "Direct numerical simulation of the effect of compression on the flow, temperature and composition under engine-like conditions," Proceedings of the Combustion Institute, vol. 35, no. 3, pp. 3069-3077, 2015, doi: https://doi.org/10.1016/j.proci.2014.06.097.
[147] C. Funk, V. Sick, D. L. Reuss, and W. J. A. Dahm, "Turbulence properties of high and low swirl in-cylinder flows," presented at the SAE Powertrain and Fluid Systems Conference & Exhibition, San Diego, CA, 2002, SAE 2002-01-2841.
[148] S. Breuer, M. Oberlack, and N. Peters, "Non-isotropic length scales during the compression stroke of a motored piston engine," Flow Turbulence and Combustion, vol. 74, pp. 145-167, 2005, doi: https://doi.org/10.1007/s10494-005-5457-8.
[149] P. Lillo, "Topological development of homogeneous-charge and stratified-charge flames in an internal combustion engine," PhD, Ann Arbor, MI, 2016.
[150] O. Güralp, P. Najt, and Z. S. Filipi, "Method for determining instantaneous temperature at the surface of combustion chamber deposits in an HCCI engine," Journal of Engineering for Gas Turbines and Power, vol. 135, no. 8, 2013, doi: 10.1115/1.4024180.